ABSTRACT

Title of Document: DEVELOPMENT OF A BOILING REGIME MAP AND GRAVITY SCALING PARAMETER FOR POOL BOILING HEAT TRANSFER

Rishi Raj, Ph.D., 2010

Directed By: Professor Jungho Kim, Department of Mechanical Engineering

Virtually all data to date regarding parametric effects of gravity on pool boiling have been inferred from experiments performed in low-*g*, 1*g*, and 1.8*g* conditions. The current work is based on observations of boiling heat transfer obtained over a continuous range of gravity levels (0*g*-1.8*g*) and varying heater sizes under subcooled liquid (FC-72/n-perfluorohexane) conditions. Variable gravity pool boiling heat transfer measurements were made during the parabolic flight campaigns organized by the European Space Agency (ESA) and NASA. Heater size was varied by using two (2.7x2.7 mm^2 and 7.0x7.0 mm^2) constant temperature microheater arrays consisting of 96 platinum resistance heaters deposited in a 10x10 configuration onto a quartz substrate. The ability to selectively power a subset of heater elements (1, 4, 9, 16, 25, 36, 64, and 96) in a square pattern out of the 10x10 configuration allowed a variation in heating area from 0.27x0.27 mm^2 to 7.0x7.0 mm^2. A parametric study on the effects of fluid properties, wall superheat, liquid subcooling, and dissolved gas concentration on boiling heat transfer was also performed.

Based on the heater sizes and the gravity levels investigated, two pool boiling regimes were identified. For large heaters and/or higher gravity conditions, buoyancy

dominated boiling and heat transfer results were heater size independent. Under low gravity conditions and/or for smaller heaters, surface tension forces dominated and heat transfer results were heater size dependent. A first ever pool boiling regime map differentiating buoyancy and surface tension dominated boiling regimes was developed. The non-dimensional ratio of heater size L_h and capillary length L_c was found suitable to differentiate between the boiling regimes. Transition between the regimes was observed to occur at a threshold value of $L_h/L_c \sim 2.1$.

Pool boiling data in the buoyancy dominated boiling regime ($L_h/L_c > 2.1$) was used to develop a gravity scaling parameter for pool boiling heat transfer. A non-dimensional temperature was defined in order to derive a gravity scaling parameter independent of dissolved gas concentrations and liquid subcooling. The power law coefficient for the gravity effect was observed to be a function of the non-dimensional wall temperature. The predicted results were found to be in good agreement with the heat transfer data over a wide range of gravity levels (0g-1.8g), dissolved gas concentrations, subcoolings, and heater surface morphologies. Use of this scaling parameter to obtain heat transfer at varying gravity levels is expected to save considerable experimental resources required to validate the performance of phase change based systems under different gravity conditions.

DEVELOPMENT OF A BOILING REGIME MAP AND GRAVITY SCALING PARAMETER FOR POOL BOILING HEAT TRANSFER

By

Rishi Raj

Dissertation submitted to the Faculty of the Graduate School of the
University of Maryland, College Park, in partial fulfillment of
the requirements for the degree of
Doctor of Philosophy
2010

Advisory Committee:
Professor Jungho Kim, Chair
Professor Avram Bar-Cohen
Associate Professor Gregory Jackson
Professor Marino di Marzo
Associate Professor Kenneth Yu

Dedication

Dedicated to my grandfather

Professor Suresh Chandra Kumar (1915-2004).

Acknowledgements

First and foremost, I am grateful to my advisor, Professor Jungho Kim, for being a constant source of encouragement and inspiration during the period of my graduate studies. This dissertation would not have been possible without his invaluable suggestions and guidance. I am thankful to Dr. Kim for always asking challenging questions and welcoming stimulating discussions. This work is built on the solid foundation of his vast experience and vision in this area. I also appreciate the guidance of my advisory committee: Dr. Avram Bar-Cohen, Dr. Gregory Jackson, Dr. Marino di Marzo and Dr. Kenneth Yu.

This work was supported by NASA Grant No. NNX08AI60A through the Advanced Capabilities Division in the Exploration Systems Mission Directorate at NASA Headquarters. I would like to personally thank our grant monitor John McQuillen for his help throughout this project. I would also like to thank the European Space Agency and NASA for accommodating our experiment on their respective parabolic flight campaigns.

I have been very fortunate to work with a number of current and former Phase Change Heat Transfer Lab personnel (Payam Delgoshaei, Greg Anderson, Jack Coursey, Bahman Abbasi, Micheal Siemann, Thierry Some, Kevin Moores, Chris Henry, Martin Karch, Markus Nicklas, Steven Fuqua, and Zan Liu). The countless discussions and arguments in which we engaged were invaluable to the progress and quality of this work. In particular, I would like thank Chris for a wonderful documentation of the previous work, Payam for designing the feedback circuits for the microheater arrays, and Jack, Martin and Markus for helping me during the preparation of the experimental setup. I would also like to acknowledge Greg, Michael, and Bahman for their suggestions

regarding the writing of my thesis. My graduate studies would not have been memorable and complete without the support of my friends Abhay, Aftab, Ajeet, Amit, Arvind, Debojyoti, Gaurav, Kunal, Nishad, Omkar, Sachin, Snehaunshu, and Suvajyoti.

Last but not the least; I would like to thank my parents and family for their unconditional love and immense support throughout my life. The academic environment I got at home always motivated me to pursue graduate studies. Finally, I would dedicate this dissertation to my grandfather for being my role model.

TABLE OF CONTENTS

LIST OF FIGURES

LIST OF TABLES

NOMENCLATURE

a	-	acceleration [m/s^2]
Bo	-	bond number
b	-	height of the embryo bubble [mm]
c	-	concentration [ppm]
C	-	concentration [moles/moles]
c_p	-	specific heat at constant pressure [W/kg-k]
D	-	bubble diameter [m]
DQ	-	potentiometer reading
f	-	departure frequency [s^{-1}]
g	-	acceleration due to gravity [m/s^2]
H	-	Henry's constant [mole/mole-Pa]
h	-	heat transfer coefficient [W/m^2-k]
h_{lv}	-	latent heat [J/kg]
k	-	thermal conductivity [W/m-k]
L	-	length scale [mm]
$\overline{M}$	-	molecular weight of vapor [kg/mol]
$\vec{n}$	-	unit vector normal to the interface
P	-	pressure [Pa]
Pr	-	Prandtl number
q''	-	heat flux [W/cm^2]
R_h	-	bubble radius [m]
$\overline{R}$	-	universal gas constant [J/mol-K]
T	-	temperature [°C]
T^*	-	temperature [°C]
TCR	-	temperature coefficient of resistance [°C^{-1}]
$\vec{t}$	-	unit vector tangent to the interface
V	-	velocity [m/s]
x	-	location along the bubble surface

y	-	coordinate perpendicular to heater

Greek

α	-	thermal diffusivity [m^2/s]
μ	-	dynamic viscosity [kg/m-s]
ν	-	kinematic viscosity [m^2/s]
φ	-	electric potential [V]
ρ	-	density [kg/m^3]
σ	-	surface tension [N/m]
$\hat{\sigma}$	-	accommodation coefficient
Θ	-	contact angle [degree]

Subscript

b	-	boiling
back	-	back of the chip
bulk	-	bulk liquid
c	-	capillary
depart	-	departure
exp	-	experimental value
f	-	forced convection, air-jet on
g	-	gas
gen	-	generated
h	-	shortest side
high	-	high gas
i	-	interface
l	-	liquid
low	-	low gas
n	-	natural convection, air-jet off
sat	-	saturation

sub	-	subcooling
v	-	vapor
w	-	superheat
wall	-	heater wall

Chapter 1: Background

1.1 INTRODUCTION

Boiling is the transition of a liquid to vapor phase when the vapor pressure of the liquid is equal to the ambient pressure. Conventionally, based on the relative motion of the bulk liquid with respect to the heater surface, boiling is divided into two categories; *pool boiling* and *flow boiling*. *Pool boiling* is the process in which the heated surface is submerged in a large pool of initially quiescent liquid, while, boiling process when all phases are under a bulk movement is termed as *flow boiling*. The relative motion of the vapor and the surrounding liquid near the heated surface in pool boiling is primarily due to the buoyancy effect. Furthermore, boiling is also distinguished depending on the temperature of the liquid pool / bulk liquid. Boiling when the bulk liquid temperature is below the saturation temperature of the liquid pool is termed as *subcooled boiling* while boiling under saturated bulk liquid is termed as *saturated boiling*.

In boiling, the variation of heat flux along a heated element results in a characteristic temperature response at the surface, reflecting a progression through regimes of heat transfer. Nukiyama in 1934 (Nukiyama 1934) identified the different regimes of pool boiling. The regimes of pool boiling are easily explained in terms of a plot of heat flux q'' versus wall superheat ΔT_w known as the *boiling curve*. A typical boiling curve is shown on Figure 1.2a. Nukiyama determined the heat flux from a horizontal nichrome wire to saturated water by measuring the current and potential drop across the wire. This arrangement termed as power–controlled heating where temperature T of the wire is a dependent variable produces a boiling curve shown by green solid arrows (path a-b-c-d-e-g). While decreasing the heat flux, a curve as represented by the

blue dashed arrows was observed (path g-f-c-b-a). Nukiyama proposed that the no hysteresis (path a-b-c-d-e-f-g during heating and path g-f-e-d-c-b-a during cooling) in the boiling curve be observed if the wall temperature is the controlled parameter and the heat flux is the dependent variable. This conjecture was consequently confirmed by Drew and Muller in 1937 (Drew *et al.* 1937).

The schematic representation of the regimes on pool boiling curve is shown in Figure 1.2b. Natural convection regime is represented by the region a-b in the boiling curve. Heat transfer is primarily due to the buoyancy effect. Increase in wall temperature initiates the growth of vapor bubbles at nucleation sites and boiling commences (Onset of Nucleate Boiling-ONB, point b). Region b-c-d-e represents the nucleate boiling regime. The violent disturbance of the hot boundary layer coupled with bulk fluid circulation induced by the motion of vapor bubbles leads to a very steep rise in the heat flux from the heater surface. Point e is the location of maximum heat flux. As the heat flux increases, bubbles generated at the surface coalesce to form vapor columns in which there are liquid droplets that fall back to the surface. Helmholtz unstable vapor columns are formed above the heater. The heater is almost surrounded by the vapor blanket and any further increase in temperature leads to a decrease in the heat transfer. This peak value is the maximum level of heat flux from the heated surface that the system can provide in a non-film boiling mode at a given pressure and is usually called the Critical Heat Flux (CHF). Leidenfrost point, the location of minimum heat flux, is represented by point f. Region f-g represents the film boiling regime. Heat transfer during film boiling is accomplished by the convection, conduction and radiation across the vapor film from the wall to the

interface. However, because liquid does not contact the surface, nucleation in surface cavities is not a part of the transport processes.

Pool boiling involves complicated non-linear processes operating over a large range of length and time scales. Boiling for large heaters and/or higher gravity conditions is buoyancy dominated and is a combination of natural convection, liquid-vapor phase change, and transient conduction. The ebullition cycle (Figure 1.1) associated with nucleation, bubble growth, departure and rewetting dominates the contribution to heat transfer. The presence of more than one phase, little understanding of the nucleation process, and a strong dependence on the fluid properties have hindered researchers from developing a completely deterministic model for heat transfer in pool boiling. The mechanism by which heat is removed from the surface and the effect of parameters such as gravity, subcooling, wall superheat, fluid properties, heater surface geometry, and structure are still unclear.

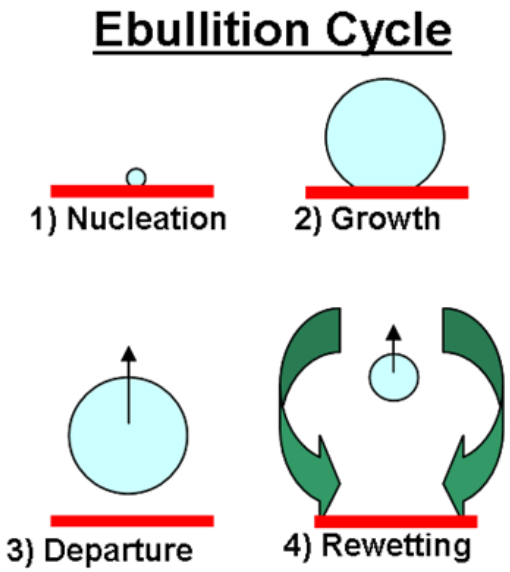

Figure 1.1: Ebullition cycle.

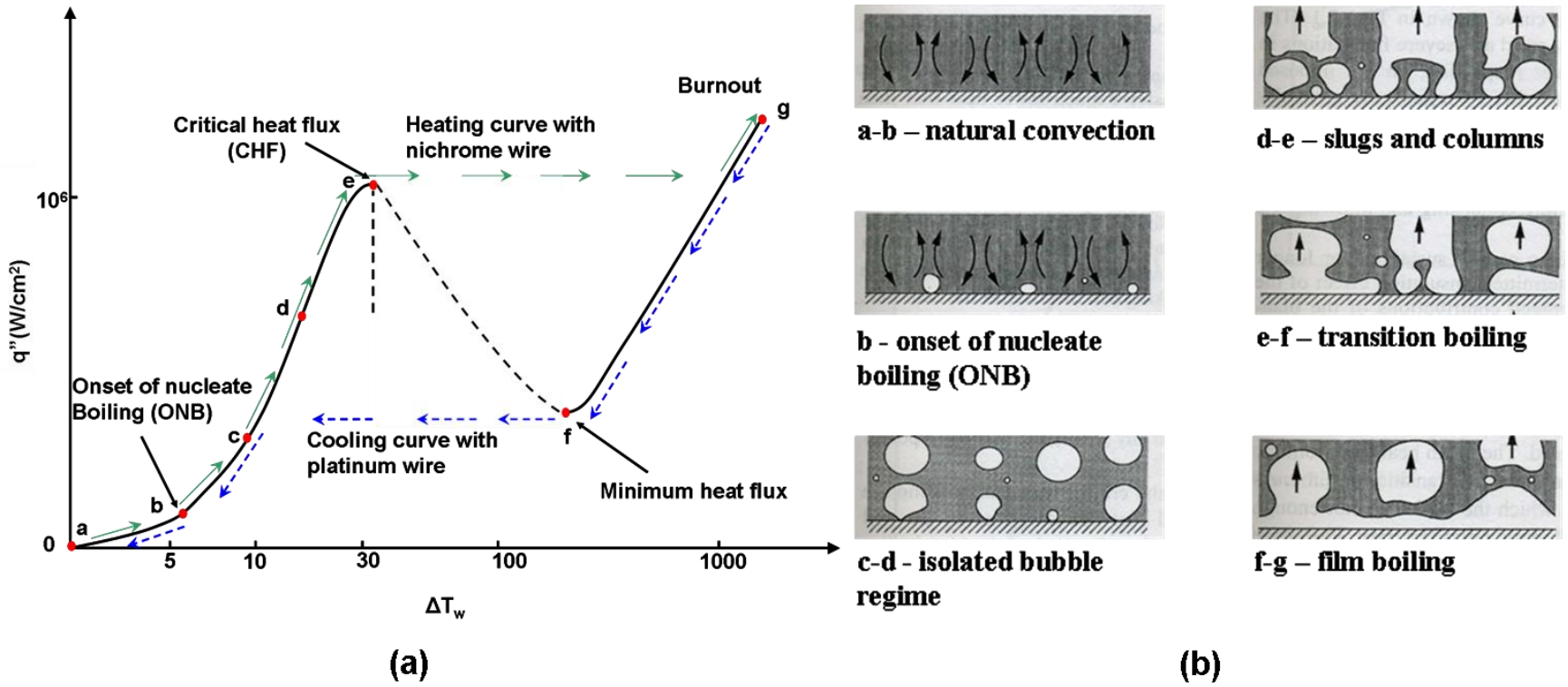

Figure 1.2: (a) A pool boiling curve, and (b) the photographic representation of heat transfer regimes (Adapted: Carey, Liquid-Vapor Phase-Change Phenomena, 1992).

Many analytical models have been developed that predict boiling behavior in earth gravity. A significant part of the classical boiling curve is based on the heat transfer behavior in the buoyancy dominated regime. Efforts have been made to characterize boiling heat transfer under earth gravity conditions for heaters much larger than capillary length scales. For large heaters and/or high gravity conditions, buoyancy dominates boiling and the boiling curve is heater size independent. All these studies estimate heat transfer from relatively large heaters in earth gravity but fail to account for boiling behavior across gravitational environments and at smaller length scales.

The primary mechanisms of heat transfer due to buoyancy effects become less significant and different mechanisms that are unimportant on earth start playing a significant role in the absence of gravity. Moreover, the relatively poor understanding of surface tension that becomes important at small length scales and/or low gravity levels is another roadblock. In the surface tension dominated boiling regime, the maximum bubble size becomes comparable to the heater size, reducing the bubble departure frequency and increasing the percentage dryout area on the heater. Particularly under microgravity conditions, a big non-departing primary bubble is observed to cover the heater (Figure 1.3).

Clearly, with the basic mechanism of heat transfer being different under these two gravity conditions (earth gravity and microgravity), an interpolation scheme for heat flux is not valid. It is important to identify the correct parametric effect of heater size and gravity to make successful prediction of heat fluxes. It is important to perform experiments over a continuous range of gravity levels and varying heaters sizes to identify the different regimes of boiling and transition points as these parameters change.

Further investigation of boiling at different gravity levels and varying parameters is also required to decipher the effect of other parameters that are usually masked under earth gravity conditions. Thermocapillary convection has been reported to be a major contributor to the overall heat transfer under microgravity conditions. Absence of gravity would also help in comprehensive physical understanding of thermocapillary convection.

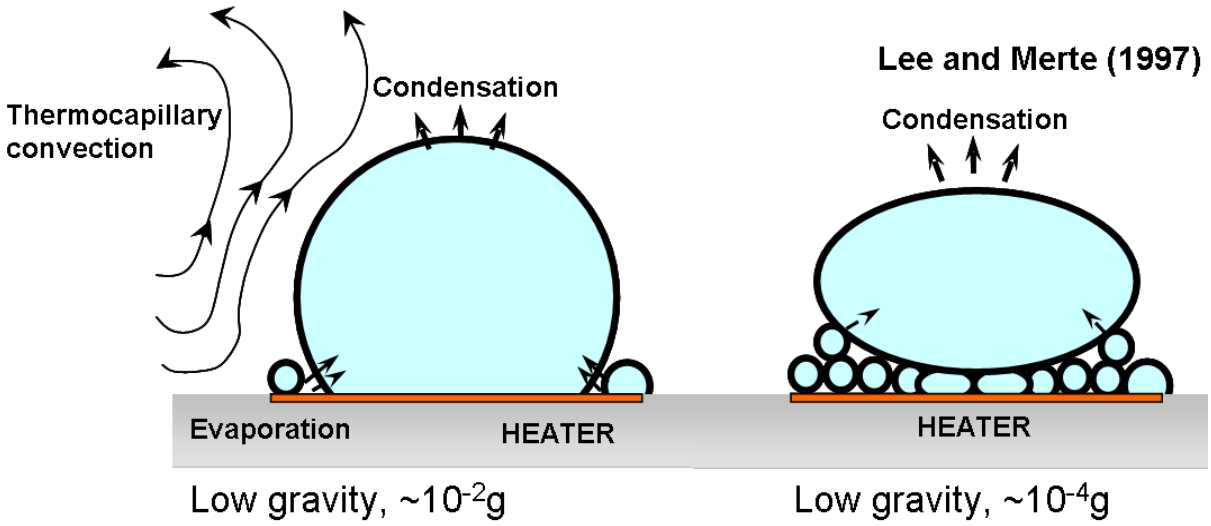

Figure 1.3: Schematic representation of boiling under low-g conditions.

1.2 APPLICATIONS

Phase change process associated with boiling play a vital role in many technical processes and their applications. The almost isothermal conditions during boiling associated with high heat transfer coefficients make the application of boiling indispensible. Applications of boiling heat transfer can be found in the following areas:

1. Cooling of electronic products,
2. Fluid handling and control,
3. Power systems,
4. Cryogenic fuel storage, and
5. Design of space based hardware.

Figure 1.4 represents the typical values of the thermal resistances for different modes of heat removal and fluids used for electronic cooling. Boiling provides smaller thermal resistances compared to the conventional modes of cooling. As a result, the heat transfer coefficient (HTC) due to boiling is order of magnitudes higher than single phase forced and natural convection.

Phase changed based thermal systems are also critical in the areas of advanced human technologies for longer duration microgravity and planetary missions. For an example, astronaut's safety and comfort depends on the thermal and humidity management of space suits. An advanced design of these suits incorporate miniature two-phase loop for heating and cooling. Similarly, a promising strategy for reducing mass requirements for cryogenic fuel storage requires optimized and synergetic design of ventless storage systems. These active ventless pressure control units would require better understanding of two-phase transport phenomena which are affected by gravity. Other

major applications include two-phase energy and power cycles, refrigeration systems, and thermal storage systems.

Experiments to date have shown that HTC during subcooled pool boiling under reduced gravity conditions are typically smaller than that observed at earth. Moreover, the heat transfer coefficients reported in literature vary significantly from experiment to experiment. The primary reason behind this inconsistency in literature is the increased importance of other mechanisms that are usually insignificant under earth gravity conditions. Little understanding of these mechanisms has stopped researchers from developing a completely deterministic model of pool boiling under these gravity conditions. As a result comparatively inefficient lower power single phase components are being used in space-based systems. Hence, it is important to understand these mechanisms and quantify the effect of parameters at those gravity levels. Quantification of gravity on two-phase flows would lead to reduction in the size and weight of these systems and significantly lower launch costs of components and space based systems.

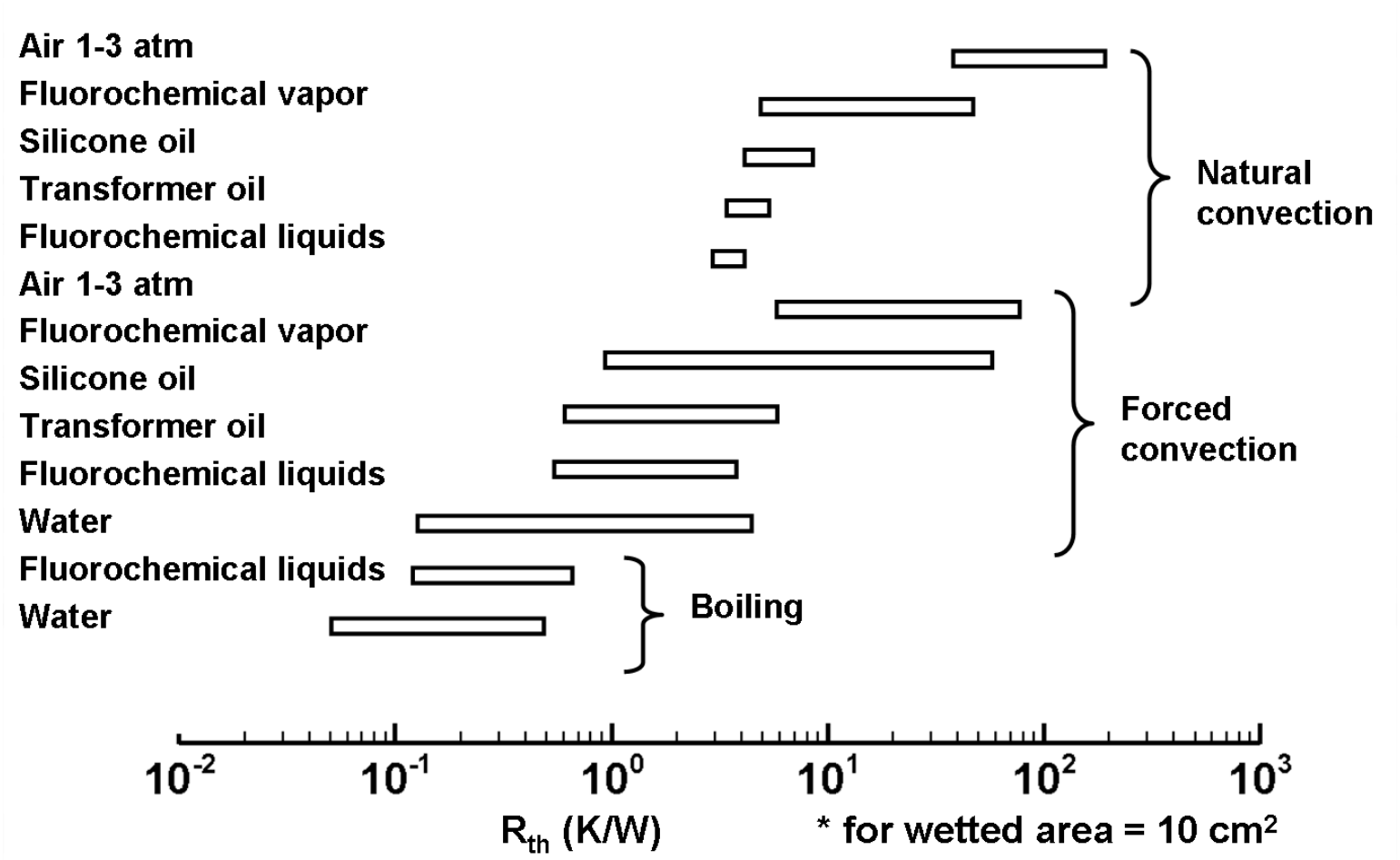

Figure 1.4: Typical value of thermal resistances encountered in major heat removal modes for electronic cooling (Courtesy: Dr. Avram Bar-Cohen, lecture notes, ENME 765).

1.3 MOTIVATION

Contemporary research is increasingly focused on miniaturization. With the advancement in device technology, the electronic industry is moving towards high-speed devices with constantly increasing thermal loads. The crisis of real estate in electronic packages coupled with the state-of-the-art manufacturing technology has led to the miniaturization of these devices. Many of these technologies have inherent scaling problems that limit functionality. In the absence of efficient cooling mechanisms, this characteristic is detrimental to performance. Understanding of boiling at these smaller length scales is hence of paramount importance to the design of these products and their successful operation.

Extension of applications utilizing multiphase heat transfer to space based technologies require understanding of boiling under different gravity conditions. An extract form NASA's Workshop on Critical Issues in Microgravity Fluids, Transport, and Reaction Processes in Advanced Human Support Technology, 2004 reads as follows:

> *"Future missions for exploration of the solar system will require enabling technologies for efficient and reliable energy generation, storage and transfer. Integration of several different engineering subsystems and strategies are envisioned. For example, energy generation may be provided by a combination of nuclear, chemical, or solar sources. Energy storage may be accomplished by rechargeable batteries, regenerative fuel cells, flywheels, or latent heat phase change processes, and energy transfer issues might range from large scale, as in cabin thermal control, to small scale, as in space suit temperature regulation. In*

most of these cases, design of the thermal subsystems becomes an important consideration.

Currently, most of the subsystems involve single-phase fluid and thermal processes; only a small number involve multiphase fluid and thermal processes. But the need for improved energy-to mass ratios suggests replacing some of the single-phase operations in favor of two-phase systems. Thus, the future design of important thermal subsystems for space applications as in boilers, condensers, evaporators, heat exchangers, normal and cryogenic fluid storage units, fuel cells, radiators, and heat pipes will all involve complex multiphase fluid flow and transport issues.

Fluid flow, heat and mass transfer, and phase separation are all affected by gravity. Unfortunately, there is a scarcity of reliable and pertinent reduced-gravity two-phase flow data. Therefore, a full understanding of both single and multiphase transport phenomena associated with the operation of the thermal and phase change subsystems in microgravity are needed for both the design of the units and their safe and efficient operation in space."

The report clearly highlights a lack of understanding of gravity effects on phase change based processes. A need for replacing single phase systems with two-phase systems was suggested to improve the energy-to mass ratio. Based on a critical review of the issues and problems associated with multiphase systems, the report recommended active research in the following two research areas:

a. Attainment of phenomenological understanding and accumulation of empirical data for boiling in microgravity.

b. Development of empirical correlations, theoretical models, and scaling laws for boiling process.

Much research effort has been focused on understanding boiling heat transfer under reduced gravity environments (Di Marco 2003; Kim 2003; and Ohta 2003). A recent report by microgravity researchers (Kim, J., Di Marco, P., Ohta, H. and Stephan, P.) also identified a need for research in the partial gravity regime. They proposed that the understanding of boiling under variable gravity environments is essential for partial gravity situations that can exist when thrusters are fired, or for operations on Moon or Mars. Moreover, partial gravity research will allow validation of scaling laws and identify their regions of applicability.

The current work is a part of the ongoing research initiative to resolve these issues for realization of two-phase systems for future space explorations. Based on these recommendations, an extensive literature survey of the boiling literature was performed to identify the critical issues that needed further attention.

Chapter 2: Literature Review

Many studies to date have successfully analyzed and modeled boiling behavior under earth gravity conditions. New technologies based on phase change heat transfer have been enabled as a result of these advances. However, boiling has not been used in spaced-based systems due to little knowledge of the physical mechanisms causing heat removal from the boiling surface. For this reason, much research effort has been directed towards understanding boiling under reduced gravity conditions (Di Marco 2003; Kim 2003; and Ohta 2003).

This chapter highlights the current status of understanding and prediction tools available for pool boiling heat flux during nucleate boiling regime. In an effort to understand the effect of gravity, a review of major pool boiling correlations largely based on earth gravity observations is presented first. Then, a comprehensive review of the low gravity work is presented. A list of available studies focusing on the effects of gravity was identified. The earth gravity and microgravity studies are then correlated to identify the inconsistencies in the literature. Considering the fact that effect of non-condensable gases on boiling heat flux becomes significant at lower gravity levels, a review of the available literature on the effects of non-condensable gases is also performed.

A review of heater size effect on pool boiling is performed next. Boiling on small heaters has often been reported to be surface tension dominated and speculated to be similar in nature to low gravity boiling. An effort was also made to identify similarities between the effect of heater size and gravity in the surface tension dominated boiling regime, if any. Moreover, the heater arrays used in this study (2.7x2.7 mm^2 and 7x7 mm^2, Figure 3.6) are relatively small compared to the conventional heaters used in

literature. Hence, it was also essential to review the effect of heater size on pool boiling heat transfer and make sure that the observed behaviors were not a manifestation of heaters being small in size.

2.1 EFFECTS OF GRAVITY

2.1.1 Pool Boiling Correlations

It has been mostly assumed in the literature that the heat transfer dependence on gravity can be captured through the use of a power law of the form $q'' \alpha a^m$ where m=constant. For example, the widely used semi-theoretical model proposed by Rohsenow 1962 is based on the assumption that the enhanced single phase convection due to local agitation of the liquid flowing behind the wake of a departing bubble was responsible for the heat transfer. He identified the velocity of a vapor bubble at the instant of departure from the heater as being the appropriate velocity scale. The bubble departure diameter was selected as the appropriate length scale. Based on these assumptions, the Rohsenow correlation (Eq. 2.1) suggests that the power law coefficient m is 1/2 in the nucleate boiling regime:

$$\frac{q''}{\mu_l h_{lv}}\left[\frac{\sigma}{g(\rho_l-\rho_v)}\right]^{1/2}=\left(\frac{1}{C_{sf}}\right)^{1/r}\mathrm{Pr}_l^{-s/r}\left[\frac{C_{pl}\left[T_w-T_{sat}(P_l)\right]}{h_{lv}}\right]^{1/r} \tag{2.1}$$

Microconvection model by Foster and Zuber 1955 used bubble growth rate as the appropriate velocity scale, however, their model is independent of gravity level (m=0). Vapor-liquid exchange model proposed by Forster and Grief 1959 (Eq. 2.2) was based on the postulation that bubbles act as microscopic pumps drawing cold liquids to the surface as the bubble departs. Based on this postulated behavior, they developed a model which did not have any implicit term to account for the effect of gravity. However, the effect of

gravity was accounted for by the maximum bubble radius until hemispherical growth, R_{max} , and bubble departure frequency, f.

$$q'' = \rho_l c_{pl} \left(\frac{2\pi}{3} \right) R^3{}_{\max} \left(\frac{1}{2} \right) (T_w - T_l) f n'_a \qquad (2.2)$$

Stephan and Abdelsalam 1980 adopted the approach of dimensional analysis along with the statistical regression of the available data to develop a correlation for nucleate pool boiling heat transfer. Based on optimal fits to the experimental data, they proposed separate correlations for water, hydrocarbons, cryogenic fluids and refrigerants. The effect of gravity was again implicit and being accommodated by including the bubble departure diameter D_d in the dimensionless terms. A summary of these models and others available in literature is presented in Table 2.1.

Semi-theoretical approaches have also been adopted to predict the critical heat flux (CHF). Four different mechanisms have been postulated as the cause of CHF in pool boiling:

- Kutateladze 1948 observed a similarity between flooding phenomena in distillation columns and CHF in pool boiling. In a distillation column, vapor rich in the more volatile component flows upward while liquid containing more of the less volatile component flows downward. If the relative velocity of the two streams becomes too large, the flow becomes Helmholtz unstable, impeding the flow of liquid to the heated surface (Figure 2.1a).
- The second mechanism is based on bubble packing due to increase in nucleation site density. Rohsenow and Griffith 1956 proposed that bubble

packing inhibits liquid flow to surface forming vapor blanket on top of heater which leads to CHF.

- Chang 1957 linked the Taylor's interface stability analysis and pool boiling phenomena. These studies influenced Zuber 1959 (Eq. 2.3) to develop a more detailed hydrodynamic model with Taylor wave motion and Helmholtz instability the key elements.

$$q''_{CHF} = 0.131\rho_v h_{lv}\left[\frac{\sigma(\rho_l - \rho_v)g}{\rho_v^2}\right]^{0.25} \quad (2.3)$$

- Haramura and Katto 1983 proposed that the smaller vapor jets connected with individual nucleation sites carry vapor to large bubble which is fed by a number of small jets as shown in Figure 2.1b. It was proposed that the thickness of these jets is small such that they are Helmholtz unstable. According to this theory, CHF is attained when the liquid film under the bubble evaporated completely during the time interval needed for bubble to grow enough to escape to the bulk liquid.

Interestingly, even though the basic postulated mechanisms are different, the power law coefficient for CHF reported by all these studies was same, 0.25. Later, Kirishenko *et al.* 1973 and Kandlikar 2001 also proposed a power law coefficient of 0.25 for CHF. This is strikingly different from the nucleate boiling case where not much agreement on power law coefficient for gravity effect was reported (Table 2.1). A summary of CHF models along with the power law coefficients m for gravity effect is presented in Table 2.2.

Table 2.1: Nucleate pool boiling correlations.

Study	**Comments**	**Gravity dependence ($q'' \alpha g^m$)**
Rohsenow, 1952	Enhanced single phase convection model	Power law behavior where m=0.5
Foster and Zuber, 1955	Microconvection model	Independent of gravity
Foster and Greif, 1959	Vapor-liquid exchange model	Gravity effect implicit in f
Tien, 1962	Inverted stagnant flow model	Independent of gravity
Stephan and Abdelsalam, 1980	Statistical correlation of data	Gravity effect implicit in D_d

Table 2.2: Critical heat flux correlations.

Study	**Comments**	**Gravity dependence ($q''_{CHF} \alpha g^m$)**
Kutateladze, 1948	Analogy between CHF and flooding in distillation columns	m=0.25
Chang, 1957	Model based on Taylor wave motion	m=0.25
Zuber, 1959	Model based on Helmholtz instability	m=0.25
Kirishenko *et al.*, 1973	Included contact angle as a parameter	m=0.25
Kandlikar, 2001	Theoretical model based on surface tension, hydrostatic pressure forces, and evaporation momentum forces	m=0.25

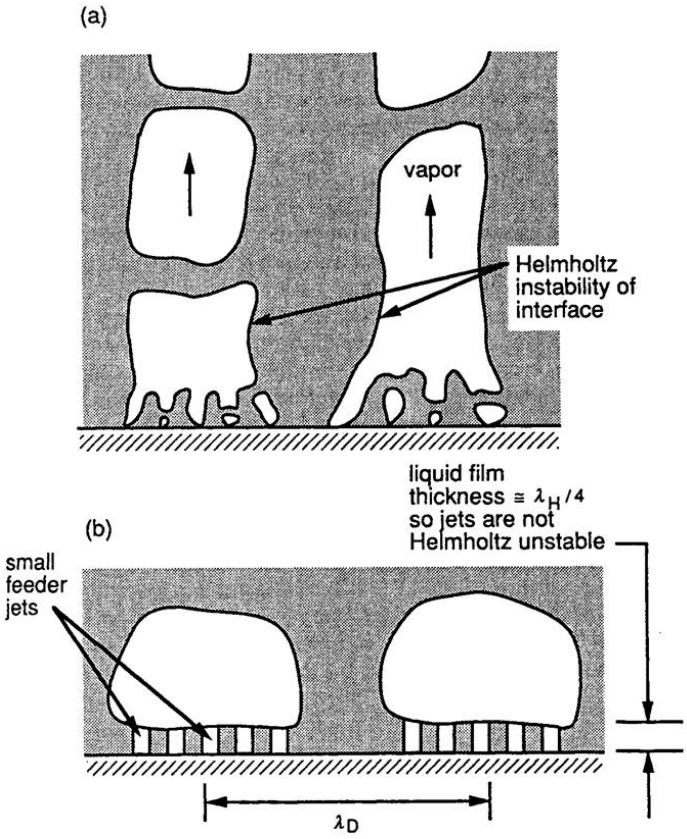

Figure 2.1: Postulated Helmholtz instability mechanisms (Van Carey, 1992).

A lack of consensus on the effect of gravity on pool boiling heat transfer during the nucleate pool boiling regime is evident from Table 2.1. It was not possible to calculate power law coefficients for all correlations except for the first two due to an indirect dependence on gravity. Hence, a survey of literature was performed to identify the major correlations for bubble departure diameter and bubble departure frequency. Table 2.3 presents the major departure diameter correlations. Many bubble departure frequency correlations were again indirectly related to gravity and depended on the departure diameter term. Hence, Fritz correlation for bubble departure diameter was used to arrive at the power law coefficient for gravity effect on departure frequency. The results obtained from this analysis are summarized in Table 2.4.

Table 2.3: Departure diameter correlations

Study	**Comments**	**Gravity dependence ($D_d \propto g^m$)**
Fritz, 1935	Balance of surface tension and buoyancy	*m*=-0.5
Zuber, 1959	Model based on surface tension, buoyancy, size of bubble and superheated liquid layer thickness	*m*=-0.33
Ruckenstein, 1963	Balance of buoyancy, drag and surface tension	*m*=-0.33
Cole, 1967	Functional dependence of *Bo* on *Ja* based on wall superheat	*m*=-0.5
Cole et al., 1968	Functional dependence of *Bo* on *Ja* based on T_c	*m*=-0.5

Table 2.4: Departure frequency correlations

Study	**Comments**	**Gravity dependence ($f \propto g^m$)**
Jakob and Fritz, 1931	Relation for hydrogen and water vapor bubbles	*m*=0.5
Zuber, 1963	Model based on analogy between bubble release and natural convection	*m*=0.75
Ivey, 1967	Balance of buoyancy, drag and surface tension	*m*=0.25 for dynamically controlled growth and *m*=1 for thermally controlled growth
Malenkov 1971	Based on bubble size	*m=0.75*
Mickic and Rohsenow, 1969	Model for thermally controlled growth	*m*=0.25

It is clear that a consensus of the effect of gravity on bubble departure frequency and bubble departure diameter is also absent. However, all combinations of bubble departure frequency and departure diameter were used to calculate dependence of gravity on nucleate boiling correlations mentioned in Table 2.1. Table 2.5 presents the result of this analysis.

Table 2.5: Nucleate boiling correlations

Study	**Gravity dependence ($q'' \alpha g^m$)**
Rohsenow, 1952	m=0.5
Foster and Zuber, 1955	m=0
Foster and Greif, 1959	$0.25 \leq m \leq 1$
Tien, 1962	m=0
Stephan and Abdelsalam, 1980	$-0.033 \leq m \leq 0.48$

Based on the available correlations for the bubble departure diameter and bubble departure frequency, it is evident that there exists no consistency in the power law coefficient for nucleate boiling regime. While the power law coefficient for gravity dependence on heat transfer varies from -0.033 to 1 in the nucleate boiling regime, a value of 0.25 for CHF is widely agreed upon in the boiling literature (Table 2.2). If these studies are to be agreed upon, a jump discontinuity in the boiling curve at CHF will be observed. Such a jump in power law coefficient is not physical and unrealistic. All these studies hint towards a lack in understanding of gravity effect on pool boiling heat transfer.

2.1.2 Microgravity Boiling

Substantial research on pool boiling under reduced gravity conditions has been performed over the years (Di Marco 2003; Kim 2003; and Ohta 2003). Under microgravity conditions, the buoyancy force is not sufficient to remove bubbles from the surface, resulting in a large coalesced bubble that is fed by many smaller nucleating bubbles surrounding it (Figure 1.3). If the liquid is subcooled, surface tension gradients can also give rise to thermocapillary convection around the bubble that can significantly enhance the heat transfer in the absence of gravity.

Most of the early low gravity experiments used ground-based facilities like drop towers (Siegel 1968) and magnetic fields to compensate for earth gravity (Verkin *et al.* 1976). Aircrafts (Oka *et al.* 1992; Straub *et al.* 1999; and Kim *et al.* 2002) and sounding rockets (Straub *et al.* 1992; Ohta *et al.* 1998; and Kim *et al.* 2002) have also been used to produce low-g environments. Lee and Merte 1997 conducted pool boiling experiments on three Space Shuttle flights with each flight consisting of nine different test runs. They reported the first ever pool boiling curves for microgravity environments using R-113 (Figure 2.2a). A larger bubble formed during the initial nucleation was observed to hover over or stay attached to the heater depending on its growth rate (Figure 2.2b). This coalesced bubble served as a vapor sink for smaller nucleating bubbles generated on the heater allowing liquid to rewet the heater and resulting in high heat transfer. The size of this bubble remained fairly constant, indicating a balance between condensation at the bubble top cap and vapor addition by the smaller nucleating bubbles at the base.

There also have been efforts to correlate both microgravity and earth gravity data using an interpolation scheme. Based on the heat transfer at microgravity and earth

gravity, Straub 2001 reported a power law coefficient of m=0.13 while Kannengieser *et al.* 2009 reported a power law coefficient of m=0.17. A general consensus on the value of power law coefficient and an explanation for wide range of predictions in the literature has long been needed.

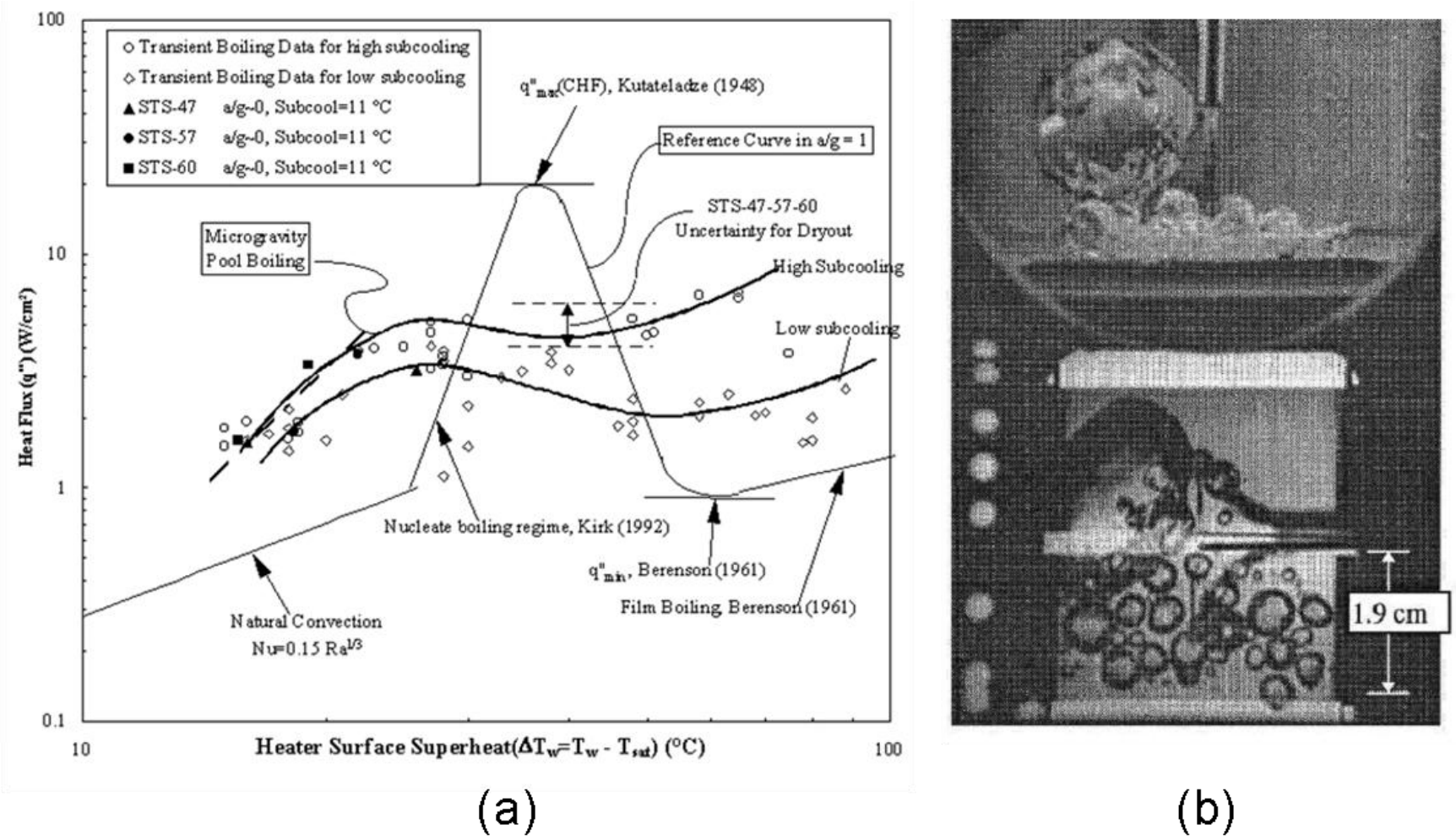

Figure 2.2: (a) Pool boiling curve and (b) representative images for boiling under microgravity conditions (Lee and Merte, 1997).

2.1.3 Hyper-Gravity Boiling

Significant effort has also been directed towards understanding the effect of gravity on boiling by performing experiments at higher gravity levels. Merte and Clark 1961 and Costello and Tuthill 1961 used centrifuges to simulate high gravity conditions (1g – 100g) in the 1950s. Figure 2.3 shows a boiling curve as reported by Merte. The influence of gravity on pool boiling heat flux was greatest in the range up to 50,000 Btu/Hr-ft^2 (28.4 W/cm^2). Surprisingly, a decrease in heat flux with gravity was observed above this value.

A review of terrestrial, microgravity and high gravity boiling studies clearly reveal a lack of consensus on the effect of gravity on pool boiling heat transfer. Although independent models for different boiling regimes and gravity levels exist, an effort to correlate these studies clearly highlights the discrepancies in the understanding of gravity effect. Much of this confusion can be attributed to lack of boiling data in the partial gravity regime, such as those in Moon (0.17g) and Mars (0.38g) environments. The partial gravity regime ($0.01g<a<1g$) has almost been left untouched by researchers (Figure 2.4) due to the difficulty in simulating these gravity levels and the corresponding cost involved. Dearth of experimental evidences in the partial gravity regime has also stopped researchers from identifying the gravity level for transition from buoyancy to surface tension dominated boiling regime and understanding the basic changes in heat transfer mechanism between these regimes. Hence, a boiling study with heat transfer data over a continuous range of gravity levels (0g-1.0g) is required to understand the effect of gravity and come up with a scaling parameter/power law coefficient for gravity effect on boiling heat flux.

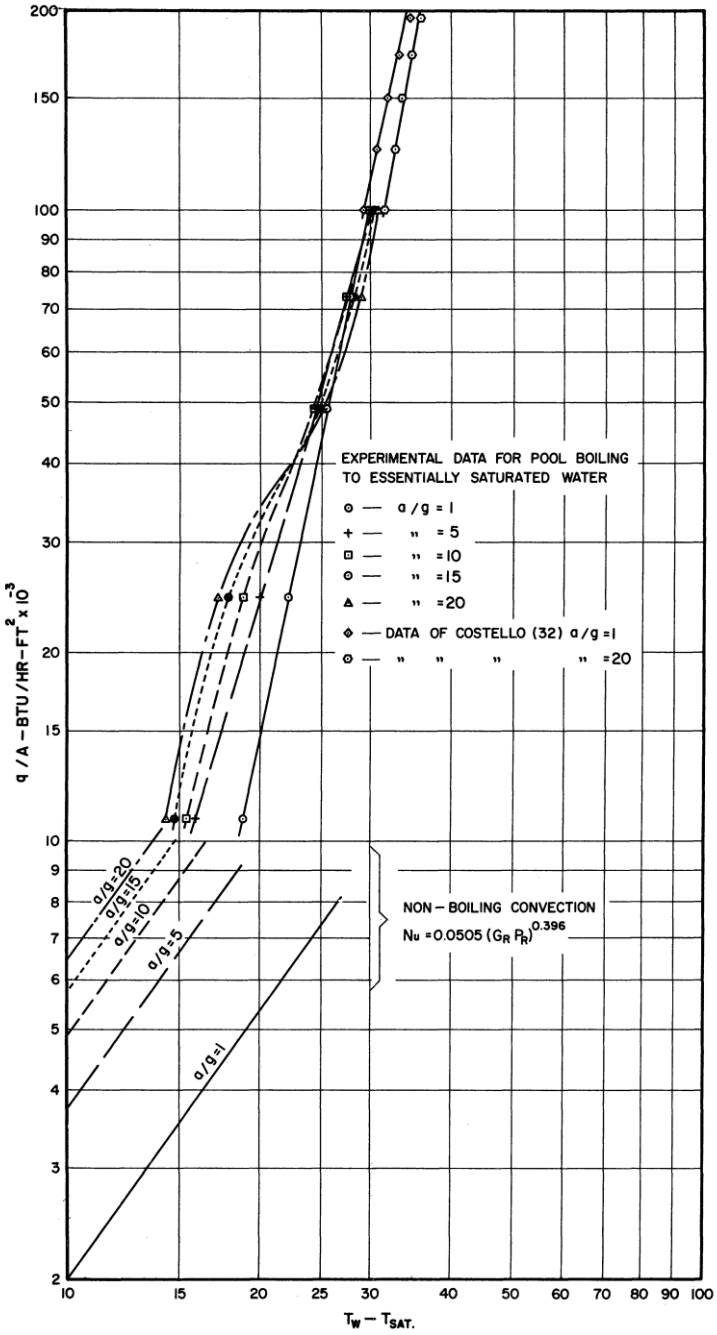

Figure 2.3: Pool boiling curve under various gravity levels (Merte and Clark, 1961).

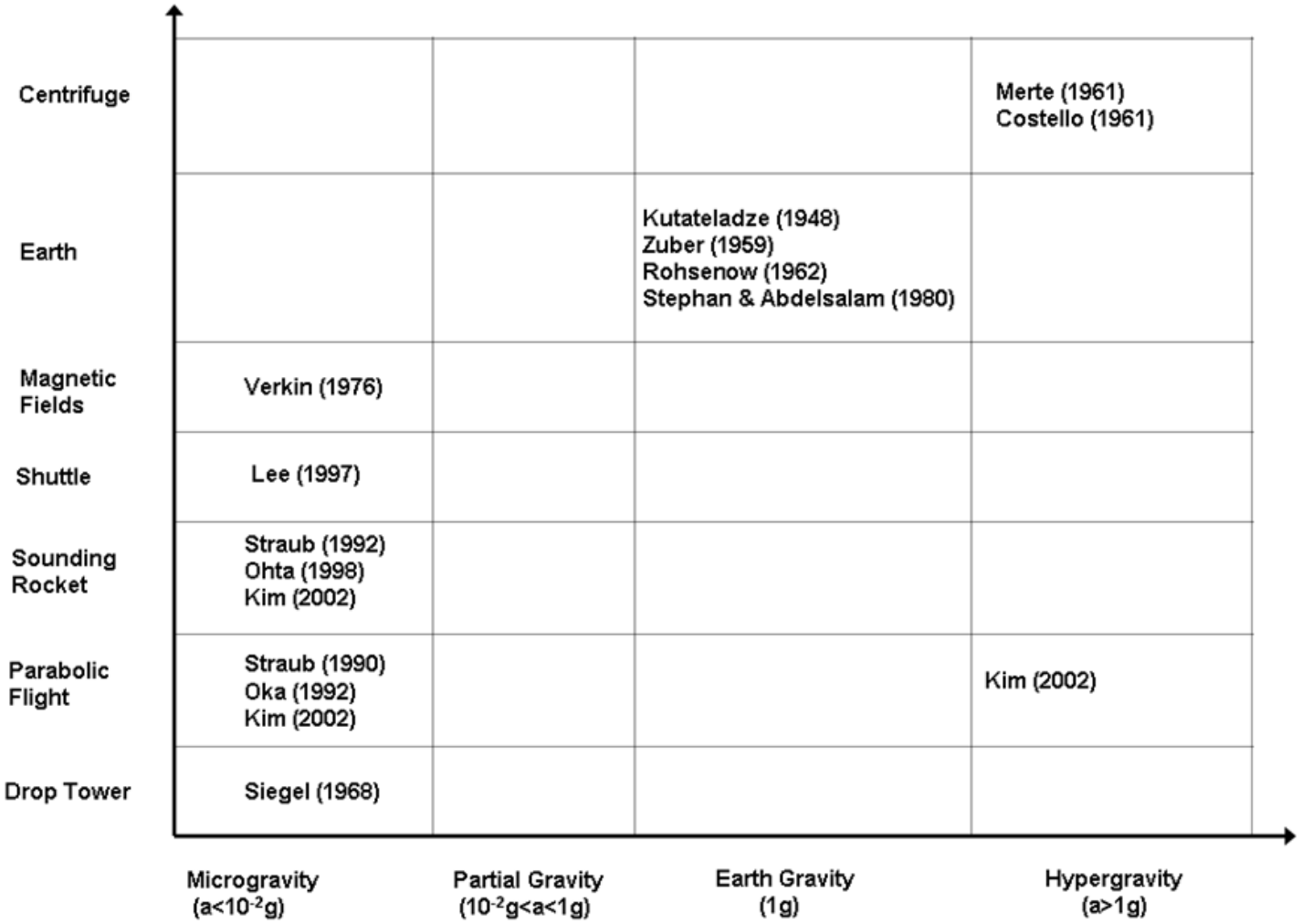

Figure 2.4: Representative summary of the pool boiling experiments across a range of gravity levels.

2.2 EFFECTS OF DISSOLVED GAS

The temperature dependence of surface tension is another important factor in determining boiling performance under microgravity environments. A nucleating bubble induces a number of interesting flow characteristics in the fluid. One such characteristic is thermocapillary flows that cause bubbles to gravitate or aggregate toward one another. One explanation of this phenomenon focuses on large surface tension gradients that exist at the immediate exterior of the bubble wall. It is well known that surface tension tends to decrease with increasing temperature. Thus, a surface tension gradient appears near the surface in the presence of a temperature gradient. This surface tension gradient sustains a shear stress gradient causing flow away from the wall surface tangent to the bubble surface. Because mass is conserved near the wall, fluid must be advected into the region near the wall from adjacent areas next to the bubble. This sets up an interesting flow pattern that results in a net flow toward the bubble from a location relatively far away. This induced flow also imparts a force on the top of the bubble acting to push the bubble into the boiling surface. Many researchers believe this induced flow causes smaller nucleating bubbles in the vicinity to aggregate or be convected toward this primary bubble.

In earth gravity, the contribution of other mechanisms is normally masked by natural convection while the absence of natural convection under reduced gravity unmasks the roles of other heat transfer phenomena. Thermocapillary convection has been observed to play an important role in heat transfer and fluid flow in these conditions. Arlabosse *et al.* 2000 quantified the contribution of thermocapillary convection to the heat transfer and proposed a heat exchange law giving the increase in

heat flux due to thermocapillary convection in comparison to conduction. Thermocapillary convection is produced by surface tension gradients along an interface which can either form due to temperature gradients, concentration gradients or electrical potential gradients (Ostrach 1982):

$$\frac{d\sigma}{dt} = \frac{d\sigma}{dT}\frac{dT}{dt} + \frac{d\sigma}{dc}\frac{dc}{dt} + \frac{d\sigma}{d\varphi}\frac{d\varphi}{dt} \tag{2.4}$$

Thermocapillary convection has not been observed in saturated pool boiling experiments performed under microgravity conditions due to the absence of a driving temperature gradient on the isothermal bubble interface (Straub 2002). However, thermocapillary convection has been widely observed in subcooled boiling experiments. Figure 2.5 is a schematic of the major transport processes occurring close to a bubble. Non-condensable gas dissolved in the liquid influences heat transfer significantly. The relationship between the dissolved gas and the physics of thermocapillary convection during subcooled boiling is not clear. It is speculated that the dissolved gas is carried inside the bubble during the evaporation at the base. Vapor condenses at the top leaving the bulk of non-condensable dissolved gases accumulating near the interface. The presence of dissolved gas inside the vapor bubble leads to the formation of a localized concentration gradient along the liquid-vapor interface. With the total pressure being constant inside the bubble, a partial vapor pressure gradient develops leading to a saturation temperature gradient along the interface. Fluids with negative temperature coefficient of surface tension lead to onset of thermocapillary convection driving the fluid away from the heater surface (Figure 2.5). Based on this reasoning, it was reported that the dissolved gas content determines the onset of thermocapillary convection and no thermocapillary motion would be observed for subcooled boiling with pure liquid.

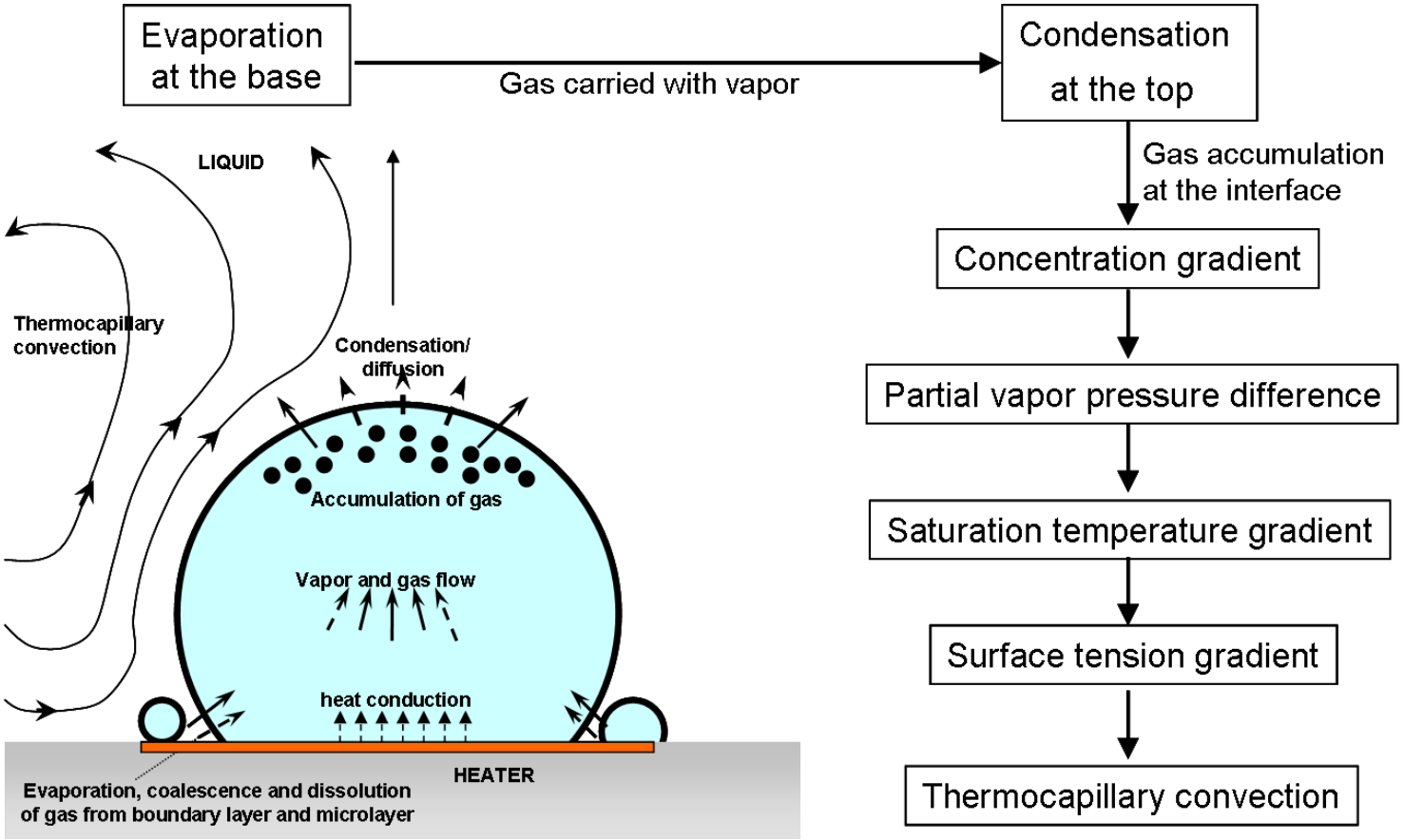

Figure 2.5: Schematic of the major transport processes in subcooled pool boiling under microgravity conditions.

However, the presence of different species (liquid, vapor and non-condensable gas) and transport processes near the interface complicates the process. Figure 2.6 is the schematic of transfer processes near the bubble interface. The processes like diffusion across the surface and dissolution in the liquid are complex and hence difficult to model.

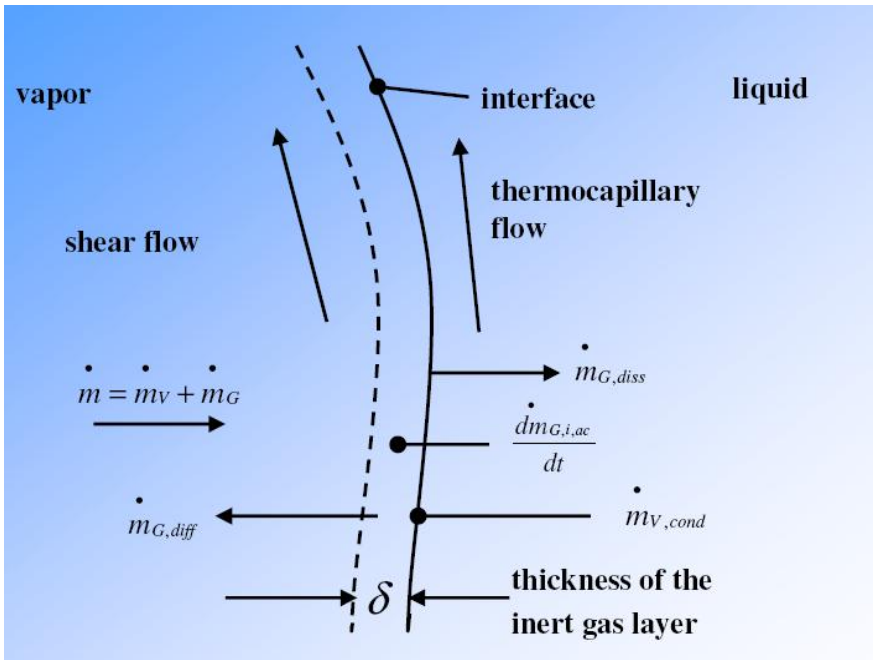

Figure 2.6: Schematic of the transport processes near the primary bubble interface.

Marek and Straub 2001 tried to decouple some of these interrelated mechanisms and study the effect of non-condensable gas. They concluded that non-condensable gases induce a driving temperature gradient along the bubble interface which leads to thermocapillary motion.

Experiments conducted by Barthes *et al.* 2007 with a downward facing heater showed that the onset of thermocapillary convection was due to the presence of non-condensable gases in the liquid (Figure 2.7a and Figure 2.7b). They observed thermocapillary flow only in the case of gassy fluid. The strength of thermocapillary

convection was expected to increase with gas concentration. On the contrary, other studies performed in reduced gravity suggest that the strength of the thermocapillary convection around the primary bubble in a gas saturated fluid (c_g ~3500ppm) was much weaker than that in a degassed fluid (c_g <3ppm), (Figure 2.7c and Figure 2.7d, Henry *et al*. 2006). It was proposed that the bubble formed in gas saturated environments is predominately a gas bubble and the partial pressure of the vapor inside the bubble is small. Moreover, the large bubble size leads to very small thermal gradient along the bubble interface and, accordingly, negligible surface tension induced thermocapillary flow. They concluded that either the non-uniform heat transfer coefficient or the contamination of the fluid might also be a possible source of thermocapillary convection. Much lower heat transfer was observed in the gas saturated case (Figure 2.8).

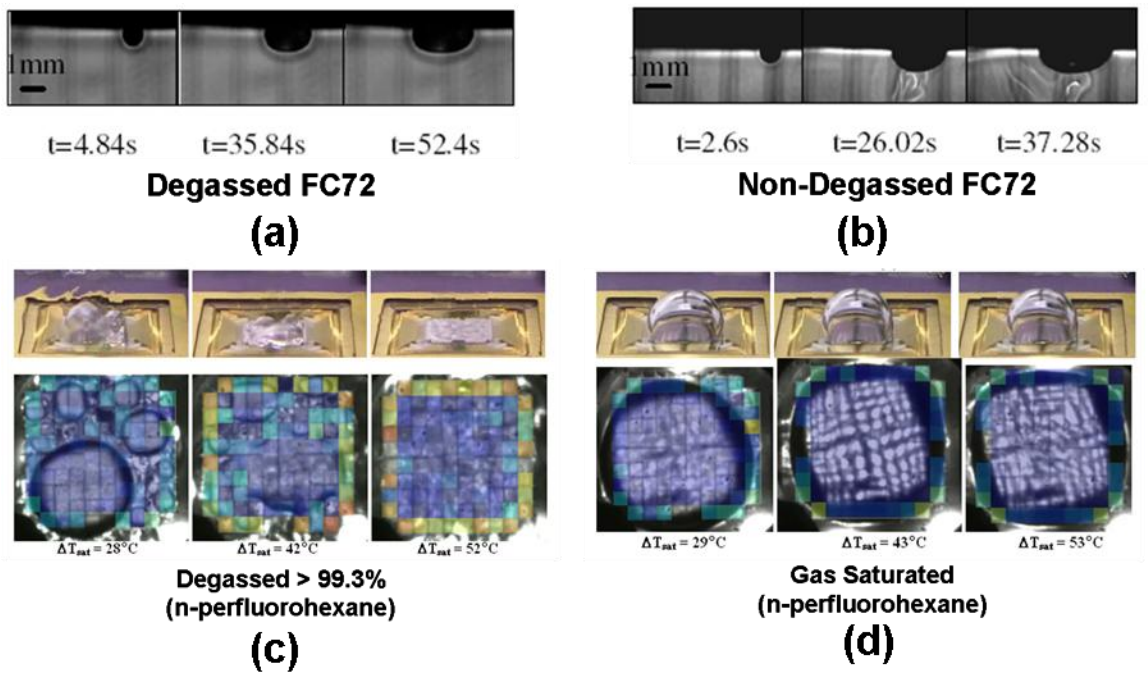

Figure 2.7: Subcooled pool boiling results on a downward facing heater for (a) degassed FC-72, and (b) non-degassed FC-72 (Barthes *et al*. 2007), and for (c) degassed and (d) gas saturated n-perfluorohexane (Henry *et al.* 2006) under microgravity conditions.

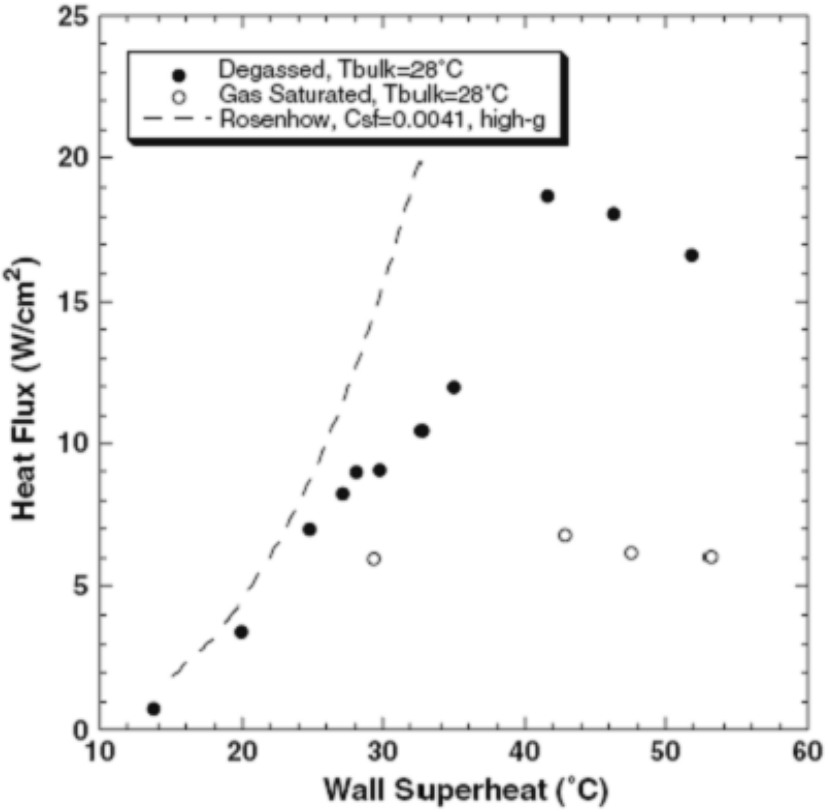

Figure 2.8: Subcooled pool boiling curve under microgravity conditions for two non-condensable dissolved gas concentrations (Henry *et al.* 2006).

There is obviously much conflicting data regarding the driving mechanism of thermocapillary convection. There is a pressing need for analytical and experimental studies to be performed over a wide range of parameters, i.e., under conditions between the two extreme cases of gas saturated and degassed condition and with a wide range of bubble radii and shapes to illuminate the behavior of thermocapillary convection over a range of conditions. The preliminary analytical studies should aim at understanding the effect of different parameters more accurately and design better experiments which would eventually help in understanding the origin of thermocapillary convection.

2.3 EFFECTS OF HEATER SIZE

It is generally understood that classical boiling is observed if the heater size is considerably larger than the departure diameter, D_d. Hence, the most suitable length scale to study heaters size independence should be the departure diameter. However, estimation of departure diameter, D_d, under actual boiling conditions is not straightforward. Experimental measurement of D_d is difficult due to increased turbulence when multiple bubbles nucleate. Although, there are correlations for D_d (Table 2.3), most of them are only valid for single bubbles and rely on other parameters (*e.g.* contact angle, departure frequency) which are not easily estimated or measured. Use of the various correlations in the literature can result in values for D_d that vary by an order of magnitude or more. For example, Yaddanapuddi and Kim 2000 compared the bubble departure diameter and frequency obtained from numerous correlations in the literature, and found they gave widely varying results, with errors between -26% to 1400%.

On the other hand, capillary length L_c (the ratio of surface tension and buoyancy forces) defined as

$$L_c = \left(\frac{\sigma}{g(\rho_l - \rho_v)} \right)^{1/2} \tag{2.5}$$

mimics the variation of departure diameter, depends only on fluid properties and gravity level, and hence is easy to estimate. Capillary length has often been adopted as the appropriate length scale influencing boiling mechanism (Di Marco and Grassi 2000). Most of the pool boiling correlations (Table 2.1) have been stated to be valid only if the heater size is considerably larger than the capillary length scale:

$$\frac{L_h}{L_c} >> 1 \qquad (2.6)$$

Boiling on small heaters under earth gravity conditions has also been studied extensively (Lin and Pisano 1991; Iida *et al.* 1994; Yin *et al.* 2004; Kim *et al.* 2002; and Henry *et al.* 2004). However, most of these studies (Lin and Pisano 1991; Iida *et al.* 1994; and Yin *et al.* 2004) on small heaters have generally focused on issues such as nucleation, bubble growth rate, and single bubble dynamics.

Figure 2.9 shows a plot of heat flux at CHF from experiments and Zuber's ($q''_{CHF}/q''_{CHF,Zuber}$) prediction versus the ratio of wire diameter and capillary length ($R' = L_h/L_c$). They reported that for smaller value of L_h/L_c, surface tension dominates over buoyancy and hence the sampling of data by Kutateladze et al. 1967, Sun and Lienhrad 1970, and Siegel and Howell 1965 no longer correlate with $q''_{CHF}/q''_{CHF,Zuber}$ versus L_h/L_c .

Based on these observations, Bakhru and Lienhard 1972 studied boiling on small diameter wires. They observed that boiling curves for small wires deviate from the classical boiling behavior. Typical boiling behavior from nucleate to film boiling was not observed for $L_h/L_c<0.15$. Heat flux was significantly smaller in this regime. Leidenfrost point and critical heat flux (CHF) were also not observed in their study. The heat transfer increased monotonically between first nucleation and full film boiling. It was concluded that the classical boiling curve (buoyancy dominated boiling) is only observed if the heater diameter is of the order of $L_h/L_c > 0.15$. They also proposed that similar behavior could be observed for large cylinders at small gravity levels, thus, proposing a similarity between heater size and gravity effects.

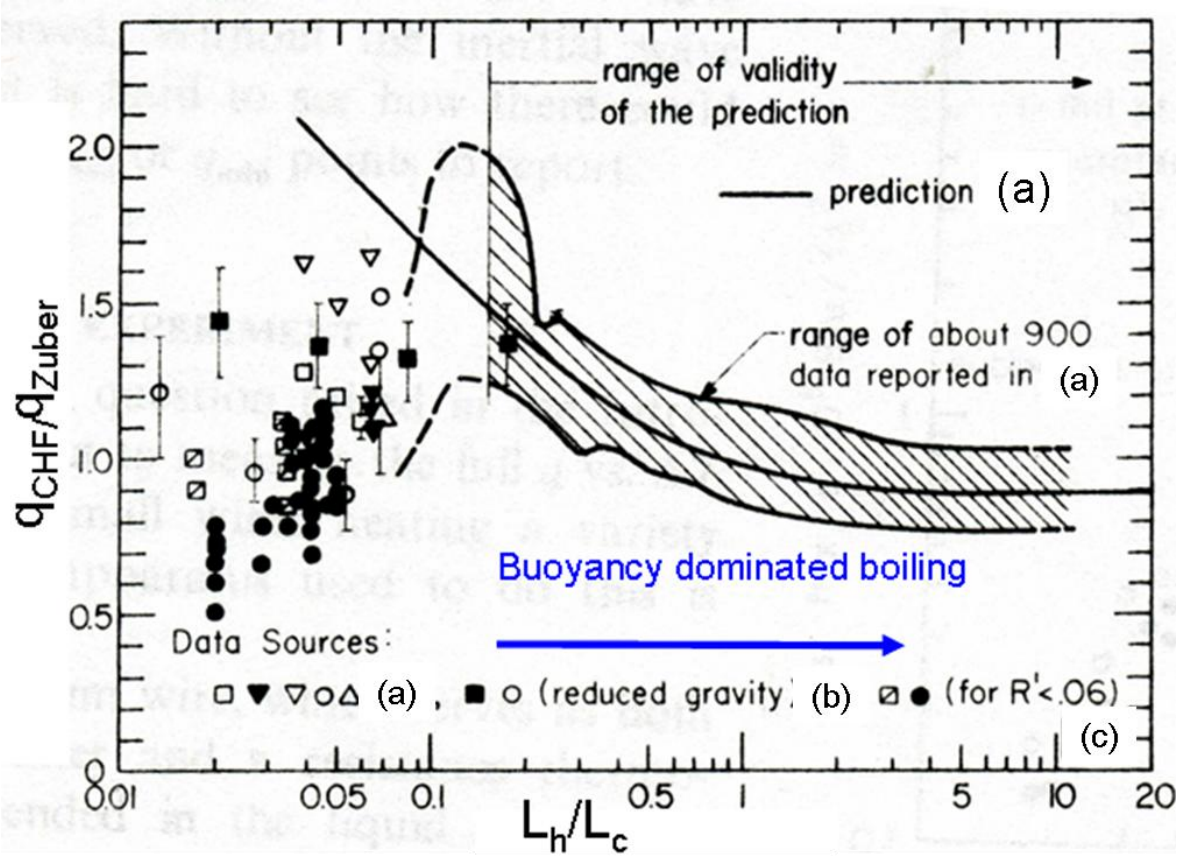

Figure 2.9: Deterioration of CHF correlation at smaller radii during boiling on wires (Adapted from Bakhru and Lienhard 1972, Data from Sun and Lienhrad 1970 [a], and Siegel and Howell 1965 [b], and Kutateladze et al. 1967 [c]).

Henry *et al.* 2004 obtained boiling curves with three heater sizes (0.81x0.81 mm^2, 1.62x1.62 mm^2, and 2.7x2.7 mm^2) in high gravity environments (~1.7 g) (Figure 2.10). At the same superheat, heat fluxes for the two larger sizes were comparable while a smaller heat flux was observed for the smallest size. It was reported that the boiling on 0.81x0.81 mm^2 heated area at 1.7g (L_h/L_c ~ 1.5) was surface tension dominated and a stable non-departing primary bubble similar to boiling in microgravity was formed.

It is likely that a threshold value of L_h/L_c exists above which boiling is dominated by buoyancy. The presence of capillary length in this ratio along with the variable gravity study suggests a similarity between gravity and heater size effect on pool boiling curve. Hence, a study of pool boiling with varying heater sizes and gravity levels is needed. The balance between buoyancy and surface tension forces can change with heater orientations too. Hence, a study of pool boiling with varying heater sizes and different orientations is also required for further understanding of pool boiling regimes.

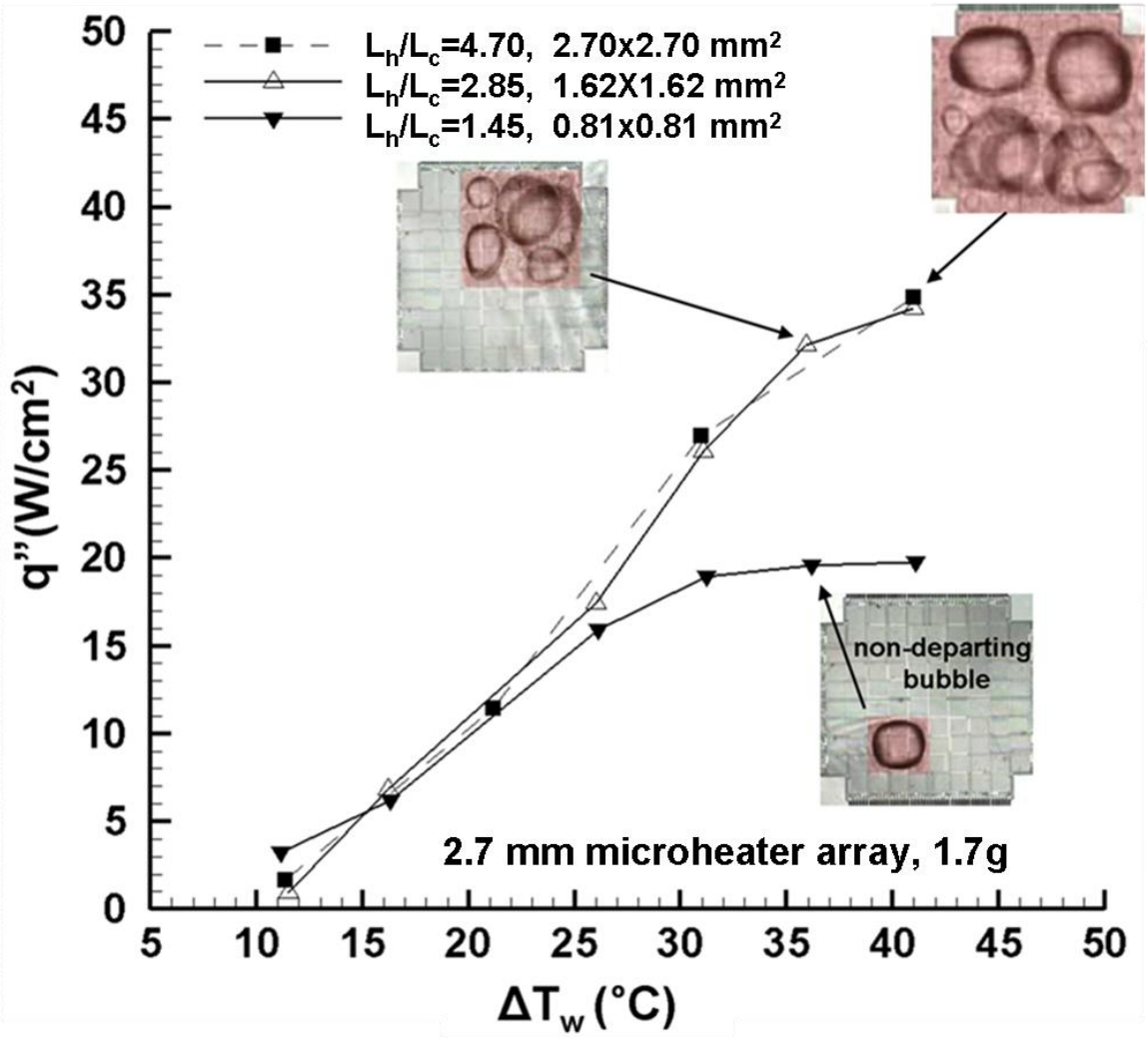

Figure 2.10: High-g (1.7g) boiling curves using FC-72 for selected heaters on 2.7x2.7 mm^2 heater ΔT_{sub}=31°C (Adapted from Henry *et al.* 2004).

2.4 RESEARCH OBJECTIVE

The primary issues in development of a deterministic model for pool boiling under a range of gravity levels and identification of boiling regimes are outlined in the previous section. A better understanding of effects of dissolved gas is also required for predicting boiling heat flux under low gravity conditions. The basic approach adopted to resolve these issues are outlined below:

- Perform preliminary numerical analysis with simplifying assumptions to observe the qualitative behavior of the important parameters under varying conditions.
- Outline an approach to systematically study these mechanisms within the limited resources available.
- Perform experiments and analyze results to confirm the behavior.
- Based on the results of the experiments, make suitable changes in the approach as and when required.
- Correlate the data obtained to resolve these issues.

The above mentioned approach along with the major application needs helped in the identification of the following major objectives for the current work:

- Identify the effect of non-condensable dissolved gas on thermocapillary convection.
- Visualize boiling phenomena across a range of gravity levels.
- Understand boiling in the surface tension dominated regime by performing experiments at lower gravity levels and/or with smaller heaters.

- Indentify the transition point of boiling from the surface tension to buoyancy dominated regime and study the effect of orientation on transition.
- Relate the effect of heater size and gravity.
- Develop a general pool boiling model valid across a host of gravity levels.

Chapter 3: Experimental Setup and Methodology

3.1 INTRODUCTION

The experimental setup was designed to study boiling process under both earth-normal and variable gravity environments. The experimental setup was composed of different components required for the operation of a constant temperature microheater array as well as the measurement of different parameters that affect boiling. All of the equipment was housed in two racks suitably designed for parabolic flight experiments. The first section of this chapter provides a detailed description of the experimental equipment. A description of the feedback circuit design methodology, heater calibration procedure, test fluids, degassing process and data acquisition technique are presented next.

A schematic of the two test racks is shown on Figure 3.1 and Figure 3.2. The primary rack (Figure 3.1) contained a sealed chamber with about three liters of working fluid at 1 atm, a microheater array to measure heat transfer distribution during boiling, a rack of electronic feedback circuits to control heater temperature, an accelerometer, some temperature and pressure sensors for parametric study, two 30 Hz video cameras for visualization, a computer, and a LCD display. All components were contained within a Vertical Equipment Rack (VER) provided by NASA and designed for use on their parabolic aircraft. The secondary rack (Figure 3.2) contained two video recorders, two displays, a triple output power supply, and a 28 VDC power supply. The components were contained in an Amco 50” Equipment Rack (AER) also provided by NASA and certified for parabolic flights. Figure 3.3 shows the two racks aboard NASA aircraft.

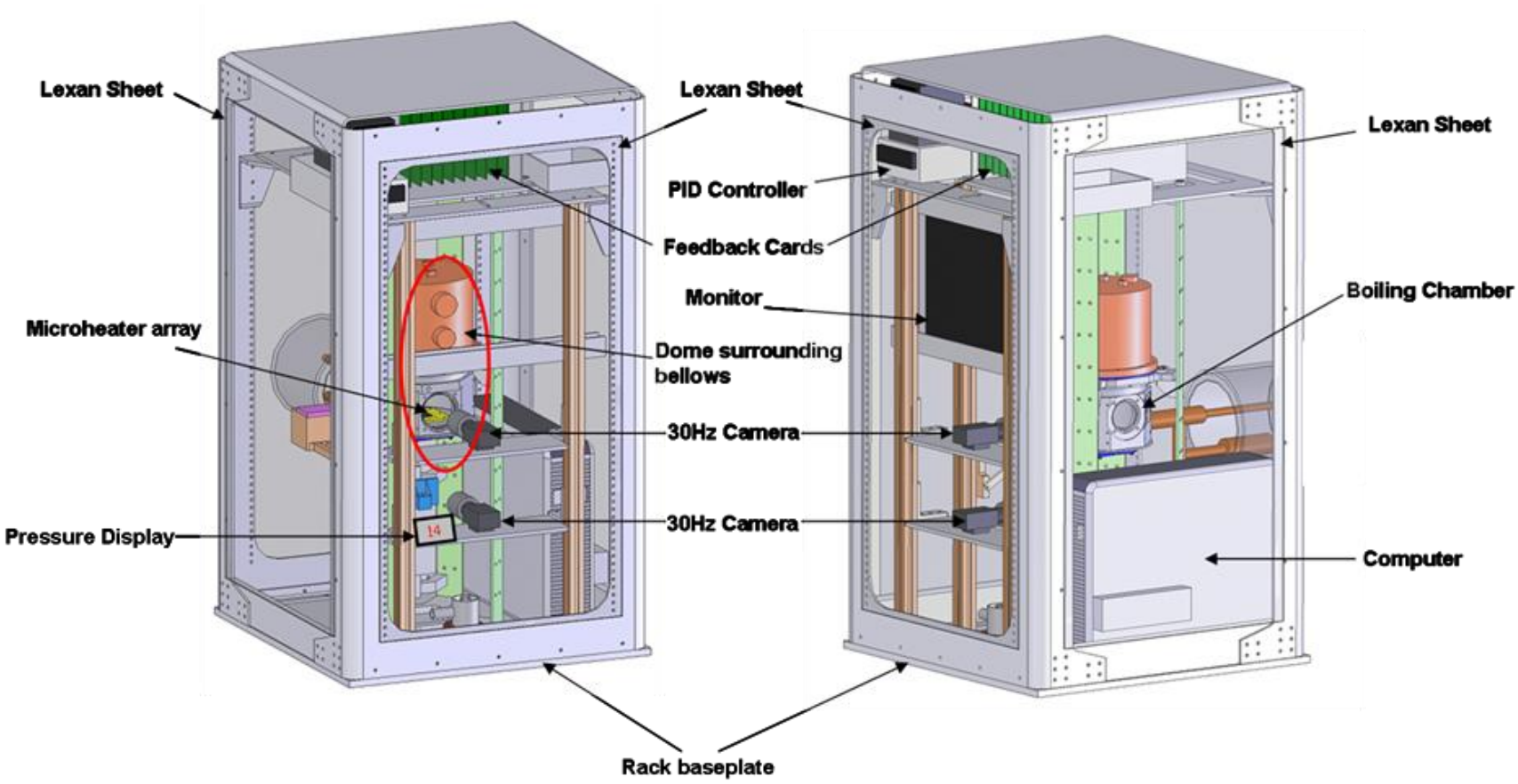

Figure 3.1: CAD model of primary rack (VER) and its components.

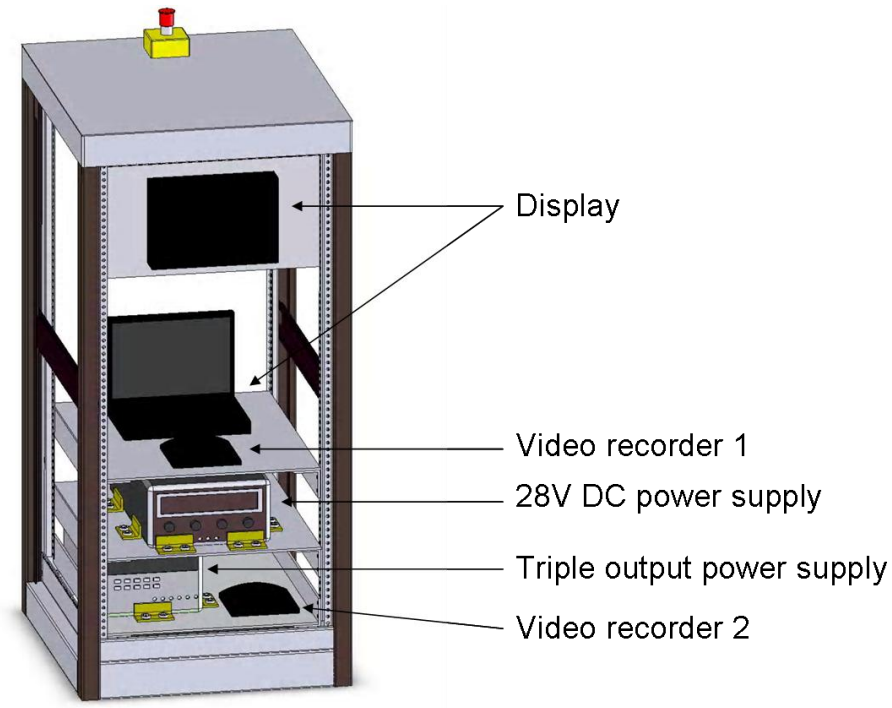

Figure 3.2: CAD model of secondary rack (AMCO) and components.

Figure 3.3: Primary (left) and secondary (right) racks aboard NASA Zero-g flight.

3.2 PRIMARY RACK

3.2.1 Test Chamber

The boiling test chamber is shown on Figure 3.4 and Figure 3.5. The bellows and the surrounding dome allowed the test section pressure to be controlled by varying the air pressure around the bellows. A PID temperature controller, a RTD probe, and six Kapton heaters attached to the boiling chamber were used to control the bulk fluid temperature. The chamber was filled with nominally 3 liters of distilled working fluid (n-perfluorohexane, FC-72, or Pentane). The working fluid was degassed to varying levels by pulling a vacuum on it. The final dissolved gas concentration in the liquid was determined using the chamber temperature and pressure, the thermo-physical properties of the test liquid, and Henry's law. A detailed description of the different components housed in the boiling chamber is mentioned in Table 3.1.

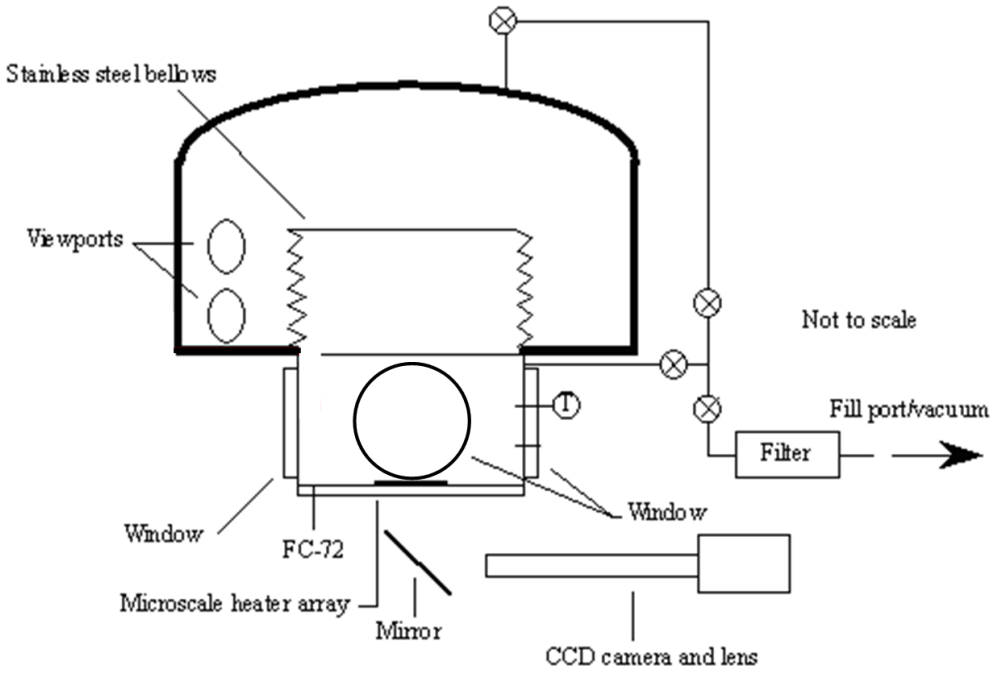

Figure 3.4: Schematic of the boiling chamber (Courtesy of J. Kim).

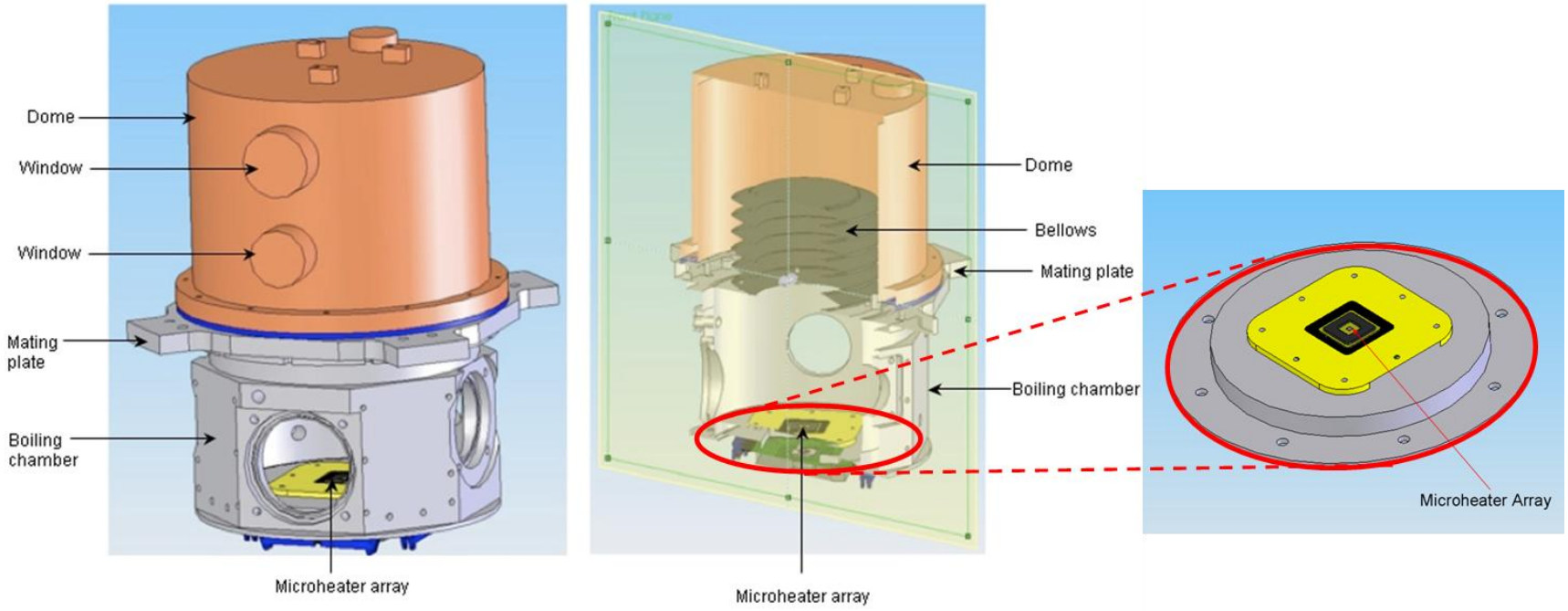

Figure 3.5: CAD model of test chamber (left) and the microheater array attachment to the base plate (right).

Table 3.1: Test chamber components

Component	Description
Dome	The dome was used to control the pressure in the test chamber through a stainless steel bellows. Two view ports allowed the position of the bellows to be observed. The test chamber was pressure tested to twice maximum expected pressure differential of 0.76 atm. The pressure during the flight was kept constant at 1 atm.
Bellows	The bellows were made of stainless steel, and were used to separate the liquid from the air within the dome. The bellows had a travel of 10cm. The bellows movement was minimal since the size of the bubbles produced by the boiling process was very small.
LED Light	The inside of the chamber was illuminated using an array LED lights. The LED lights were attached to the mating plate from above and are within the dome. They were in contact with the test liquid.
Temperature probe	A Type K probe was used to measure temperature of boiling chamber at the surface. A PID controller used this to control power to heaters attached to the outside of boiling chamber. The bulk temperature of the liquid within the test chamber never exceeded 50°C.
Pressure probe	Cooper Instruments: PTG-PX01C1-015A5T
Kapton Heaters	Thin-film heaters were attached to the outside of the boiling chamber to control the temperature. The power to the heaters was controlled using a PID controller. A thermocouple probe on the chamber wall measures the temperature. The rate of heating was fairly slow—it typically required about ½ hour for the temperature within the chamber to stabilize.
Mating Plate	The outside dome, the boiling chamber, and the bellows all connect to the mating plate (Figure 3.5).

3.2.2 Microheater Array

Two microheater arrays, 7 mm and 2.7mm each, consisting of 96 platinum resistance heaters deposited in a 10x10 configuration (four corners missing, 96 heaters) onto a quartz substrate were used to measure the heat transfer distribution (Figure 3.6). Each heater in 7 mm and 2.7 mm array was nominally 0.7x0.7 mm^2 and 0.27x0.27 mm^2 in area, respectively. Power was transferred via gold power leads 1 μm thick. Individual heaters in the 7 mm microheater array had a nominal resistance of 250 Ω and a temperature coefficient of resistance TCR of 0.0023°C^{-1}. Reader is referred to Rule and Kim, 1999 for the details of the construction of the microheater array. The properties of the two microheater arrays are summarized in Table 3.2.

Table 3.2: Comparison of the 7mm and 2.7 mm microheater arrays.

Microheater	Area of each element (mm^2)	Heater resistance (Ω)	TCR (°C^{-1})
7mm	0.7x0.7	~250	~0.0023
2.7mm	0.27x0.27	~975	~0.0021

The heater was mounted on a pin grid array (PGA) package using epoxy adhesive. Wire-bonding was used to make the electrical connection between the pads on the PGA package and the heater leads. The complete package (Figure 3.7) was then mounted on a stack of PGA sockets soldered to a printed circuit board (PCB). Four ribbon cables provided the electrical connection between the heater and feedback circuits.

The main advantage of the microheater array is that it simultaneously provides time and space resolved temperature and heat flux measurements under nucleating bubbles. The ability to selectively power a subset of the heater elements (1, 4, 9, 16, 25,

36, 64, and 96) in a square pattern out of the 10x10 configuration made the microheater array ideal for use in a variable heater size study. For example (Figure 3.6), powering a 3x3 configuration, *i.e.* 9 elements resulted in heated areas of 2.1x2.1 mm^2 and 0.81x0.81 mm^2 on 7mm and 2.7mm heaters respectively.

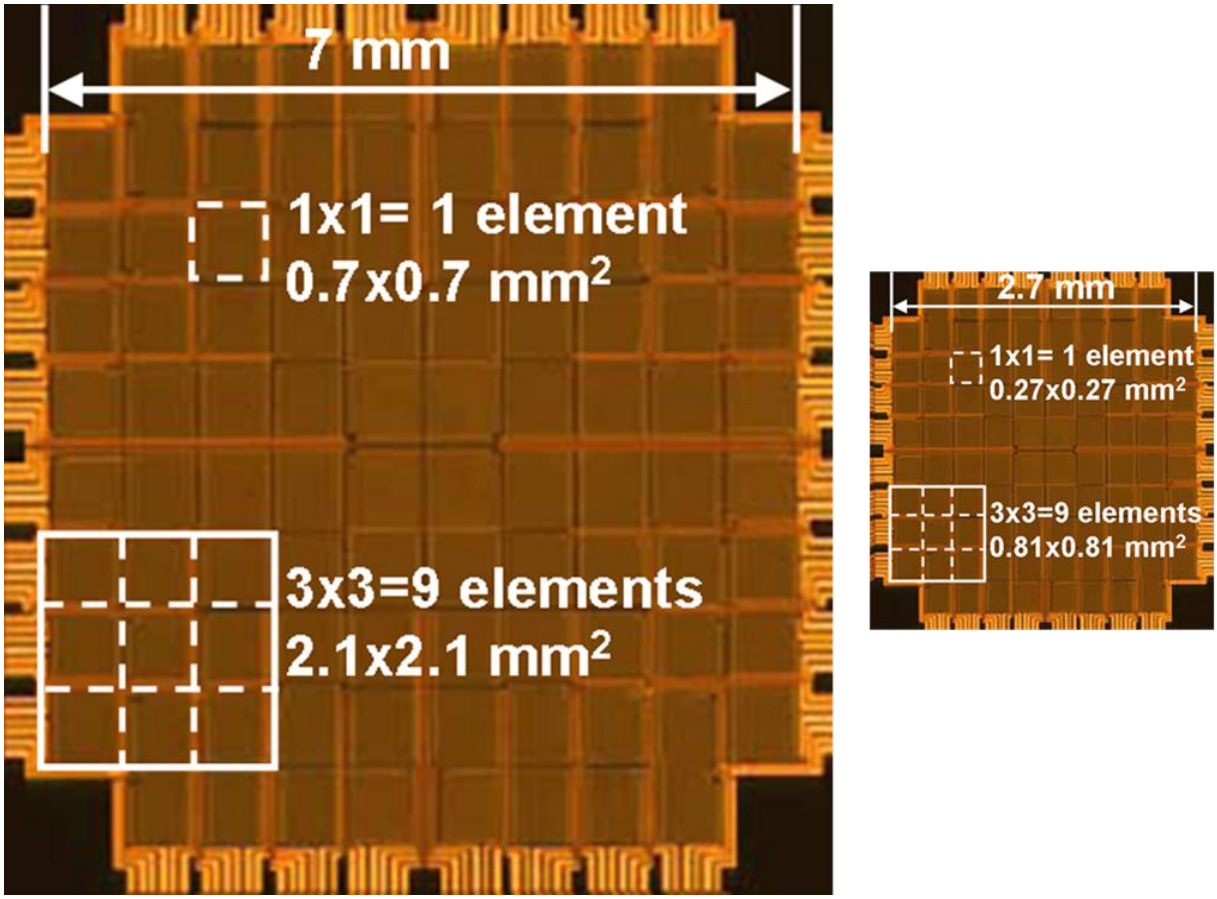

Figure 3.6: 7 mm (left) and 2.7 mm (right) microheater arrays.

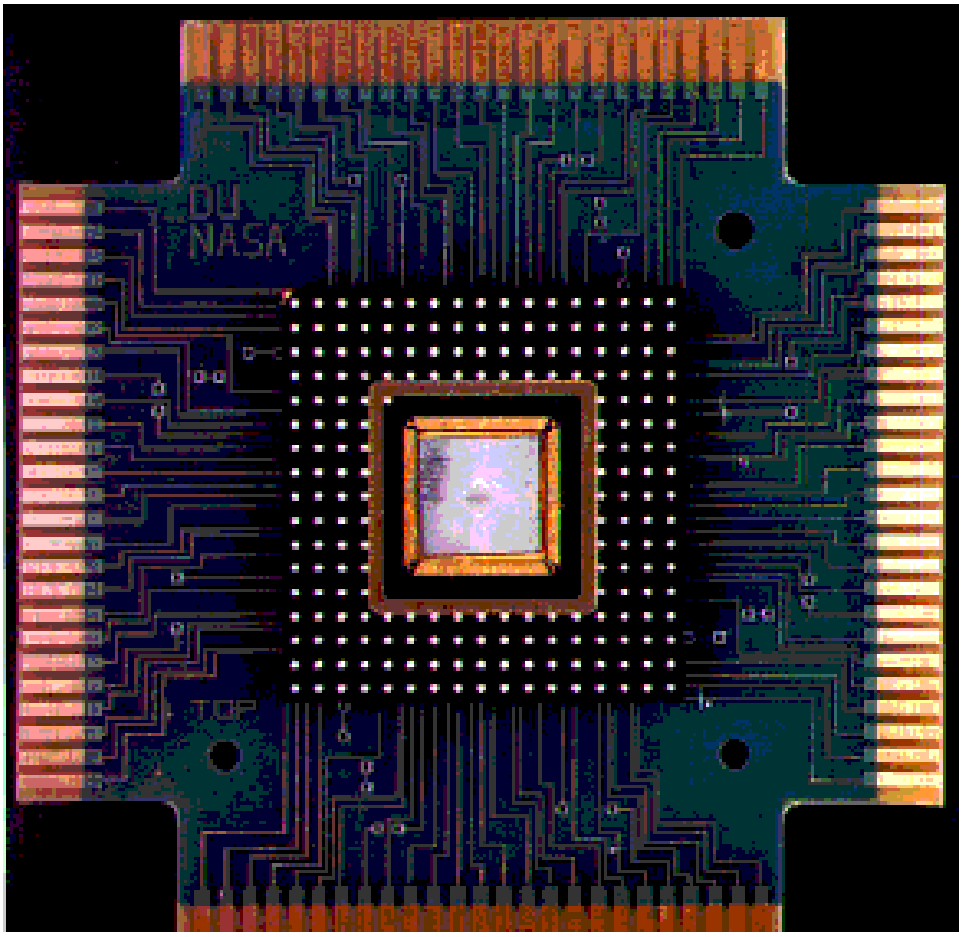

Figure 3.7: Heater array connected to PCB (Courtesy of J. Kim).

3.2.3 Electronic Feedback Circuits

The temperature of each heater in the array was kept constant by a bank of feedback circuits similar to those used in constant temperature hot-wire anemometry (Figure 3.8a). A picture of a card cage containing 96 feedback circuits is shown on Figure 3.8b. The chopper op amp was used to sense an imbalance in the Wheatstone bridge represented by R_1, R_h, R_3, R_4, and R_{DP}. If case of an imbalance, the op-amp outputs a proportional voltage to the gate of the transistor allowing additional current to flow from

the 28 volt source through the bridge. This current caused an increase in the temperature of the heater (joule heating). Microheater arrays have a positive temperature coefficient of resistance (TCR) as described in Table 3.2. An increase in the temperature of the heater resulted in an increase in the heater resistance. The resistance of the heater continued to rise until an equilibrium state within the bridge circuit was reached.

The Wheatstone bridge balance was adjusted by changing the digital potentiometer wiper position. Control of the wiper position was performed through a 3-wire serial interface to a personal computer and digital I/O card. This change in right hand side resistance of the bridge caused the current to flow through the heater array heating it up until the bridge was once again balanced.

The circuit was designed to minimize the power dissipation on the right hand side of the bridge (R_3, $R_4 >> R_1$, R_h). The frequency response of the feedback circuit was very high (15 kHz). As a result, the entire process occurred very quickly (~66μs), making the heater suitable for studying dynamic behavior of the boiling process (O[10Hz]). During the data acquisition process, the time-varying voltage across the heater resistance, V_{out} in Figure 3.8a, was measured. This voltage along with the heater resistance at the given temperature was used to determine the total power dissipated by the heater.

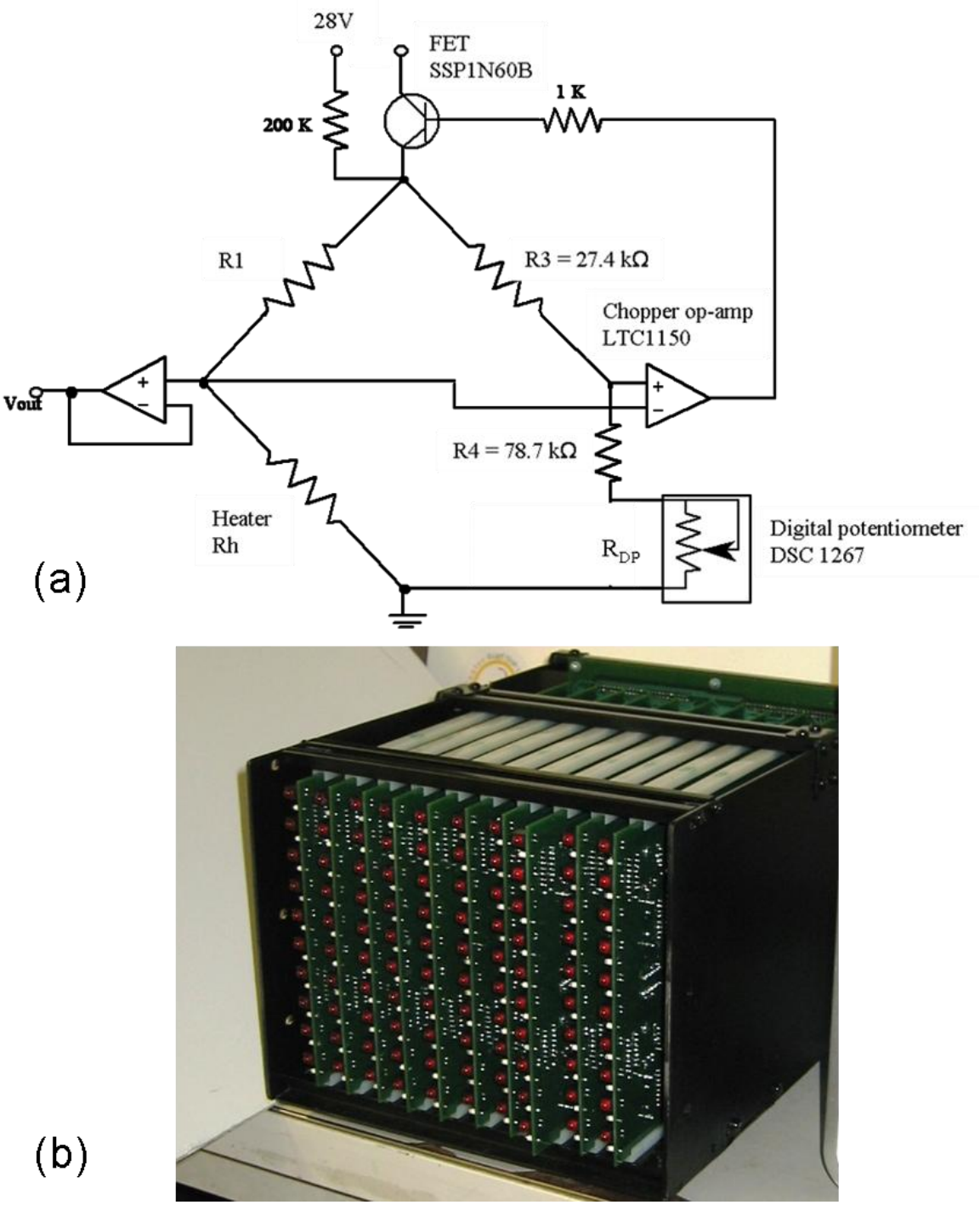

Figure 3.8: Feedback circuits for heater temperature control: (a) schematic of a single feedback circuit, and (b) the card cage containing 96 feedback circuits.

3.2.4 PID Temperature Controller

A PID temperature controller in conjunction with a two thermocouples and Kapton thin film heaters was used to hold the fluid within the chamber at the desired temperature. An RTD (first thermocouple) measured the temperature at the outer surface of the chamber and the controller was used to output a pulse-width modulated signal to the solid-state relay. An independent self-adhesive thermocouple with a separate display measuring the temperature inside the the boiling chamber was also used to provide a correct estimate of the temperature in case of the failure of the controller.

When the relay saw a high signal, a switch was closed and the heaters attached to the outside of the boiling chamber were connected to the 28VDC power supply. The temperature of the liquid in the boiling chamber was controlled to within ±1°C of the set temperature using a PID controller with pulse-width-modulation. The maximum liquid temperature we used for testing was 50°C. The temperature was displayed and recorded during the test.

If the PID controller failed and allowed the temperature to rise beyond 1˚C of the set temperature, power to the heaters could be turned off manually. In case the first RTD failure, an unwanted increase in the second thermocouple (self-adhesive) temperature would provide a signal to turn off the heaters manually making the overall system double redundant. As far as the overheating due to microheater array was concerned, the fluid temperature was never expected to be greater than 56°C. In case of a failure on part of feedback cards resulting in the overheating of the microheater array, this dual redundant system would again display the unwanted high temperature of the bulk fluid and the whole heater array system could be turned off manually.

Table 3.3: Components used to control bulk fluid temperature.

Component	Description
PID controller	OMEGA CNi 16, Controls bulk fluid temperature
Heaters	Thin film, Kapton heater,
Thermocouple	Type K, 1/8’ diameter, stainless steel sheath, ungrounded. Was inserted into the boiling chamber using a Swagelock fitting.
Thermocouple	Type K, super fast response self-adhesive thermocouple. Was glued to the outer surface of the boiling chamber.

3.2.5 Imaging

Two video cameras were used to obtain side and bottom images of the boiling process. One camera used a long focal length lens that images the boiling process through the bottom of the heater. The other camera was used to image the flow field around the bubble. The output of the video cameras was recorded onto two digital recorders housed in secondary rack.

Table 3.4: Components used for imaging.

Component	Description
Video cameras (2)	Sony N50, XC-75
Video recorders (2)	Neuros OSD digital recorder

3.2.6 Computer and Monitor

A personal computer containing two A/D cards was used to set the heater temperatures and collect data. A flat panel monitor was mounted within the rack. A list of components is given in Table 3.5.

Table 3.5: Computer and monitor specifications.

Component	Description
Computer	Optiplex 745
Monitor	KDS, 15” LCD monitor

3.2.7 Bottom Side Cooling

Backside cooling of the heater array was required to minimize the lateral conduction and to prevent individual heaters from shutting off at low heat transfer levels. Air was forced through a 1.6 mm diameter nozzle placed 10 mm from the backside of the heater. The cooling air flow was maintained by a compressed air bottle with pressure regulation nominally set at 150 kPa. The average ambient pressure inside the aircraft was measured to be 83 kPa and the air-jet temperature varied between 22°C and 24°C. The ambient pressure was 100 kPa (1 atm) during ground experiments. A pressure regulator was used to reduce the pressure to about 150 kPa before the nozzle. A schematic of the backside cooling system is shown in Figure 3.9.

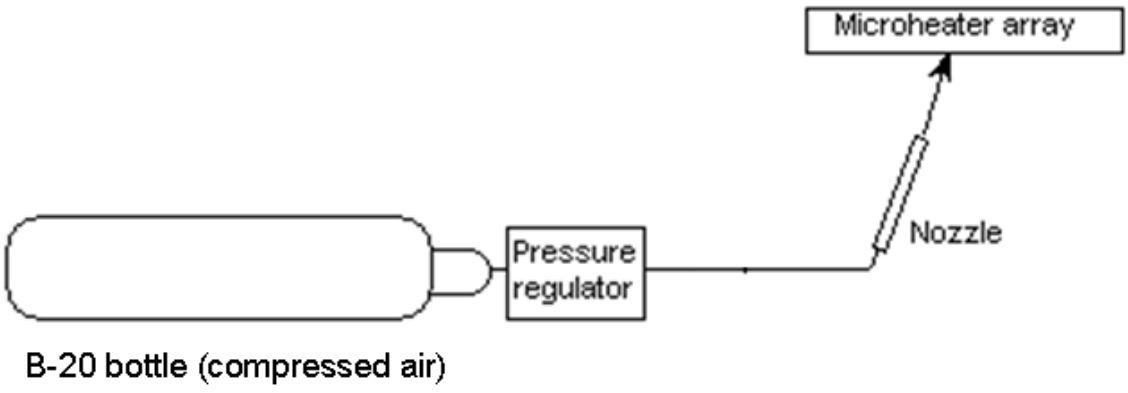

Figure 3.9: Schematic of the bottom side cooling system.

3.3 SECONDARY RACK

3.3.1 Power Supplies

Power was supplied during the experiment from the 110VAC outlet and 28 VDC supply. Two power strips were used to distribute the power to the various components in both the primary and secondary racks. The heaters on the boiling chamber were supplied directly from the aircraft 28VDC. A list of components is given in Table 3.6.

Table 3.6: Power supply specifications.

Component	Description
Triple output supply	Agilent 3631, triple output power supply. The digital potentiometer (+5V) required +5V. The negative on the op-amp required -1V.
28V DC power supply	Sorensen LH35-10. Power to the microheaters came primarily from this supply. Maximum capability is 35 V and 10 A.

3.3.2 Imaging

The output of the video cameras (primary rack) was recorded onto two video recorders located in the secondary rack. The video recorder digitizes the analog videos and stores them in a USB drive. Two DVD players were used as the display for these two cameras. A list of components is provided in Table 3.7.

3.4 ELECTRICAL SYSTEM

This section describes the electrical system used for the parabolic flight campaigns as well as earth gravity experiments. A schematic of the electrical system is shown on Figure 3.10 and Figure 3.11. The load requirements of the individual

equipments housed in the two racks are summarized in Table 3.8 and Table 3.9. The setup had two power strips. The primary power strip was housed in secondary rack and drew the power from 110 VAC power supply. The secondary power strip housed in the primary rack drew power from the primary power strip. Table 3.10 is the load table for the primary power strip while Table 3.11 is the load table for the secondary power strip. The nominal and maximum current values were well within the limits of both the power strips.

Table 3.7: Components of the imaging system.

Component (Number)	Description
Display (2)	Memorex DVD player- MVDP1102
Video recorder (2)	Neuro OSD MPEG Recorder

Table 3.8: Electrical load for the individual equipments in primary rack

Rack # 1 (Primary rack)	
Components	Max. Power Consumption [W]
Electronic feedback circuits	50 (est)
CCD cameras+lenses	10 (est)
CCD cameras+lenses	10 (est)
Heaters on side of boiling chamber	95
Computer	250 (est)
LCD monitor	25 (est)
Temperature Display 1	6
Temperature Display 2	4
Total	450 (est)

Table 3.9: Electrical load for the individual equipments in the secondary rack

Rack # 2 (Secondary Rack)	
Components	Max. Power Consumption (W)
28VDC power supply	280 (est)
Triple output power supply	80 W (est)
Video Recorder (2 in number)	20 W (est)
Display (2 in number)	60 W (est)
Total	440 W (est)

Table 3.10: Load table for primary power strip

Power Source Details	Nominal Current (max)
Name: Primary power strip	Recorder 1 – 0.1 A
Voltage: 125VAC, 60 Hz	Recorder 2 – 0.1 A
	Triple output power supply – 0.2 (0.5) A
	28 V DC power supply – 1.0 (2) A
	Display 1 and 2 – 0.25 A
	Secondary power strip – 1.4 (3.1) A
Max Outlet Current: 15 A	Total Current Draw: 3.3 (6.3) A

Table 3.11: Load table for secondary power strip

Power Source Details	Nominal Current (max)
Name: Secondary power strip	Camera 1 – 0.2 A
Voltage: 125VAC, 60 Hz	Camera 2 – 0.2 A
	Computer – 0.6 (2.3) A
	Monitor – 0.2 A
	Temperature Display 1 – <0.1 A
	Temperature Display 2 – <0.1 A
Max Outlet Current: 15 A	Total Current Draw: 1.4 A (3.1)

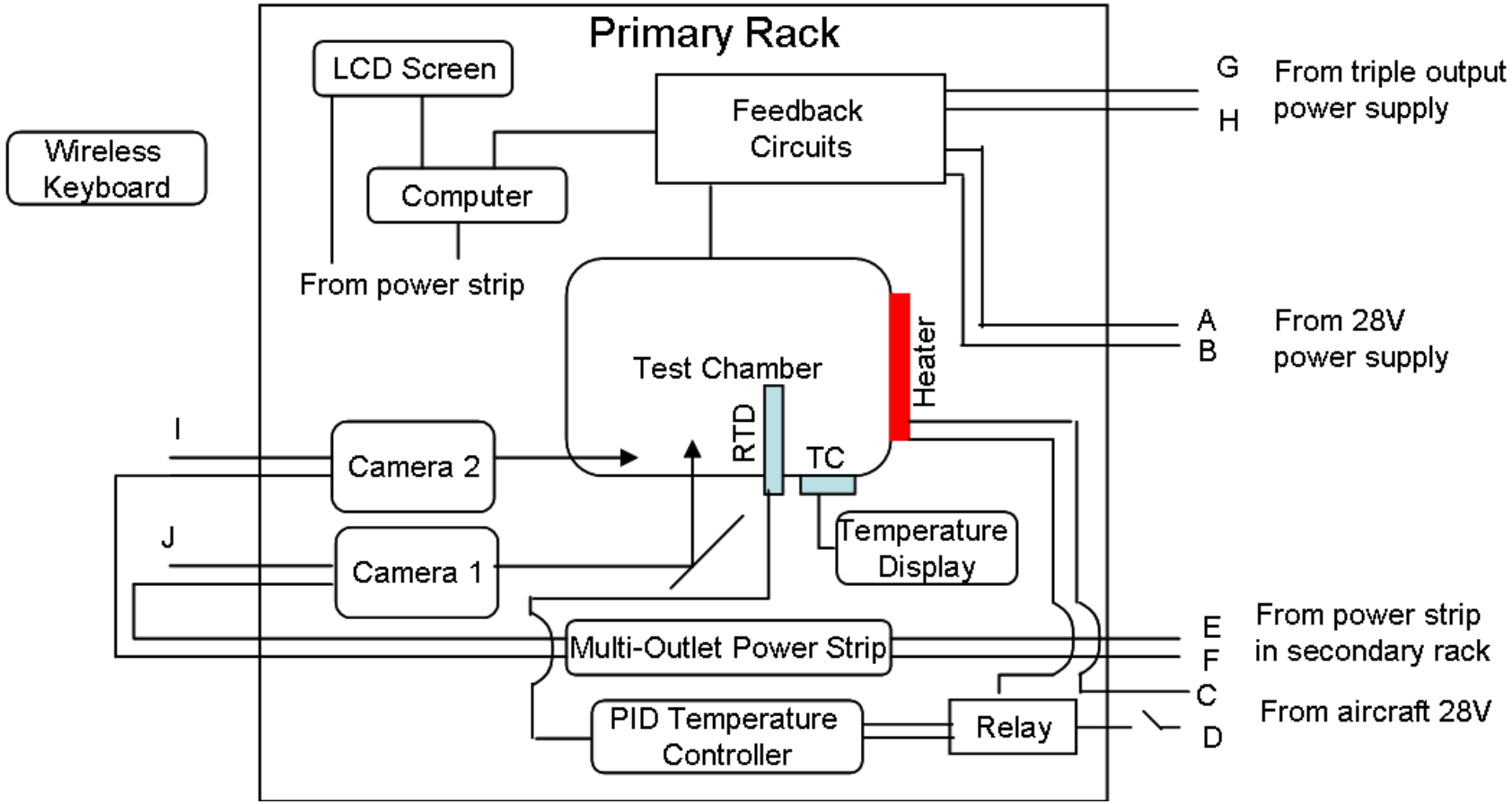

Figure 3.10: Schematic of the electrical system housed in primary rack.

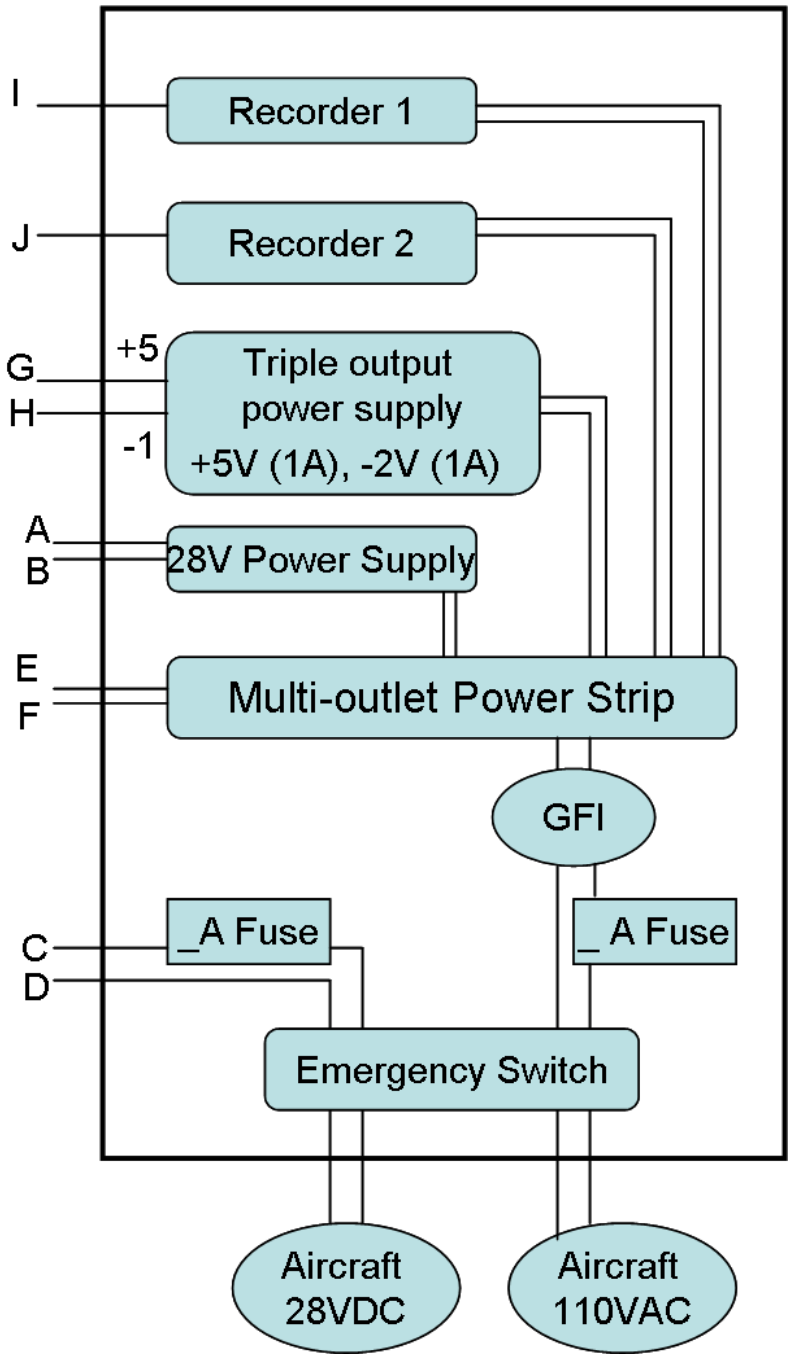

Figure 3.11: Schematic of electrical system housed in secondary rack.

3.5 FEEDBACK CIRCUIT DESIGN

The successful operation of the microheater array depends on the design of the feedback circuits. The primary objective of the design was to maximize the temperature resolution of the array across the temperature range of operation while maximizing the heat flux at higher temperatures. Hence, a bi-objective optimization problem was formulated as follows:

$$\max\ f_1 = DQ_{100°C} - DQ_{65°C} \tag{3.1}$$

$$\max\ f_2 = \frac{V^2}{Rh_{120°C}}\ \ @T = 120°C \tag{3.2}$$

Figure 3.8a shows the basic schematic of the feedback circuit. The heater resistance was measured at the reference temperature of 25˚C. The TCR of the array was calculated by observing the resistance change of the individual elements per degree rise in temperature. With the TCR and the known heater resistance at a reference temperature known, the heater resistance was calculated at any temperature using the following relation:

$$Rh_T = Rh_{Tref}\,(1 + TCR(T - T_{ref})) \tag{3.3}$$

The digital potentiometer resistance can be linearly varied between 0 to 20kΩ in 512 steps. This setting value is called the DQ value corresponding to a given heater temperature. The DQ value of the potentiometer is a function of the four resistances as follows;

$$DQ_T = \left(R3\frac{Rh_T}{R1} - R4\right)\frac{511}{R_{pot}} \tag{3.4}$$

The two equality constraints imposed on the problem are stated as follows;

h_1: $$DQ_{5°C} = R3\frac{Rh_{5°C}}{R1} - R4 = 0 \quad (3.5)$$

h_2: $$DQ_{120°C} = \left(R3\frac{Rh_{120°C}}{R1} - R4 \right)\frac{R_{DP}}{511} = 511 \quad (3.6)$$

The bi-objective optimization problem with Eq. 3.1 and 3.2 as the objective functions, Eq. 3.5 and 3.6 as the constraints, and values of parameters (Table 3.12) was solved using a Matlab optimization code. The results of this multi-objective optimization problem (7 mm microheater) are stated in Table 3.13.

Table 3.12: Value of parameters used in optimization routine

Quantity[units]	Value
R_{DP}[kΩ]	20
TCR[$^oC^{-1}$]	0.0023

Table 3.13: Feedback circuit design values

Quantity[units]	Value
R_{DP}[kΩ]	20
TCR [$^oC^{-1}$]	0.0023
R1[kΩ]	R_h/3
R3[kΩ]	27.4
R4[kΩ]	78.7

3.6 HEATER CALIBRATION

The heater array was calibrated using a constant temperature oven. PID temperature controllers, two thermocouples, and two thin film heaters were used to maintain a constant temperature environment inside the oven. The oven was designed symmetrically and the heater to be calibrated was kept in the center to obtain the best possible isothermal conditions and avoid any temperature gradient. The heater was allowed to equilibrate within the oven for two hours before the calibration program was run. The temperature of the heater array was measured using a NIST calibrated thermocouple which was attached close to the heater surface using Kapton high-temperature tape. Pictures of this setup are shown in Figure 3.12.

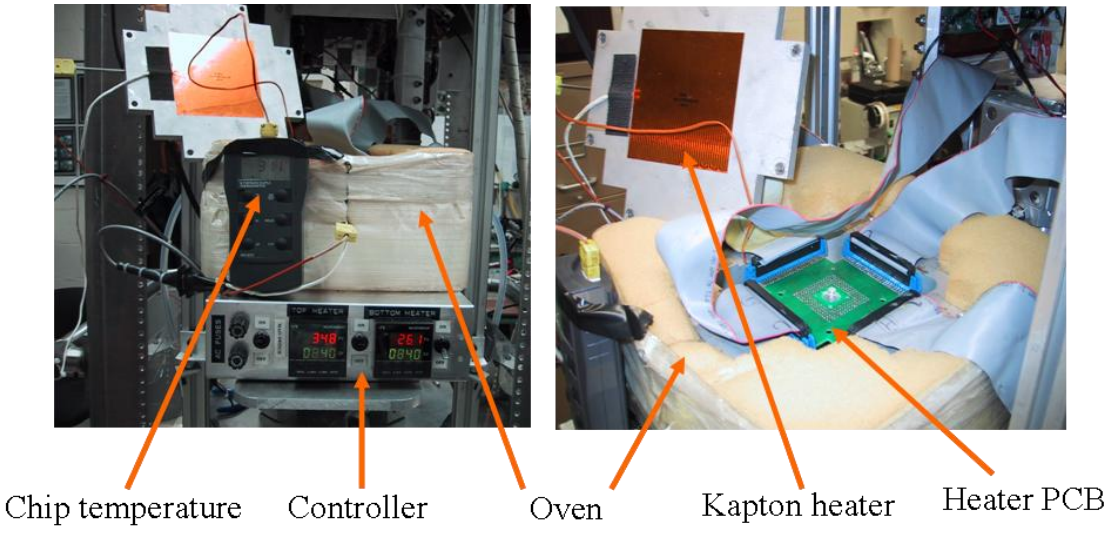

Figure 3.12: Calibration oven (left), view of the PCB board (right) inside the oven (Courtesy of Chris Henry).

At thermal equilibrium inside the oven, the calibration program determined the digital potentiometer resistance setting which balances the Wheatstone bridge (Figure

3.8a). Calibration process was performed at 9 temperature increments ranging from 25°C to 100°C. A plot of the obtained DQ value versus temperature for three sample heaters is shown on Figure 3.13. The theoretical DQ value based on the TCR of the heaters and the experimental value were very close validating the calibration procedure. Even though the DQ values corresponding to different heaters at any temperature were different, the slope of the curve and hence the TCR was almost same (0.0023 $^{\circ}C^{-1}$). Finally, the potentiometer was set to the DQ corresponding to the desired temperature during the actual experiment.

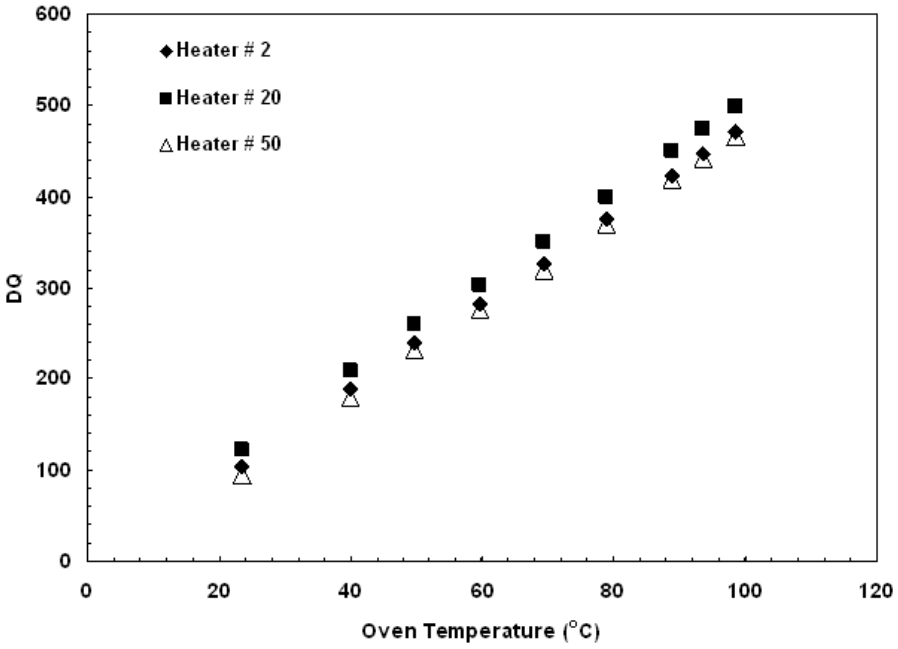

Figure 3.13: Digital potentiometer set points (DQ) versus temperature for three sample heaters.

3.7 TEST FLUID

Two fluids, namely FC-72 (C_6F_{14}, T_{sat}=56.6°C at 1 atm) and Pentane (C_5H_{12}, T_{sat}=36°C at 1 atm), were used in the current study. Theories on the origin of thermocapillary convection indicate that surface active contaminants may play a significant role in the interfacial kinetics at the two-phase interface. As a result, it was essential to quantify the purity of the fluid for experiments under microgravity environments. Hence, 98.9% straight chain isomer of FC-72 (n-perfluorohexane, T_{sat}=56°C at 1 atm) was used during the microgravity/variable gravity experiments. FC-72 and n-perfluorohexane have similar thermo-physical properties except for the saturation temperature. The fluid properties of interest to the current work are summarized in Table 3.14.

Table 3.14: Thermo-physical properties of the test fluid at saturation.

Properties	FC-72	Pentane
ρ_l [kg/m^3]	1614	609.9
ρ_v [kg/m^3]	14.8	2.99
μ [kg/ms]	6.4e-04	1.7e-04
C_p [J/kgK]	1097	2367
h_{fg} [J/kg]	83536	357753
k_l [W/mK]	0.0522	0.1133
σ [N/m]	0.009	0.0136
β [1/K]	0.0094	0.00167
MW [kg/kmole]	338	72
T_{sat} @ 1 atm [˚C]	56.6	36

3.8 DEGASSING

The air concentration in the test liquid was reduced by repeatedly pulling a vacuum on the vapor/air above the liquid. For a given partial pressure of gas (P_g) above the liquid, the dissolved gas concentration C_g (moles gas/mole liquid) in the liquid phase is given by Henry's law;

$$C_g = H(T)P_g \tag{3.7}$$

For air in FC-72, H has been measured to be 5.4×10^{-8} mole/mole-Pa for 31 °C<T<60 °C. P_g (partial pressure of air) can be determined from a measurement of the total pressure (P_T) and temperature (T_{sat}) of the gas above the liquid after it has come to equilibrium in a sealed container from:

$$P_g = P_{tot} - P_{sat}(T_{sat}) \tag{3.8}$$

where P_{sat} is the saturation pressure of the liquid at the measured temperature T_{sat}.

In practice, the test rig was turned upside down, and the pressure around the bellows was lowered to pull the bellows down and to create a vapor/gas space above the liquid. The chamber pressure and temperature were measured just before degassing, and the pressure measurements were corrected to obtain what the total pressure would be at a reference temperature of 25 °C. A vacuum pump was then connected to the chamber and the pressure above the liquid was lowered long enough to boil the liquid for a few seconds, ensuring that all of the vapor/air was removed. Once the liquid was degassed, the pressure around the bellows was brought up to 1 atm—since there was no pressure differential across the seals in the boiling chamber, gas infiltration back into the liquid was minimized. Table 3.15 lists the saturation pressure measurements made for n-perfluorohexane.

From these measurements,

$P_{sat,n\text{-}per}(T=23.5°C)=29365$ Pa

From the database for FC-72,

$P_{sat,FC\text{-}72}(T=23.5°C)=28322$ Pa

Assuming that the slope of the saturation pressure curve with temperature is same for FC-72 and n-perfluorohexane for all practical purposes, *i.e.*

$$(dp/dT_{@\ saturation})_{FC\text{-}72} = (dp/dT_{@\ saturation})_{n\text{-}per} \quad (3.9)$$

Table 3.15: Saturation pressure measurement of n-perfluorohexane

Vacuum Run #	T (°C)	P_{gauge} (inches of Hg)	P_{gauge} (Pascal)	$P_{absolute}$ (Pascal)
1	23.9	-7.5	-25398	75927
2	23.9	-16	-54182	47143
3	23.7	-19.25	-65188	36137
4	23.6	-20.1	-68066	33259
5	23.5	-21.25	-71960	29365
6	**23.5**	**-21.25**	**-71960**	**29365**

A correction term for n-perfluorohexane was calculated as follows:

$P_{correction} = P_{sat,n\text{-}per} - P_{sat,FC\text{-}72} = 1043$ Pa

Based on the above two equations, we get,

$$P_{sat,n\text{-}per} = P_{correction} + P_{sat,FC\text{-}72} \quad (3.10)$$

A check was performed to see the difference in pressures at saturation condition. At the saturation temperature of n-perfluorohexane,

$P_{sat,n\text{-}per,check}(T=56°C)=101325$ Pa (atm)

From the FC-72 database at the same temperature,

$P_{sat,FC\text{-}72,check}(T=56°C)=100204$ Pa

$P_{correction,check}= P_{sat,n\text{-}per,check}-P_{sat,FC\text{-}72,check} =1121$ Pa

This correction value is very close the experimental calculation term validating the assumption of constant slope for the two fluids (1043 Pa). Once the correction term was obtained for n-perfluorohexane, degassing was performed. The degassing readings for the ESA Parabolic Flight Campaign are listed below:

After degassing and settling, Day 1: $P_{total,\ sensor} = 6.08$ psi, T = 11.3 °C

Before adding gas, Day 2: $P_{total,\ sensor} = 8.23$ psi, T = 25.7 °C

After adding gas and settling, Day 2: $P_{total,\ sensor} = 10.92$ psi, T = 25.2 °C

The pressure sensor had an offset in the reading. The reading was corrected for the offset as follows:

$P_{total,\ actual}= (P_{total,\ sensor}-P_{offset})*SF* 6894.75729$ Pa

where the scaling factor, SF = 14.70/14.79=0.9936

$P_{sat,\ FC\text{-}72}(T)$ is calculated from the database of FC-72,

$P_{sat,\ n\text{-}per}(T)= P_{sat,FC\text{-}72}(T)+ P_{correction}$

$P_{gas,\ n\text{-}per}(T)= P_{total,\ actual} -P_{sat,\ n\text{-}per}$

$$C_g = H(T)^* P_{gas,n\text{-}per}(T) *10^6 \quad (3.11)$$

Table 3.16 is the summary of the gas concentration measurement. The dissolved gas concentration was 220 ppm for the low gas case while 1216 ppm for the high gas case. Similar methodology was adopted for other dissolved gas concentrations used in this study.

Table 3.16: Pressure after degassing during the parabolic flight campaign

Run #	T (°C)	$P_{total,sensor}$ (psi)	$P_{total,actual}$ (Pascal)	$P_{sat,FC\text{-}72}(T)$ (Pascal)	$P_{sat,n\text{-}per}$ (Pascal)	$P_{gas,n\text{-}per}$ (Pascal)	C_g (ppm)
1	11.3	6.08	20895	15726	16769	4126	222.8
2	25.7	8.23	36310	31200	32243	4066	**219.6**
3	25.2	10.92	54054	30499	31542	22512	**1216**

3.9 DATA ACQUISITİON

The data acquisition system consisted of two 64 channel data acquisition cards Measurement Computing PCI-DAS6071) contained within a personal computer. The data acquisition technique during the earth gravity and variable gravity experiments are described below.

3.9.1 Earth Gravity Experiments

The selected heater elements for any given configuration/size were set to the desired temperature before the start of each data acquisition run. The two cameras and the air-jet were activated after which the data acquisition commenced. The LED array illuminating the boiling chamber was then turned on and the step change in the voltage

across the LED was recorded by the data acquisition system. A change in illumination observed in the video was used to synchronize the video and the data. The data acquisition system was programmed to stop acquisition after 25 seconds. Heat flux, LED voltage, pressure, and bulk liquid temperature data were acquired at 300 Hz while the bottom and side view images were acquired at 29.97 Hz.

3.9.2 Variable Gravity Experiments

The heater array was set to a desired temperature before the start of each parabola during the 1-g period. The two cameras and the air-jet were activated during the middle of the hypergravity (>1.5g) period and data acquisition was started a few seconds before the transition to low-g began. The LED array illuminating the boiling chamber was then turned on; the step change in the voltage across the LED recorded by the data acquisition system and the change in illumination observed in the video were used to synchronize the video and the data. The data acquisition system was programmed to stop acquisition after 30 s. The low-g data corresponded to approximately 18 s, while 6-8 s of transition data and about 4-5 s of hypergravity data were obtained. Heat flux, acceleration, pressure and bulk liquid temperature data was acquired at 100 Hz while the bottom and side view images were acquired at 29.97 Hz.

Chapter 4: Data Reduction and Uncertainty Analysis

4.1 INTRODUCTION

The task of data reduction involved converting the acquired voltage signals to quantities of importance to the current study. Raw data from the accelerometer, LED voltage, and bulk liquid temperature were converted into engineering relevant quantities. Based on the experimental conditions and scope of the studies, different approaches were used to estimate the amount of heat utilized for boiling. The data reduction procedure along with an uncertainty analysis is provided in this chapter.

4.2 DATA REDUCTION

4.2.1 Raw Heat Flux Calculation

As was discussed in previous chapter, the data acquisition unit measured the instantaneous voltage from each heater element at the prescribed frequency. The voltage reading (V_{out}) along with heater resistance (Rh_T) at that temperature (T) and the area (A) were used to calculate the raw heat transfer ($q''_{gen,i}$) for each individual heater element (i^{th}):

$$q''_{gen,i} = \frac{V_{out,i}^2}{A_i Rh_{T,i}} \tag{4.1}$$

The nominal area of each element in the 7 mm and 2.7 mm microheater arrays was 0.7x0.7 mm^2 and 0.27x0.27 mm^2, respectively. As was discussed in the heater calibration section, the heater resistance varied with temperature. Changes in heater temperature changed the heater resistance according to the following relation:

$$Rh_{T,i} = R_{ref,i}(1 + TCR * (T - T_{ref})) \tag{4.2}$$

where TCR is the temperature coefficient of resistance for the microheaters (Table 3.2). Finally, the spatially averaged heat flux was calculated as follows:

$$q''_{gen} = \frac{\sum_{i=1}^{N} q''_{gen,i}}{N} \tag{4.3}$$

It is important to note that only a portion of the total heat generated was actually delivered to the fluid. The remaining portion was either lost to the backside cooling fluid or was conducted laterally to the substrate. The next section describes the methodologies adopted to estimate the portion of heat transfer utilized for boiling.

4.2.2 Substrate Conduction

A simplified resistance network model was used to identify the relative magnitudes of lateral conduction and backside cooling losses. Figure 4.1 shows a schematic of the chip along with major heat transfer paths.

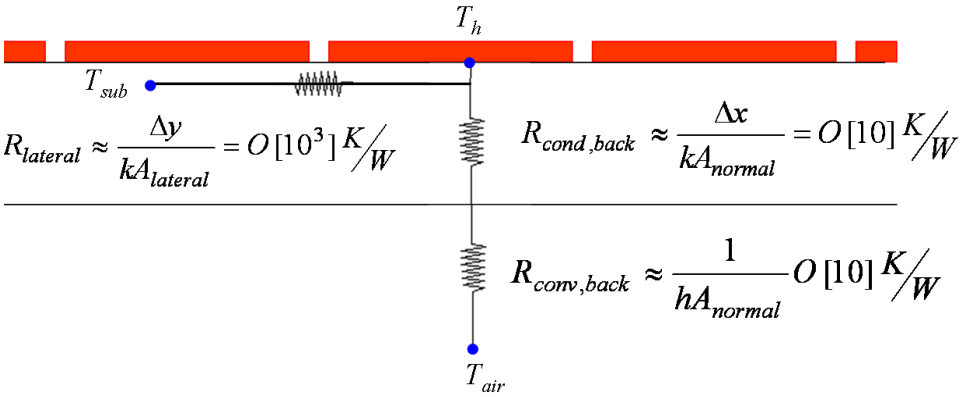

Figure 4.1: Simplified resistance network model for the major heat transfer paths in the microheater array (Δx and Δy are dimension of the chip vertical and lateral directions respectively).

Based on the heater geometry and material properties of the chip, the values of thermal resistances for different heat transfer paths are shown. The thermal resistance in the lateral direction is almost two orders of magnitudes higher than that to the backside of the chip, resulting in negligible lateral conduction losses. This assumption was also validated by 3-D COMSOL^{TM} model. Two separate boundary conditions were used at the side walls. In the first analysis, the side walls were assumed to be adiabatic. In the second analysis, the side walls were prescribed the bulk liquid temperature (closer to the actual experimental condition). It was found that the difference between the results of the two analyses (max. 3%) were negligible. Moreover, the lateral conduction term was within 1% of the backside losses.

Based on the above assumption, heat transfer paths within the chip are illustrated in Figure 4.2. Only a portion of the total heat generated (q''_{gen}) was removed by the liquid (q''_{b}). The remaining portion was lost to the ambient either through natural convection or forced convection (q''_{back}). Figure 4.2 (left) represents the case without air-jet (subscript *n*)–a small amount of heat ($q''_{back,n}$) was lost through the back of the chip by natural convection to the ambient air. Figure 4.2 (right) represents the situation with air-jet (subscript *f*), *i.e.* forced convection whereby considerably more heat ($q''_{gen,f}$) was lost to the ambient.

The energy balance for the natural and forced convection cases are given by

$$q''_b = q''_{gen,n} - q''_{back,n} \qquad \text{(natural convection)} \qquad (4.4)$$

$$q''_b = q''_{gen,f} - q''_{back,f} \qquad \text{(forced convection)} \qquad (4.5)$$

If the heater surface is at the same temperature for both the cases, the heat supplied to the liquid $q_b^{"}$ for boiling remains unchanged, so

$$q_{gen,f}^{"} - q_{gen,n}^{"} = q_{back,f}^{"} - q_{back,n}^{"} \tag{4.6}$$

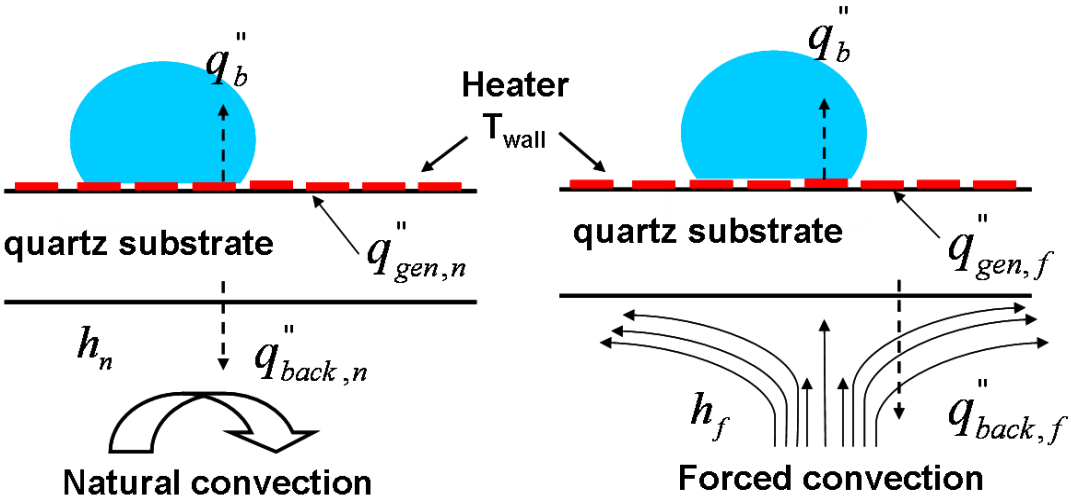

Figure 4.2: The schematic of the heat transfer contributions for the natural convection (left) and forced convection (right) cases.

Spatially-averaged heat flux data was calculated with the air-jet on ($q_{gen,f}^{"}$) and the air-jet off ($q_{gen,n}^{"}$) at 1.8g for wall superheats of 39°C and 44°C. The natural convection heat transfer coefficient h_n of 10 W/m^{2}K was assumed at the back of the chip for the case without the air-jet. A typical COMSOL^{TM} model is shown of Figure 4.3. The 96 elements are prescribed to be a specified heater temperature (*e.g.* T_w=100°C or 373.15 K, Figure 4.3). The COMSOL^{TM} model results were used in the analysis after performing grid independence tests only. Figure 4.4 shows a typical mesh used for substrate conduction analysis while Table 4.1 shows the corresponding mesh parameters.

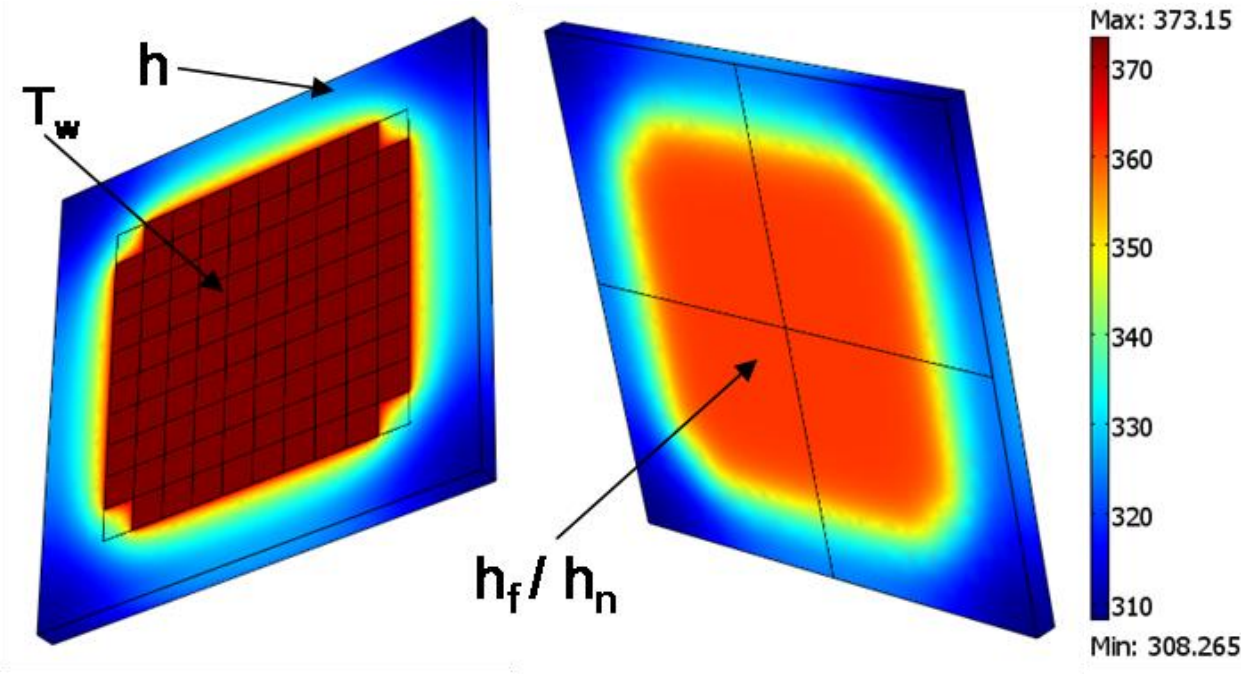

Figure 4.3: A typical COMSOL^{TM} model of the microheater array.

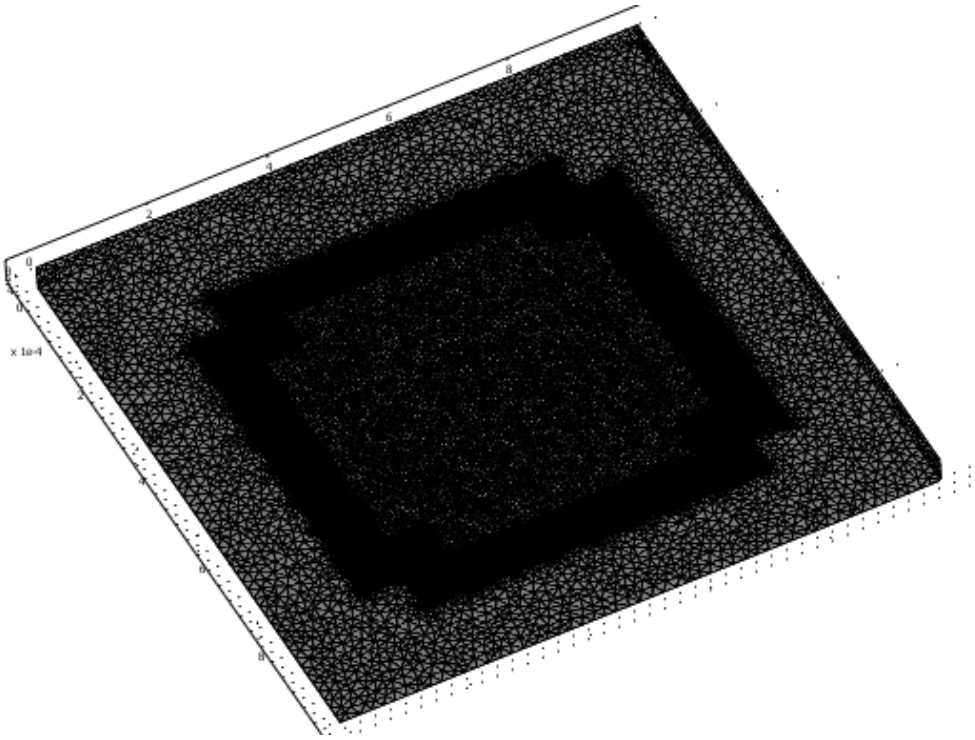

Figure 4.4: A typical mesh used for substrate conduction analysis.

Table 4.1: Mesh parameters.

Parameter	Value
Number of degrees of freedom	363299
Number of mesh points	52295
Number of elements	232463
Tetrahedral	232463
Prism	0
Hexahedral	0
Number of boundary elements	52494
Triangular	52494
Quadrilateral	0
Number of edge elements	3048
Number of vertex elements	134
Minimum element quality	0.231
Element volume ratio	0

The 3-D COMSOL^{TM} model with appropriate boundary conditions and h_n of 10 W/m^{2}K was used to calculate $q''_{back,n}$. With all three quantities known, Eq. 4.6 was solved for $q''_{back,f}$ (Table 4.2). With the forced convection substrate conduction loss known, the COMSOL model was used to back-calculate the forced convection heat transfer coefficient (h_f). A value of 554 W/m^{2}K for a wall superheat of 39°C and 547 W/m^{2}K for that of 44°C was obtained from the COMSOL model (Table 4.1). A mid value of 550 W/m^{2}K was assumed for h_f for further calculations at all temperatures. Use of a uniform, area averaged h_f is justifiable since the heat transfer results presented below are also area averaged. This forced convection heat transfer coefficient with other appropriate

boundary conditions was used to calculate the substrate conduction losses at other temperatures.

Table 4.2: Substrate conduction calculation

Quantity	q" (W/cm^2, ΔT_w =39°C)	q" (W/cm^2, ΔT_w =44°C)
$q''_{gen,\,f}$	28.1	31.5
$q''_{gen,\,n}$	23.2	26.4
$q''_{back,\,n}$	0.2	0.2
$q''_{back,\,f}$ (h_f,W/m^{2}K)	5.1 (554)	5.3 (547)

The constant temperature boundary condition assumption for the microheater array gets worse with decreasing heater size. However, the heat transfer coefficient at the back of the chip was the same regardless of the heater size. For cases where the constant temperature boundary condition cannot be applied (heated areas smaller than 2.8x2.8 mm^2, 16 elements, 7 mm microheater), a constant heat flux boundary condition was applied at the heaters in the COMSOL simulations. This heat flux was iteratively varied until the area averaged temperature of the heated area equaled the set temperature of the heater. This value of heat flux ($q''_{back,f}$) was subtracted from the raw heat transfer to obtain the heat flux utilized for boiling.

When performing local analysis, the area averaged approach adopted in the previous section for heater averaged analysis could not be applied. It was essential to quantify the substrate conduction losses from individual heater elements. As a result, two experiments were performed to obtain a better estimation of the fraction of heat utilized

for boiling. For both cases, the raw voltage data obtained from the i^{th} heater element was first converted to time averaged raw heat flux ($q''_{gen,i}$). In the first case where boiling was initiated, a portion of the total heat generated ($q''_{gen,i,f}$) was utilized for boiling while a significant portion was lost to the backside cooling jet through forced convection (subscript *f*). The second case without boiling (natural convection case-subscript *n*) served as the baseline. A significant portion the time averaged raw heat flux $q''_{gen,i,n}$ by the i^{th} heater element was lost to the cooling jet through forced convection while the losses through natural convection on top of the heater were relatively small. The difference between the raw heat flux for the first case and the baseline gave us the heat flux utilized for boiling ($q''_{boiling,i}$) by i^{th} heater element.

$$q''_{boiling,i} = q''_{gen,f,i} - q''_{gen,n,i} \tag{4.7}$$

Finally, an average over *N* the active elements was computed to plot the boiling curves for different conditions.

$$q''_{boiling} = \sum_{i=1}^{N} \left(q''_{gen,f,i} - q''_{gen,n,i} \right) / N \tag{4.8}$$

where N=9, 16, 25, 36, 64, and 96.

4.3 UNCERTAINTY ANALYSIS

Uncertainty propagation analysis (Coleman and Steele 1999) was used to calculate the overall uncertainty in the value of measured parameters. For a general case of an experimental result, *r*, computed from *J* measured variables $X_{1...J}$, the data reduction equation can be written as:

$$r = r(X_1, X_2, \ldots, X_J) \tag{4.9}$$

and hence, the uncertainty in the experimental result is given by

$$U_r^2 = \left(\frac{\partial r}{\partial X_1}\right)^2 U_{X_1}^2 + \left(\frac{\partial r}{\partial X_2}\right)^2 U_{X_2}^2 + \cdots + \left(\frac{\partial r}{\partial X_J}\right)^2 U_{X_J}^2 \qquad (4.10)$$

where U_r is the uncertainty in the result, U_{X1} is the uncertainty in the variable X_1, etc. The individual uncertainty U_x of the measured variable/parameter was based on the resolution/least-count of the corresponding sensors. In case a curve fit/regression approach was adopted for the measurement of certain quantities, the individual uncertainty U_x was based on the standard deviation of the measured parameters from the curve used. The next three sections describe the uncertainty in the value of measured parameters for the different sets of experimental results presented in this work.

4.3.1 Variable Gravity Experiments

Substrate conduction and g-jitter were the two major sources of uncertainty in the heat flux. The uncertainty in q''_{gen} is negligible since the voltage and heater resistance were accurately measured. Higher uncertainties in substrate conduction were associated with the partitioning of q''_{gen} into q''_b and q''_{back}. Natural convection heat transfer coefficients for gases can vary from 2 W/m^{2}K to 25 W/m^{2}K (Incropera *et al.*, Fundamental of Heat and Mass Transfer, 2007). The uncertainty in $q''_{back,n}$ due to the selection of h_n of 10 W/m^{2}K in the previous section was computed to be 0.21 W/cm^2. According to Eq. 4.6, this uncertainty in $q''_{back,n}$ results in the same uncertainty in $q''_{back,f}$. Since forced convection heat transfer coefficients h_f of 554 W/m^{2}K and 547 W/m^{2}K were obtained from the COMSOL^{TM} modeling, a mid value of 550 W/m^{2}K was selected for the calculations of substrate conduction at all temperatures. The maximum deviation in

the heat transfer coefficient due to this selection was 4 W/m^{2}K. This error in the heat transfer coefficient resulted in an uncertainty of 0.06 W/cm^2 in $q''_{back,f}$ and hence in q''_b.

The resolution of 0.002g in the accelerometer data was the maximum uncertainty in the measurement of acceleration. The rapid fluctuations in the acceleration value from the mean (g-jitter) resulted in uncertainty in the estimation of q''_b. Fluctuations in acceleration due to g-jitter was used to quantify the uncertainty in the heat flux in all three regimes; high-g, transition and low-g. The raw acceleration data (a^*_{data}) is plotted in blue on Figure 4.5. The red line is the smooth polynomial fit (a^*_{fit}) on the raw data.

Let,

$$\frac{a}{g} = a^* \tag{4.11}$$

Fluctuation in the acceleration data can be quantified by calculating the difference between the raw acceleration data and the corresponding curve fit as defined below.

$$\Delta a^* = a^*_{data} - a^*_{fit} \tag{4.12}$$

The standard deviation in acceleration for each regime was calculated using the following formula;

$$\sigma_{a^*} = \sqrt{\frac{\sum_{n=1}^{N}\left(a^*_{data,n} - a^*_{fit,n}\right)^2}{N}} \tag{4.13}$$

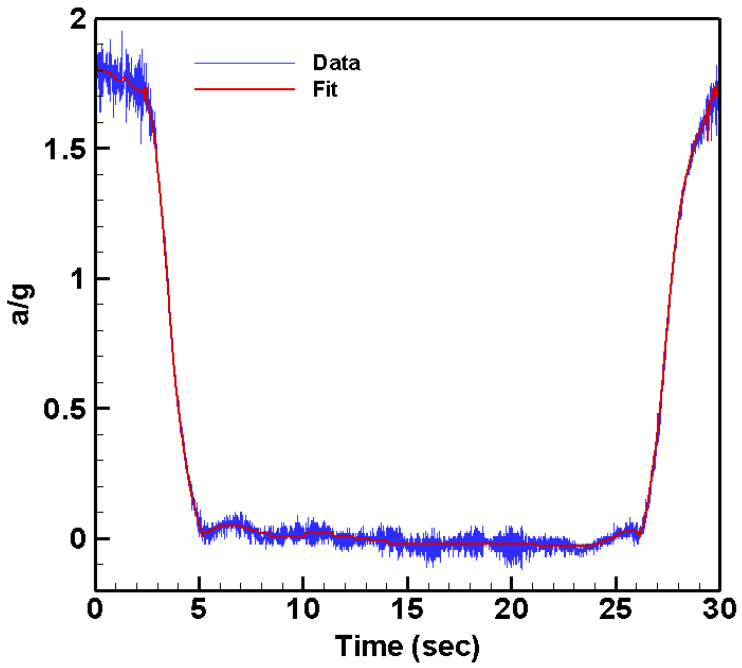

Figure 4.5: Raw acceleration data and the corresponding fit during one parabola.

Figure 4.6 shows the raw heat flux data (q''_{data}) as a function of time for one parabola. A curve fit (q''_{fit}) for the variation of heat flux with acceleration is also performed for all three zones (red curve). A parametric dependence can be found between the acceleration and the heat flux from the two curve fit equations (q''_{fit} and a^*_{fit}).

$$q''_{predicted} = f(a^*) \tag{4.14}$$

If g-jitter were responsible for the fluctuations in heat flux, the value of the function $f(a^*_{data})$ evaluated at the raw acceleration points should equate to the raw heat flux data (q''_{data}).

$$q''_{predicted}(a^*_{data}) = q''_{predicted}(a^*_{fit} + \Delta a^*) = f(a^*_{fit} + \Delta a^*) \tag{4.15}$$

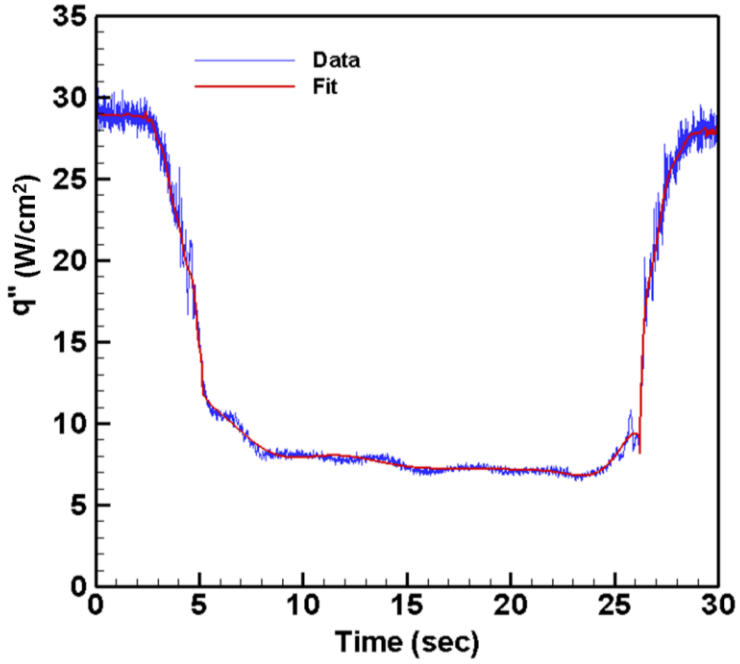

Figure 4.6: Heat flux data and the corresponding curve fit during one parabola.

The difference between the raw data and the predicted value of heat flux and is the uncertainty in the heat flux due to g-jitter.

$$\Delta q^{"} = q^{"}_{data} - f(a^{*}_{data}) \tag{4.16}$$

$$q^{"}_{rms} = \sqrt{\frac{\sum_{n=1}^{N}\left(q^{"}_{data,n} - f(a^{*}_{data,n})\right)^2}{N}} \tag{4.17}$$

The root mean square (RMS) error in the heat flux and the standard deviation of the acceleration was computed at all temperatures. Figure 4.7 and Figure 4.8 are the plots of the RMS error in heat flux and the standard deviation in the acceleration for all three regimes at various temperatures for the high and low gas cases respectively.

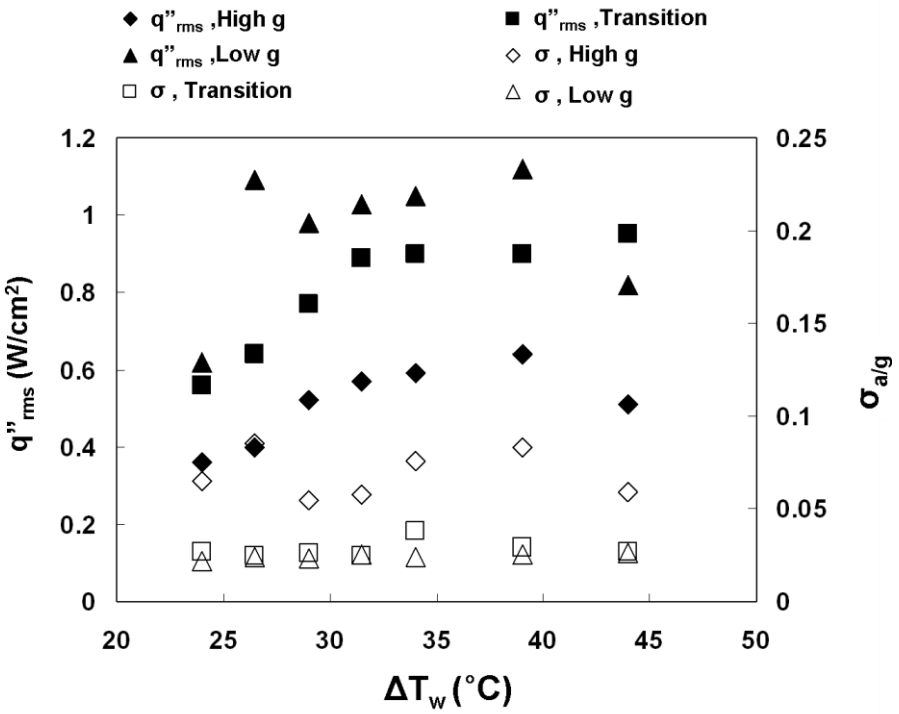

Figure 4.7: q''_{rms} and σ_{a^*} as a function of wall superheat for high gas (1216ppm).

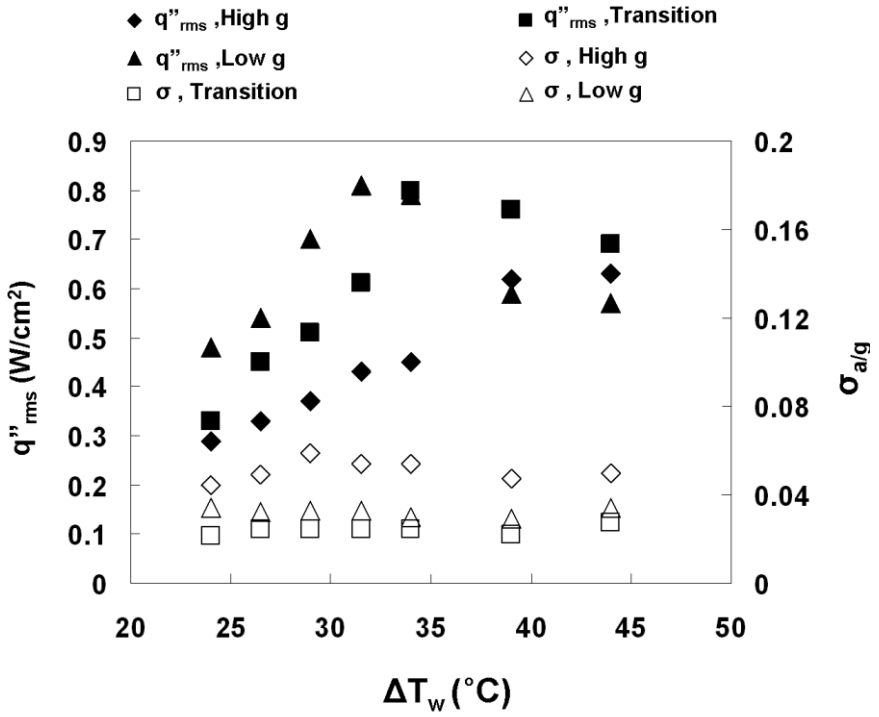

Figure 4.8: q''_{rms} and σ_{a^*} as a function of wall superheat for low gas (220ppm).

The standard deviation of the acceleration for all the test cases in the hypergravity, transition and low-g regimes were strictly less than 0.085g, 0.037g and 0.034g respectively. The associated uncertainty in the heat flux due to g-jitter for each of the regimes was found to be less than 1.12 W/cm^2. Hence, the overall uncertainty in the heat flux values at any temperature due to all these sources and acceleration was not more than 1.14 W/cm^2.

Experimental measurement of saturation pressure of n-perfluorohexane was performed at 25°C. The database value of $(dp/dT)_{sat}$ was used to calculate the saturation pressure at all other temperatures. The error in the calculation of the saturation pressure of n-perfluorohexane was not more than 84 Pa. Near room temperature, the vapor pressure of n-perfluorohexane changes by 3,280Pa/°C and the value of H is 5.4x10^{-8} mole/mole-Pa. Hence, the uncertainty in the saturation temperature was about 0.026°C while the uncertainty in the gas concentration c_g was at most 4.5 ppm. Uncertainties in the measurement of temperature (Techne, Inc. model WSP350 PRT with TECAL Accutemp RTD indicator) and pressure (PTG PX01C1-015A5T 15 PSIA, 0.01% FC accuracy) during the degassing procedure (68 Pa and 0.001°C, respectively) introduce additional uncertainty of about 3.7 ppm in the measurement of gas concentration. Hence, the total uncertainty in the gas concentration c_g should not exceed 5.8 ppm.

The thermistor used to measure the fluid temperature and the RTD used to control the chamber sidewall temperature were calibrated in a constant temperature bath using a NIST calibrated thermometer to within 0.2°C. For a given flight, the bulk liquid temperature never varied by more than 1.7°C. Hence, the uncertainty in bulk liquid temperature is estimated to be less than 1.7°C. The uncertainty of 0.2°C associated with

the calibration temperature and a temperature resolution of 0.27°C due to the least count of the digital potentiometer used in the feedback circuit could at most introduce an uncertainty of 0.33°C in the measurement of wall temperature. The variation in acceleration introduced a variation of about 4800 Pa in the hydrostatic pressure at the heater surface. Uncertainty in pressure measurement due to sensor resolution and hydrostatic pressure was found to introduce an uncertainty of less than about 1.44°C in the saturation temperature. Table 4.3 is a summary of conservative estimate of the uncertainties in different parameters.

Table 4.3: Summary of uncertainty estimates in the value of measured parameters.

Quantity	Uncertainty
q" [W/cm^2]	1.2
T_{bulk} [°C]	2
T_{wall} [°C]	0.5
T_{sat} [°C]	1.5
ΔT_w [°C]	1.6
a [g]	0.01
c_g [ppm]	6

4.3.2 Heater Size Study

Substrate conduction was again the major source of uncertainty in the heat flux. Similar to the variable gravity experiments, the uncertainty in q''_{gen} was negligible since the voltage and heater resistance were accurately measured. Higher uncertainties in substrate conduction were associated with the partitioning of q''_{gen} into q''_b and q''_{back}. Natural convection heat transfer coefficients for gases can vary from 2 W/m^{2}K to 25

W/m^{2}K (Incropera *et al.*, Fundamental of Heat and Mass Transfer, 2007). The uncertainty in $q''_{back,n}$ due to the selection of h_n of 10 W/m^{2}K in the previous section was computed to be 0.21 W/cm^2. According to Eq. 4.6, this uncertainty in $q''_{back,n}$ results in the same uncertainty in $q''_{back,f}$. The maximum deviation in the averaged heat transfer coefficient from the individual value at each superheat was 40 W/m^{2}K. This error in the heat transfer coefficient resulted in an uncertainty of 0.6 W/cm^2 in $q''_{back,f}$ and hence in q''_b.

The thermistor used to measure the fluid temperature and the RTD used to control the chamber sidewall temperature were calibrated in a constant temperature bath using a NIST traceable thermometer to within 0.2°C. For the given set of experiments, the bulk liquid temperature never varied by more than 0.4°C. Hence, the uncertainty in bulk liquid temperature is estimated to be less than 0.45°C. The uncertainty of 0.2°C associated with the calibration temperature and a temperature resolution of 0.29°C due to the least count of the digital potentiometer used in the feedback circuit could at most introduce an uncertainty of 0.35°C in the measurement of wall temperature. A summary of the uncertainty estimates is given on Table 4.4.

Table 4.4: Summary of uncertainty estimates in the value of measured parameters.

Quantity	Uncertainty
q" [W/cm^2]	0.65
T_{bulk} [°C]	0.45
T_{wall} [°C]	0.35
T_{sat} [°C]	1.5
ΔT_w [°C]	1.5

4.3.3 Orientation Study

The uncertainty in pressure due to the calibration of the pressure sensors was less than 900 Pa. An uncertainty of 900 Pa in pressure P resulted in an uncertainty of 0.27°C in the saturation temperature T_{sat}. The uncertainties associated with microheater calibration (0.08°C) and temperature resolution (0.26°C) due to the least count of the potentiometer could at most introduce an uncertainty of 0.26°C in the measurement of wall temperature T_{wall}. An uncertainty of 0.27°C in T_{sat} and 0.26°C in T_{wall} could at most introduce an uncertainty of 0.38°C in the estimation of wall superheat ΔT_w. The standard deviation in the reading of the four thermistors used for the measurement of bulk liquid temperature T_{bulk} was never more than 1.8°C. An uncertainty of 0.27°C in T_{sat} and 1.8°C in T_{bulk} resulted in a maximum uncertainty of 1.82°C in the estimation of subcooling ΔT_{sub}. The uncertainty in q''_{gen} is negligible since the voltage and heater resistance were accurately measured. However, higher uncertainties (1.4 W/cm^2) in heat flux q'' were associated with the partitioning of generated heat into that utilized for boiling and the other component lost to cooling jet at the back of the chip. A summary of uncertainty estimates in the value of measured parameters is shown on Table 4.5.

Table 4.5: Summary of uncertainty estimates in the value of measured parameters.

Quantity	Uncertainty
q" [W/cm^2]	1.4
T_{bulk} [°C]	1.8
T_{wall} [°C]	0.3
T_{sat} [°C]	0.3
ΔT_w [°C]	0.4
ΔT_{sub}[°C]	1.8

Chapter 5: Variable Gravity Pool Boiling Experiments

5.1 INTRODUCTION

Most correlations for heat flux in the nucleate boiling regime are described using an equation of the form:

$$q'' = f(c_g, c_p, h_{lv}, p, \alpha, \mu, \rho_l, \rho_v, \sigma, \Delta T_{sub}) * \Delta T_w^n \left(\frac{a}{g}\right)^m \tag{5.1}$$

All these correlations assume that heat transfer dependence on gravity can be captured through the use of a power law where *m*=constant. However, the literature survey presented in Chapter 2 highlighted a lack of consensus on the value of power law coefficient *m*. This discrepancy in the literature can be attributed to the fact that virtually all work to date regarding parametric effects of gravity on pool boiling has been inferred from experiments performed in low-g, 1-g or 1.8-g conditions.

The primary objective of this work is to bridge the gap between the experiments conducted at low-g and high-g. Taking the logarithm of Eq. 5.1 yields

$$\log(q'') = m \log\left(\frac{a}{g}\right) + c \tag{5.2}$$

where $c = \log(f) + n \log\left(\Delta T_w\right)$

If the power law dependence is valid, a linear variation in log(*q''*) vs. log (*a*/g) with slope *m* is expected for a given fluid at a constant superheat. Changes in wall superheat and gas concentration should affect the intercept *c* only and not affect the slope *m*. Results of variable gravity pool boiling experiments are analyzed in this chapter to verify the validity of power law dependence based on a constant *m*.

5.1.1 Test Conditions

The current work is based on observations of boiling heat transfer experiments performed over a continuous range of gravity levels (0g - 1.8g) under subcooled liquid conditions (C_6F_{14}- n-perfluorohexane, ΔT_{sub}=26°C, 1 atm), and two gas concentrations (220 ppm and 1216 ppm). A constant temperature microheater array with a heated area of 7x7 mm^2 was used to vary the heater temperature between 65°C (ΔT_w=9°C) and 100°C (ΔT_w=44°C). The pressure was maintained at 1 atm throughout the experiment. A summary of the test conditions is shown on Table 5.1.

Table 5.1: Summary of test conditions

Fluid	n-perfluorohexane
Area [mm^2]	7 x 7 (96 elements)
c_g [ppm]	220 and 1216
ΔT_{sub} [°C]	26°C
P [atm]	1
ΔT_w [°C]	9, 14, 19, 24, 26.5, 29, 31.5, 34, 39, and 44

5.1.2 Variable Gravity Environment

Data was collected during the 48th ESA Parabolic Flight Campaign organized in March, 2008. A typical parabola during microgravity flights along with the acceleration levels is shown on Figure 5.1. Thirty parabolas were flown per flight, and three flights were made. The parabolic flight campaign has been primarily used to study phenomena under low-g and hypergravity (>1.5g) conditions. However, as can be seen in the Figure 5.1, there was a transition period of approximately 3-5 s when the acceleration varied continuously from hypergravity to low-g and vice versa. This period is generally

considered too short for a process to reach equilibrium and hence unsuitable for making any measurements. However, data was acquired for this period throughout the transition from hypergravity to low-g and vice versa. In order to study heat transfer during this transition, the heat flux must be in quasi-steady state at any given gravity level.

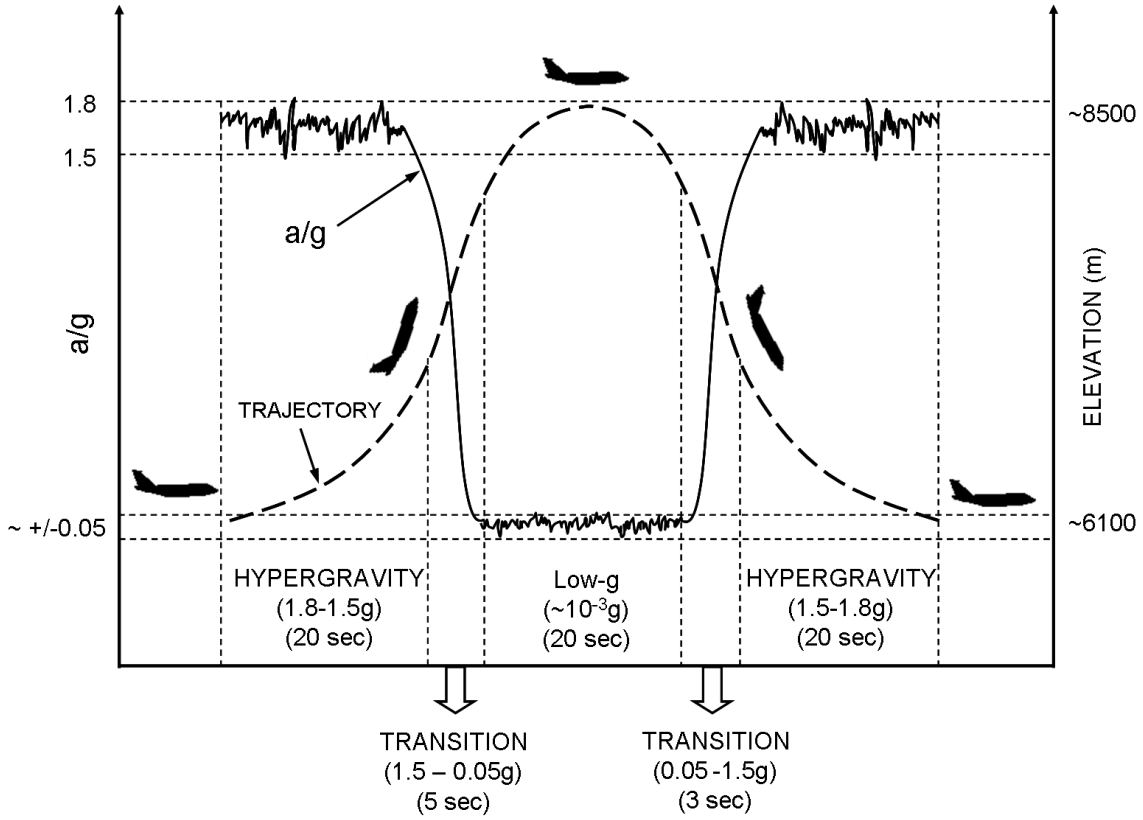

Figure 5.1: Schematic of the trajectory of the parabolic flight with corresponding acceleration levels.

5.1.3 Quasi-steady state

A plot of q_b'' versus acceleration during the transition from hypergravity to low-g and vice versa at ΔT_w=9°C and ΔT_w=44°C is shown on Figure 5.2. Ideally, if the flow field and heat transfer profiles have sufficient time to achieve steady state at each

acceleration level, there should be no difference in the two curves. However, a hysteresis effect in the heat flux curve is present at the lower superheat (ΔT_w=9°C) (Figure 5.2a). This was observed whenever the superheat was not sufficient to initiate nucleation, and heat transfer was by natural convection. As the gravity changes, time is required for the flow field and heat transfer profiles to develop and achieve steady state. Before the transition from high-g to low-g, the natural convection flow field was fully developed. During the transition from high-g to low-g, the flow field required more time to achieve steady state than was available, resulting in higher heat transfer than the expected quasi-steady value. Similarly, during the transition from low-g to high-g, the heat transfer was lower than the expected quasi-steady value.

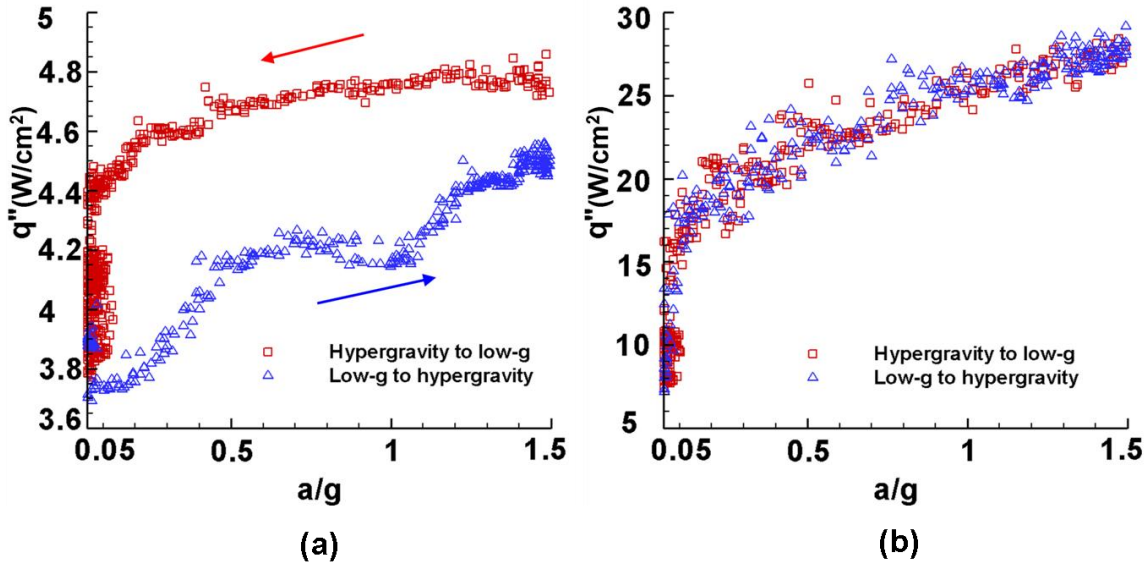

Figure 5.2: Heat flux vs. acceleration during transition for (a) ΔT_w=9°C and (b) T_w=44°C.

However, at ΔT_w=44°C (Figure 5.2b), the heat transfer is independent of the direction of transition. At this temperature, the majority of heat transfer is due to bubble

growth and bubble departure. Since bubble departure frequencies can be as high as 30-40 Hz at normal gravity, the heat transfer during the transitions when boiling occurs are quasi-steady. The 15 kHz response of the heater and feedback circuit and the data acquisition frequency of 100 Hz rule out any chances of discrepancies due to data collection.

5.2 EFFECTS OF GRAVITY

To verify the assumed power law dependence, the boiling heat flux data was binned based on gravity level into equal intervals of 0.005g. The average heat flux within each bin was assigned to the midpoint acceleration of each bin. Data points corresponding to negative acceleration values (g-jitter) were rejected. An example of the data is shown in Figure 5.3. The red squares correspond to the binned data for transition from hypergravity to low-g while the blue triangles correspond to the data during transition from low-g to hypergravity. A sharp change in heat flux is observed between 0.1g-0.2g indicating a distinct change in the heat transfer mechanism, and rules out the possibility of use of a unified power law for gravity dependence as per Eq. 5.1. The heat transfer regime that occurs below the transition acceleration will hereafter be referred to as the *low-g regime*, while the regime above this transition will be referred to as the *high-g regime*. Any acceleration higher than 1.5g is referred to as *hypergravity*.

Comparison of these plots with the video revealed that a primary bubble formed and remained attached to the surface in the low-g regime, while regular bubble departure occurred in the high-g regime. The three images on the right (Figure 5.3, solid arrows at 0.3g, 0.85g, and 1.68g respectively) correspond to departing bubbles in the high-g regime. The dryout area and the average bubble departure diameter decreased with

increasing gravity. Smaller bubble departure diameter corresponded to an increase in departure frequency which, coupled with the decreased dryout area, resulted in an increase in heat transfer with gravity. The image on the left (dashed arrow) is that of a non-departing primary bubble in the low-g regime with large dryout area and hence lower heat transfer. The presence of a third regime where the bubble departs due to fluid inertia cannot be ruled out for larger heaters. Based on the results of Lee and Merte, 1997, the presence of a third regime at very low gravity levels (~10^{-4}g) and larger heaters (~19x38 mm^2) was observed. A large bubble formed during initial nucleation hovered over the heaters acting as a vapor sink for smaller bubbles generated on surface resulting in constant rewetting of the heater surface and high heat transfer. Aparajith *et al.*, 2003 8reported a decrease in departure time and departure diameter due to bubble coalescence under low gravity conditions (~10^{-2}g). The time averaged heat flux increased with the number of coalescing bubbles. However, the current set of experiments with 7x7 mm^2 heater size did not enter any such heat transfer regime.

Similar qualitative dependence on gravity was also observed at other wall superheats as well (Figure 5.4). The gravity dependence (m) became stronger with increasing wall superheat in the high gravity regime as seen in Figure 5.4 and Figure 5.5, suggesting that the wall superheat and acceleration effects are not independent as suggested by Eq. 5.1. As will be stressed again in the next few sections, the parametric effects of gravity, wall superheat, and gas concentration are highly interlinked, ruling out the possibility of simple power law correlations. The dependence of gravity on heat transfer is small in the low-g regime ($0.01<m<0.1$, Figure 5.5).

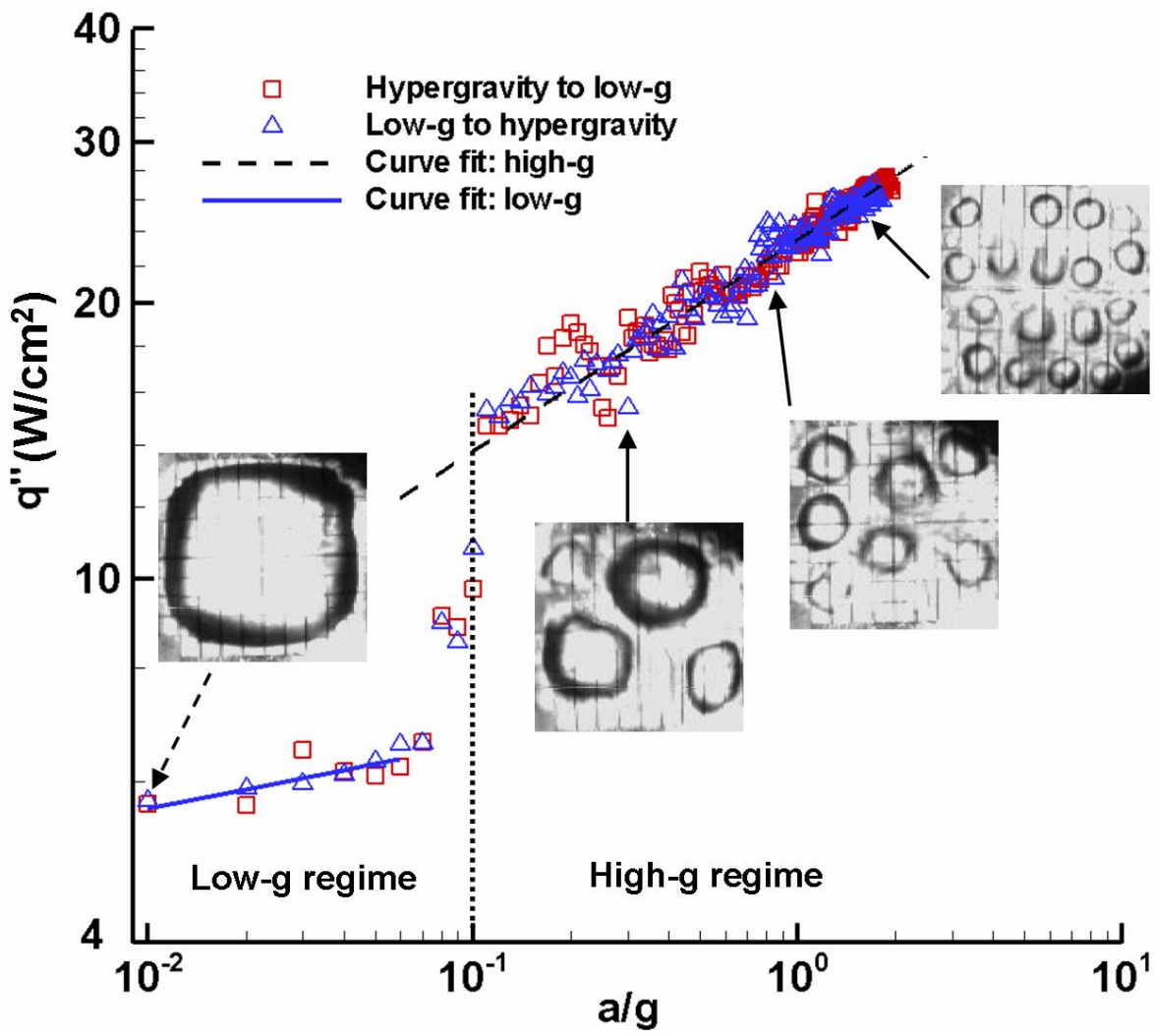

Figure 5.3: Plot of heat flux vs. acceleration for high gas case (c_g ~1216ppm), at ΔT_w=44°C, with superimposed bottom view images at 0.01g, 0.3g, 0.85g and 1.68g.

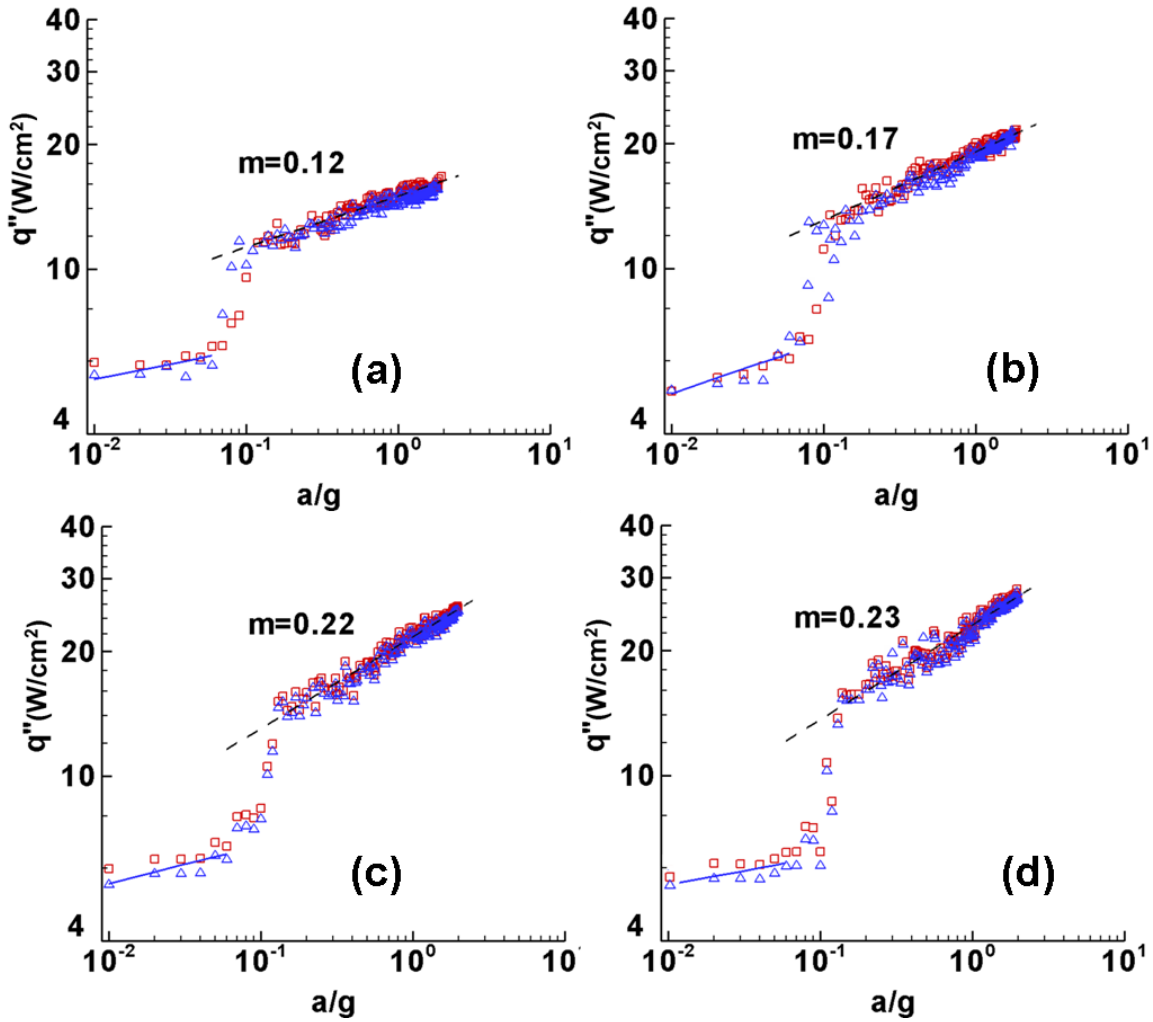

Figure 5.4: Plot of heat flux vs. acceleration for the high gas case (c_g ~1216ppm) for ΔT_w (a) 24°C, (b) 29°C, (c) 34°C, and (d) 39°C.

Figure 5.4 shows that the change in heat transfer regime occurred between 0.10g to 0.22g. As mentioned earlier, the transition in heat flux coincides with the transition between the high-g regime (departing bubbles) and low-g regime (non-departing primary bubble). Henceforth, the acceleration at which bubble departure stops during the transition to low-g or the acceleration at which the primary bubble departs during the transition to hypergravity will be referred to as the departure acceleration (a_{depart}).

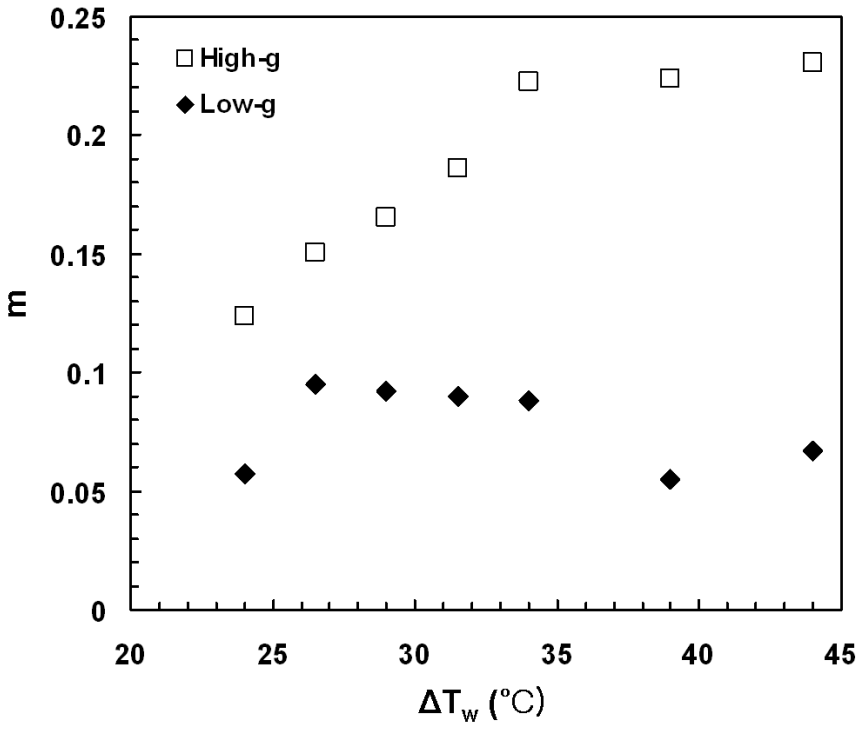

Figure 5.5: A plot of the power law coefficient *m* in low-g and high-g regime.

The Fritz correlation (Eq. 5.3) was used to calculate the value of a_{depart}. The Fritz correlation is simply a force balance between buoyancy and surface tension for a single bubble in quasi-equilibrium. Forces due to thermocapillary flow and interactions at the heater surface due to bubble coalescence are unaccounted for. All these simplifications along with the experimental limitation like g-jitter add to the deviation in the predicted values. However, this simplified analysis could prove useful in the study of bubble dynamics based on the force balance between the surface tension and buoyancy.

$$0.0208\,\theta = \sqrt{\frac{a_{fritz}(\rho_l - \rho_v)D_{depart}^2}{\sigma}} \tag{5.3}$$

The apparent contact angle of the bubble was calculated from side view images. Ten points were placed on the bubble surface close to the heater, and 2nd, 3rd and 4th order

polynomial fits were obtained (Figure 5.6). The camera was inclined at 20° from the horizontal and was accounted for in the calculation of the coordinates. The tangent was calculated at the intersection of the fit and the heater surface and used to find the apparent contact angle. The apparent contact angle varied from 69° to 72° for the high gas case (1216 ppm) and all wall superheats. The deviation between the measured apparent contact angles for all images and the three polynomial fits was smaller than 4°.

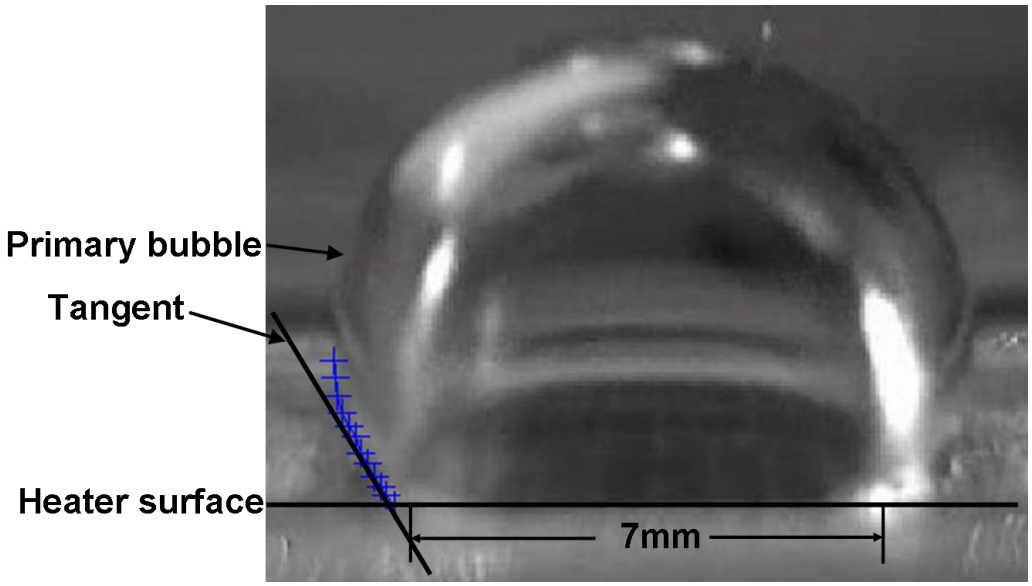

Figure 5.6: A representative figure of the primary bubble along with the selected points on the bubble surface for contact angle calculation.

The departure diameter was calculated from the bottom view images. An estimate of the error in the calculation of departure diameter was found to be 0.15 mm. Based on the uncertainties of 4° in the apparent contact angle and 0.15mm in the departure diameter, the error for each data point was evaluated. Based on 29.97 Hz video frequency and the rate of change of acceleration during transition, gravity changed no more than

0.02g between two successive frames. The minimum resolution of the accelerometer is about 0.002g. Thus, the uncertainty in the experimental value of a_{depart} is about 0.02g.

Values of a_{depart} obtained from the Fritz correlation and experiment (Figure 5.7) agree well, indicating that the surface tension and buoyancy are the principal parameters governing bubble departure. The value of a_{depart} does not show any clear dependence on wall superheat.

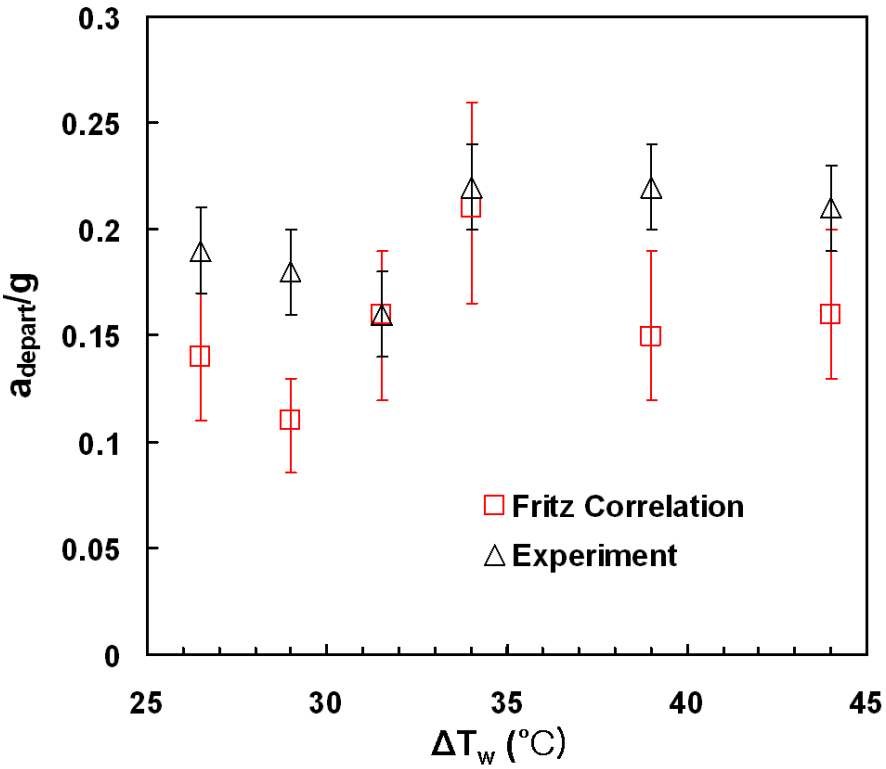

Figure 5.7: Comparison between the values of a_{depart} obtained from the Fritz correlation and experiment.

5.3 EFFECTS OF WALL SUPERHEAT

Boiling curves for the high gas case at a number of gravity levels are shown on Figure 5.8. For 0.3g, 0.6g, 1g and 1.3g, the flow at ΔT_w=9°C and ΔT_w=14°C was not in

quasi-steady equilibrium so this data was not included in Figure 5.8. Heat transfer increases with wall superheat in the high-g regime. As can be seen from the superimposed bottom view images (solid arrow), most of the heated area experienced natural convection at lower superheats resulting in low heat transfer. With the onset of nucleate boiling, a significant increase in the slope of the boiling curve is observed. Further increases in wall superheat results in additional nucleation sites being activated. For a given acceleration level, the bubble departure frequency increased with superheat due to an increase in the bubble growth rate, contributing to the increase in heat transfer.

A sudden decrease in heat transfer is evident as the acceleration decreases from 0.3g to 0.1g due to the transition to low-g regime–this corresponds to the formation of a non-departing primary bubble with large dryout area on the heater. The effect of wall superheat is not very clear for the high gas case in the low-g regime (dashed curves, Figure 5.8). At low wall superheat (ΔT_w=19°C, dashed arrow) and 0.1g, a large primary bubble with a few satellite bubbles formed, resulting in low heat transfer. At intermediate wall superheats (ΔT_w=29°C -31.5°C) for the same gravity level, more nucleating sites became activated and a primary bubble formed amidst numerous satellite bubbles. Lateral movement of the primary bubble along the heater array allowed coalescence and removal of the satellite bubbles allowing new bubbles to be nucleated. For 0.1 g, the heat transfer reached a maximum at ΔT_w=31.5°C. At higher superheat (ΔT_w=44°C), a large primary bubble nearly enveloped the entire heater resulting in lower heat transfer. As the acceleration is decreased to lower levels (0.007g and 0.05g), the heat transfer decreases as well, but the uncertainty in acceleration due to g-jitter becomes comparable to the acceleration values themselves.

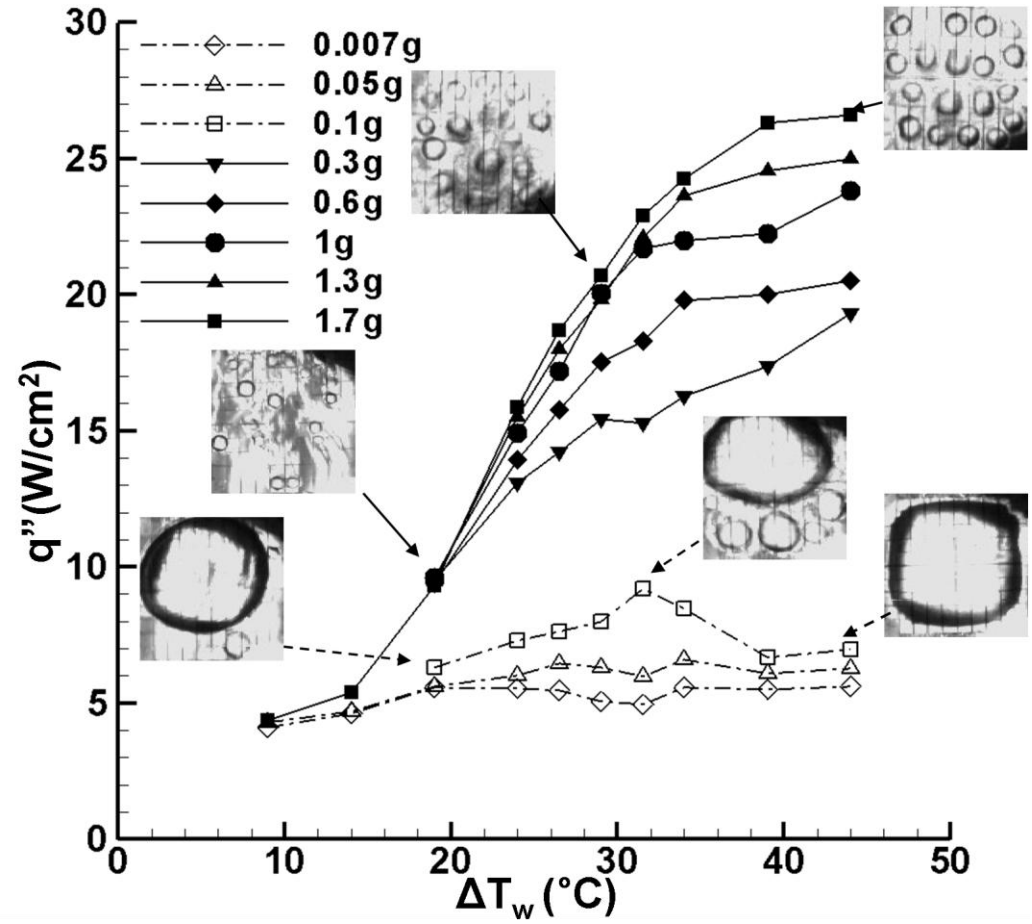

Figure 5.8: Boiling curve at different gravity levels for high gas (*cg* ~1216ppm) with superimposed bottom view images for 1.7g and 0.1g at different temperatures.

5.4 EFFECTS OF NONCONDENSABLE GAS

A plot of the heat flux versus acceleration for the low gas case also shows the presence of two regimes (Figure 5.9 and Figure 5.11). Similar to the high gas case in the high-g regime, bubble departure diameter decreased with acceleration while the departure frequency and nucleate site density increased (Figure 5.9, solid arrows), resulting in higher heat transfer. Dependence on gravity (*m*) increased with wall superheat in the high-g regime (Figure 5.10 and Figure 5.11).

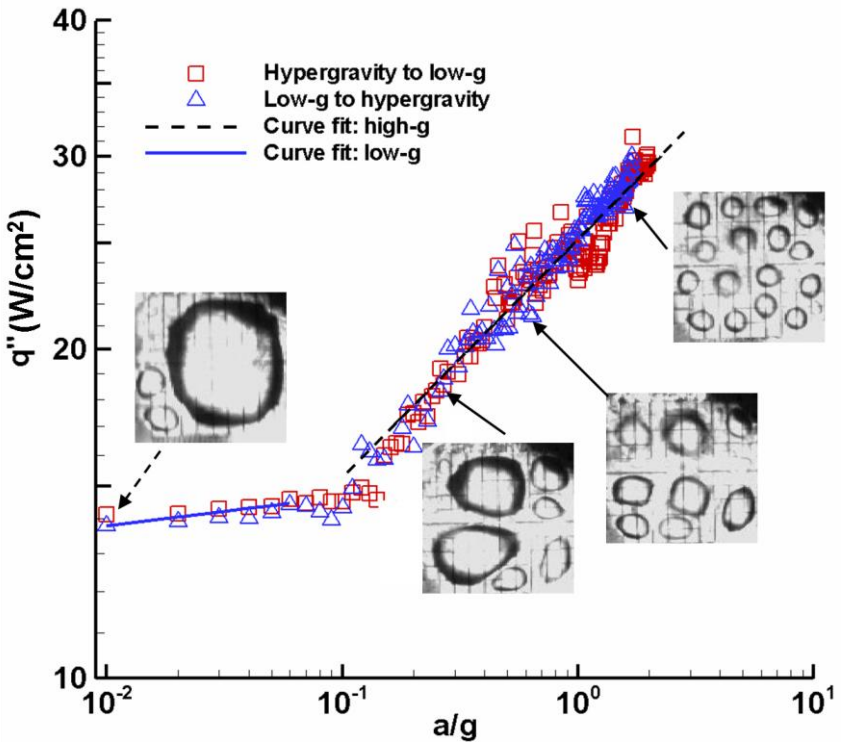

Figure 5.9: Plot of heat flux vs. acceleration for low gas case (c_g ~220ppm), at ΔT_w =44°C, with superimposed bottom view images at 0.01g, 0.28g, 0.74g and 1.71g.

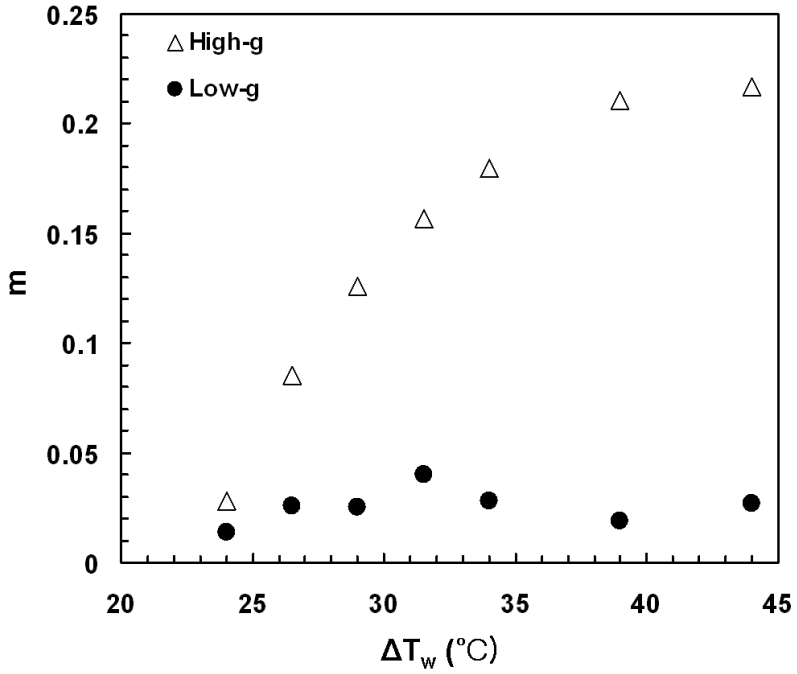

Figure 5.10: A plot of the slope *m* (Eq. 5.2) in low-g and high-g regime.

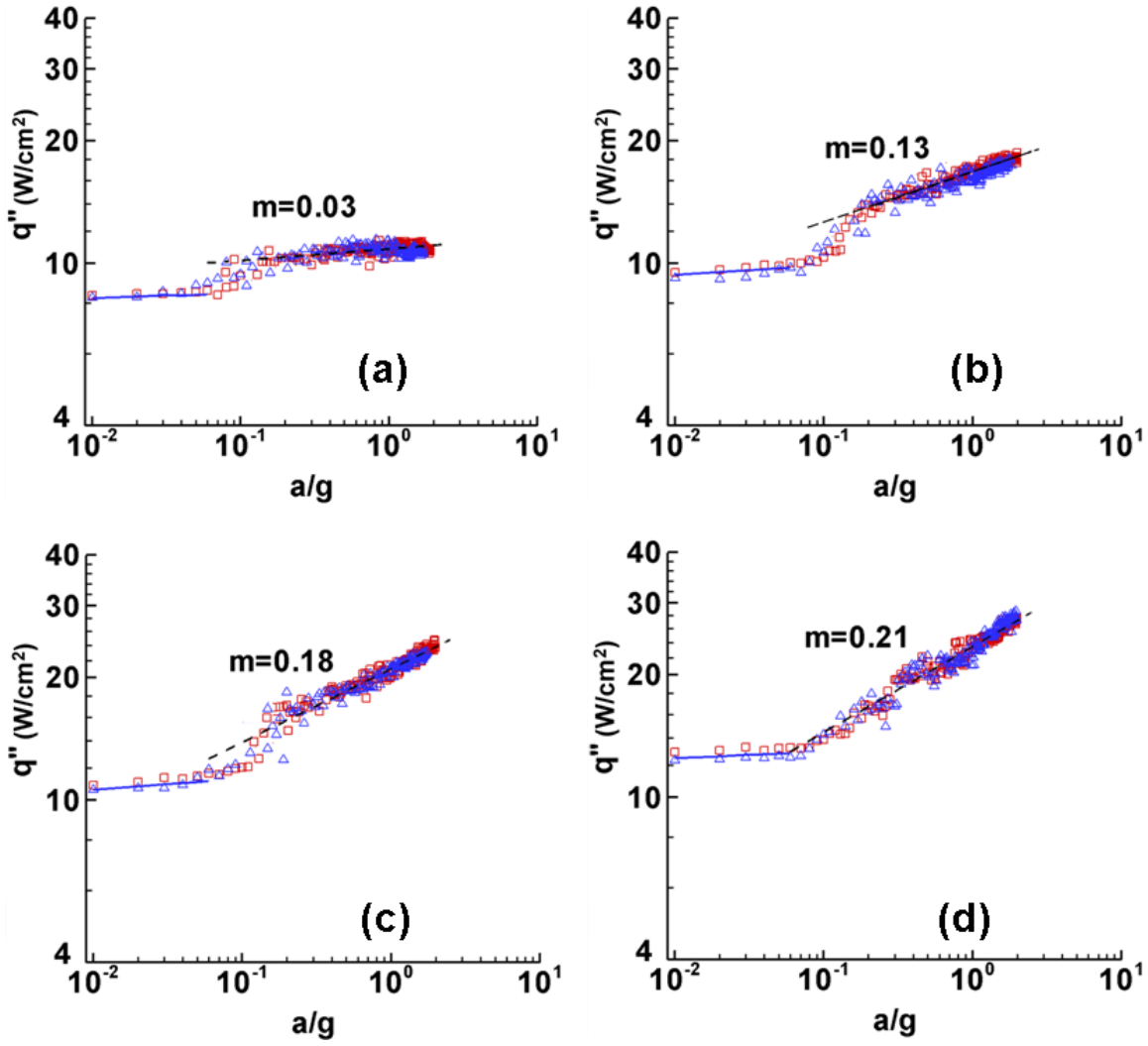

Figure 5.11: Plot of heat flux vs. acceleration for the high gas case (c_g ~220ppm), full heater (96 elements) for ΔT_w (a) 24°C, (b) 29°C, (c) 34°C, and (d) 39°C.

Boiling curves for both low and high gas cases at three acceleration levels are shown on Figure 5.12a. At low wall superheats, natural convection is the prominent heat transfer mechanism resulting in similar heat transfer coefficients for both gas concentrations. In the high-g regime (1g and 1.7g), the slope of the boiling curves increased significantly after the onset of nucleate boiling. However, onset of nucleate boiling for the low gas concentration (open symbols) occurred at higher superheat (as

observed by other researchers (You *et al.*, 1995; Rainey *et al.*, 2003; Honda *et al.*, 2002) since the presence of dissolved gas reduces the vapor pressure required to activate nucleating bubbles. For the accelerations in the high-g regime, nucleate boiling heat transfer is lower for the low gas case than for the high gas case (Figure 5.12a-b) which is consistent with the observations of Rainey *et al.* and Honda *et al.*. The presence of gas results in faster bubble growth and increased bubble departure frequency, resulting in higher heat transfer.

The size of the primary bubble that forms in low-g is smaller for the low gas case than for the high gas case (Figure 5.12a). For boiling within the low-g regime, the influence of gas on heat transfer is opposite of that observed in the high-g regime–heat transfer for the low gas case was higher than for the high gas case (Figure 5.12b). Similar observations based on the experimental work were reported by Henry *et al.*0, 2006 where heat fluxes for the degassed fluid (c_g<3ppm) were higher than for gas saturated fluid (c_g~3500ppm). At lower gravity levels, thermocapillary convection can be a major contributor to the heat transfer. Thermocapillary convection results from surface tension gradients along the bubble interface which can form due to temperature gradients.

$$\frac{d\sigma}{dx} = \frac{\Delta\sigma}{\Delta T}\frac{\Delta T}{\Delta x} \tag{5.4}$$

The first term on the right hand side of Eq. 5.4 is a function of the fluid property while the second term is a function of the available temperature difference along the bubble interface and bubble size.

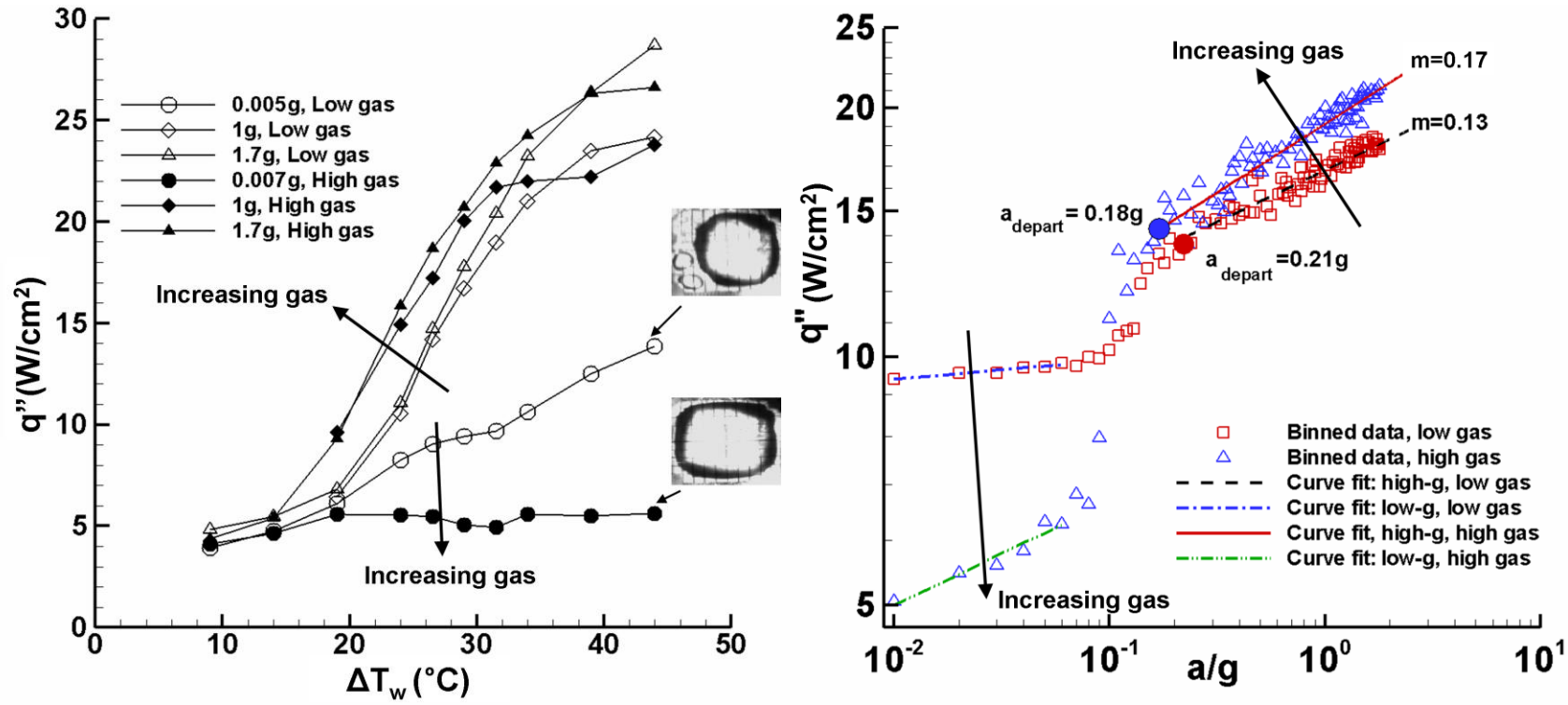

(a) (b)

Figure 5.12: (a) Boiling curve at three accelerations for low and high gas, (b) heat flux vs. acceleration in at ΔT_w =29°C, for two dissolved gas concentrations.

Figure 5.13 illustrates the differences between the primary bubbles that form at two gas concentrations. The temperature difference between the heater and the bubble top is generally similar for both cases ($\Delta T=T_{wall}-T_{bulk}$). However, due to the smaller bubble diameter ($D_{low}<D_{high}$) and larger contact angle for the low gas case ($\theta_{low}>\theta_{high}$), the available length for the surface tension variation was significantly smaller ($\Delta x_{AB}<\Delta x_{CD}$) for the low gas case. The resulting increase in temperature and surface tension gradients along the bubble interface lead to stronger thermocapillary flows for the low gas case, which combined with the smaller dryout area results in higher heat transfer. For a high gas case, a larger bubble is formed with a smaller surface tension gradient and a large dryout area resulting in decreased heat transfer in the low-g regime (Figure 5.12a-b).

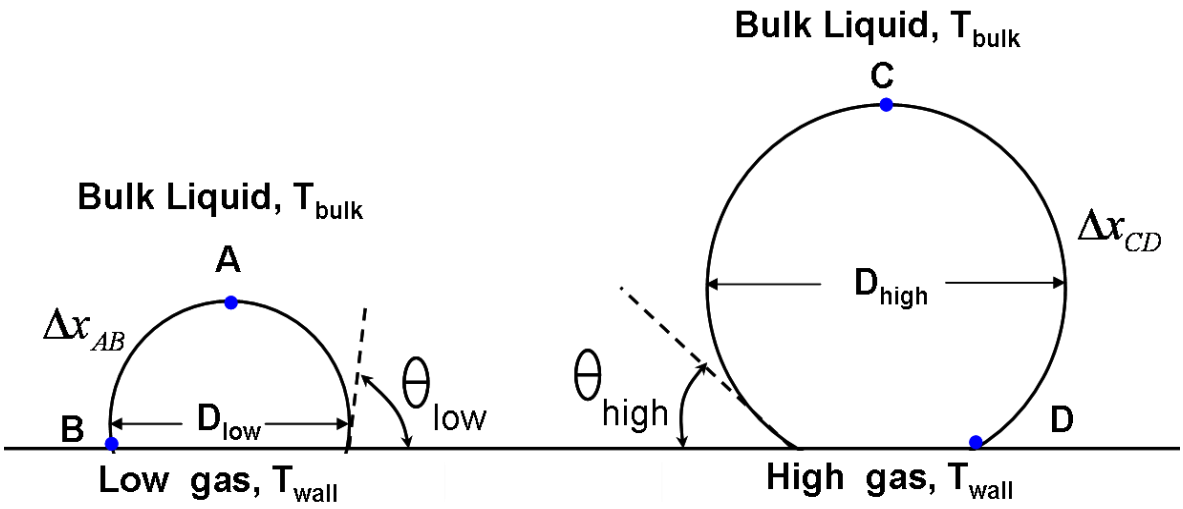

Figure 5.13: A schematic of the bubble size and apparent contact angle for the two gas concentrations in the low-g regime.

Numerical simulations (APPENDIX A) were also performed to confirm this behavior and those observed by Henry *et al.*, 2006. A qualitative study of the effects of dissolved gas content, bubble shape and size, and heat transfer coefficient on the strength of thermocapillary convection was performed to offer a possible explanation for the existing confusion. Due to the presence of different complex and interrelated mechanisms, the individual mechanisms were decoupled and their overall effect on thermocapillary convection was studied.

The results obtained for different bubble radii and contact angles suggest that the strength of thermocapillary convection is determined by the combined effect of the dissolved gas concentration, bubble shape and size, and the variation in evaporation or condensation heat transfer coefficient along the bubble interface. While the increase in dissolved gas content helps in the development of the required temperature variation along the bubble interface, the resulting increase in size by orders of magnitude (Figure 5.13) lowers the temperature gradient and heat transfer across the interface. This ultimately results in a lowering of the strength of the thermocapillary convection in the gassy bubble case. The reader is referred to APPENDIX A for the details of the numerical simulation.

The acceleration at which transition occurs between the heat transfer regimes was again compared with the prediction from the Fritz correlation (Eq. 5.3). The apparent contact angle was measured to vary between 79°-84° for the low gas case (220 ppm). The Fritz correlation suggests transition to occur between 0.25g-0.31g while the experimental value of a_{depart} varied between 0.19g-0.33g, (Figure 5.14).

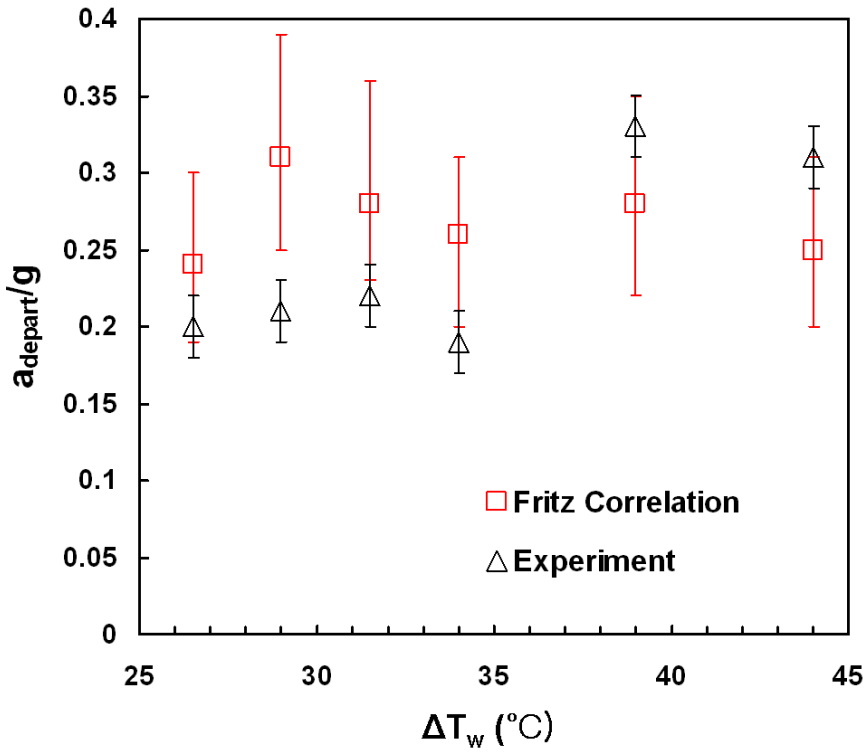

Figure 5.14: Comparison between the values of a_{depart} obtained from the Fritz correlation and experiment (low gas).

The experimentally measured values of a_{depart} for the two gas levels can be compared from Figure 5.7 and Figure 5.14. With the exception of one data point (ΔT_w =24°C), transition was observed to occur at lower accelerations for the high gas case. Figure 5.10b shows the value of a_{depart} obtained from experiment for the two gas concentrations at ΔT_w =29°C. For the high gas case, the high-g regime extended to lower accelerations (blue triangles). An increase in bubble diameter due to the presence of dissolved gas increases the buoyancy force while the surface tension force normal to the heater surface decreases due to the smaller contact angle. The combination of these two effects, *i.e.* an increase in the buoyancy force and a decrease in the surface tension force case shifts a_{depart} to lower accelerations for the high gas case.

5.5 EFFECTS OF SUBCOOLING

Additional data at two lower subcoolings, namely 16.6ºC (T_{bulk}=40ºC) and 6.6ºC (T_{bulk}=50ºC) were collected during the NASA FAST (Facilitated Access to the Space Environment for Technology Development and Training) reduced gravity flight campaign in August, 2009. The test fluid was FC-72 (different isomers of C_6F_{14}, T_{sat}=56°C at 1 atm) and the gas concentration was maintained at c_g=174 ppm. The experimental procedure and the data reduction techniques were similar to the previous campaign.

The transition from high-g to low-g and vice versa was not smooth during the NASA flights and occurred over a much shorter time (~1-2 s). There was also no 1-g period between two successive parabolas. As a result, the time interval between two parabolas was not sufficient for data storage and hence the second transition (low-g to high-g) was also used for data storage purposes. The absence of data during the second transition made it impossible to validate the quasi-steady state assumption during transition and extract variable gravity boiling curves from the NASA campaign. As a result, only the high gravity (1.7g) and the earth gravity results were available under different subcoolings.

A different microheater array was also used to verify the dependence of heater surface properties (*e.g.* nucleation site density) on pool boiling heat flux. The microheater used for the ESA campaign will hereafter be referred to as Heater 1 (all the results in the previous section) while that used for the NASA flights will be referred to as Heater 2. The microheater temperature during the NASA flights was varied between 65°C (ΔT_w=8.4°C) and 100°C (ΔT_w=43.4°C), and the pressure was maintained at 1 atm

throughout the experiment. Three heated areas were used to study the heater size effect: 2.1x2.1 mm^2 (3x3 elements), 3.5x3.5 mm^2 (5x5 elements), and 7.0x7.0 mm^2 (10x10 elements). A summary of test conditions for NASA campaign is presented in Table 5.2.

Table 5.2: Summary of test conditions

Fluid	FC-72
Area [mm^2]	7 x 7, 3.5 x 3.5, and 2.1 x 2.1, Heater 2
c_g [ppm]	174
ΔT_{sub} [°C]	6.6°C and 16.6°C
P [atm]	1
ΔT_w [°C]	8.4, 13.4, 18.4, 23.4, 25.9, 28.4, 30.9, 33.4, 38.4, and 44.4

The experimental heat flux values at 1g and 1.7g are shown on Figure 5.15. The curves represented by solid line and closed square symbols are 1g boiling curves. Closed triangles represent the experimental data at high-g (1.7g). As observed during the ESA campaign, the heat flux increased with increasing gravity. The boiling curve in the early nucleate boiling regime remains unaffected by subcooling. However, the heat flux values at higher superheats ($\Delta T_w \geq 20$°C) increase with increasing subcooling. The boiling curve was found to be independent of heater size suggesting buoyancy dominated boiling regime.

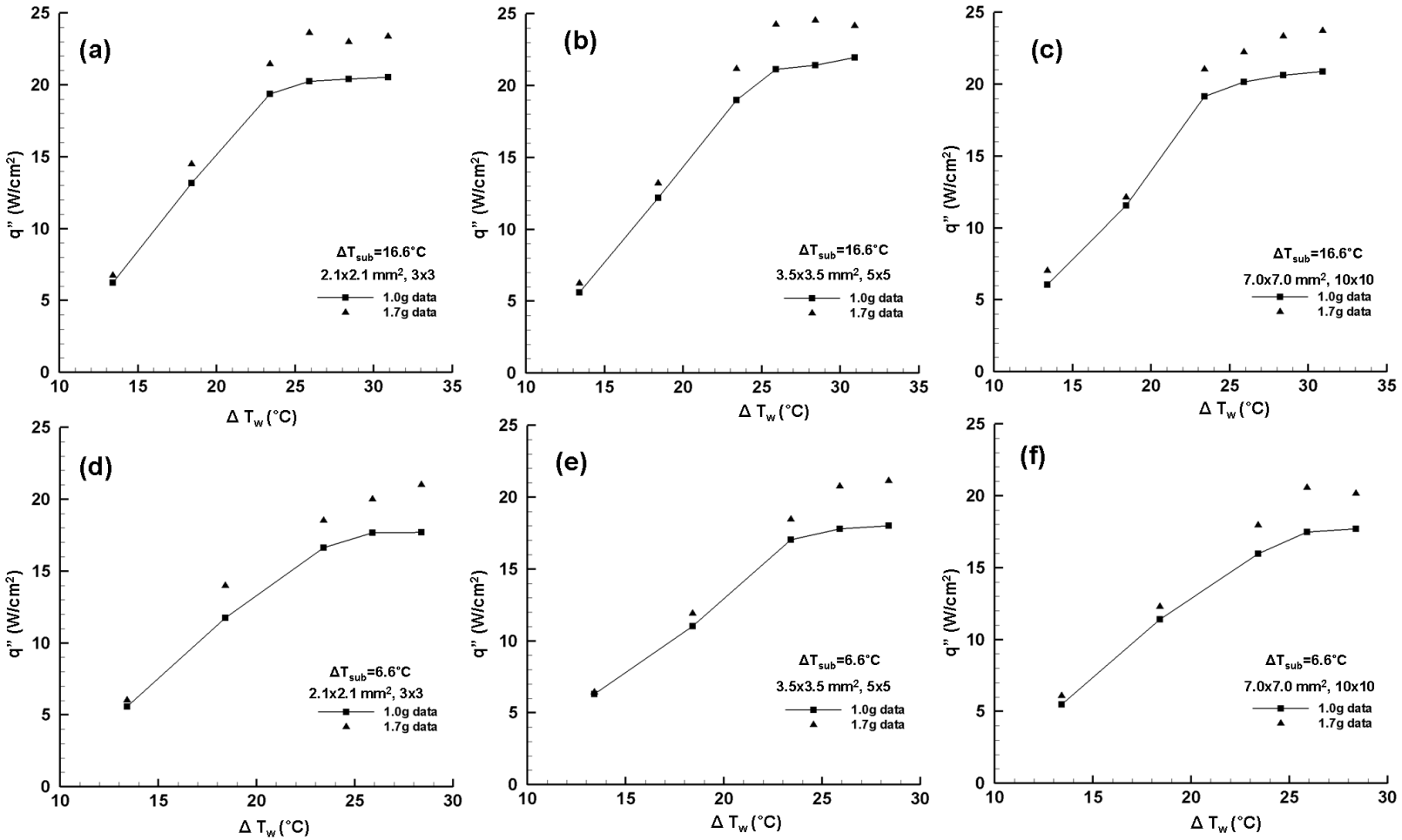

Figure 5.15: Heat flux for various heaters sizes and subcooling, (a) 2.1x2.1 mm^2 and 16.6°C, (b) 3.5x3.5 mm^2 and 16.6°C, (c) 7.0x7.0 mm^2 and 16.6°C, (d) 2.1x2.1 mm^2 and 6.6°C, (e) 3.5x3.5 mm^2 and 16.6°C, (f) 7.0x7.0 mm^2 and 6.6°C (Heater 2).

5.6 GRAVITY SCALING PARAMETER

The variation of the slope (*m*) for both gas concentrations in the high-g regime with wall superheat is shown on Figure 5.16. The square symbols represent the slope *m* for the high dissolved gas concentration case (~1216 ppm) while the diamond symbols represent the low dissolved gas concentration case (~220 ppm). Again, it is clear that use of a constant *m* to describe the variation of gravity as reported in much of the existing literature is not valid since it is a function of wall superheat and is also dependent on the dissolved gas concentration.

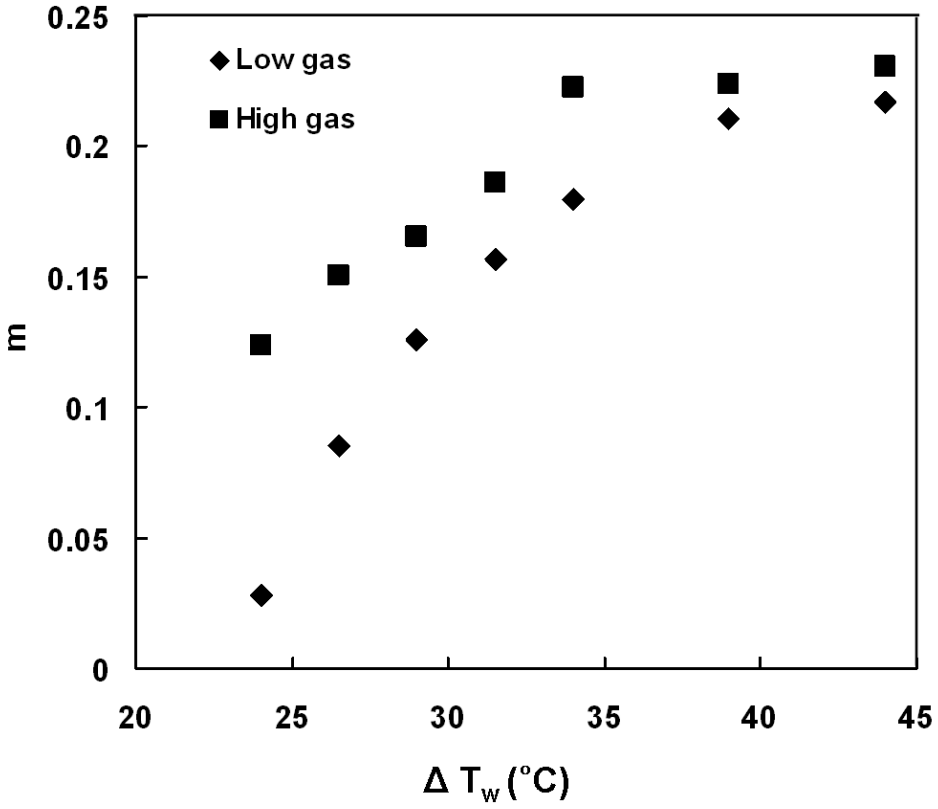

Figure 5.16: Plot of the power law coefficient m vs. superheat for the two gas levels.

Referring to Figure 5.8 ($a \geq 0.3g$), the pool boiling curve near the onset of nucleate boiling (ONB) is independent of the acceleration level (slope m approaches zero). This is due to the fact that the heat transfer due to natural convection is small compared to that due to boiling. The typical heat flux values encountered in the natural convection (0.7-1.4 W/cm^2) regime is comparable to the experimental uncertainty (1.2 W/cm^2) making it impossible to see any observable differences between different gravity levels. However, the absolute value of heat flux (~4W/cm^2) reported for the natural convection regime (ΔT_w=9°C and ΔT_w=14°C) is higher than the expected range (0.7-1.4 W/cm^2). This is due to the fact that a few nucleation sites were active within the heater even at these temperatures. At higher superheats, the slope approaches a value of 0.25 (Figure 5.16), similar to what is predicted by the correlation of Kutateladze 1948 and Zuber 1959 for gravity effects on CHF. If we assume that CHF at all gravity levels occur at the same superheat, a non-dimensional wall temperature can be defined as follows:

$$T^* = \frac{T_w - T_{ONB}}{T_{CHF} - T_{ONB}} \tag{5.5}$$

For the high gas case, the natural convection regime was observed for wall superheats lower than 14ºC while boiling was first observed at a superheat of 19ºC. The temperature resolution of 5ºC near ONB did not allow exact identification of superheat at ONB. Hence, the average superheat of 16.5ºC (T_{ONB}=72.5ºC) was selected as ONB for the high gas case. For the low gas case, natural convection regime was observed until the wall superheat of 19ºC while boiling was first observed at a wall superheat of 24ºC. As a result, ONB was assumed to occur at a superheat of 21.5ºC (T_{ONB}=77.5ºC).

The wall superheats investigated in the current experiment were not high enough (Figure 5.8) for distinct identification of CHF. As a result, two analyses were conducted

to understand the sensitivity of superheat at CHF on the scaling parameter. The trend of the boiling curve suggests that the CHF should occur close to a superheat of 44ºC. For the first analysis (Analysis 1), CHF was assumed to occur at a wall superheat of 44ºC (T_{CHF}=90ºC) for both dissolved gas concentrations. For the second analysis (Analysis 2), an interpolation of the boiling curve at 1.7g (steady conditions) was performed to estimate the superheat at CHF. This resulted in a superheat of 46.5ºC (T_{CHF}=92.5ºC) for the high dissolved gas concentration and 49ºC (T_{CHF}=95ºC) for the low dissolved gas concentration. A lower value of superheat at CHF for the high dissolved gas concentration is expected.

As mentioned earlier, there existed an uncertainty of 5ºC in the estimation of ONB. Moreover, repeated use of the heaters could possibly result in slight changes in surface properties leading to a few degree changes in temperature at ONB. Hence, two additional analyses (Analysis 3 and Analysis 4) were performed to understand the sensitivity of ONB on the scaling parameter. Table 5.3 summarizes the results of the sensitivity analysis. The results presented in the next few sections are based on the assumption of Analysis 2. However, an examination of the root means squared (RMS) errors in the heat flux prediction due to the lack of knowledge of exact ONB and CHF showed that the difference between the four analyses are insignificant (Table 5.3).

The variation of m for the two gas concentrations as a function of the non-dimensional temperature T^* is shown on Figure 5.17. The curves for the two gas concentrations overlap, indicating that the shapes of the two curves are similar if the appropriate scaling parameter for temperature is used.

A curve fit was performed on the data assuming *m* approaches a value of 0 for *T**=0 and a value of 0.25 for *T**=1. A simple curve satisfying these conditions that fits the data well is given by:

$$m = \frac{0.9T^*}{1 + 2.6T^*} \tag{5.6}$$

Based on this variation of *m*, the heat flux at any two gravity levels can be related as follows:

$$\frac{q_2}{q_1} = \left(\frac{a_2}{a_1} \right)^m \tag{5.7}$$

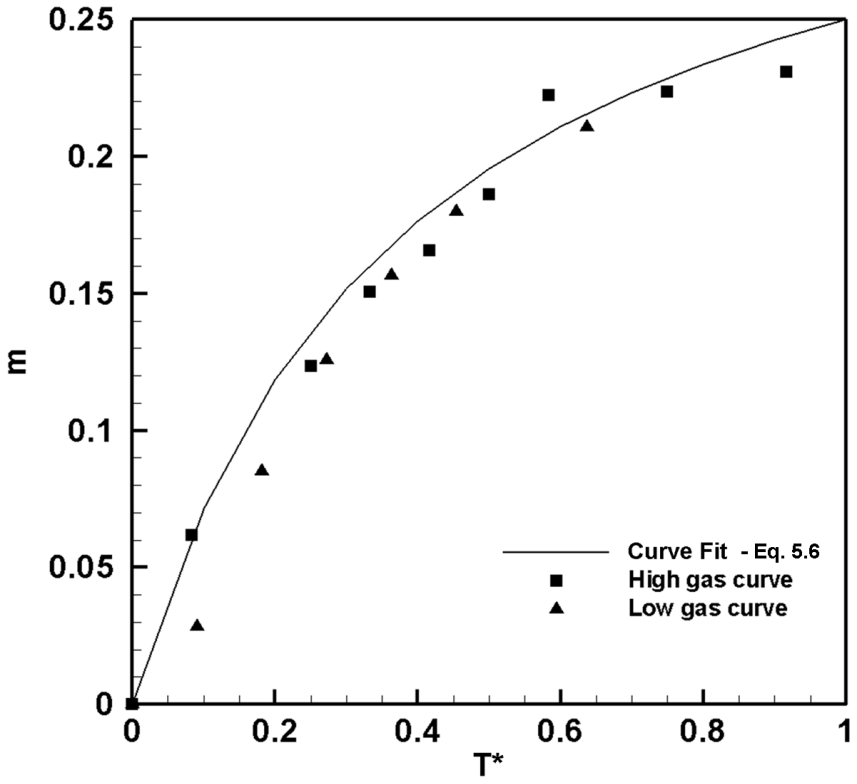

Figure 5.17: Plot of the slope m vs. non-dimensional wall temperature the two gas levels.

This scaling parameter can be used to predict the heat transfer at any gravity level in the buoyancy dominated boiling regime (L_h/L_c>>1) if the heat transfer under similar conditions at any other gravity level in this regime is known. A convenient choice for q_1 would be the experimentally determined boiling curve in earth gravity ($a_1=g$). Moreover, since correlations available in the literature are based on earth gravity observations, they could also be used for q_1. The next section validates the applicability of this scaling parameter at four gravity levels and two gas concentrations.

5.6.1 Validation of Results

The pool boiling curves for various gravity levels shown in Figure 5.8 (high gas case, c_g~1216 ppm) were used to validate the applicability of the scaling parameter. The boiling curve at 1g was chosen to be q_1 and used to predict the boiling curves at 0.3g, 0.6g, 1.3g and 1.7g. The results of the prediction and the actual data along with the earth gravity results are shown on Figure 5.18. The prediction and the experimental data are in very good agreement, indicating the suitability of the scaling parameter.

Boiling curves similar to those in Figure 5.8 were also obtained for the low gas case [15]. ONB was delayed for the low gas case. This is also clear from Figure 5.10 where the value of m approaches a value of zero (ONB) at higher wall superheat. Prediction and experimental results (Figure 5.19) are also in very good agreement, further demonstrating the effectiveness of the proposed scaling parameter to account for gas content. The root mean square errors between the predicted and experimental results using the four analysis approaches are shown in Table 5.3. The four analyses seem to be insensitive to the superheat at ONB and CHF. The errors for the high gas case as well as the low gas case are small and of the same magnitude. The maximum error was 0.37

W/cm^2, considerably smaller than the typical heat flux values at these acceleration levels and within the experimental uncertainty of 1.2 W/cm^2.

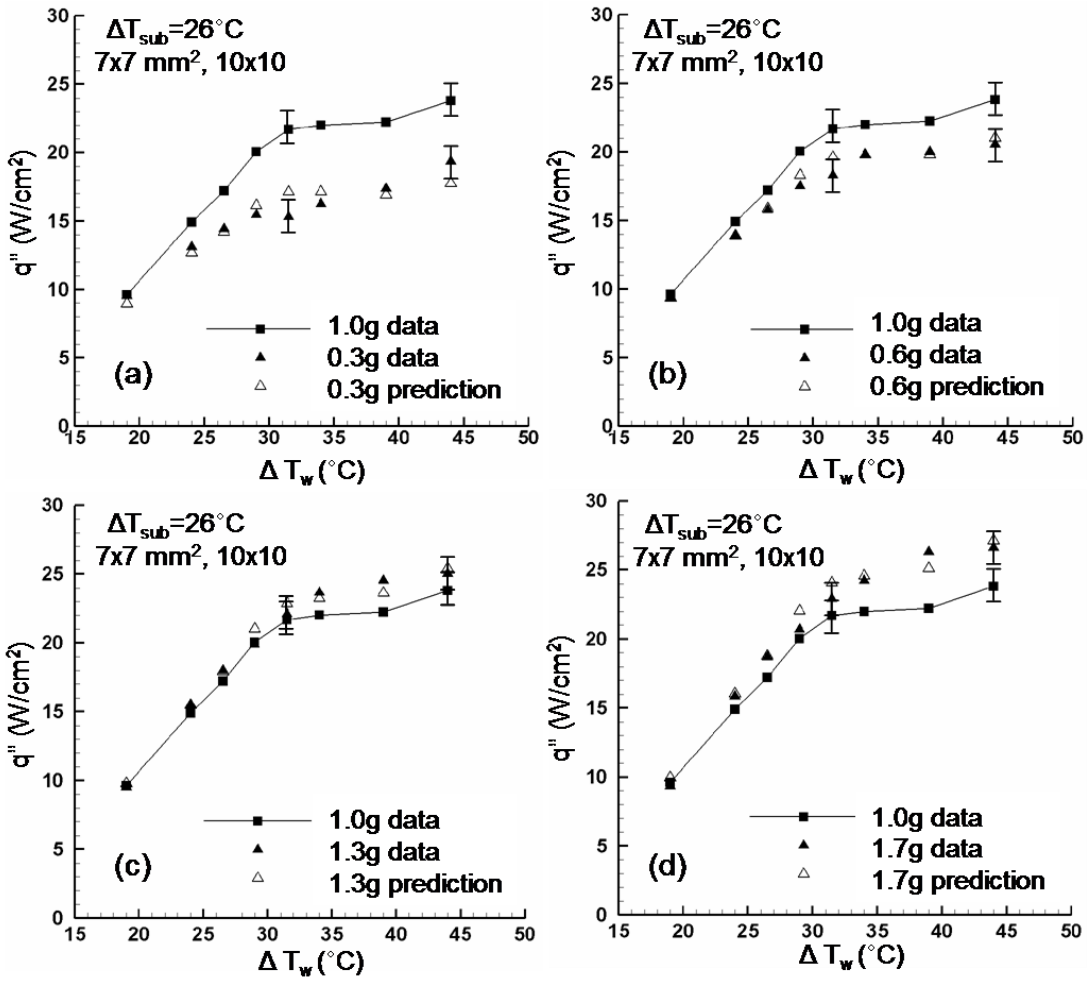

Figure 5.18: Comparison of the measured and predicted heat flux for the high gas case (~1216ppm) and full heater (7.0x7.0 mm^2) at (a) 0.3g, (b) 0.6g, (c) 1.3g, and (d) 1.7g, (Heater 1).

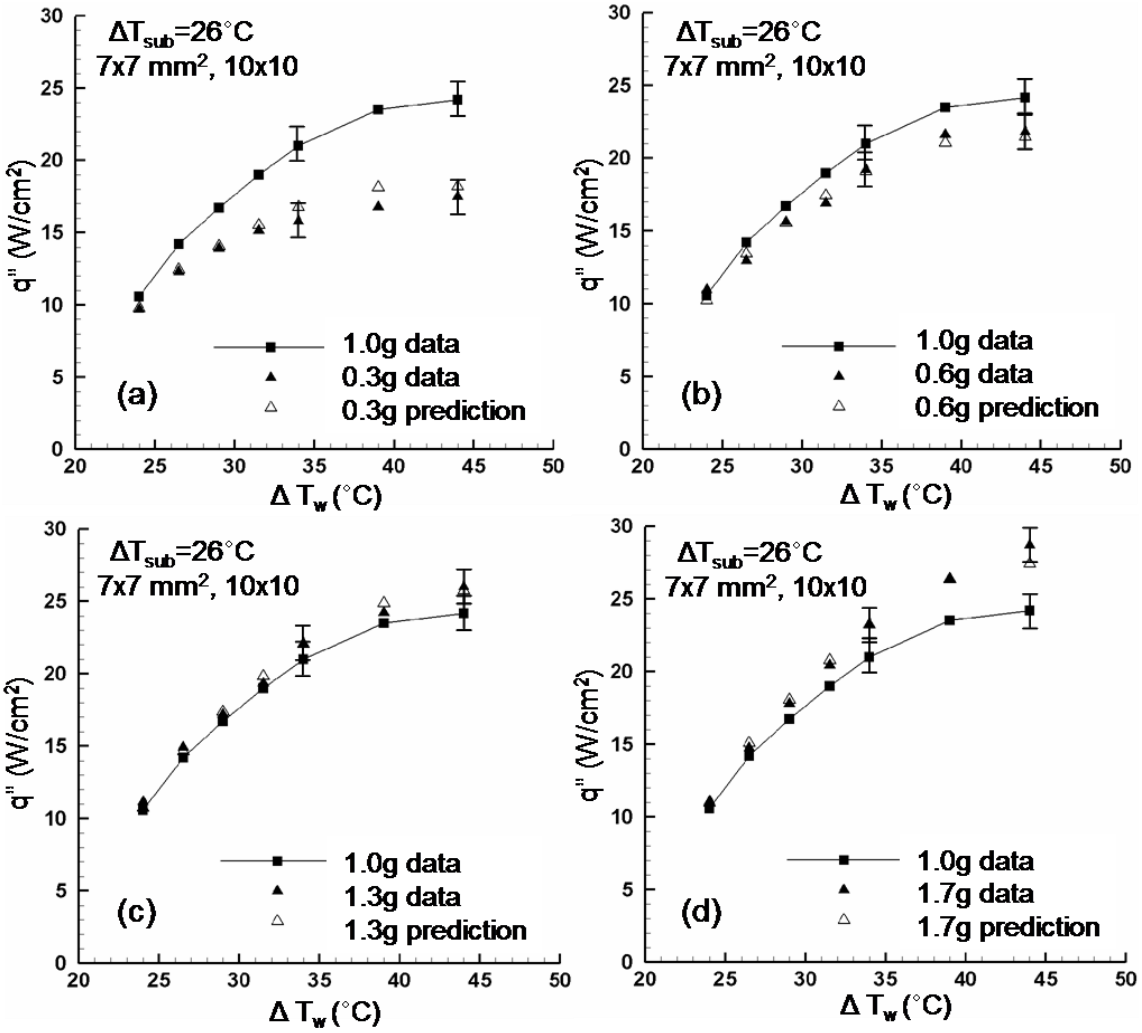

Figure 5.19: Comparison of the measured and predicted heat flux for the low gas case (~220ppm) and full heater (7.0x7.0 mm^2) at (a) 0.3g, (b) 0.6g, (c) 1.3g, and (d) 1.7g, (Heater 1).

Table 5.3: Sensitivity analysis of ONB and CHF on the gravity scaling parameter..

	High Gas (~1216 ppm)				Low gas (~220ppm)			
	Analysis 1	Analysis 2	Analysis 3	Analysis 4	Analysis 1	Analysis 2	Analysis 3	Analysis 4
T_{ONB} (°C)	72.5	72.5	70	75	77.5	77.5	75	80
T_{CHF} (°C)	90	92.5	92.5	92.5	90	95	95	95
a/g	q''_{rms} (W/cm^2)							
0.3	0.35	0.35	0.36	0.37	0.24	0.28	0.25	0.29
0.6	0.19	0.21	0.20	0.23	0.19	0.18	0.19	0.18
1.3	0.23	0.22	0.23	0.21	0.16	0.15	0.15	0.16
1.7	0.30	0.29	0.31	0.27	0.20	0.20	0.22	0.21

5.6.2 Effect of Subcooling

As explained in the previous section, additional parabolic flight experiments were performed with different subcooling in August 2009. These results were also used to verify the validity of scaling parameter at different subcoolings ΔT_{sub}, namely 16.6ºC (T_{bulk}=40ºC) and 6.6ºC (T_{bulk}=50ºC). A different microheater array was also used to verify the dependence of heater surface properties (*e.g.* nucleation site density) on the scaling parameter.

The experimental heat flux values along with the prediction results are shown in Figure 5.20. The curves represented by solid line and closed square symbols are 1g boiling curves. The earth gravity heat flux value was multiplied by the scaling parameter to predict the heat flux at hypergravity (1.7g) conditions (open triangles). Closed triangles represent the experimental data at high-g (1.7g). Three heated areas were used to study the heater size effect: 2.1x2.1 mm^2 (3x3 elements), 3.5x3.5 mm^2 (5x5 elements), and 7.0x7.0 mm^2 (10x10 elements). The ratio of heater size to capillary length L_h/L_c was significantly larger than 1 for this data, the hence boiling curves were in the buoyancy dominated boiling regime.

Good agreement was found between the experimental results and prediction at both subcoolings and three heater sizes. The root mean square errors between the predicted and the experimental results at two subcoolings are shown in Table 5.4. Although the root mean square error is slightly larger than that observed in the previous set of experiments (ESA campaign), the maximum error was again considerably smaller (0.57 W/cm^2) than the typical heat flux magnitude and uncertainty (1.2 W/cm^2) at these acceleration levels.

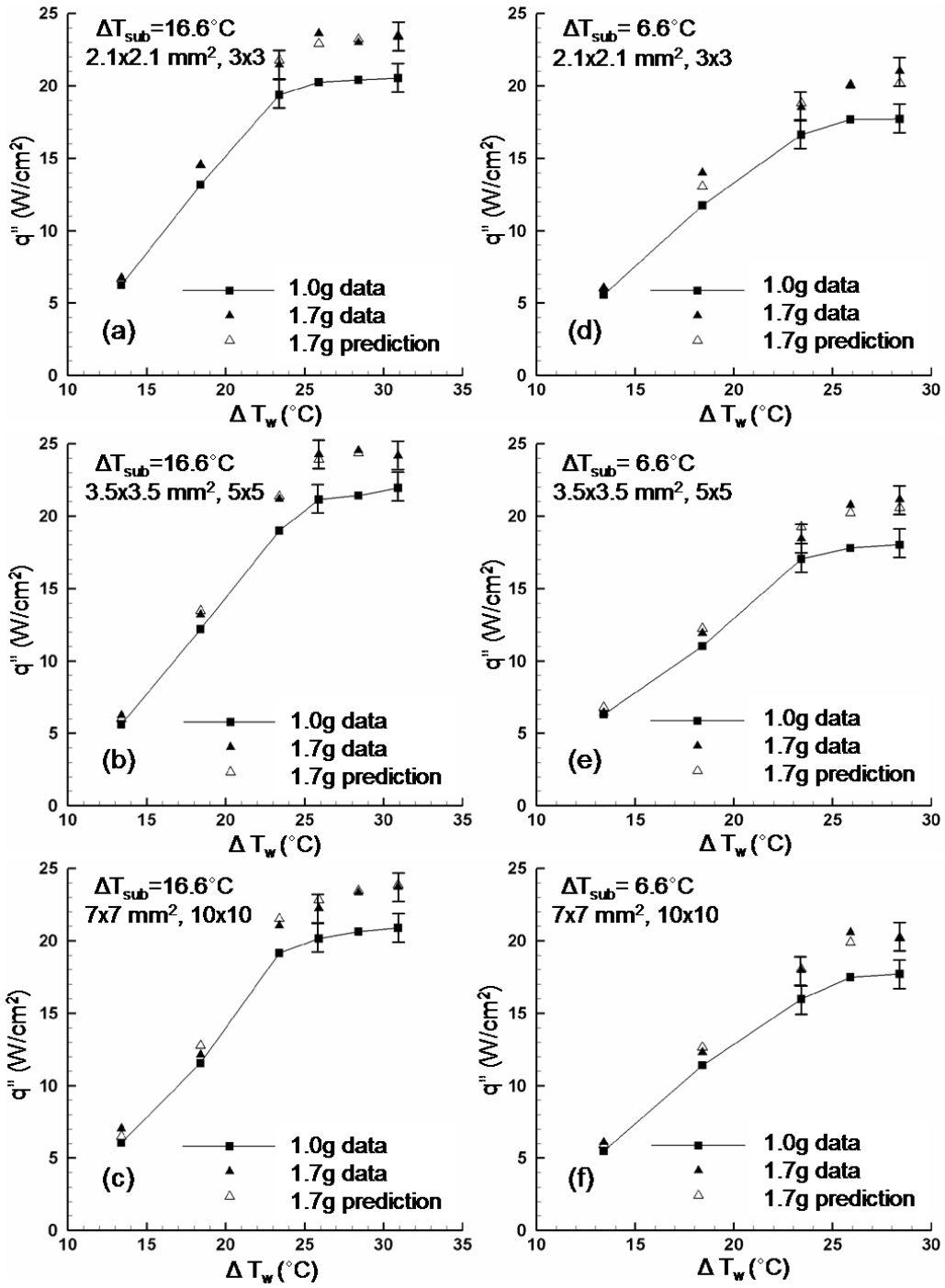

Figure 5.20: Comparison of the measured and predicted heat flux for various heaters size and subcooling, (a) 2.1x2.1 mm^2 and 16.6°C, (b) 3.5x3.5 mm^2 and 16.6°C, (c) 7.0x7.0 mm^2 and 16.6°C, (d) 2.1x2.1 mm^2 and 6.6°C, (e) 3.5x3.5 mm^2 and 16.6°C, (f) 7.0x7.0 mm^2 and 6.6°C (Heater 2).

Table 5.4: Room mean square error between the predicted and experimental results.

	q''_{rms} (W/cm^2)	
Size	ΔT_{sub} =16.6ºC	ΔT_{sub} =6.6ºC
2.1x2.1 mm^2 (3x3 elements)	0.34	0.57
3.5x3.5 mm^2 (5x5 elements)	0.43	0.55
7.0x7.0 mm^2 (10x10 elements)	0.47	0.36

Figure 5.21 shows a plot of the experimental and predicted results for all the test conditions discussed above. The prediction error was considerably smaller (<10%) than that for the conventional boiling correlations based on the use of a constant power law coefficient.

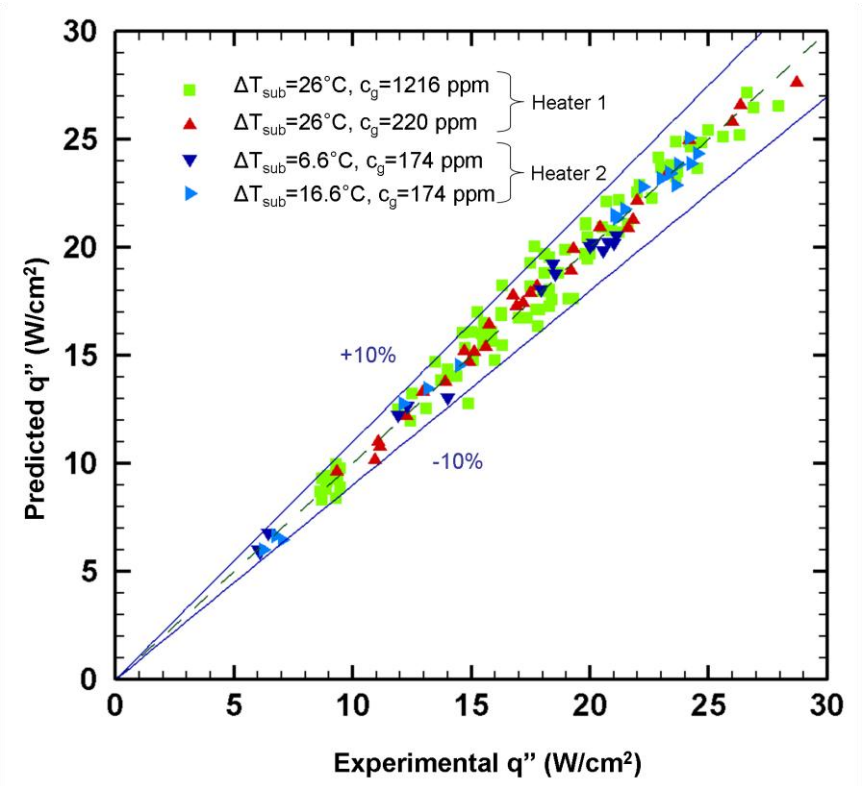

Figure 5.21: Comparison of the experimental and predicted heat flux values using the gravity scaling parameter.

5.6.3 Guidelines for Using Scaling Parameter

The scaling parameter can be used as a tool to predict boiling heat flux at any gravity level if the data under similar experimental conditions are available at any other gravity level. Figure 5.22 shows the comparison of the results at two subcooling using the same heater. A large compilation of pool boiling data in the literature (including the current work) suggests that the rate of nucleate pool boiling heat transfer is relatively insensitive to the liquid subcooling. However, CHF increases with subcoolings. Moreover, the temperature/superheat at which CHF is observed increases with subcooling. The change in CHF or the corresponding wall superheat is accounted for in the scaling parameter and prediction is accurate if experimental data at same subcooling and any gravity level is available (1 g in the current case).

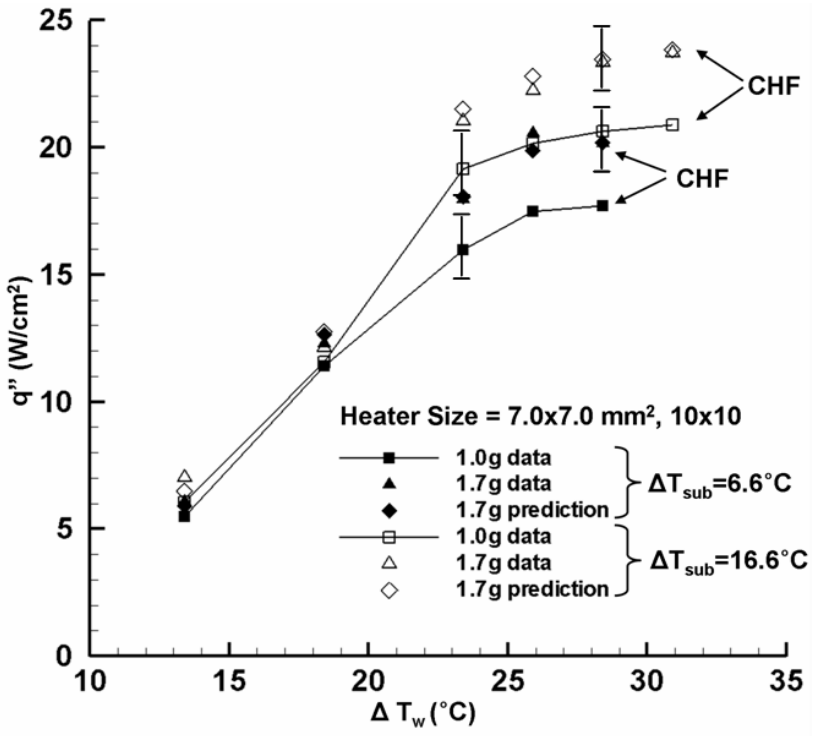

Figure 5.22: Comparison of the measured and predicted heat flux at two subcoolings (Heater 2).

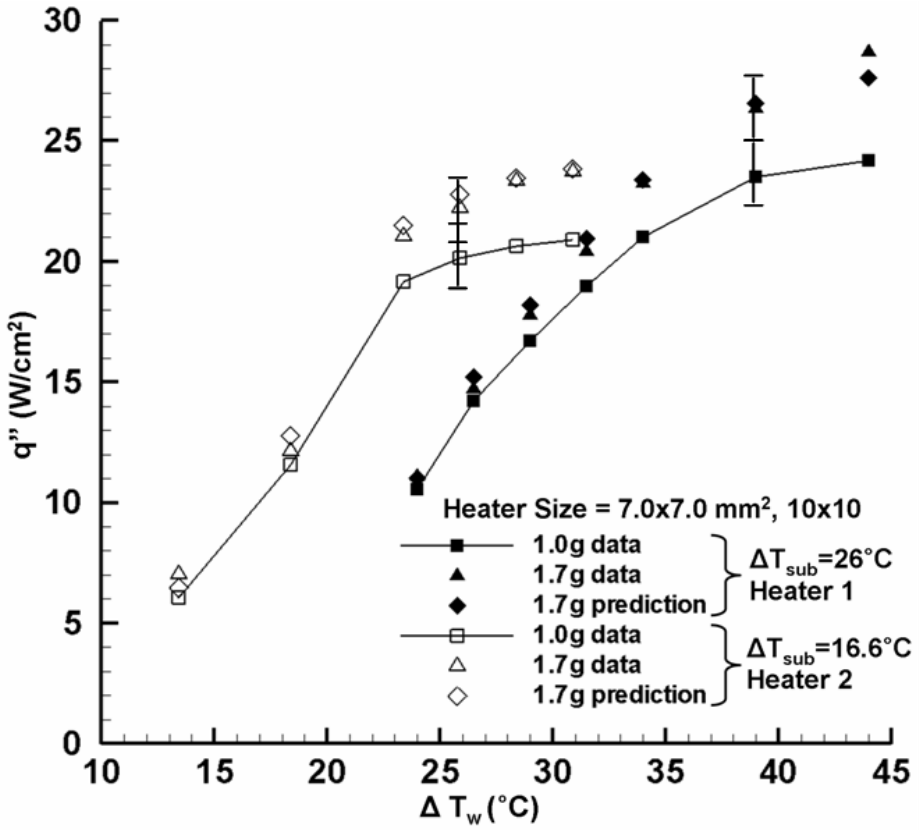

Figure 5.23: Comparison of the measured and predicted heat flux for two microheater arrays.

A comparison of the results obtained from the two heaters with different surface morphologies as evidenced by different boiling curves is shown on Figure 5.23. The closed symbols represent the boiling curves for Heater 1 (ΔT_{sub} =26.6ºC) while the open symbols represent the boiling curves for Heater 2 (ΔT_{sub} =16.6ºC). The superheat at ONB was observed to be different for the two heaters. However, for each case, the scaling parameter is valid and the corresponding earth gravity data can be used to predict the heat flux at 1.7g. The non-dimensional temperature T^* accounts for the change in superheat at ONB and the corresponding shift in the boiling curve.

5.7 SUMMARY

The heat flux variation with gravity at various wall superheats and for two gas concentrations were studied under subcooled pool boiling conditions. The effects of the test parameters are summarized below.

a. *Gravity effects*

Two heat transfer regimes were observed; a low-g regime (primary non-departing bubble) and high-g regime (departing bubbles). The low-g regime was dominated by the presence of a primary bubble and surrounding satellite bubbles. The dependence of heat flux on gravity was small in the low-g regime while a larger dependence was observed in the high-g regime. The slope of the heat flux vs. acceleration curve was different in the two regimes, ruling out the possibility of a unified power law dependence across all gravity levels.

b. *Wall superheat effects*

In the high-g regime, the heat flux increased with wall superheat. The effect of wall superheat in the low-g regime was not clear and dependent on the dissolved gas concentration. Wall superheat did not appear to influence the acceleration at which the transition in heat transfer mechanisms occurred. The power law coefficient for the gravity effect was observed to be a function of wall superheat.

c. *Non-condensable gas effects*

Onset of nucleate boiling occurred at lower wall superheat for the high gas case. The presence of dissolved gas increased the nucleate boiling heat

transfer in the high-g regime but decreased the heat transfer in the low-g regime. In the low-g regime, the size of primary bubble increases with gas concentration leading to larger dryout area and weaker thermocapillary convection. Transition from the low-g to high-g regimes occurred at higher acceleration for the low gas case compared to the high gas case.

d. Effect of Subcooling

The boiling curve in the early nucleate boiling regime remains unaffected by subcooling. Heat flux values at higher superheats were observed to increase with increasing subcooling in the high-g regime.

Variable gravity pool boiling data in the buoyancy dominated boiling regime was used to develop a scaling parameter to account for change in heat flux with gravity during subcooled pool boiling. Wall temperature was suitably non-dimensionalized. The predicted results were found to be in good agreement with the heat transfer data over a wide range of gravity levels in the buoyancy dominated boiling regime ($L_h/L_c >> 1$), three gas concentrations, three subcoolings, and two surface morphologies. Although the scaling parameter was obtained by the analysis of subcooled pool boiling experimental data for n-perfluorohexane/FC-72, it is expected to be valid for refrigerants with similar properties. Use of this scaling parameter to obtain heat transfer at varying gravity levels can save considerable experimental resources required to validate the performance of phase change based systems under different gravity conditions.

Chapter 6: Heater Size Effect

6.1 INTRODUCTION

Most of the pool boiling correlations and models assume the heater is sufficiently large and boiling is independent of heater size (Rohsenow, 1962; Foster and Zuber, 1955; Stephan and Abdelsalam, 1980; Kutateladze, 1948; Zuber, 1959). For a large heater and/or higher gravity conditions, boiling is buoyancy dominated. The scaling parameter developed in the previous chapter was also stated to be valid for buoyancy dominated boiling. Buoyancy dominated surface tension forces when the heater size is considerably larger than the capillary length scale:

$$\frac{L_h}{L_c} >> 1 \tag{6.1}$$

where the capillary length L_c is used to quantify the interplay between surface tension to body forces:

$$L_c = \left(\frac{\sigma}{g(\rho_l - \rho_v)} \right)^{1/2} \tag{6.2}$$

The objective of this chapter is to identify the transition criteria between surface tension and buoyancy dominated boiling regimes. This will allow determine the applicability range of various boiling models and also the scaling parameter developed in the previous chapter.

The first section presents the results of pool boiling with three heater sizes under variable gravity conditions. As will be shown later, these experiments alone were not sufficient to arrive at the transition criteria. As a result, additional pool boiling

experiments with varying heater sizes and two fluids (FC-72 and pentane) were performed under earth gravity conditions. Finally, a pool boiling regime map was developed by combining the current results and those published in literature.

6.2 VARIABLE GRAVITY RESULTS

6.2.1 Test Conditions

Data was obtained for three heater sizes (Figure 6.1): full array (96 elements), half array (48 elements) and quarter array (24 elements). The gas concentration and subcooling were maintained at ~1216ppm and ΔT_{sub}=26°C, respectively. The heater temperature was varied between 65°C (ΔT_w=9°C) and 100°C (ΔT_w=44°C), and the pressure was maintained at 1 atm throughout the experiment. A summary of experimental conditions is presented in Table 6.1.

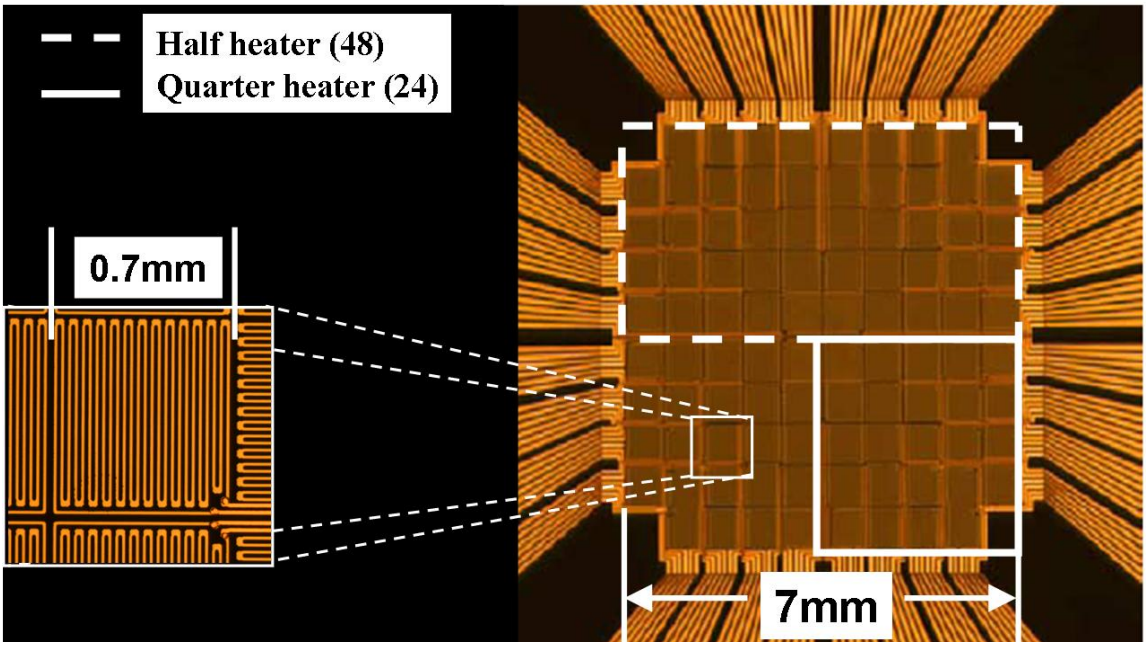

Figure 6.1: Platinum resistance heater array, each element = 0.7 x 0.7 mm^2.

Table 6.1: Summary of test conditions

Fluid	n-perfluorohexane
Area [mm^2]	7 x 7 (full), 3.5 x 7 (half), and 3.5 x 3.5 (quarter)
c_g [ppm]	1216
ΔT_{sub} [°C]	26°C
P [atm]	1
ΔT_w [°C]	9, 14, 19, 24, 26.5, 29, 31.5, 34, 39, and 44

6.2.2 Heater Size Effect

Boiling curves for the three heater sizes at four accelerations are shown on Figure 6.2. In the high-g regime (Figure 6.2 a-c), the boiling curves are independent of the heater size. The bottom view images in Figure 6.2 show that the heater size is sufficient for the nucleation site density (and hence the heat transfer) to remain unaffected. A heater size effect is observed in the low-g case, however. Heat flux increases as the heater size decreases.

Similar to the observations of Henry *et al.*, 2004 a laterally oscillating primary bubble was observed at lower superheats (ΔT_w<29°C) for the quarter and half heaters (double sided arrow on Figure 6.2d). Occasional rewetting due to translation of the primary bubble along the full heater was also observed. The frequency of oscillation was inversely related to the heater size–slow oscillations for the full heater and rapid oscillations for the quarter heater. More frequent oscillations result in more frequent rewetting and removal of the satellite bubbles, resulting in shorter bubble life cycle and hence higher heat transfer. The dryout area fraction (the ratio of dry area to heated area)

was observed to decrease with decreasing heater size resulting in an increase in heat flux. At higher superheats $\Delta T_w \geq 39°C$, a stable primary bubble occupying the entire heater was observed for all three sizes (Figure 6.2d), but the heat transfer was higher for the smaller heater. It is speculated that this is due to stronger thermocapillary convection around the smaller primary bubbles. Although the temperature difference available for thermocapillary convection remains the same for the three cases, a decreasing heater size results in a larger temperature gradient and stronger thermocapillary convection (APPENDIX A). Further experiments with particle image velocimetry (PIV) and various heater sizes are required to verify this hypothesis.

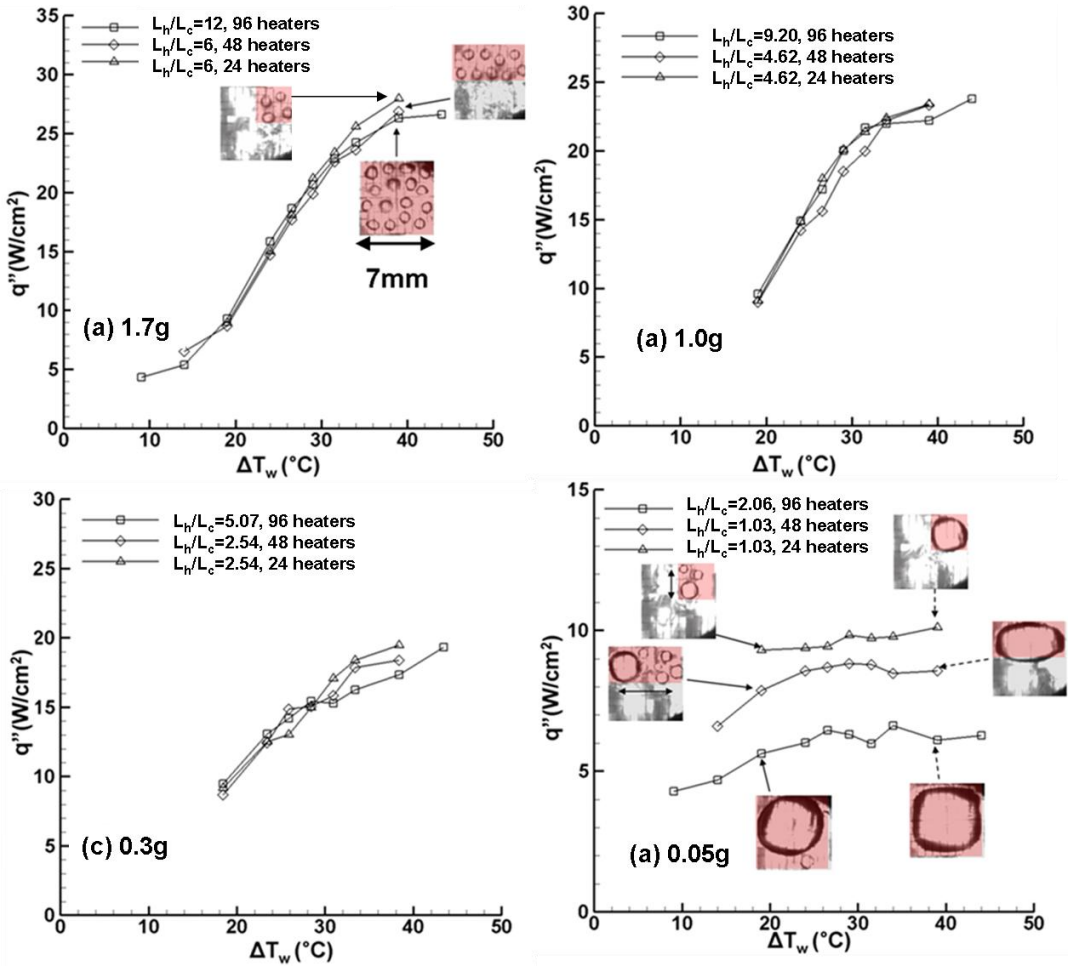

Figure 6.2: Boiling curve for three different heater sizes using n-perfluorohexane, high gas (c_g ~1216ppm) at (a) 1.7g and (b) 1g, (c) 0.3g, and (d) 0.05g.

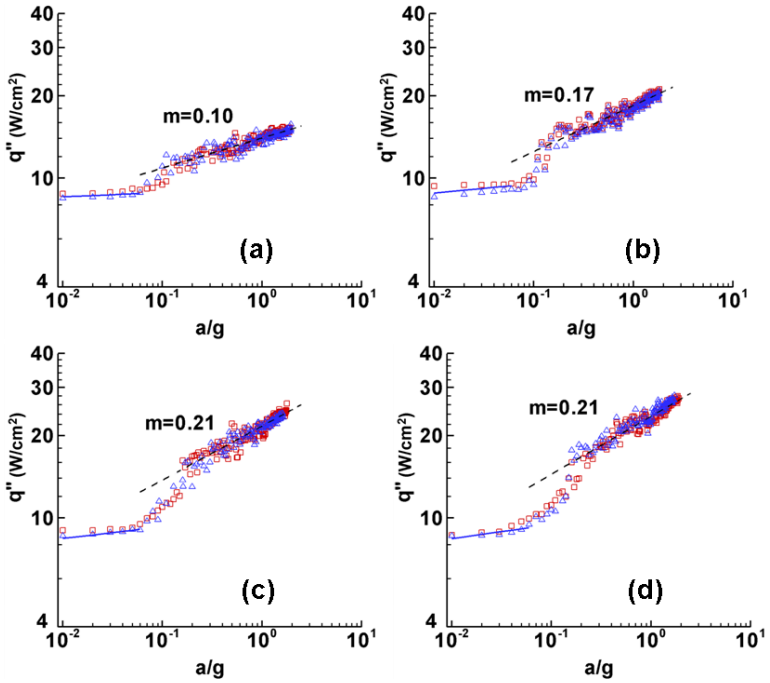

Figure 6.3: Plot of heat flux vs. acceleration for the high gas case (c_g ~1216ppm), half heater, for ΔT_w (a) 24°C, (b) 29°C, (c) 34°C, and (d) 39°C.

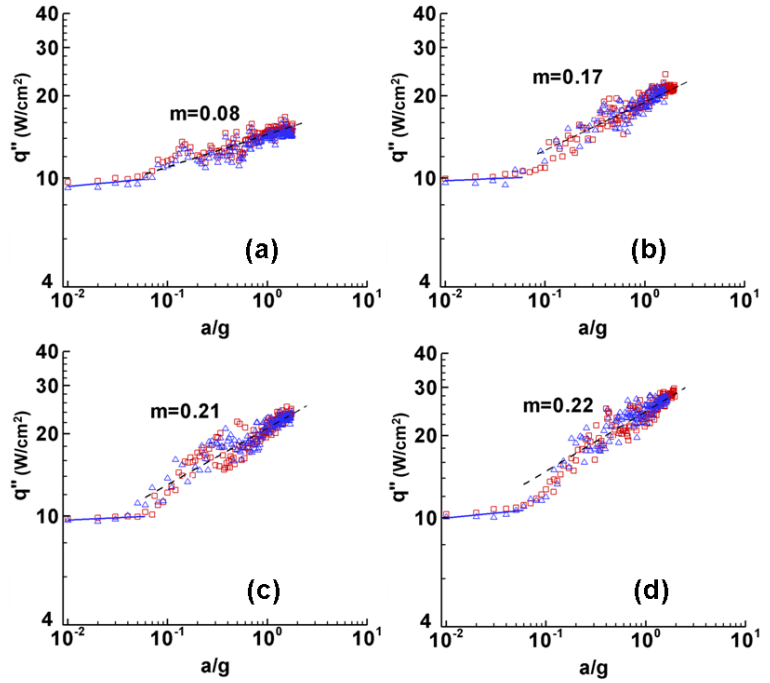

Figure 6.4: Plot of heat flux vs. acceleration for the high gas case (c_g ~1216ppm), quarter heater, for ΔT_w (a) 24°C, (b) 29°C, (c) 34°C, and (d) 39°C.

The logarithmic plots of heat flux vs. acceleration for the half and quarter heaters in the high-g and low-g regime are shown on Figure 6.3 and Figure 6.4. Similar to the full heater case (Figure 5.4), gravity dependence (m) was observed to increase with wall temperature in the high-g regime. Moreover, as observed for the boiling curves, the quarter, half and full heater configurations had similar variations in slope and hence heat transfer in the high-g regime. In the low-g regime, gravity dependence was small.

Insight into the effect of heater size on heat transfer can be obtained by considering the ratio of heater size to the capillary length, L_h/L_c (Henry *et al.*, 2004). L_h is the length of the shortest side for a given heater configuration: 7 mm for the full heater and 3.5 mm for the half and quarter heaters. If L_h/L_c is large, then the heater size should not affect the heat flux. For small values of L_h/L_c, the size of the departing bubbles becomes of the same order as the heater size, and heater size is expected to influence the heat transfer. At L_h/L_c=1, a/g is 0.012 for the full heater and 0.05 for the half and quarter heaters. At 1.7g, 1g, and 0.3g (high-g regime), L_h is much larger than L_c, so the heat flux is independent of heater size. In the low-g regime, however, L_h is comparable to or smaller than L_c, indicating there should be a heater size effect. As discussed above, this behavior was observed in the boiling curve at 0.05g (Figure 6.2d). The heat transfer results were heater size independent at 1.7g irrespective of subcooling (Figure 6.2 and Figure 6.5).

It is clear that a threshold value of L_h/L_c exists above which boiling is dominated by buoyancy. The presence of capillary length in this ratio along with the variable gravity study suggests a similarity between gravity and heater size effect on pool boiling curve. Hence, a study of pool boiling with varying heater sizes and gravity levels is needed. If

the transition between surface tension and buoyancy dominated regime is found to occur at a constant L_h/L_c over a wide range of gravity level and heater size, it might be possible to simulate many of the partial and low gravity experiments (surface tension regime) in an earth gravity environment using small heaters.

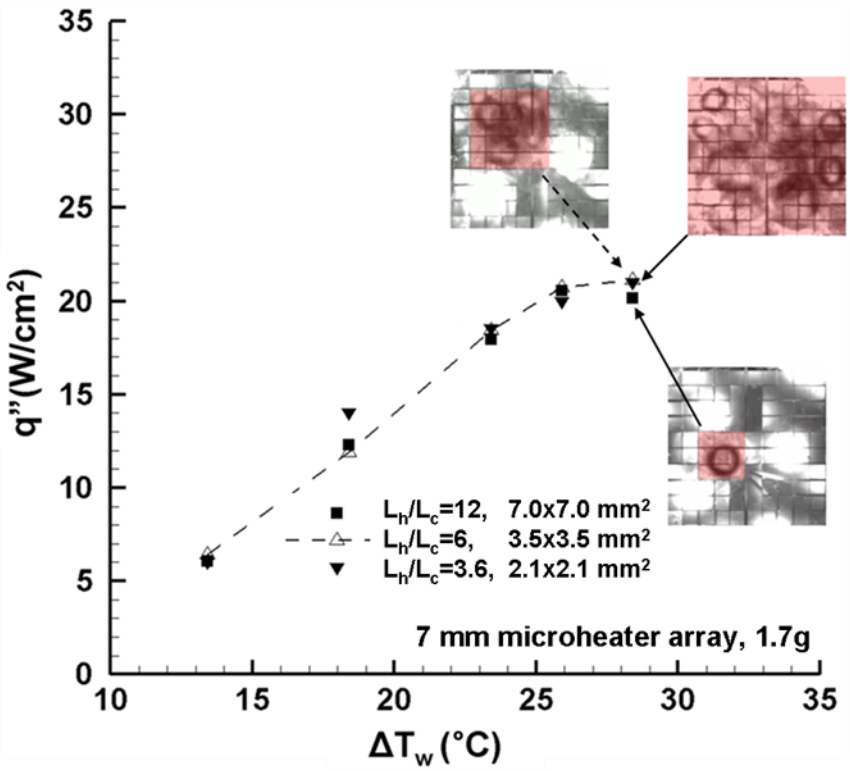

Figure 6.5: High-g (1.7g) boiling curves for selected heaters on 7x7 mm^2 heater, ΔT_{sub}=6.6°C.

6.3 EARTH GRAVITY RESULTS

This chapter identifies the threshold value of L_h/L_c above which pool boiling is dominated by buoyancy and is *heater size independent*. As identified in the previous section, further experiments with varying L_h/L_c are required to arrive at the threshold value for transition between surface tension and buoyancy dominated boiling regimes.

Figure 6.6a show the variation of L_h/L_c with a/g for three heater sizes investigated in the previous chapter. Red stars represent surface tension dominated boiling while the green stars represent buoyancy dominated boiling (Figure 6.6a). Transition between the regimes occurs in the unresolved zone between these points.

Variable gravity experiment opportunities being rare, a variable heater size study was performed under earth gravity conditions with two fluids (FC-72 and Pentane). Use of a 2.7 mm microheater array and a 7.0 mm microheater array provided higher resolution allowing accurate estimation of threshold L_h/L_c (Figure 6.6b). The effect of gravity was explained by correlating the current results with those performed at other gravity levels. A pool boiling regime map was developed by combining the current results and those published in literature.

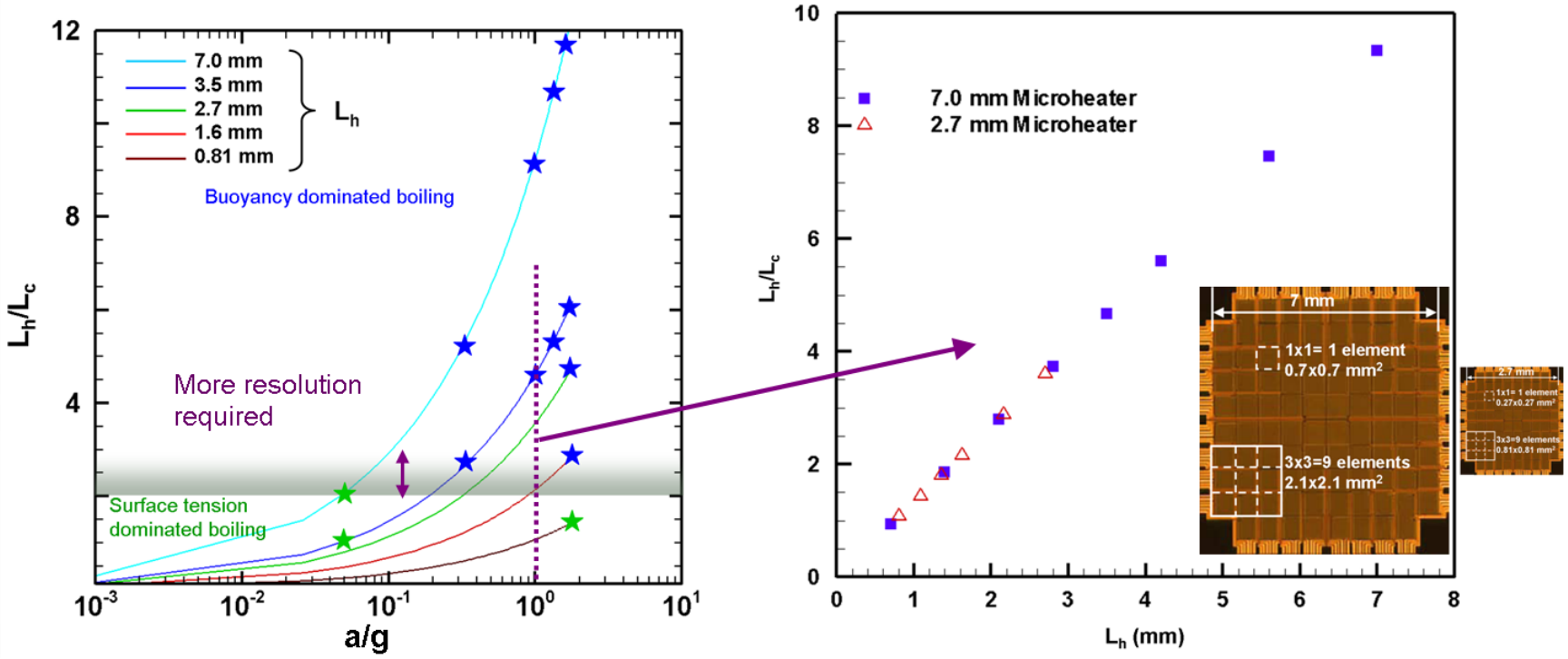

Figure 6.6: A plot of (a) L_h/L_c vs. a/g and (b) L_h/L_c vs. L_h for FC-72.

6.3.1 Test Conditions

At first glance, a complete investigation of the heater size effect would require around 800 experiments (ten sizes each for 7mm and 2.7 mm microheater array, two subcoolings, about ten wall superheats for full nucleate boiling curve, and at least two fluids). However, observations from the analysis of the data acquired in the early stages of the experiment revealed that many of these parameters have a negligible effect on heater size independence and hence do not require a detailed investigation at all the possible conditions. As a result, fewer tests (~300) were sufficient to understand and explain the effect of these parameters and arrive at a threshold value of L_h/L_c.

Earth gravity subcooled pool boiling experiments were performed at a pressure of 1 atm. The heater temperature was varied to acquire data in the nucleate boiling regime. Different heater sizes L_h were obtained by operating a subset of heaters in the array as explained in the previous section. Table 6.2 provides a complete list of experimental conditions used in this study.

Table 6.2: Summary of test conditions

	FC-72		Pentane
Microheater	7 mm	2.7 mm	7mm
T_{sat} [°C]	56.6	56.6	36
ΔT_{sub} [°C]	8.6 and 26.6	16.6	8
T_w [°C]	65, 70, 75, 80, 82.5, 85, 87.5, 90, 95, and 100	75, 77, 78, 79, 80, 82.5, and 85	60, 65, 70, 75, 77.5, 80, 82.5, 85, 87.5, and 90
L_h [mm]	0.7, 1.4, 2.1, 2.8, 3.5, 4.2, 5.6, and 7.0	0.81, 1.08, 1.35, 1.62, 2.16, and 2.7	0.7, 1.4, 2.1, 2.8, 3.5, 4.2, 5.6, and 7.0
L_c [mm]	0.75	0.75	1.51

In the following sections, results from subcooled pool boiling experiments under earth gravity using numerous heater sizes and varying experimental conditions (Table 6.2) are presented. For ease of understanding, this section has been divided into the following subsections: Heater size effect, effect of nucleation site density, effect of subcooling, and effect of fluid properties. The test matrix was optimized to minimize the number of experiments and efficiently arrive at threshold value of L_h/L_c. As a result, some overlap between the sections was unavoidable. However, the reader will have a clear understanding of the effect of parameters on heater size independence towards the end of the section.

6.3.2 Heater Size Effect

Boiling curves for numerous heater sizes using a 7 mm microheater array and FC-72 were obtained in normal earth gravity with the heater facing upward. Subcooling was maintained at 26.6°C. Figure 6.7 presents the boiling curve for the various heater sizes tested. Most of the heated area experienced natural convection at lower superheats resulting in low heat transfer. Nucleation was observed to occur between ΔT_w=13.4°C and ΔT_w=18.4°C. With the ONB, a significant increase in the slope of the boiling curve was observed. Further increase in wall superheat resulted in additional nucleation sites being activated. The boiling curves for 9 heater elements (2.1x2.1 mm^2) or larger were similar and followed the same trend, *i.e.* the boiling curves were *heater size independent* (buoyancy dominated regime). For heated areas with 1 and 4 elements, nucleation was also observed to occur between ΔT_w=13.4°C and ΔT_w=18.4°C but the slope of the boiling curve was smaller and lower heat transfer was observed in the nucleate boiling regime (surface tension dominated regime).

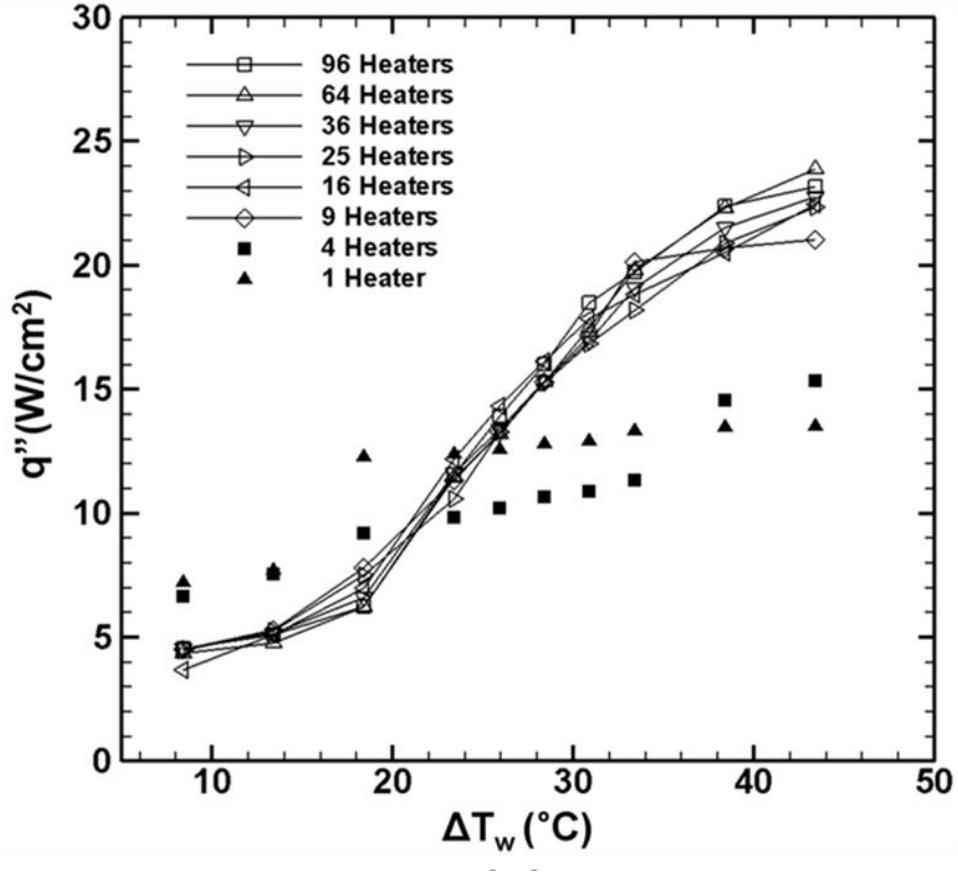

Figure 6.7: Boiling curve for different heater sizes at using FC-72, ΔT_{sub} =26.6°C, P= 1 atm, 7 mm microheater array.

The bottom view images and the departure frequencies provide more insight into the mechanism responsible for this behavior. Figure 6.8 shows bottom view images for 36, 9 and 4 heaters at three superheats. At the lower superheat (ΔT_w=23.4°C), the bubble departure diameter was similar for all three cases (Figure 6.8). Departure diameter increased with wall superheat (ΔT_w=30.9°C and 38.4°C). The difference in the bubble departure diameter is more pronounced at higher superheat close to CHF (ΔT_w=38.4°C). For the 4 heater case, bubble growth was limited by the heater size. For the 36 heater case, four relatively large bubbles formed while just one primary bubble formed for the 9

heater case. Visually, the 36 heater configuration can be achieved by combining four cases with 9 heaters. Hence, although the total heat dissipated was four times for the 36 heaters case, the heat flux and as a result the boiling curves were similar.

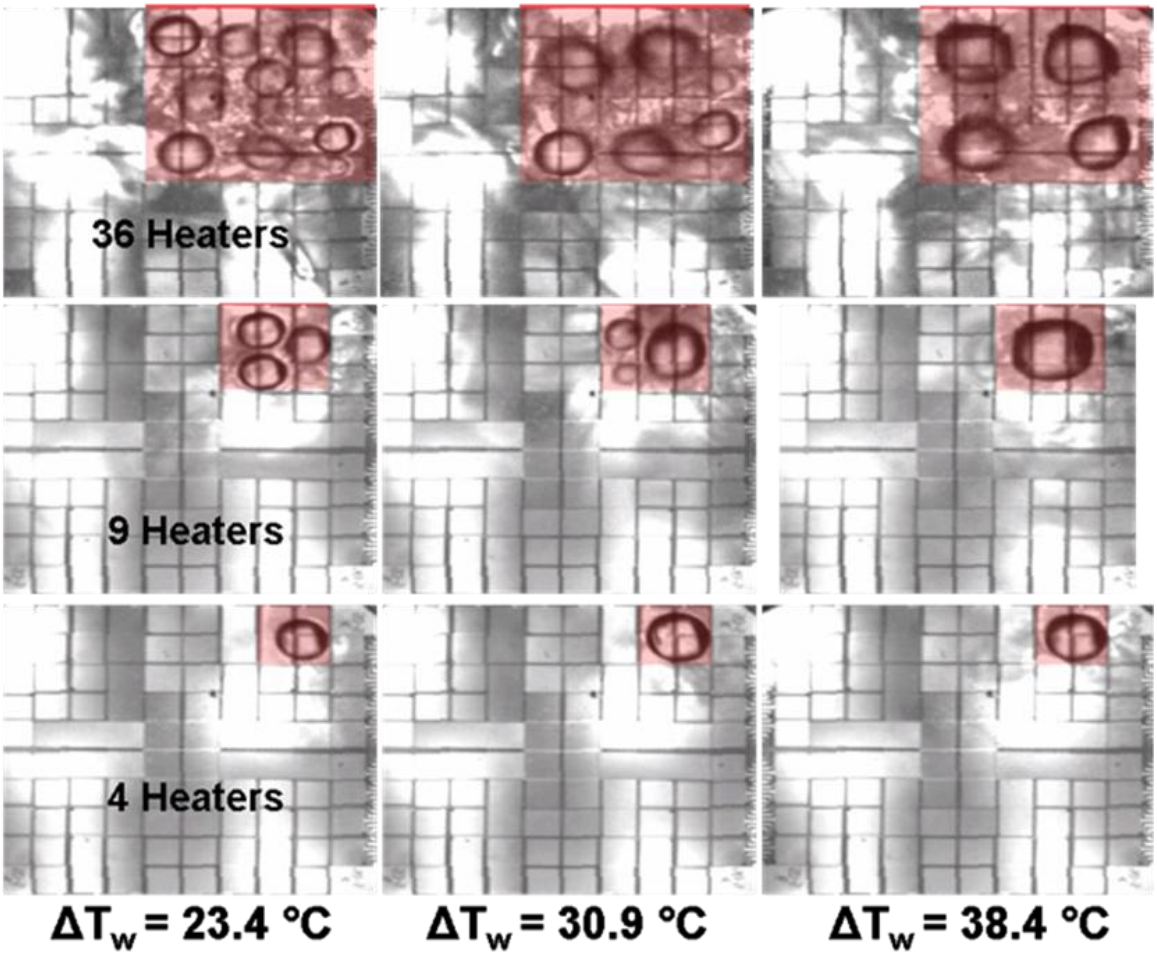

Figure 6.8: Bottom view images for 36, 9 and 4 heaters at three superheats, ΔT_{sub} =26.6°C, P= 1 atm, and 7 mm microheater array.

The boiling behavior for the 9 and 36 heaters are representative of the buoyancy dominated regime while the behavior for the 4 heater configuration illustrated boiling behavior in the surface tension dominated regime. Figure 6.9 presents the departure

frequency for 1, 4, 9, and 16 heater cases. The departure frequency was calculated by correlating the bottom view images, side view images and the heat transfer data. The low video capture frequency of 29.97 Hz and increased turbulence due to larger number of bubbles made it difficult to distinguish between the bubble cycles for the larger heated areas (>16 heaters). The departure frequency of the coalesced bubble (Figure 6.8) in the surface tension dominated regime (≤4 heaters) was significantly smaller than the bubble departure frequency in the buoyancy dominated regime (≥9 heaters). The departure frequency varied from 0.20 to 0.27 Hz for 1 heater case while it varied from 0.8 to 2.33 for the 4 heater case. For larger heaters (9 and 16 elements), the shape, size and hence the departure frequency was not limited by the heated area and was observed to be as high as 11 Hz. For the smaller heaters, bubble growth was limited by the heater size and surface tension dominated over buoyancy. Bubble growth was not spherical once the diameter was comparable to heater size. Further evaporation forced the bubble to stretch towards the top allowing contact with relatively cooler liquid. Contact with cold liquid increased condensation, decreasing the bubble growth rate and hence the departure frequency. The decrease in the departure frequency was primarily responsible for the overall decrease in heat transfer for smaller heaters.

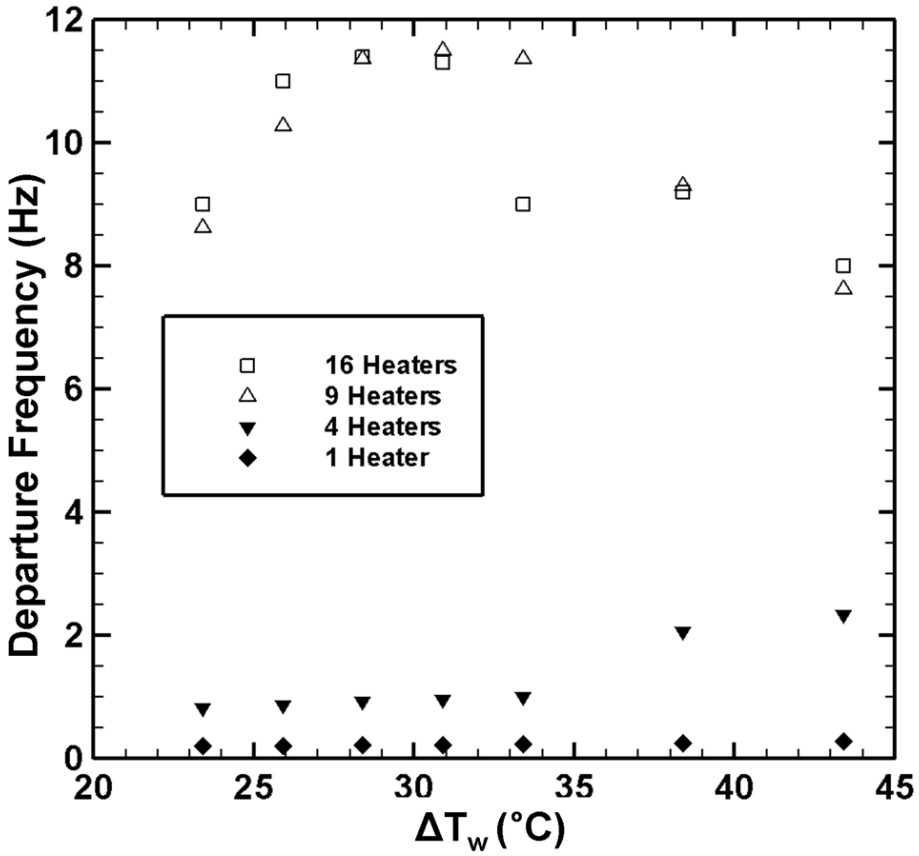

Figure 6.9: Departure frequency versus superheat for FC-72, ΔT_{sub} =26.6°C, P= 1 atm, and 7 mm microheater array.

Use of a 7 mm microheater array limited the length scale resolution to 0.7 mm. The capillary length/departure diameter of FC-72 is of the same order as the minimum length scale (0.7 mm) under earth gravity conditions. Additional experiments were performed with FC-72 and the 2.7 mm microheater array where each element was 0.27x0.27 mm^2. Use of a different microheater array implied different nucleation characteristics. Even though the nucleation characteristics changed the value of heat flux at a given superheat and the slope of the boiling curve, the minimum heater length above which heater size independence was observed was not affected. Subcooling was set at

16.6°C and was different from the subcooling for the previous set of experiments using the 7 mm microheater array (26.6°C). As will be explained in the later section, subcooling does not affect the transition between regimes and the minimum heater length for heater size independence remains unchanged.

The boiling curves obtained at earth gravity using the 2.7 mm microheater array are shown on Figure 6.10. ONB was observed between a wall superheat of ΔT_w=18.4°C and ΔT_w=20.4°C. The boiling curves were found to be heater size independent for cases where the heater size was larger than 1.62x1.62 mm^2 (6x6 heaters). The value of heat flux at CHF was significantly lower for square heaters smaller than 1.62 mm a side, suggesting surface tension dominated boiling. This is consistent with the results obtained using the 7 mm microheater array where the transition occurred between 1.4x1.4 mm^2 (4 heaters) and 2.1x2.1 mm^2 (9heaters). A non-departing, stable coalesced bubble similar to microgravity conditions was observed for the smallest size (9 heaters), similar to the observations of Henry *et al.*, 2004 under 1.7g conditions.

The shape of the boiling curves for the smaller heated area cases which are in the surface tension dominated boiling regime does not follow any specific trend (1 and 4 heaters-Figure 6.7 and 9, 16 and 25 heaters-Figure 6.10). This situation is very similar to those under microgravity conditions (Henry *et al.*, 2004; Kim, 2003) where the shape of the boiling curves differ significantly even under a slight variation of experimental conditions. Although, no concrete explanations are available in the literature, it is speculated that many other parameters that have inconsequential effect under earth gravity become dominant under microgravity conditions. The above mentioned smaller heated area cases are also in the surface tension dominated boiling regime like

microgravity boiling, and hence no definite trend of the boiling curve. Further investigations are required to identify the root cause behind such variation.

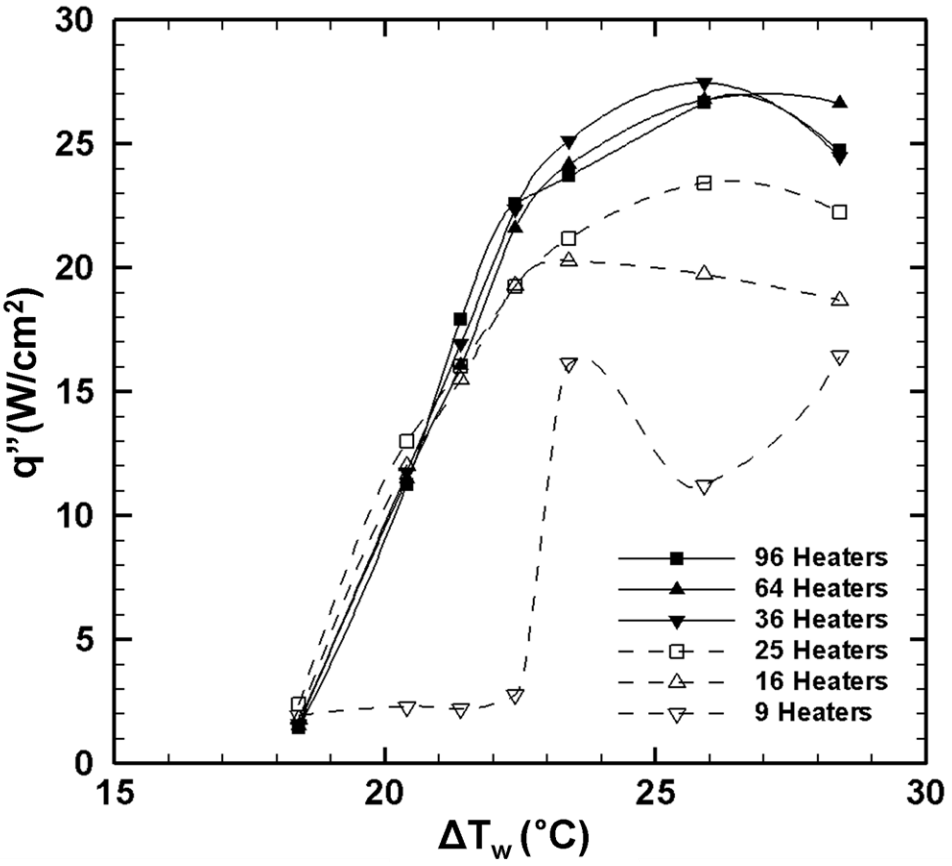

Figure 6.10: Boiling curve for different heater sizes using FC-72, ΔT_{sub} =16.6°C, P= 1 atm, and 2.7 mm microheater array.

6.3.3 Effect of Nucleation Site Density

ONB and the slope of the boiling curve depend on the surface properties (microstructures) of the heater used. For the 2.7 mm microheater, ONB was observed to occur at a higher wall superheat (18.4°C-20.4°C) compared to that for 7 mm microheater array (13.4°C-18.4°C). The slope of the boiling curve for the 2.7 mm microheater array (Figure 6.10) in the nucleate boiling regime was also significantly larger compared to

what was observed for the 7 mm microheater array (Figure 6.7). The large slope in the nucleate boiling regime for the 2.7 mm microheater array can be attributed to a very uniform nucleation site density on the heater surface. The uniformity in the microstructures allows all nucleation sites to activate over a narrow range of temperature causing a sudden increase in heat flux at ONB. Large slope in the boiling curve resulted in CHF at a significantly lower wall superheat of 25.9°C for the 2.7 mm microheater array. Even though the nucleation characteristics (ONB) and heat transfer behavior (CHF) change with heaters (Figure 6.5, Figure 6.7, and Figure 6.10), the heater size independence effect was observed for all these cases.

Even within a heater, the nucleation characteristics might vary. This section highlights the non-uniformity in the nucleation site density within a heater by discussing heat transfer results obtained for various sizes using different subsets of heaters within a single microheater array. The thermal boundary layer of the superheated liquid above the heated surface plays an important role in ONB. Hsu's model (1962) for the criteria of ONB postulates that the embryo bubble would grow and the cavity would activate if the equilibrium superheat was equaled or exceeded all around the perimeter of the embryo bubble. This occurs if the temperature at $y=b$ (height of the embryo bubble) is greater than the equilibrium superheat temperature. The thickness of the superheated boundary layer is affected by the area of the heated surface. For an example, a schematic representation of two cases with different heater sizes, large (7x7 mm^2) and small (1.4x1.4 mm^2), is shown on Figure 6.11. As the heater size decreases, the thermal boundary layer thickness decreases due to increased edge effects. As a result, for a cavity at the center of the smaller heater, the temperature at $y=b$ (height of the embryo bubble)

will be smaller than that for the larger heater, thus reducing the chances of nucleation. Cavities that might have nucleated on a large heater may not nucleate as the heater size is decreased. Moreover, fewer candidate nucleation sites in a smaller heated area might also be responsible for delayed nucleation.

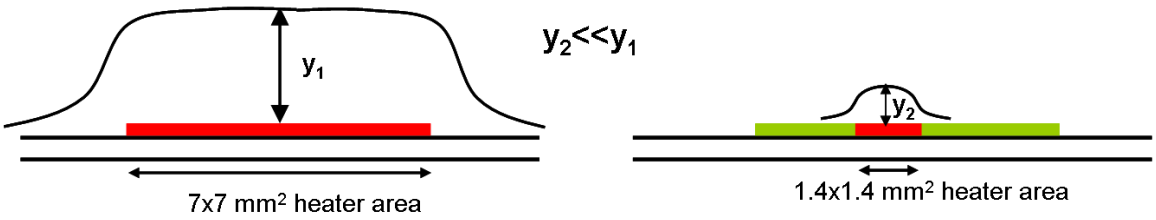

Figure 6.11: A schematic of the boundary layer thickness *y* over heaters of various sizes.

For a large heated area, the distribution of the nucleation site density is mostly uniform and the average superheat required for nucleation is also uniformly distributed. However, if we concentrate on a smaller area, the non-uniformity in nucleation site density and superheat for nucleation becomes prevalent. To explain this, a heater under two heating conditions is considered; first, when the full heater is operated while the second when only a quarter (A/B/C/D) is operated (Figure 6.12). The candidate nucleation sites are shown by red dots and blue stars. Blue starts are assumed to activate at a lower temperature (T_1) compared to the red dots (T_2). When the heater temperature is set to T_3 such that, $T_1<T_3<T_2$, boiling will start in the first case where the full heater is operated. Creation of bubble in the blue star cavity could activate other nucleation sites in case some vapor/gas gets trapped in any of the red cavities. However, for the second case, only one out of four cases will lead to boiling. Hence, the non-uniformity in active

nucleation site density and the delay in the onset of nucleate boiling are visibly more pronounced in the second case.

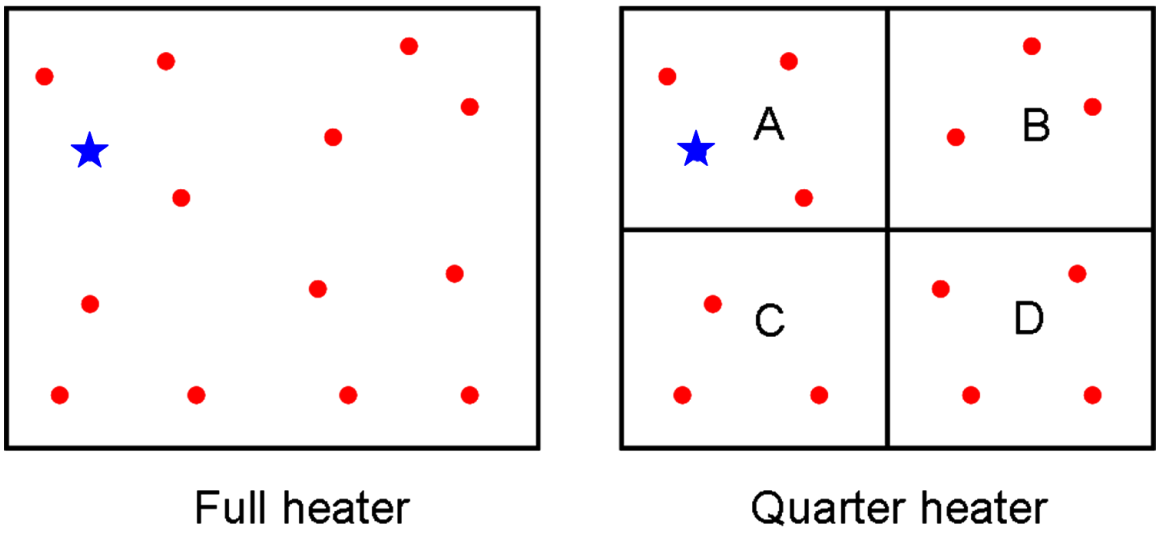

Figure 6.12: Schematic representation of nucleation site density distribution on a heater.

Nucleation was observed to be dependent on the size and location of the heated areas. There are patches on the array where the nucleation site density is less and/or the required superheat for ONB is higher and nucleation can be delayed (*e.g.* dashed lines, Figure 6.13). On the other hand, solid curves represent cases on the microheater array where the required superheat was either lower or the number of nucleation sites were higher. As a result, ONB occurred at lower temperature. Even for the cases where nucleation was delayed, the rest of the nucleate boiling curve was unaffected and heat flux values were similar to what was observed for the early nucleation (solid lines).

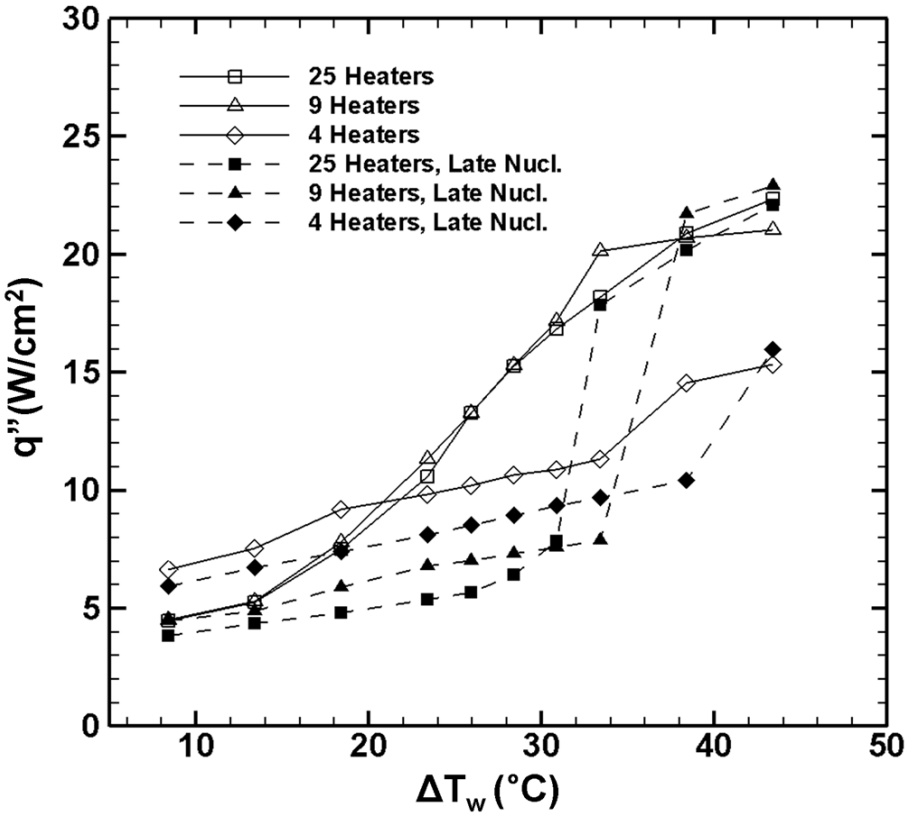

Figure 6.13: Boiling curve for different heater sizes for normal and delayed nucleation, ΔT_{sub} =26.6°C, P= 1 atm, and 7 mm microheater array.

6.3.4 Effect of Subcooling

The effect of subcooling was studied by performing experiments at different subcooling with the 7 mm microheater array. Boiling curves for numerous sizes at a lower subcooling (ΔT_{sub}=8.6°C) are shown on Figure 6.14. Boiling was heater size independent for 9 or more heaters, similar to what was observed for the ΔT_{sub}=26.6°C case (Figure 6.7). This is also consistent with the observations of Henry *et al.*, 2004 where the transition between regimes was observed at same heater size at all four subcoolings investigated (ΔT_{sub}=8°C, 16°C, 25°C, and 31°C).

The departure frequency in the buoyancy dominated regime was higher for lower subcooling (Figure 6.15a) since the condensation at the bubble top was reduced allowing the bubble to grow more rapidly. The effect of subcooling on departure frequency in the surface tension dominated regime is shown on Figure 6.15b. For high superheats ($\Delta T_w \geq$ 34˚C), departure frequency was higher for the lower subcooling case. However, departure frequency at low superheats was higher for higher subcooling. Moreover, no departure was observed for the 1 heater case and lower subcooling (ΔT_{sub} =8.6°C). Once nucleated, the bubble was observed to oscillate in size. Irrespective of the non-departing bubble, heat transfer was similar to the case with higher subcooling (ΔT_{sub} =26.6°C). A strong convective current observed near the bubble top for ΔT_{sub} =8.6°C is thought to be responsible for the high heat transfer even without departure. The actual mechanism behind this convective current is in dispute (Straub, 2002; Marek *et al.*, 2001; Barthes *et al.*, 2007) and requires further investigation.

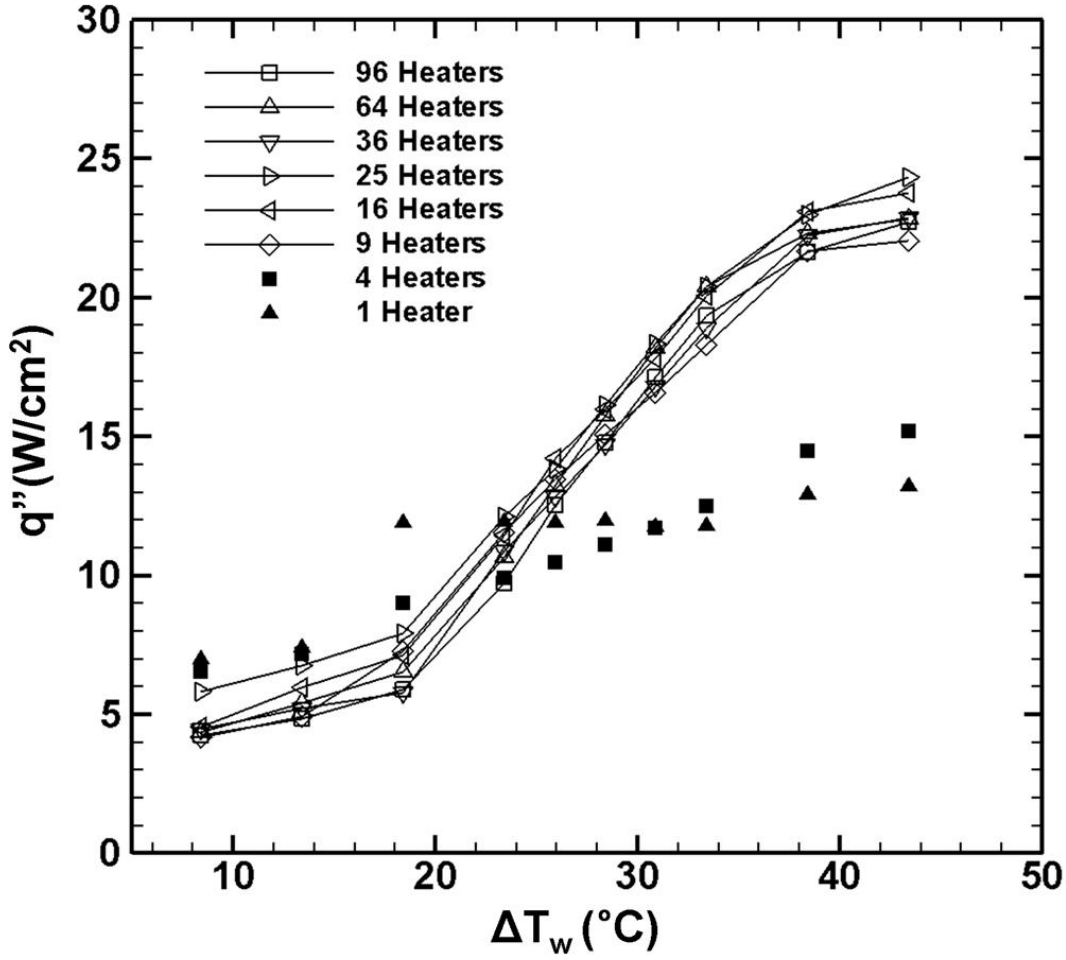

Figure 6.14: Boiling curve for different heater sizes using FC-72, ΔT_{sub} =8.6°C, P= 1 atm, and 7 mm microheater array.

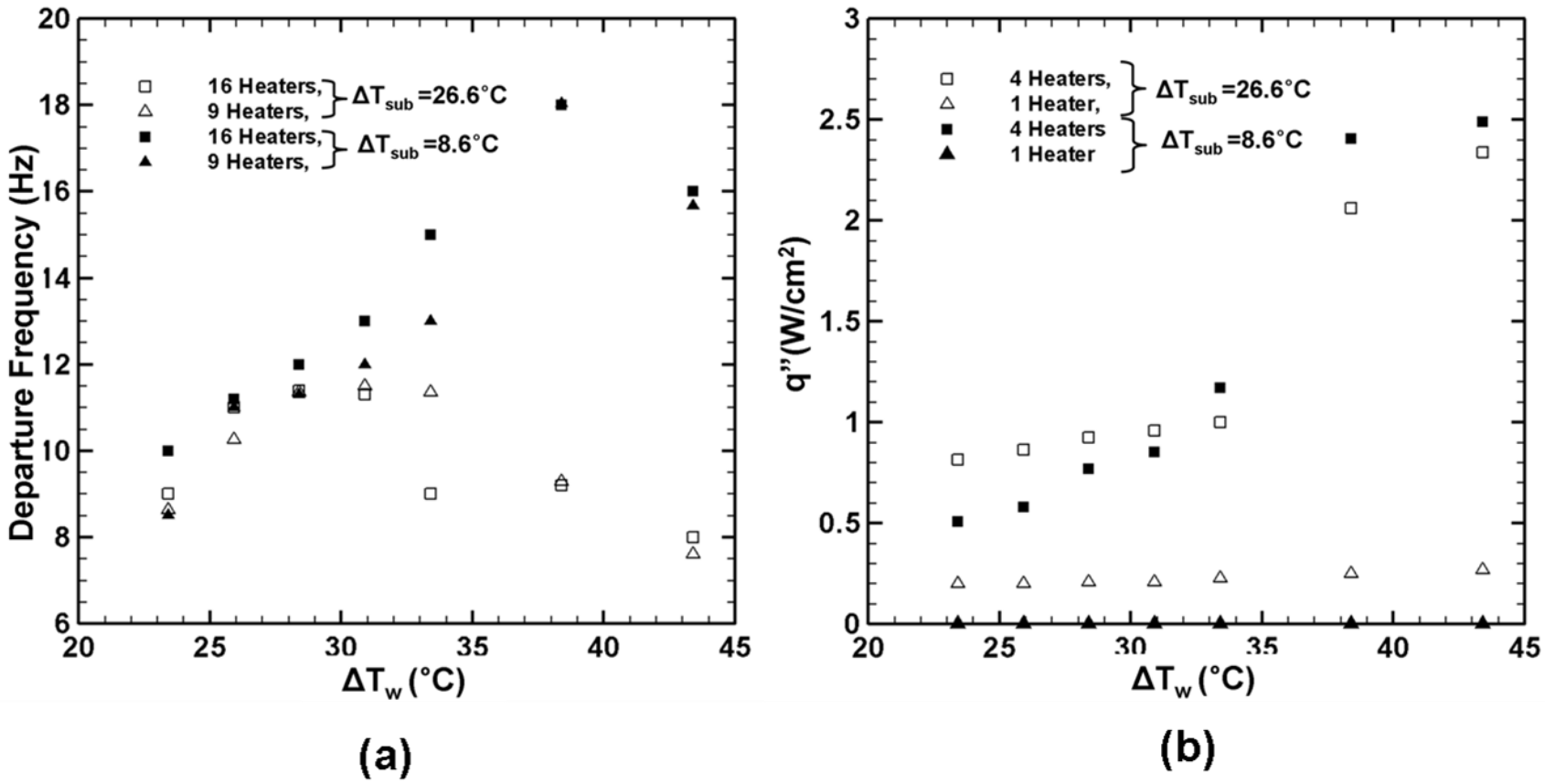

Figure 6.15: Departure frequency versus superheat for the (a) buoyancy dominated regime and, (b) the surface tension dominated regime at two subcoolings using 7 mm microheater array.

6.3.5 Effect of Fluid Properties

All the above studies and those presented in the literature review section showed two boiling regimes for FC-72; a *heater size independent regime* where buoyancy dominated and a *heaters size dependent regime* where surface tension forces dominate. These observations encouraged further experiments with a different fluid to understand the effect of fluid properties on transition. The capillary length L_c of pentane (1.51mm) is twice that of FC-72 (0.75 mm) at earth gravity. Hence, pentane (T_{sat}=36°C at 1 atm), was used to verify the heater size dependence results observed in the previous section. Subcooling was maintained at 8°C. The heater temperature was varied between 60°C (ΔT_w=24°C) and 90°C (ΔT_w=54°C), and the pressure was maintained at 1 atm throughout the experiment.

The boiling curves under earth gravity conditions for various heater sizes using the 7 mm microheater array are shown on Figure 6.16. Two boiling regimes were observed and *heater size independent* results were observed only for heaters larger than 3.5x3.5 mm^2 (25 heaters). It was not possible to measure D_d without significant uncertainty due to increased turbulence and complex merger processes. However, careful observation of the bottom view videos showed that D_d for pentane (Figure 6.17b) was approximately two times that for FC-72 (Figure 6.17a). As a result, the heater size independent behavior was observed at larger size (25 heaters) compared to that for FC-72 (9 heaters). Decreased departure frequency with decreasing heater size was attributed for the decrease in heat transfer in the surface tension dominated regime. Again, vigorous boiling and increased turbulence did not allow accurate measurements.

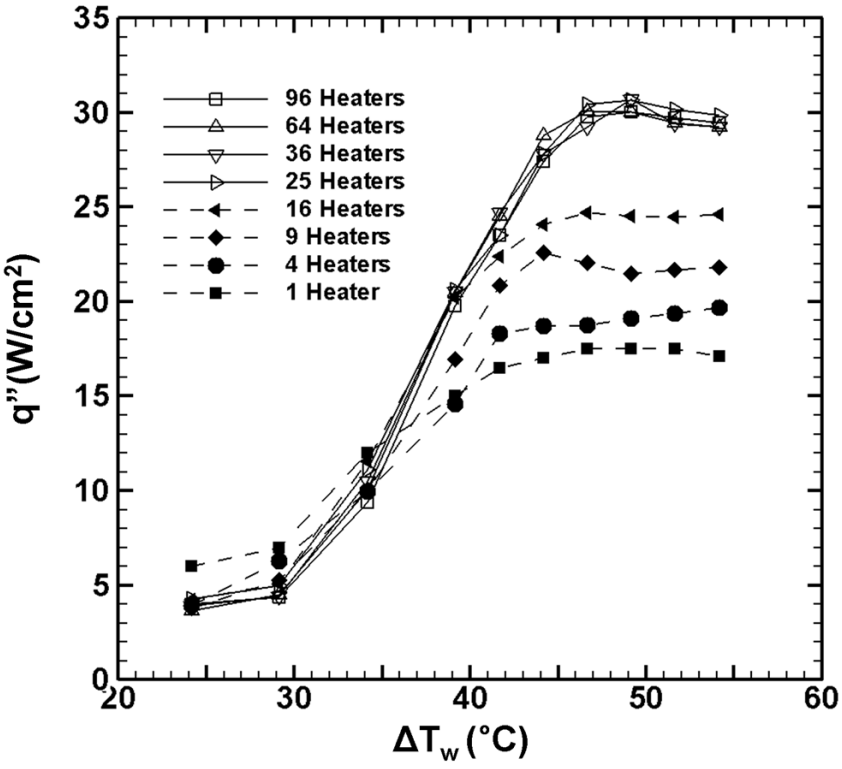

Figure 6.16: Boiling curves at different heater sizes for pentane, ΔT_{sub} =8°C and P= 1 atm, and 7 mm microheater array.

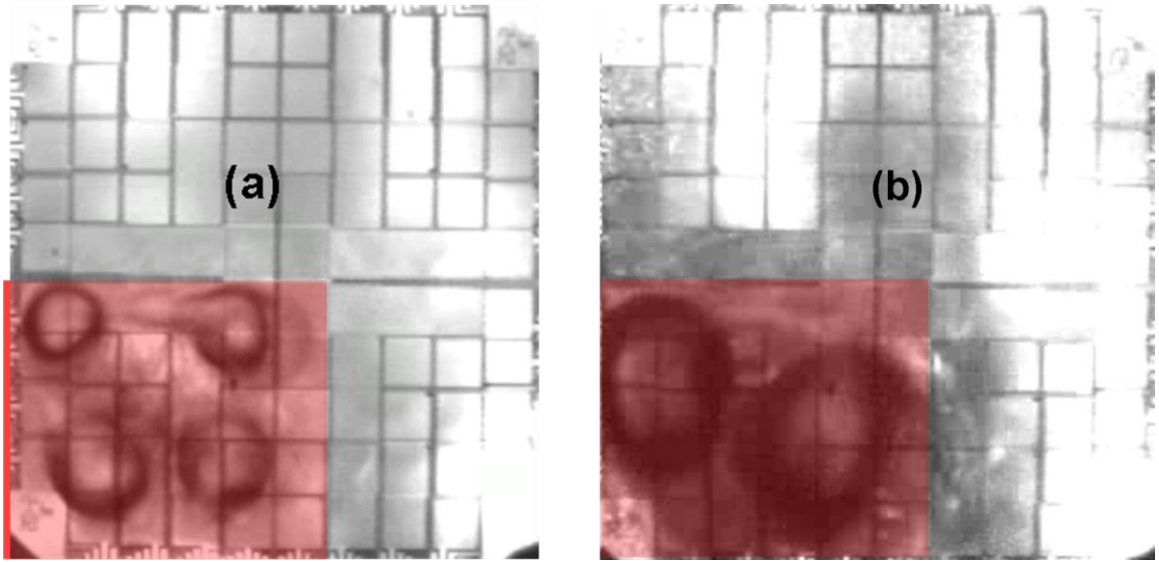

Figure 6.17: Bottom view image for 25 heaters; (a) FC-72, ΔT_{sub} =8.6°C, and (b) pentane, ΔT_{sub} =8°C, P= 1 atm, ΔT_w ~40°C, and 7 mm microheater array.

6.4 POOL BOILING REGIME MAP

The results from the earth gravity experiments using two fluids, variable gravity experiments (ESA and NASA campaigns), and those from Henry *et al.*, 2004 are compiled in Table 6.3 and Table 6.4. Under earth gravity conditions for FC-72 (L_c=0.75 mm), the minimum heater size L_h above which boiling was buoyancy dominated was 1.62 mm (36 heaters, 2.7 mm heater, Figure 6.10), resulting in a value of L_h/L_c=2.1. Similarly, the minimum value of L_h/L_c from the 1.7g experiments of Henry *et al.*, 2004, was 2.8 while a value of 2.5 was obtained from the variable gravity experiment. The capillary length L_c of pentane at normal earth gravity is 1.51 mm. Based on the element width of 0.7mm and 5x5 heater configuration (25 heaters, Figure 6.16), the minimum value of L_h/L_c above which boiling was heaters size independent was found to be 2.3. Table 6.3 presents the minimum value of L_h/L_c at which heat transfer results were *heater size independent*.

Table 6.3: Minimum value of L_h/L_c for heater size independence.

	Henry *et al.*, 2004 (FC-72, 2.7mm)	Variable gravity (FC-72, 7mm) (ESA)	Earth gravity (FC-72, 7 mm)	Earth gravity (Pentane, 7 mm)
g [m/s^2]	1.7	0.3	1	1
L_h [mm]	1.62	3.5	1.62	3.5
L_c [mm]	0.58	1.38	0.75	1.51
L_h/L_c	2.8	2.5	**2.1**	2.3

Table 6.4 shows the maximum value of L_h/L_c at which the heat transfer results were observed to be in the *heater size dependent* regime. The value was found to range between 1.4 and 2.1 for different experimental conditions. Comparison of the two tables reveals that the transition between regimes occurs at a threshold value of L_h/L_c=2.1.

Table 6.4: Maximum value of L_h/L_c for heater size dependent boiling.

	Henry *et al.*, 2004 (FC-72, 2.7mm)	Variable gravity (FC-72, 7mm) (ESA)	Earth gravity (FC-72, 7 mm)	Earth gravity (Pentane, 7 mm)
g [m/s^2]	1.7	0.05	1	1
L_h [mm]	0.81	7	1.4	2.8
L_c [mm]	0.58	3.34	0.75	1.51
L_h/L_c	1.39	**2.1**	1.9	1.9

Based on the above observations, a pool boiling regime map was developed for flat heated surfaces (Figure 6.18). The test conditions corresponding to the data points presented on Figure 6.18 are summarized in Table 6.5. Non-dimensionalized acceleration a/g and the ratio of heater size to capillary length L_h/L_c were used as the two axes. A line of constant L_h/L_c divides pool boiling into two regimes: *heater size independent/buoyancy dominated boiling regime* and *heater size dependent/surface tension dominated boiling regime*. Data in the *heater size dependent/surface tension dominated boiling regime* (solid symbols) lie below the line L_h/L_c=2.1 while all the data in the *heater size independent/buoyancy dominated regime* (open symbols) lie above the line L_h/L_c=2.1. This transition criterion also seems to be independent of the gravity level and holds for two fluids investigated.

Table 6.5: The test conditions corresponding to the data presented in Figure 6.18.

	Henry *et al.*, 2004 (FC-72)	Variable gravity (FC-72, NASA)	Variable gravity (FC-72, ESA)	Earth gravity (FC-72, 7 mm)	Earth gravity (Pentane, 7 mm)
g [m/s^2]	1.7	1.7	0.05, 0.3, 1, and 1.7	1	1
L_h [mm]	0.81, 1.62, and 2.7	2.1, 3.5, and 7.0	3.5, and 7.0	0.27, 0.54, 0.7, 0.81, 1.08, 1.35, 1.4, 1.62, 2.1, 2.16, 2.7, 2.8, 3.5, 4.2, 5.6, and 7.0	0.7, 1.4, 2.1, 2.8, 3.5, 4.2, 5.6, and 7.0
L_c [mm]	0.58	0.58	3.34, 1.38, 0.75, 0.58	0.75	1.51
ΔT_{sub} [°C]	31	6.6	26	8.6, 16.6, and 26.6	8

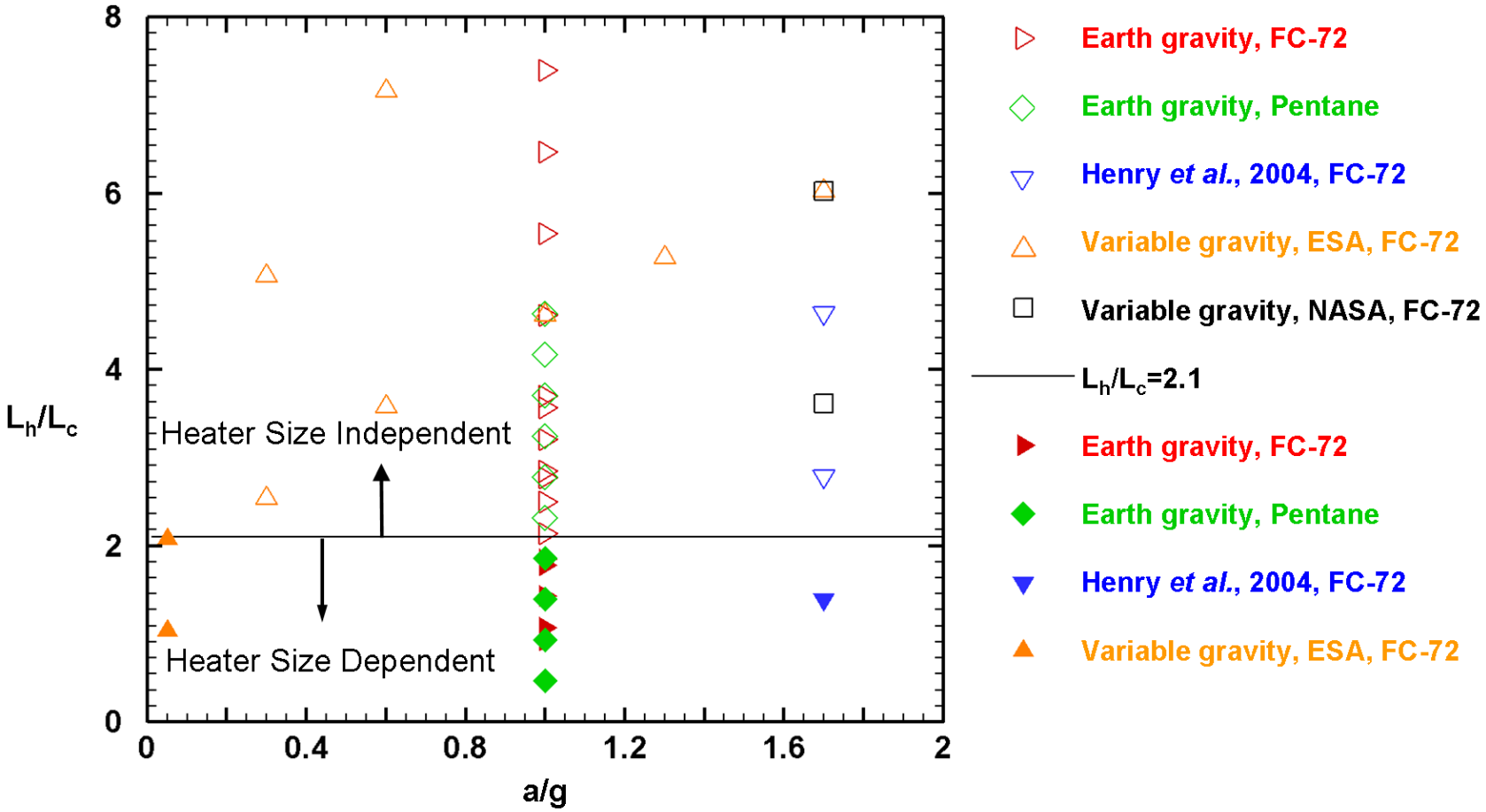

Figure 6.18: Pool boiling regime map for flat surfaces.

6.5 OREINTATION EFFECTS

The balance between buoyancy and surface tension forces can change with heater orientations. Hence, a study of pool boiling with varying heater sizes and different orientations is required for further understanding of pool boiling regimes. The objective of this section is to identify the threshold value of L_h/L_c at different orientations above which pool boiling is dominated by buoyancy and heat transfer results are *heater size independent*. Pool boiling experiments with varying heater sizes and four orientations were performed under earth gravity conditions. The boiling images were correlated with local heat flux values for better understanding of the phenomena. A comparison of the CHF values with those available in literature was made.

6.5.1 Test Conditions

FC-72 (C_6F_{14}, T_{sat}=56.6°C at 1 atm) was used as the test fluid. Pressure and subcooling were maintained at 1 atm and 16.6°C, respectively. The microheater temperature was varied between 75°C (ΔT_w=18.4°C) and 85°C (ΔT_w=28.4°C) during the experiment. Experiments were performed at 4 orientations and 6 sizes. The detailed test matrix is summarized in Table 6.6.

Table 6.6: Summary of test conditions

Orientation [°]	0, 45, 90, and 135
ΔT_{sub} [°C]	16.6
P [atm]	1
L_h [mm]	96,64,36,25,16, and 9
ΔT_w [°C]	18.4,20.4,21.4, 22.4,23.4,25.9, and 28.4

Pool boiling curves for the 96 heaters case and an orientation of 0°, 45°, 90°, and 135° are shown on Figure 6.19. At all orientations, onset of nucleate boiling (ONB) was observed to occur between ΔT_w =18.4°C and ΔT_w =20.4°C. CHF was observed to occur between ΔT_w =25.9°C and ΔT_w =28.4°C. As discussed in the previous section, the large slope in the nucleate boiling regime can be attributed to a very uniform nucleation site density on the heater surface.

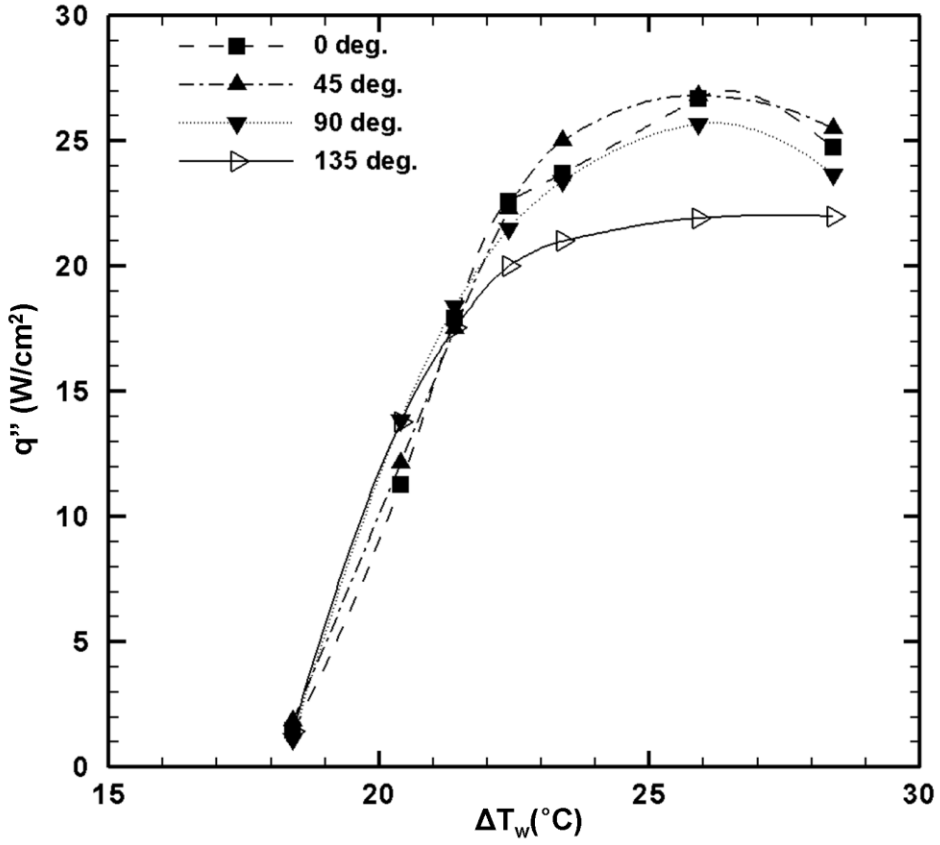

Figure 6.19: Boiling curves for four orientations with 96 operational elements.

As reported by many researchers, the heat flux at higher superheats for the 135° orientation was significantly lower than that for the other three orientations. For any heater oriented at θ>90°, a component of gravity pushes the nucleating bubbles against

the heater. We speculate this to be responsible for the decrease in heat transfer observed for the 135° case. There was no observable difference between the heat transfer results for the other three orientations.

6.5.2 Threshold Lh/Lc

The results of subcooled pool boiling experiments with six sizes at four orientations are shown on Figure 6.20. Similar to the observations with upward facing heaters, *heater size independent* and *heater size dependent* boiling regimes were observed for all four orientations. However, the minimum heater size L_h (1.35 mm) for *heater size independent* buoyancy dominated boiling for 45°, 90°, and 135° was smaller than that for 0°. This is different from heater facing upward case where transition was observed to occur at L_h=1.62 mm. Based on L_h of 1.35 mm and a capillary length L_c of 0.75 mm at earth gravity, transition between the regimes occurs at a threshold value of L_h/L_c=1.8 for these three orientations.

Similar to the upward facing heater case (0°); there is no specific trend that the boiling curves follow in the surface tension dominated boiling regime. This situation is very similar to those under microgravity conditions (Henry *et al.*, 2004; Kim, 2003) where the shape of the boiling curves differs significantly and does not follow any specific trend. It is usually argued that parameters that have inconsequential effect under earth gravity become dominant under microgravity conditions. As a result, even a slight variation of experimental conditions which otherwise does not affect boiling results in significant changes in the heat flux. The smaller heated area cases (L_h/L_c<2.1 for 0° and L_h/L_c<1.8 for 45°, 90°, and 135°) are also in the surface tension dominated boiling

regime, and hence possibly susceptible to other parameters causing huge fluctuations in the heat flux values.

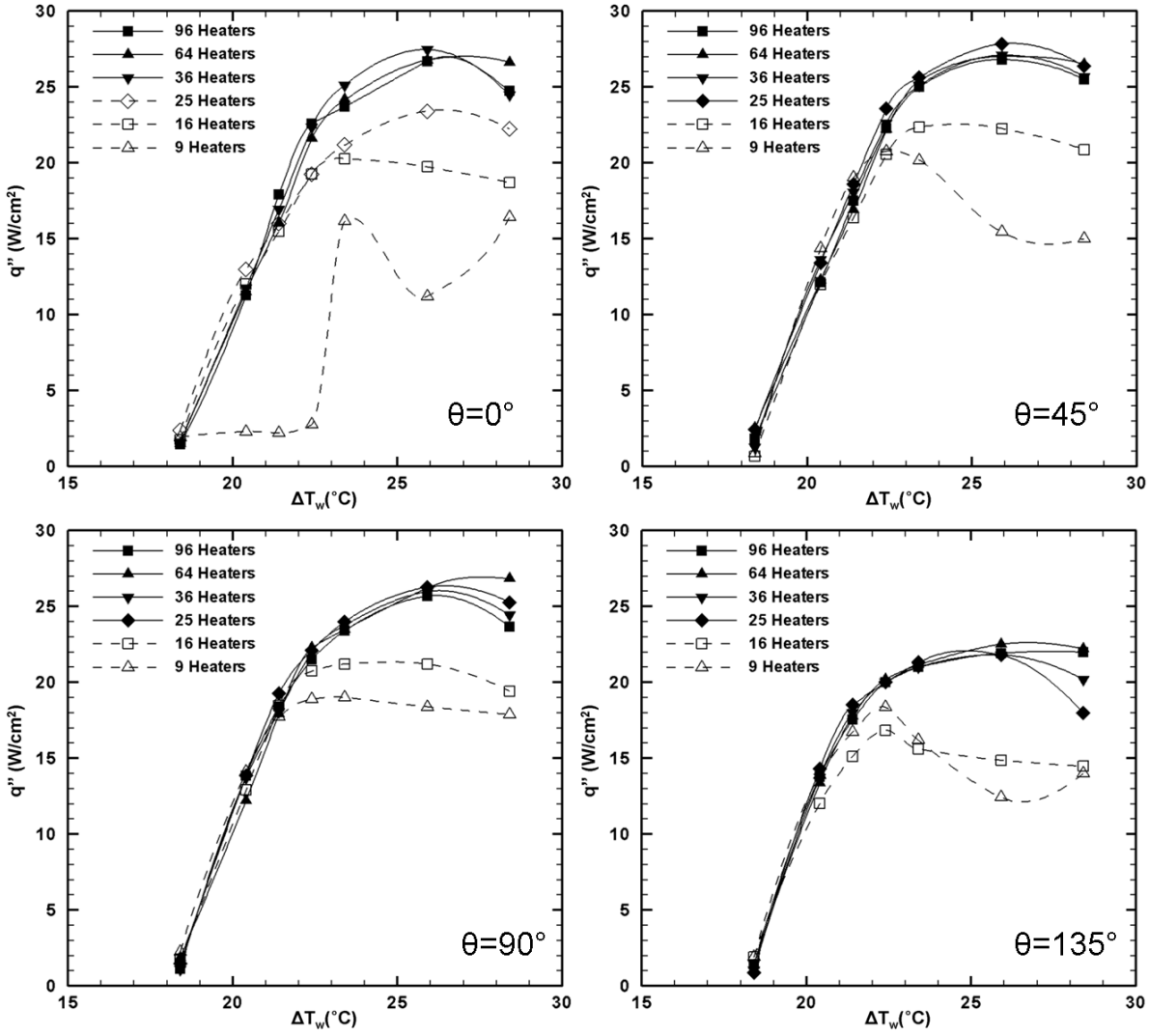

Figure 6.20: Boiling curve for six heater sizes at four orientations.

6.5.3 Local Measurements and Fractal Pattern

The bottom view images of boiling for three sizes and four orientations at a wall superheat of ΔT_w =25.9°C are shown on Figure 6.21. As expected, the boiling images are

symmetrical for the upward facing heater case while the non-spherical bubbles appear to depart north for the other three cases. This is due to the fact that for 45°, 90°, and 135° cases, a component of gravity acts parallel to the heaters surface.

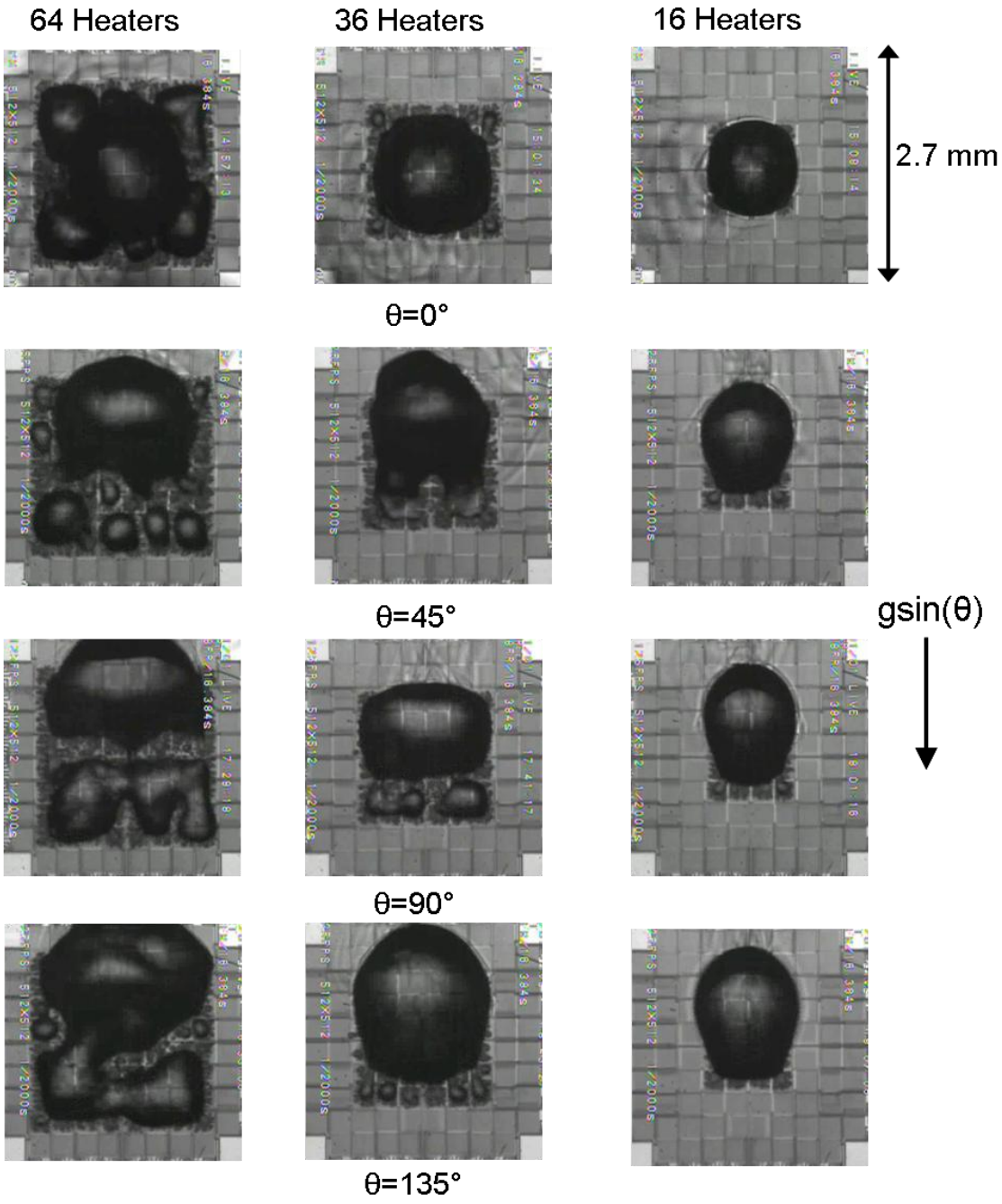

Figure 6.21: Bottom view images for three sizes and four orientations at a wall superheat of ΔT_w =25.9°C.

For the upward facing heater case, normal departing bubbles (f_d>10) were seen for the 96, 64 and 36 heaters cases while slowly departing bubbles ($f_d \leq 10$) were observed for the 25, and 16 heaters cases. A non-departing primary bubble similar to microgravity was observed for the 9 active heaters case. This again highlights the fact that surface tension dominated boiling similar to microgravity conditions can also be observed under normal earth gravity given that the value of L_h/L_c<2.1. Concentrating further on the upward facing heater case, a fractal pattern is observed for all three sizes. A large primary bubble is seen to form on the heater. The primary bubble is fed by smaller satellite bubbles that surround it. The satellite bubbles themselves were surrounded by even smaller bubbles which fed them, resulting in an almost fractal pattern to the boiling process.

The formation of a primary bubble similar in size to the heater surrounded by satellite bubbles were also observed in videos of microgravity boiling taken by Merte and Chiaramonte, 2001 on a rectangular heater 19.1x38.1 mm^2. Later, Kim *et al.*, 2002 also reported similar observations, again under microgravity conditions. They observed that the primary bubble formed from the coalescence of smaller bubbles that grew on the surface in low gravity. They suggested an approach to modeling boiling in low gravity or on small heaters in earth gravity where a large primary bubble forms that is fed by smaller bubbles, which in turn are fed by even smaller bubbles. It was proposed that increasing the heater size would just increase the size of the primary bubble. No predictions were made on weather this fractal pattern could be seen under earth gravity conditions.

However, there have been studies in literature (Yu and Cheng, 2002; Yang et al., 2001; Xiao and Yu, 2007) which utilized fractal pattern to develop models for pool boiling heat transfer under earth gravity conditions. The current results are the first visual confirmation of such fractal patterns in boiling under earth gravity conditions. Although the heaters used in this study can arguably be considered to be small (≤2.7 mm a side), *heater size independent* behavior discussed in the previous sections show that boiling is in the buoyancy dominated regime for heaters larger than 1.62 mm (L_h/L_c>2.1). Increasing the heater size further than this would simply repeat the pattern and the heat flux would remain unchanged. As argued by Kim *et al.*, 2002 for microgravity, the size of the primary bubble follows the heater size in the surface tension dominated boiling regime (L_h/L_c<2.1). However, in the buoyancy dominated boiling regime, the primary bubble size is limited by the departure diameter and could be significantly smaller than the heater size (64 heaters case and 0°, Figure 6.20). This similarity in the observations of microgravity experiments by Kim *et al.* and the current results under earth gravity again support the similarity in the role of heater size and gravity in the surface tension dominated boiling regime.

Presence of fractal pattern for the upward facing heater case was also confirmed by time averaged heat flux maps presented in Figure 6.22 (64, 36 and 16 heaters, 0°). For the 64 heaters case, the heat flux maps show a primary low heat flux zone surrounded by four secondary/satellite low heat flux zones. The low heat flux zone represents the dryout area within a bubble. The fractal pattern becomes more prominent in the fully developed nucleate boiling regime/higher superheats (ΔT_w >25.9°C). Comparing the three sizes for upward facing heater case (Figure 6.22, left), the fractal pattern becomes less prominent

as the size of the heated area is decreased. This is a direct manifestation of loss in percentage resolution with smaller number of elements available for the smaller heated areas. Reduction in the total number of elements with size only allows an averaged representation on a scale larger than that required to resolve the corresponding smaller primary and satellite bubbles formed in these cases. This is also confirmed by the fact that no such pattern was seen with experiments performed with 7 mm microheater array where the minimum length scale (0.7 mm) was comparable to the departure diameter/capillary length (L_c~0.75 mm) and almost three times that of the current situation (0.27 mm). However, if the heater size is reduced such that the number of elements remain the same (implying correspondingly smaller elements with same percentage resolution), we propose that the fractal pattern would be more evident.

All these observations confirm the presence of fractal pattern in boiling phenomena. Fractal pattern in boiling is present in both the surface tension dominated (low gravity and small heaters) and buoyancy dominated boiling regimes (high gravity and large heater). It is just a matter of having sufficient resolution for the associated length scales. Moreover, the nucleation site density on the heater should be uniformly distributed. A non-uniform surface such that cavities activate over a wide range of superheats and are non-uniformly distributed over the heater surface does not allow fractal patterns to be observed.

Figure 6.21 also shows the bottom view images for the other three orientations. The fractal pattern is lost due to a directional bias imposed by the component of gravity parallel to the heater surface. However, a primary bubble (north of the heater) fed by smaller satellite bubbles (south edge) was also observed for these orientations. Surface

tension forces dominated at smaller length scales and departure frequency was again observed to decrease with size.

The boiling pattern in the buoyancy dominated boiling regime (36 and 64 heaters, Figure 6.21) was significantly different from those of 45°, and 90°. Moreover, the time averaged heat flux maps for 0° (36 and 64 heaters, Figure 6.22) were also significantly different from those of 45° and 90° cases (36 and 64 heaters, Figure 6.22 and Figure 6.23). Yet, the area averaged heat flux values at any superheat and hence the boiling curves were similar for all three cases. This can be explained by paying a closer look at the detailed heat flux maps and the corresponding bottom view images. For the 45° and 90° cases, there was a decrease in heat flux towards north boundary. This decrease was compensated by numerous satellite bubbles nucleating on the south boundary. As a result, the south boundary saw significantly large heat transfer compensating for the losses experienced by the north boundary.

Significantly lower heat flux values for the 135° (Figure 6.20) compared to the other three orientations was also confirmed by the local heat flux maps shown on Figure 6.23. A component of gravity perpendicular to the heater pushed the bubbles onto the heater surface delaying departure. As a result, a significant portion of the heated area was dry for longer time (north portion of the heater, Figure 6.23), decreasing the heat transfer. However, satellite bubbles on the trailing edge (south) again resulted in relatively higher transfer for these elements.

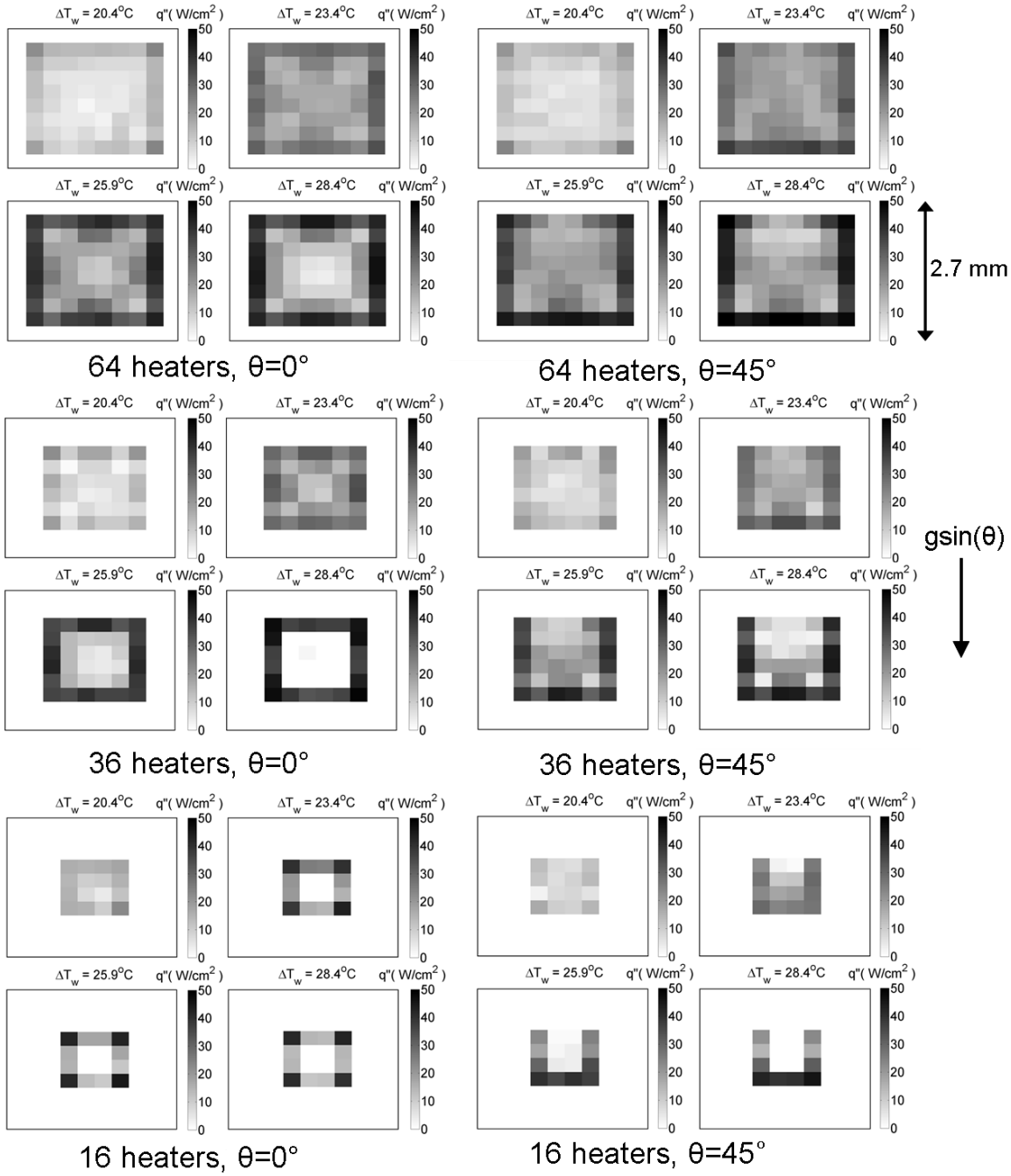

Figure 6.22: Time averaged local heat flux distribution for three heater sizes at 0° and 45°.

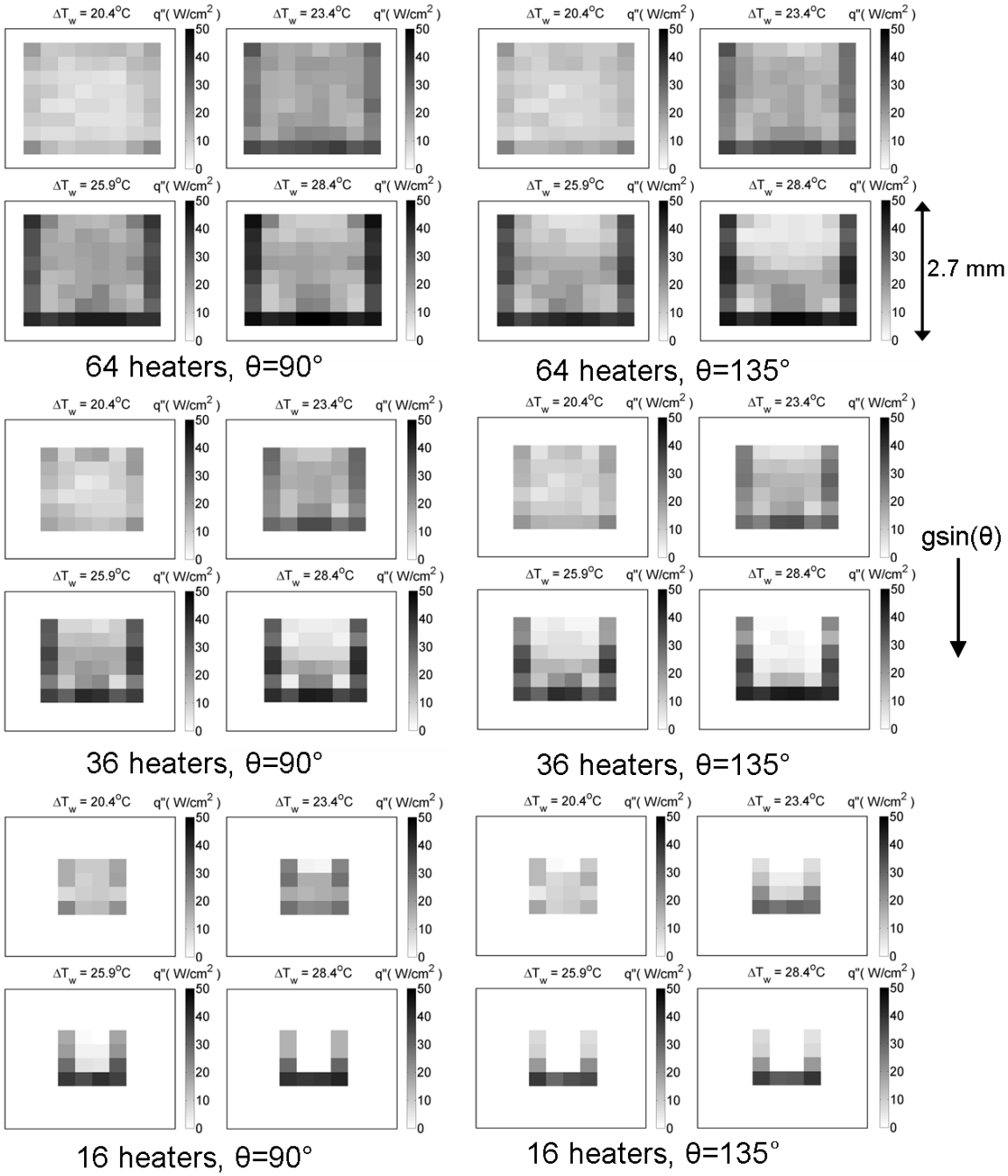

Figure 6.23: Time averaged local heat flux distribution for three heater sizes at 90° and 135°.

6.5.4 CHF

This section focuses on effect of orientation and heater size on the value of heat flux at CHF. Figure 6.24 shows a plot of normalized CHF (the ratio of CHF at any orientation to that at 0° for any given size) versus orientation in the *heater size independent* boiling regime. A comparison with the models of Brusstar and Merte, 1994 and Chang and You, 1996 is presented. Brusstar and Merte developed a correlation based on the experimentally observed relationship between bubble residence time and CHF for R-113. The model divides orientations into two regions: an upward facing heater region ($0°<\theta\leq 90°$) where no change in CHF is observed and a downward facing heater region ($90°<\theta\leq 180°$) where CHF changed continuously with angle.

Brusstar and Merte – R113 (1994)

$$\frac{q''_{CHF,\theta}}{q''_{CHF,0°}} = \begin{cases} 1.0 & 0° < \theta < 90° \\ |\sin\theta|^{1/2} & 90° < \theta < 180° \end{cases} \tag{6.3}$$

The model by Chang and You predicted a continuous decrease in heat flux with increasing orientation:

Chang and You – FC-72 (1996)

$$\frac{q''_{CHF,\theta}}{q''_{CHF,0°}} = 1.0 - 0.00120\tan(0.414\theta)\theta - 0.122\sin(0.318\theta) \tag{6.4}$$

The magnitude of the normalized CHF values for the three sizes in the *heater size independent* boiling regime show good agreement with the results of Brusstar and Merte. No significant decrease in heat flux value at CHF was observed for the upward facing region ($0°<\theta\leq 90°$). However, significantly lower CHF was observed at 135°. Also, this trend was observed for all three sizes in the *heaters size independent* pool boiling regime. The correlation of Chang and You does not predict the current data well.

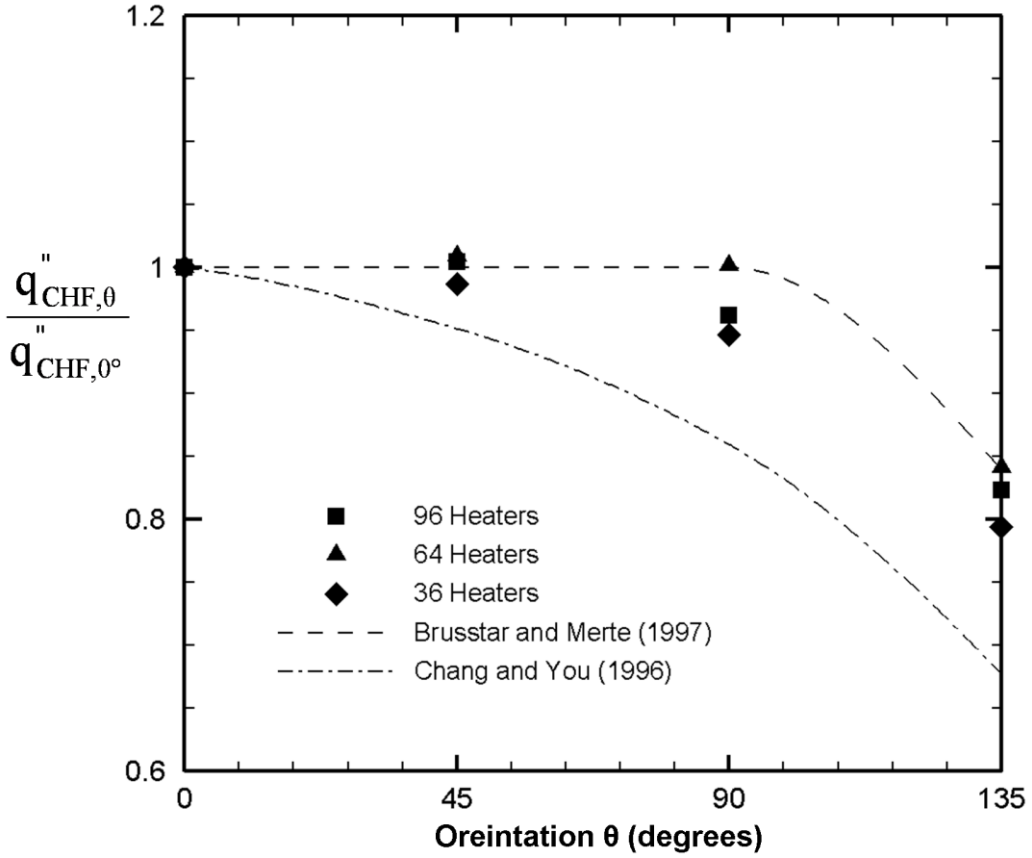

Figure 6.24: CHF value comparisons with published data.

The variation of normalized CHF (ratio of CHF for any given size to CHF for the 96 heaters case at the same orientation) versus L_h/L_t for all the experimental cases discussed in this paper is shown on Figure 6.25. L_t is the length at which transition was

observed for any given orientation (1.62 mm for 0° and 1.35 mm for 45°, 90°, and 135°, Figure 6.20). It should be noted here that the pool boiling curves in the surface tension dominated boiling regime do not follow the classical boiling curve shape. No typical boiling behavior from nucleate to film boiling was observed. Hence, by CHF, we mean the maximum observed heat flux for the experimental results presented in this paper.

A clear demarcation between two regimes is observed at L_h/L_t=1. To the left of this value, CHF decreases with decreasing heater size. Towards the right, *i.e.* buoyancy dominated boiling; CHF is independent of the heater size confirming the *heater size independent* behavior.

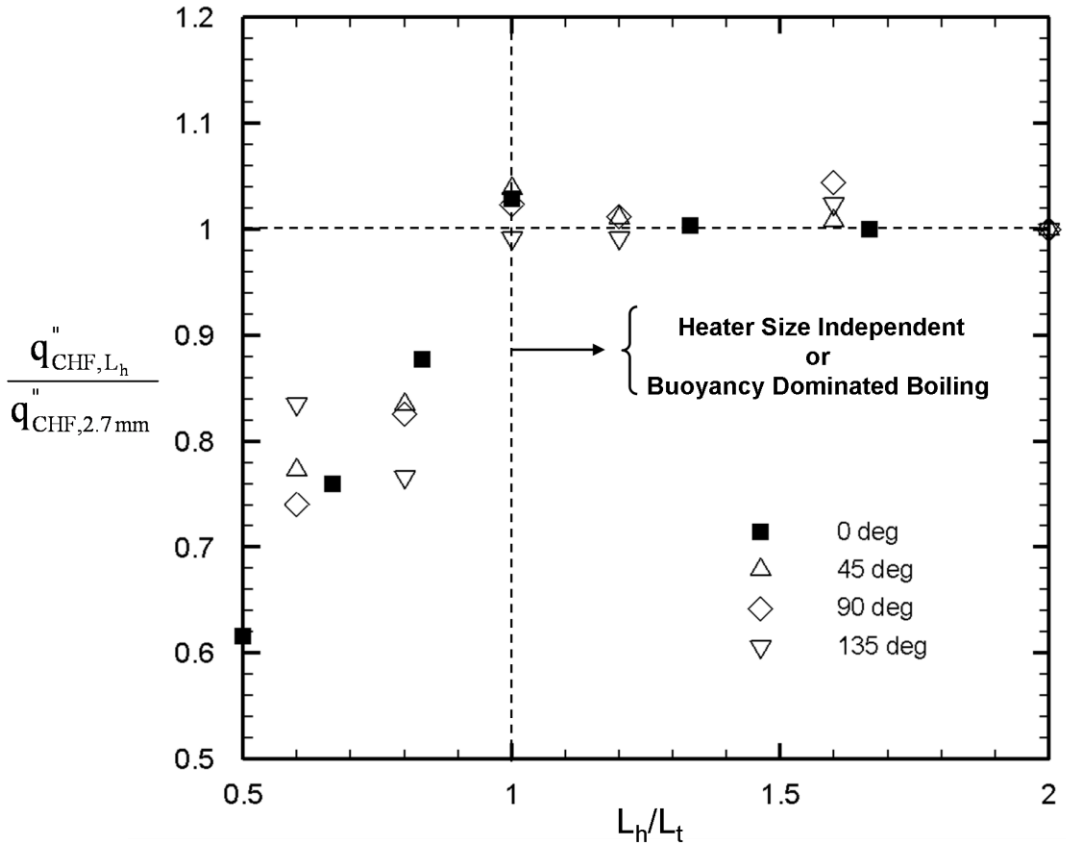

Figure 6.25: Normalized CHF versus L_h/L_t.

6.6 SUMMARY

To summarize, subcooled pool boiling of FC-72 at earth gravity was found to be buoyancy dominated for heated areas equal to or larger than 1.62x1.62 mm^2 (36 elements, 2.7x2.7 mm^2 heater, Figure 6.10). The heat flux was *heater size independent* when $L_h/L_c>2.1$. When L_h/L_c was smaller than this, surface tension dominated boiling and heat flux decreased. Similar behavior was observed for pentane and the threshold value of L_h/L_c was found to be 2.3, indicating the current results for FC-72 may also be applicable to other fluids.

Two pool boiling regimes similar to upward facing heater case were also observed for heater orientations of 45°, 90°, and 135°. Transition between the regimes was observed at a threshold value of $L_h/L_c\sim1.8$. Heaters oriented at 135° showed significantly smaller heat transfer compared to the other three orientations. Heat transfer in the surface tension dominated boiling regime was smaller and boiling curves did not follow the classical boiling behavior at all four orientations. A fractal pattern in boiling was observed for the upward facing heaters. This was also confirmed by the local heat flux measurements.

Chapter 7: Conclusions

This chapter presents the intellectual contributions made to the scientific community and the anticipated benefits for the industry resulting from the advances reported as part of this dissertation. Based on the outcome of the current research, a list of possible research directions in boiling heat transfer is proposed in the last section.

7.1 INTELLECTUAL CONTRIBUTIONS

This work is a part of the ongoing research in the field of pool boiling for use in practical applications requiring high heat flux dissipation under earth gravity as well as low gravity conditions. The major roadblocks in the accurate prediction of pool boiling heat flux across a range of gravity levels were identified. The sections below highlights the accomplishments made as a part of this dissertation.

7.1.1 Characterization of Pool Boiling over a Range of Gravity Levels

Observations from the first pool boiling experiment over a continuous range of gravity levels were presented. The heat flux variation with gravity at various wall superheats for two gas concentrations and three heater sizes was studied under subcooled pool boiling conditions. Different physical mechanisms were explained and in part visualized by the images of boiling process at various gravity levels. These were the first ever experimental visualization of boiling behavior over a continuous range of gravity levels.

Based on a sudden jump in heat flux with decreasing gravity level, two heat transfer regimes were reported. Above a certain threshold gravity level, boiling was reported to be buoyancy dominated and heat transfer results were heater size independent. Surface tension dominated boiling was reported below this threshold gravity

level and heat transfer results were heater size dependent. Normal bubble departure was observed in the buoyancy dominated boiling regime while a non-departing coalesced bubble surrounded by smaller satellite bubbles was observed in the surface tension dominated boiling regime. Based on the fundamentally different boiling patterns and a sudden jump in heat flux at the transition, a unified power law approach for gravity effect as adopted in the literature was ruled out.

Higher dissolved gas concentration was reported to initiate the onset of nucleate boiling at lower wall superheats. The presence of dissolved gas increased nucleate boiling heat transfer in the high-g regime but decreased the heat transfer in the low-g regime. Numerical simulations highlighted the importance of bubble shape, size and heat transfer coefficient on thermocapillary convection in the low-g boiling regime. An increase in the bubble size due to increased gas concentration resulted in a lower temperature gradient along the interface reducing the strength of thermocapillary convection. These observations were also qualitatively complemented by experimental observations under microgravity conditions.

7.1.2 Development of a Gravity Scaling Parameter for Pool Boiling Heat Transfer

Variable gravity pool boiling data in the buoyancy dominated boiling regime was utilized to develop a gravity scaling parameter for pool boiling heat transfer. The power law coefficient was found to be dependent on the wall temperature, contradictory to a constant power law coefficient as used in the current literature. Wall temperature was suitably non-dimensionalized to identify a scaling law independent of dissolved gas concentration and subcooling. The predicted results were found to be in good agreement

with the heat transfer data over a wide range of gravity levels, two gas concentrations, three subcoolings, and two surface morphologies.

7.1.3 Development of a Pool Boiling Regime Map

As a part of this task, an effort was made to quantify when heaters can be called "small heaters" during boiling heat transfer. It was shown that the term "small heater" is not completely descriptive of the boiling conditions. The term "small heaters" and/or "low gravity" conditions are better expressed as "surface tension dominated boiling." Heat transfer results were reported to be "heater size dependent" in this regime. Similarly, the "buoyancy dominated boiling/classical boiling" was suggested to be a better expression for boiling under "high gravity" conditions and/or for "large heaters." Heat transfer results were reported to be heater size independent in this regime. The non-dimensional ratio L_h/L_c which incorporates the effect of gravity and heater size was found suitable to differentiate between the boiling regimes. Transition between the regimes was observed to occur at L_h/L_c ~2.1 for upward facing heaters. A fractal pattern in boiling was observed in the boiling images for the upward facing heaters. This was also confirmed by the local heat flux measurements obtained from the microheater arrays.

Similar to the upward facing heater case, two pool boiling regimes were also observed for heater orientations of 45°, 90°, and 135°. Transition between the regimes was observed at a threshold value of L_h/L_c~1.8.

Based on the heater size results at various gravity levels and with two fluids, a novel pool boiling regime map distinguishing buoyancy and surface tension dominated boiling regimes was developed.

7.2 ANTICIPATED BENEFITS

Even though significant experimental evidence was present for boiling under earth gravity, microgravity and hypergravity conditions, hardly any experimental data was available for pool boiling in the partial gravity regime. Confirmation of quasi-steady boiling behavior with constant temperature heaters during transition period of a parabolic flight maneuver has opened a new direction for partial gravity research. Additional data in the partial gravity boiling regime will help resolve many outstanding issues related to gravity effect on boiling. Extension of the pool boiling regime map to different fluids and conditions will help the boiling community organize the available data and models based on their regions of applicability. The vast quantity of available pool boiling data could be grouped in two categories, namely, buoyancy and surface tension dominated boiling regimes. This effort will resolve many inconsistencies as observed in boiling literature due to correlation of data in different regimes.

The influence of heater size evaluated for different fluids will be quite valuable to anyone contemplating a heater design for variable gravity. The transition between regimes was found independent of gravity level. The next step would be to verify if heat flux values for boiling in low gravity is also similar to heat flux values with small heaters in earth gravity provided the value of L_h/L_c is the same under these two conditions. If true, this might possibly allow simulation of many of the partial and low gravity experiments (surface tension regime) in an earth gravity environment using small heaters.

Visualization of boiling under variable gravity environments and successful development of a gravity scaling parameter will substantiate further research in this direction. Although the scaling parameter was obtained by the analysis of subcooled pool

boiling experimental data for n-perfluorohexane/FC-72, it is expected to be valid for refrigerants with similar properties. Validation of the gravity scaling parameter with different fluids, at different subcoolings, and experimental conditions will initiate performance quantification of phase change based technologies under variable gravity environments eventually leading to their implementation in real life space systems.

NASA's prospective International Space Station (ISS) based Microheater Array Boiling Experiment (MABE) is a further step in the direction of studying pool boiling in an actual space environment. It is important to identify the issues that need attention and should be studied using this ISS based experiment. The results from the current work would help in identifying the appropriate test matrix for the ISS experiment.

7.3 DIRECTIONS FOR FUTURE RESEARCH

Based on the outcome of this dissertation and the current trends in boiling research, some recommendations for future work are summarized below:

1. Visualization of boiling phenomena at various gravity levels with different fluids and under different experimental conditions.
2. Development of a mechanistic model to justify observations from variable gravity experiments.
3. Verification of / improvement in the gravity scaling parameter for pool boiling heat transfer.
4. Additional data to build a comprehensive database for the development of a pool boiling regime map.
5. Further research with high spatial resolution heaters at smaller length scales under earth gravity environment is required to understand boiling in

the surface tension dominated regime. The correlation/comparison of the data with microgravity results would allow a possible unification of heater size and gravity theories.

6. It is required to perform additional experiments with better spatial resolution to identify the fractal patterns in boiling. This would allow a possible extension of single bubble boiling models to actual experimental conditions with multiple bubbles using a fractal pattern approach.
7. Additional numerical studies with a moving liquid-vapor interface are required to understand the origin of thermocapillary convection.

APPENDIX A: Thermocapillary Convection

8.1 INTRODUCTION

Complete understanding of the origin of thermocapillary convection during subcooled boiling has remained elusive to date. Some recent studies have speculated that the presence of dissolved gas inside the vapor bubble leads to the formation of a localized concentration and temperature gradient along the liquid-vapor interface and thus to the onset of thermocapillary convection. These studies reported that the dissolved gas content determines the onset of thermocapillary convection and no thermocapillary motion was observed for subcooled boiling with pure liquid. On the contrary, other experiments performed in reduced gravity suggest that the strength of the thermocapillary convection around the primary bubble in a gas saturated fluid was much weaker than that in a degassed fluid. This work presents a qualitative study of the effects of dissolved gas content, bubble shape and size, and heat transfer coefficient on the strength of thermocapillary convection and offers possible explanations for the existing confusion. Due to the presence of different complex and interrelated mechanisms, the individual mechanisms were decoupled and their overall effect on thermocapillary convection was studied.

8.2 GOVERNING EQUATIONS AND BOUNDARY CONDITIONS

A schematic representing the various phenomena occurring in the liquid is shown in Figure 8.1. Vapor and gas are added to the bubble by the evaporation taking place near the bubble base. The heater surface (solid-gas interface) is at a constant temperature T_{heater}. The ratio of the gas and vapor entering the bubble during evaporation is assumed to be constant, with the molar ratio of the gas and vapor entering the bubble

being equal to the molar ratio in the bulk liquid. The gas and vapor are convected within the bubble and the vapor condenses where the bubble interface temperature is below the saturation temperature. A portion of the gas diffuses into the liquid, leaving the remaining gas to accumulate at the interface. Since the total pressure inside the bubble is constant, a gas concentration gradient is created along the interface leading to a gradient in the partial vapor pressure and hence a gradient in the saturation temperature along the interface. The concentration of the non-condensable gas is higher at the top of the bubble, and the saturation temperature along the interface increases from the top of the bubble to the base where evaporation takes place. These temperature gradients generate the thermocapillary flow in the liquid side from the higher temperature towards the lower temperature, transferring the warm condensed liquid to the bulk liquid.

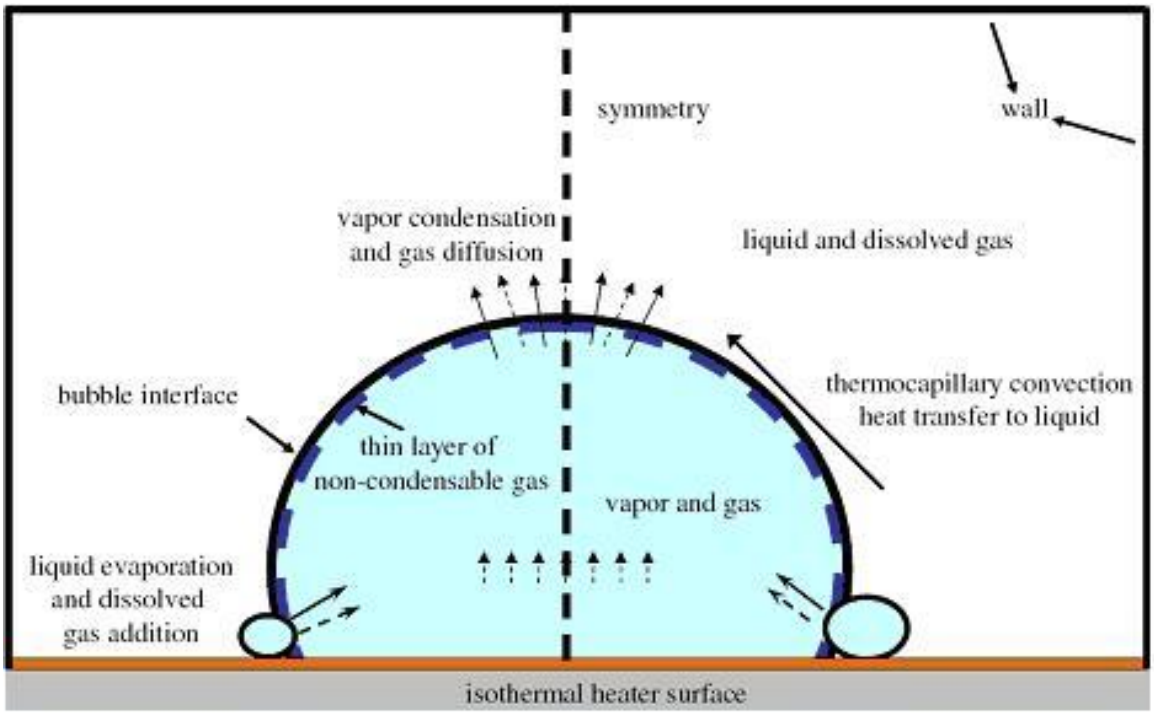

Figure 8.1: Subcooled boiling in reduced gravity condition.

The condensation or evaporation heat transfer occurring at the bubble interface is given by

$$q_i^{"} = h_i (T_v - T_i) \tag{8.1}$$

where the vapor temperature and the heat transfer coefficient at the interface can be calculated as (Carey, 1992).

$$T_v = T_{sat}\left(1 + \frac{2\sigma}{h_{lv}\rho_v R_b}\right) \tag{8.2}$$

$$h_i = \frac{2\hat{\sigma}}{2-\hat{\sigma}} \frac{h_{fg}^2 \rho_v}{T_v} \left(\frac{\overline{M}}{2\pi \overline{R} T_v}\right)^{1/2} \left[1 - \frac{p_v}{2h_{lv}\rho_v}\right] \tag{8.3}$$

Plesset and Sadhal, 1982 suggested that adjustment for curvature in Eq. 8.2 is only applicable to droplets and should not be used for bubbles. There is still some controversy regarding this, however. For the system under consideration here, only a very small pressure difference between the bubble and the bulk liquid results due to the relatively large bubble radius, so this controversy does not affect the current analysis.

The accommodation coefficient $\hat{\sigma}$ is defined as the fraction of molecules crossing the interface in the normal direction that condense/evaporate and are not reflected. For a completely pure fluid, the accommodation coefficient can be assumed to be unity (Mills, 1965). The values of accommodation coefficient for ethanol, methanol, n-propyl alcohol, and water have been reported to be in the range of 0.02 to 0.04 (Paul, 1962), and is known to depend strongly on contamination and the deviation from the kinetic theory model used to define accommodation coefficient. In the presence of dissolved gas more vapor molecules will be reflected at the interface, and the dissolved gas concentration

variation may cause a variation in the value of accommodation coefficient, and hence the heat transfer coefficient, along the interface (Christopher *et al.*, 2001).

Based on Eq. 8.1, it can be said that when the interfacial temperature is higher than the vapor temperature inside the bubble, evaporation occurs and heat is added to the bubble. On the other hand, when the interfacial temperature is lower than the vapor temperature, condensation takes place and heat is released to the liquid. For boiling in a subcooled liquid, some part of the bubble interface near the base will see evaporation taking place while condensation will occur along the rest of the interface. Eq. 8.4 -8.7 represents the four conservation law for a steady state condition.

The first equation is the mass conservation equation for the liquid and the gas. The second and the third equations are the momentum and the energy equation for the liquid. The last equation is the gas diffusion equation in the liquid domain.

$$\nabla \cdot \left(\rho_{l,g} \vec{V}\right) = 0 \tag{8.4}$$

$$\vec{V} \cdot \nabla \vec{V} = \nu \nabla^2 \vec{V} - \frac{\nabla p}{\rho_l} = 0 \tag{8.5}$$

$$\vec{V} \cdot \nabla \left(C_p T\right) = \frac{1}{\rho_l} k \nabla^2 T \tag{8.6}$$

$$\vec{V} \cdot \nabla \left(c_g\right) = \alpha_D \nabla^2 c_g \tag{8.7}$$

Though the gas diffusion equation does not directly influence the flow field significantly, it is a major factor in determining the gas concentration profile along the bubble interface and hence the interfacial temperature which finally drives the thermocapillary convection. The boundary conditions at the five boundaries of the liquid domain are shown in Table 8.1.

Table 8.1: Boundary condition for the five boundaries

Boundary	Fluid	Thermal	Gas Diffusion
Heater	No slip	$T = T_{heater}$	Insulated
Side Wall	No slip	Adiabatic	$c_g =$ constant
Top Wall	No slip	$T = T_{bulk}$	$c_g =$ constant
Symmetry	$u = 0$ and $\frac{\partial v}{\partial x} = 0$	$\frac{\partial T}{\partial x} = 0$	$\frac{\partial c_g}{\partial x} = 0$
Interface	$\mu \frac{\partial \vec{u}}{\partial \vec{n}} = \frac{d\sigma}{dT} \frac{\partial T}{\partial \vec{t}}$	$q_i^{"} = h_i (T_v - T_i)$	$c_g = f(T_i, p_v)$

8.3 NUMERICAL MODEL

A simplified numerical model was developed to qualitatively study the problem of subcooled boiling in the absence of gravity and understand the effect of the dissolved gas on the flow field and heat transfer. The gas concentration was assumed to only affect the flow field by causing a change in the heat transfer coefficient. As discussed earlier, with increasing gas concentration inside the bubble, the accommodation coefficient will decrease, lowering the value of heat transfer coefficient. Moreover, the interface temperature is also directly related to the gas content at the interface.

The heat transfer coefficient was calculated using Eq. 8.3 for the pure vapor case, and then the value was lowered in steps to qualitatively incorporate the effect of gas. This effect was taken into account by comparing the two extreme cases, the gas saturated bubble which is larger in size and can be assumed to have an insulated bubble interface due to very small evaporation and condensation rates, and a pure vapor bubble with a very high heat transfer coefficient calculated using Eq. 8.3 which is much smaller in size.

It was observed in the experiments that the bubble in the degassed case was much flatter than the spherical shape observed in the gas saturated case (Henry *et al.*, 2006). The strong flow in the degassed case applies a reaction force on the bubble and changes its shape. Moreover, surface tension variation results in non-uniform radius of curvature along the interface (Carey, 1992 and Christopher *et al.*, 2001). Thus the bubble is never ideally spherical in shape and changes with the flow and temperature profile. In this study, spherical bubble will be assumed for the rest of the analysis.

The governing equations and the boundary conditions are the same as described in Table 8.1 except that the gas diffusion was not considered in the simulation and the effect was incorporated by varying the heat transfer coefficient. The commercially available software COMSOL 3.3^{TM} was used to simulate the problem. The surface tension stresses at the interface were modeled using the weak form boundary condition. The results of the software were validated by exactly reproducing the results of Zebib *et al.*, 1985. An effort was made to choose values of different parameters such that they represent the experimental conditions of Henry *et al.*, 2006 as far as possible. Table 8.2shows the bubble interface phase change parameters and subcooling and wall superheat conditions.

Table 8.2: Bubble interface phase change heat transfer parameters

$h_i \ (W/m^2K)$	$T_{bulk} \ (K)$	$\Delta T_{sat} \ (K)$	$p_{total} \ (Pa)$	$\hat{\sigma}$
3.59e4	28	28	101,325	0.03

Table 8.3: Physical parameters at the reference temperature

k	ρ_l	c_p	$d\sigma/dT$	μ
(W/mK)	(kg/m^3)	(W/kgK)	(N/mK)	(kg/ms)
0.0532	1680	1107	-1.8e-4	4.35e-4

The values of the physical parameters (Table 8.3) were calculated at the reference temperature of 329.5 K. Though n-perfluorohexane was used in the actual experiment, FC-72 was used to calculate the physical properties at the above mentioned reference temperature. This will not have any significant effect on the analytical results since FC-72 is simply an isomeric mixture of n-perfluorohexane with very similar properties.

As mentioned earlier, the effect of the size of the bubble was studied by varying the bubble diameter from a small value of 0.01 mm to a large bubble of diameter 7.68 mm. Thus, the vapor temperature inside the bubble will vary based on Eq. 8.2. The temperature of the vapor inside the bubble was also calculated for all these different cases and is tabulated below (Table 8.4).

Table 8.4: Vapor temperature *(K)* as a function of bubble diameter

0.01*mm*	0.03*mm*	0.06*mm*	0.12*mm*	$_D$>0.24*mm*
330.56	329.95	329.80	329.72	~329.65

8.4 RESULTS AND DISCUSSION

Steady state simulations of the thermocapillary flow around bubble of various sizes with different amounts of dissolved gas for subcooled boiling under zero gravity

situations were performed. The streamline and velocity profiles for the 0.01 mm and 7.68 mm diameter bubble ($\theta_{contact} = 42.5^0$) are shown in Figure 8.2 (the geometry in the second case is scaled by a factor of 768 to increase the bubble size for clarity). The heat transfer coefficient for the smaller bubble was taken to be 35,900 W/m2-K (Eq. 8.3) while the larger bubble was assumed to be insulated. The larger bubble was observed in the case of gas saturated liquid and simulates a gassy bubble with negligible evaporation and condensation. This was done to obtain a qualitative comparison between the current simulation results and the experimental results of Henry et al., 2006.

The maximum velocity at the bubble top, i.e. along the symmetry boundary for the smaller pure vapor bubble was around 0.094 m/s (Figure 8.2a). This typically high velocity agrees qualitatively with the experimental observations of Henry et al. where they observed similar behavior for the case of n-perfluorohexane at similar subcooling and wall superheat. For the larger gas bubble formed in the case of gas saturated liquid under similar conditions, the maximum velocity at the bubble top was observed to be around 0.028 m/sec (Figure 8.2b). Though this value seems to be higher than the velocity observed during the experiment, it is considerably smaller than that for the pure vapor case. The differences in the behavior for the gas saturated case could be due to the possible effect of gradient in the gas concentration along the bubble interface and hence a non-constant heat transfer coefficient.

Table 8.5 shows the bubble top velocities for various bubble sizes and heat transfer coefficients. For a particular size bubble, the strength of the thermocapillary convection was observed to increase with the heat transfer coefficient, reach a maximum and then decrease. The value of the heat transfer coefficient at the maximum

thermocapillary convection was observed to decrease with an increase in the size of the bubble. For a given heat transfer coefficient, the strength of the thermocapillary convection first increased, reached a peak, and then decreased with increasing bubble size. The peak was observed to occur at lower diameters with increasing heat transfer coefficient.

The variation of velocity with heat transfer coefficient and radius of the bubble clearly show that thermocapillary convection does not monotonically change with non-condensable gas content. This variation in the bubble top velocity lends credence to the hypothesis that the strength of thermocapillary convection is not only a function of the dissolved gas content, but depends on other parameters such as heat transfer coefficient and temperature gradient as well. Figure 8.3 shows the temperature variation along the bubble interface for the two cases, a pure vapor bubble of 0.01mm radius and a gas saturated larger bubble of 7.68 mm diameter.

It can be clearly seen that the temperature drop for the smaller vapor bubble occurs throughout the interface and is almost constant. For the larger gas saturated bubble, most of the drop occurs near the bubble base and rest of the interface has very small temperature gradient. Moreover, because of the very small size of the pure vapor bubble, the gradient is much higher for the smaller bubble leading to more thermocapillary convection. This might also be the cause of the negligible thermocapillary convection observed for the gas saturated case where the bubble is larger in size.

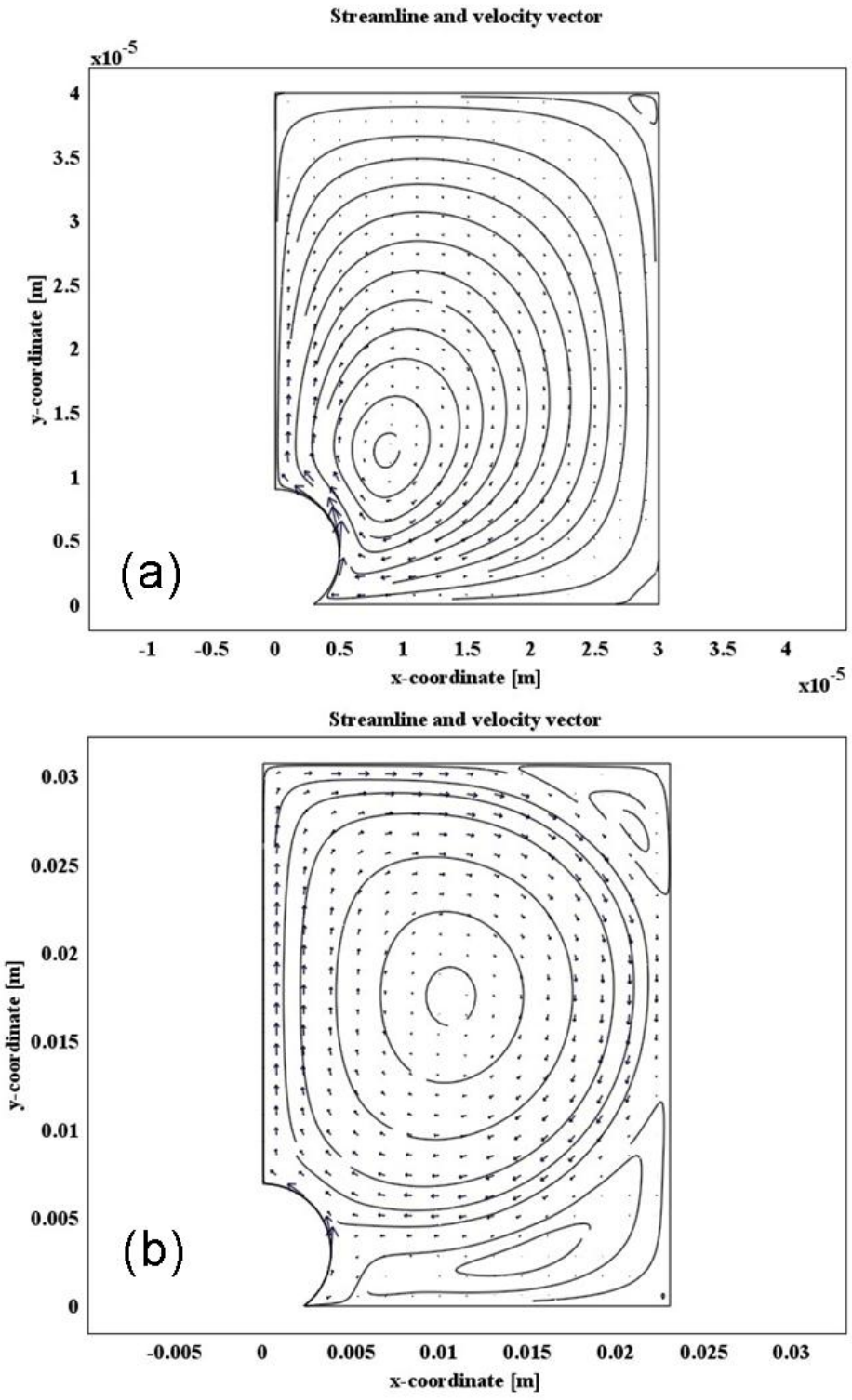

Figure 8.2: Stream line and velocity profile for (a) 0.03mm and (b) 7.68 mm bubble.

Table 8.5: Maximum velocity at the bubble top for a range of parameters

	Velocity at the bubble top *(m/s)*					
$h_i (W/m^2K)$	0	10	100	1000	10,000	35,900
D(mm)						
0.01	0.031	0.031	0.033	0.047	0.090	0.094
0.03	0.038	0.043	0.044	0.066	0.101	0.068
0.06	0.057	0.057	0.061	0.080	0.093	0.047
0.12	0.066	0.067	0.069	0.080	0.056	0.036
0.24	0.067	0.067	0.068	0.076	0.051	0.019
0.48	0.062	0.062	0.063	0.066	0.037	0.006
0.96	0.056	0.056	0.056	0.053	0.025	0.003
1.92	0.047	0.047	0.047	0.043	0.016	
3.84	0.037	0.037	0.037			
7.68	0.028	0.028				

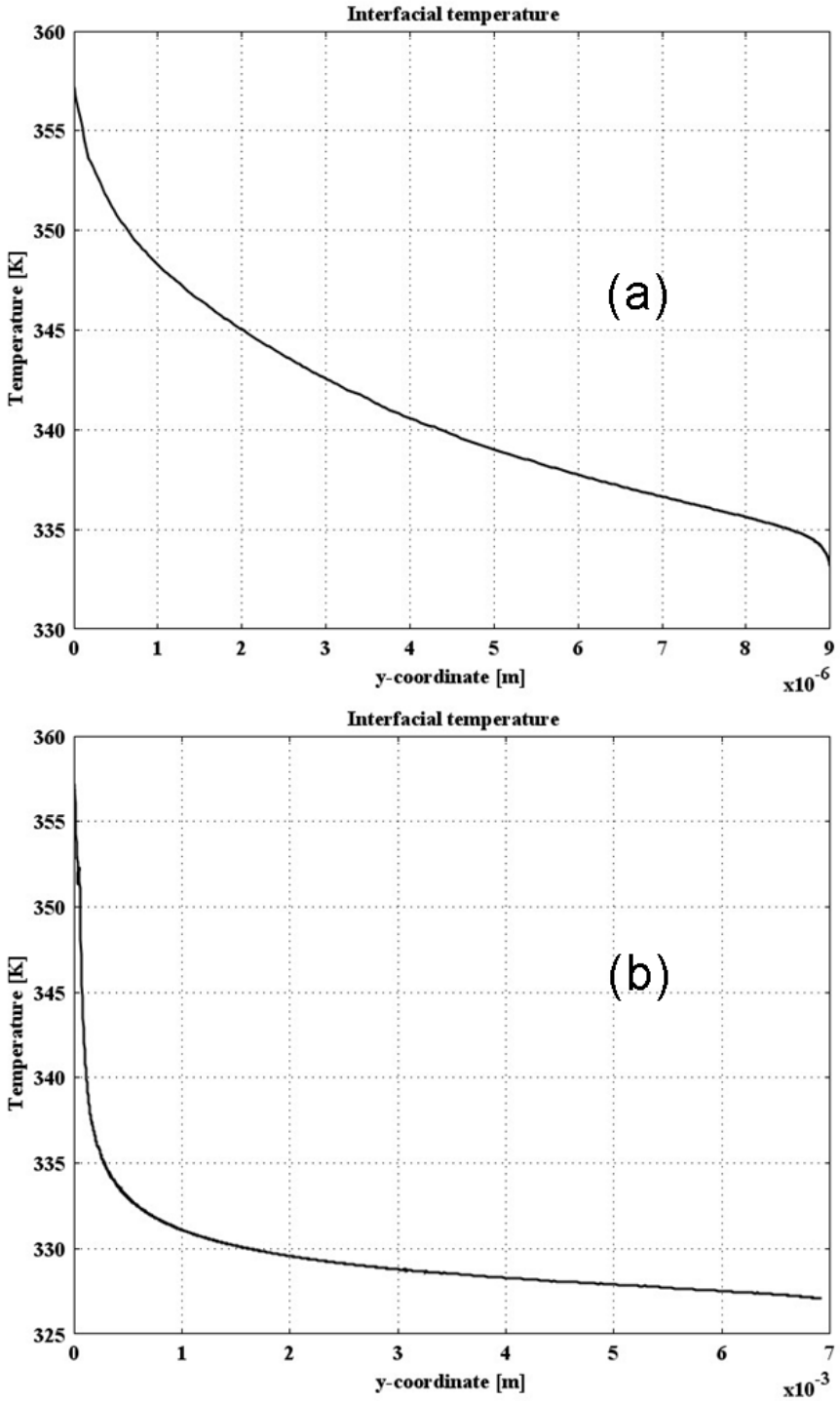

Figure 8.3: Temperature as a function of y-coordinate along the bubble interface: (a) pure vapor bubble of 0.01 mm radius and a (b) gas saturated bubble of 7.68 mm radius.

Although these results and analysis do not directly correspond to actual experimental situation until and unless the gas concentration along the bubble is simulated more precisely, they do provide some insight into the role played by the heat transfer coefficient and the bubble size in the determination of the strength of the thermocapillary convection. Straub, 2002 proposed that the gas concentration increases towards the bubble top and hence the saturation vapor pressure and saturation temperature, which is the interface temperature, decreases. In all the above cases, the gas concentration was assumed to be uniform throughout the bubble providing a uniform heat transfer coefficient.

8.4.1 Effect of Variable Heat Transfer Coefficient

To understand the dissolved gas effect more precisely, the gas concentration was varied linearly from the bottom to the top. Instead of a constant heat transfer coefficient assumption, the heat transfer coefficient was varied linearly with y-location along the bubble. The value at the bubble base was assumed to be the maximum and calculated using Eq. 8.3. The results are presented in Figure 8.4. Though the variation in the actual case might not be exactly similar and the value at the bubble top may be different, this case is better representative of the actual condition when compared to the constant heat transfer coefficient analysis. The results show an increase in the magnitude of the maximum velocity at the bubble top by about 40% when compared to the constant heat transfer coefficient case, suggesting that the resulting variation in heat transfer coefficient influences the thermocapillary flow in addition to the dissolved gas content.

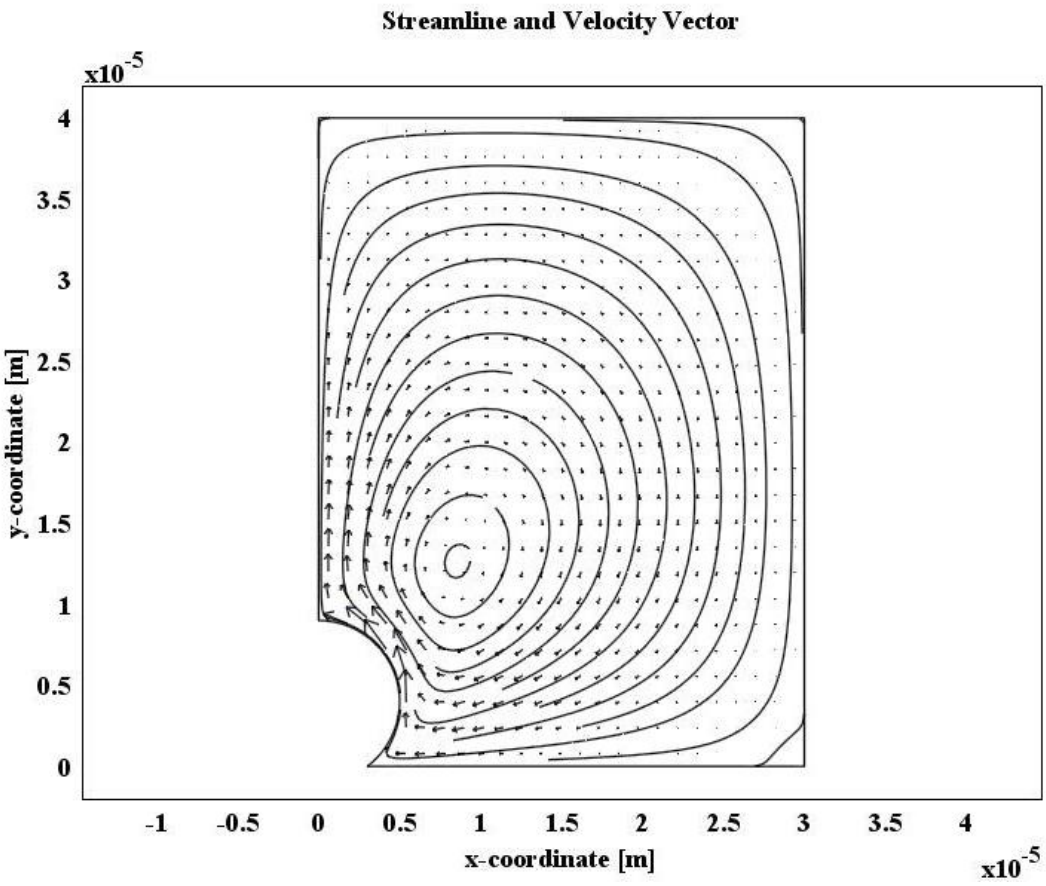

Figure 8.4: Stream line and velocity profile with the variable h_i along the bubble interface for 0.01 mm bubble.

8.4.2 Effect of Bubble Shape

In the experiments performed by Henry *et al.*, 2006, it was observed that the bubble was flat for the pure vapor case. To simulate the actual experimental conditions, the contact angle of the bubble for the smaller radius case was changed from $\theta_{contact} = 42.5^0$ to $\theta_{contact} = 115^0$. Again, this resulted in the increase in the magnitude of the maximum velocity at the bubble top by about 53% when compared to sphere like shape considered in the previous simulations (Figure 8.5).

Thus, it can be said that though the actual condition is complex and needs to be studied in more detail, the strength of the thermocapillary convection is an indirect function of dissolved gas content, which in turn determines the variation in heat transfer coefficient and the bubble shape and size.

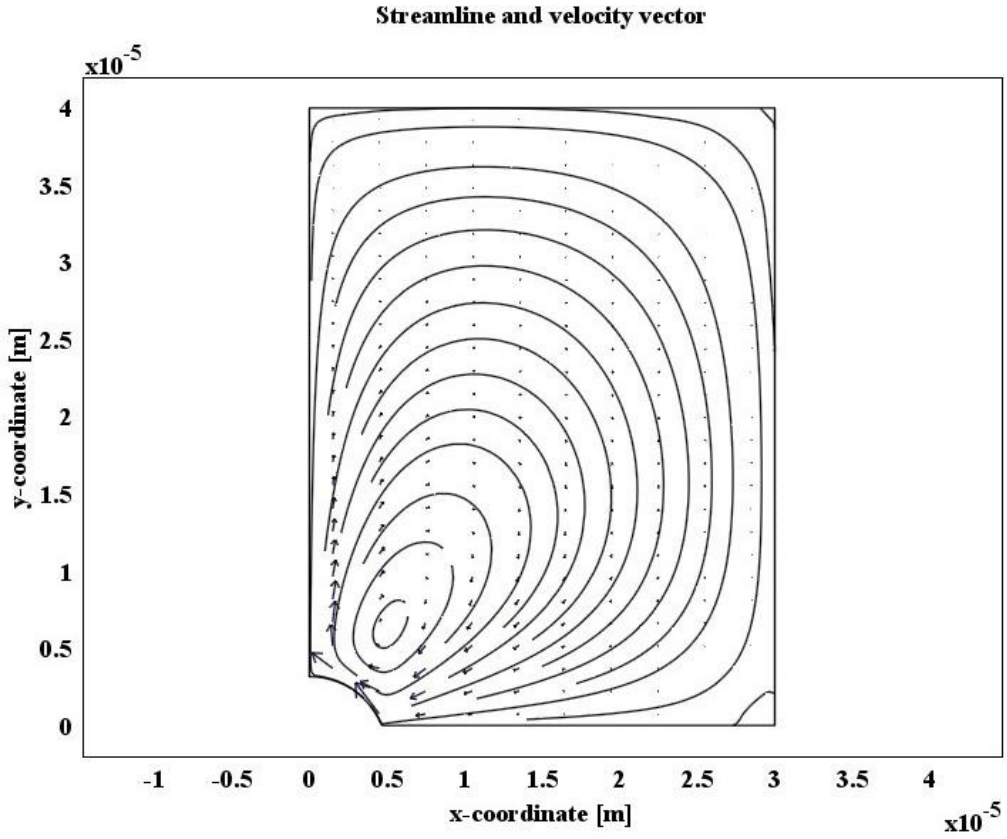

Figure 8.5: Stream line and velocity profile for a flat bubble.

8.5 SUMMARY

The present work has explored the effect of dissolved gas on subcooled boiling. The results obtained for different bubble radii and heat transfer coefficients suggest that the strength of thermocapillary convection is determined by the combined effect of the dissolved gas concentration, bubble shape and size, and the variation in evaporation or

condensation heat transfer coefficient along the bubble interface. While the increase in dissolved gas content helps in the development of the required temperature variation along the bubble interface, the resulting increase in size by orders of magnitude lowers the temperature gradient and heat transfer across the interface. This ultimately results in a lowering of the strength of the thermocapillary convection in the gassy bubble case.

Bibliography

Aparajith, H. S., Dhir, V. K., Warrier, G., and Son, G., 2003, "Numerical Simulation and Experimental Validation of the Dynamics of Multiple Bubble Merger during Pool Boiling under Microgravity conditions," *Microgravity Transport Processes Conference*, Davos, Switzerland, Sep. 14-19.

Arlabosse, P., Tadrist, L., Tadrist, H., and Pantaloni, J., 2000, "Experimental Analysis of the Heat Transfer Induced by Thermocapillary Convection around a Bubble," *ASME J. Heat Transfer*, **122**, pp. 66-73.

Bakhru, N., and Lienhard, J. H., 1972, "Boiling from Small Cylinders," *Int. J. Heat Mass Transfer*, **15**, pp. 2011–2025.

Brusstar, M. J., and Merte, H., Jr., 1994, "Effects of Buoyancy on the Critical Heat Flux in Forced Convection," *AIAA Journal of Thermophysical Heat Transfer*, **8** (2), 322-328.

Barthes, M., Reynard, C., Santini, R., and Tadrist, L, 2007, "Non-condensable Gas Influence on the Marangoni Convection During a Single Vapor Bubble Growth in a Subcooled Liquid," *EPL*, **77**, pp. 14001-p1-14001-p5.

Carey, V. P., 1992, "Liquid-vapor Phase-Change Phenomena," Hemisphere Publication Corporation.

Chang, Y. P, 1957, "A Theoretical Analysis of Heat Transfer in Natural Convection and in Boiling," *Trans. ASME*, **79**, pp. 1501-1513.

Chang, J. Y., and You, S. M., 1996, "Heater Orientation Effects on Pool Boiling of Micro-Porous-Enhanced Surfaces in Saturated FC-72," *ASME Journal of Heat Transfer*, **118**, pp. 937-943.

Chiaramonte, F. P., and Joshi, J. A., 2004, "Workshop on Critical Issues in Microgravity Fluids, Transport, and Reaction Processes in Advanced Human Support Technology," Technical report, NASA/TM—2004-212940.

Christopher, D. M., Wang, B. X., and Peng, X. F., 2001, "Convection and Evaporation of Microlayer Underneath Bubble Under Microgravity," *Heat Transfer-Asian Research*, **30** (1), pp. 1-10.

Cole, R., 1967, "Bubble Frequencies and Departure Volumes at Subatmospheric Pressures," *AIChE Journal*, **13**, pp. 779-783.

Colemna, H. W., and Steele, W., 1999, "Experimentation and Uncertainty for Engineers," Wiley-Interscience, ISBN-10: 0471121460.

Cole, R., and Rohsenow, W. M., 1968, "Correlation of Bubble Departure Diameters for Boiling of Saturated Liquids," *Chem. Eng. Prog. Symp*. Series, **65,** pp. 211-213.

Costello, C. P., and Tuthill, W. E., 1961, "Effect of Acceleration on Nucleate Pool Boiling," *Chem. Eng. Prog. Sym*., **57**, pp. 189-196.

Di Marco, P., 2003, "Review of Reduced Gravity Boiling Heat Transfer: European Research," *Jpn. Soc. Microgravity Appl. J*., **20**(4), pp. 252-263.

Di Marco, P. and Grassi, W., 2000, "Pool Boiling in Microgravity: Assessed Results and Open Issues," *Third European Thermal-Sciences Conference*, September 10–13, 2000, ETS, Pisa, Italy.

Drew, T. B., and Mueller, C., 1937, "Boiling", *Trans. AIChE*, **33**, p. 449.

Foster, H. K., and Zuber, N., 1955, "Dynamics of Vapor Bubbles and Boiling Heat Transfer," *AIChE Journal*, **1**, pp. 531-535.

Foster, H. K., and Grief, R., 1959, "Heat Transfer to a Boiling Liquid – Mechanisms and Correlations," *ASME Journal of Heat Transfer*, **81**, p. 45.

Fritz, W., 1935, "Berechnung des Maximalvolume von Dampfblasen," *Phys. Z.*, **36**, pp. 379-388.

Haramura, Y., Katto, Y., 1983, "A New Hydrodynamic Model of Critical Heat Flux, Applicable Widely to Both Pool Boiling and Forced Convective Boiling on Submerged Bodies in Saturated Liquid," *International Journal of Heat and Mass Transfer*, **26**, pp. 389-399.

Henry, C. D., and Kim, J., 2004, "A Study of the Effects of Heater Size, Subcooling, and Gravity Level on Pool Boiling Heat Transfer," *International Journal of Heat and Fluid Flow*, **25**, pp. 262-273.

Henry, C. D., Kim, J., and McQuillen, J., 2006, "Dissolved Gas Effects on Thermocapillary Convection During Subcooled Boiling in Reduced Gravity Environments," *Heat and Mass Transfer*, **42**, pp. 919-928.

Honda, H., Takamastu, H., and Wei, J. J., 2002, "Enhanced Boiling of FC-72 on Silicon Chips with Micro-Pin-Fins and Submicron-Scale Roughness," *ASME Journal of Heat Transfer*, **124** (2). pp. 383-390.

Hsu, Y., 1962, "An Analytical and Experimental Study of the Thermal Boundary Layer and the Ebullition Cycle in Nucleate Boiling," NASA TN-D-594, 1962.

Iida, Y., Okuyama, K., and Sakurai, K., 1994, "Boiling Nucleation on a Very Small Film Heater Subjected to Extremely Rapid Heating," *Int. J. Heat Mass Transfer*, **37**, pp. 2771–2780.

Incropera, F. P., Dewitt, D. P., Bergman, T. T., and Lavine, A. S., 2007, "Fundamentals of Heat and Mass Transfer," Sixth ed., Wiley, p.8, Chap. 1.

Ivey, H. J., 1967, "Relationships between Bubble Frequency, Departure Diameter and Rise Velocity in Nucleate Boiling," *Int. J. Heat and Mass Transfer*, **10**, pp. 1023-1040.

Jakob, M., and Fritz, W., 1931, "Versuche uber den Verdampfungsvorgang," Forsch. Ingenieurwes, **2**, pp. 435-447.

Kannengieser, O., Colin, C., Bergez, W., and Lacapere, J., 2009, "Nucleate Pool Boiling on a Flat Plate Heater Under Microgravity Conditions: Results of Parabolic Flight, and Development of a Correlation Predicting Heat Flux Variation due to Gravity," *Proceeding of the 7th ECI International Conference on Boiling Heat Transfer*, Florianopolis, Brazil, May 3-7, 2009.

Kandilkar, S. G., 2001, "A Theoretical Model to Predict Pool Boiling CHF Incorporating Effects Contact Angle and Orientations," *ASME Journal of Heat Transfer*, **123**, pp. 1071-1079.

Kim, J., Benton, 2002, "Highly Subcooled Pool Boiling Heat Transfer at Various Gravity Levels," *International Journal of Heat and Fluid Flow*, **23**, pp.497-508.

Kim, J., Benton, J. F. and Wisniewski, D., 2002, "Pool Boiling Heat Transfer on Small Heaters: Effect of Gravity and Subcooling," *International Journal of Heat and Mass Transfer*, **45** (9), pp. 3921-3934.

Kim, J., 2003, "Review of Reduced Gravity Boiling Heat Transfer: US Research," *Jpn. Soc. Microgravity Appl. J.*, **20** (4), pp. 264-271.

Kim, J., Di Marco, P., Ohta, H., and Stephan, P., "Phase Change Heat Transfer in Microgravity," http://www8.nationalacademies.org/SSBSurvey/DetailFileDisplay.aspx?id=274.

Kirishenko, Ya. A., and Cherniakov, P. S., 1973, "Determination of the First Critical Thermal Flux on Flat Heaters," *J. Eng. Physics*, **20**, 699-702.

Kutateladze, S. S., 1948, “On the Transition to Film Boiling Under Natural Convection,” *Kotloturbostroenie,* No. 3, pp. 10-12.

Kutateladze, S. S., Valukuna, N. V., and Gogonin, I. I., 1967, “Influence of Heater Size on the Peak Heat Flux in Saturated Liquids,” *Inzh. Phyx. Zh*., **12**, pp. 569-575.

Lin, L., and Pisano, A., 1991, “Bubble Forming on a Microline Heater,” *Proc. ASME Winter Annual Meeting, Dynamic Systems and Control Division*, **32**, pp. 147–163.

Lee, H. S., and Merte, Jr. H., 1997, “Pool Boiling Curve in Microgravity,” *Journal of Thermophysics and Heat Transfer,* **11**(2), pp. 216-222.

Malenkov, I. G., 1971, “The Frequency of Vapor Bubble Separation as a Function of Bubble Size,” *Fluid Mech.-Sov. Res.*, **1**, pp. 36-42.

Marek, R., and Straub, J., 2001, “The Origin of Thermocapillary Convection in Subcooled Nucleate Pool Boiling,” *International Journal of Heat and Mass Transfer*, **44**, pp. 619-632.

Merte, Jr. H., and Clark, J. A., 1961, “Pool Boiling in Accelerating Systems,” *ASME Journal of Heat Transfer*, **83**, pp. 233-242.

Merte, H., and Chiaramonte, F. P., 2001, “Pool Boiling Experiment,” NASA Glenn Research Center Video, GRC 396, 2001.

Mikic, B. B., and Rohsenow, W. M., 1969, “Bubble Growth Rates in Pure and Binary Systems: Combined Effect of Relaxation and Evaporation Microlayers,” *Progress in Heat and Mass Transfer*, **2**, pp. 283-292.

Mills, A. F., 1965, “The Condensation of Steam at Low Pressure,” Technical Report on NSF GP-2520. 39: Space Sciences Laboratory, University of California, Berkeley.

Nukiyama, S., 1934, "The Minimum and Maximum Values of Heat Q Transmitted from Metal to Boiling Water Under Atmospheric Pressure," *J. Jap. Soc. Mech. Eng*., **37**, pp. 367-374.

Ohta, H., Kawaji, M., Azuma, H., Kakehi, K., and Morita, T. S., 1998, "Heat Transfer in Nucleate Pool Boiling Under Microgravity Condition," *Heat Transfer*, **2**, pp. 401-406.

Ohta, H., 2003, "Review of Reduced Gravity Boiling Heat Transfer: Japanese Research," *Jpn. Soc. Microgravity Appl. J*., **20** (4), pp. 272-285.

Oka, T., Abe, Y., Tanak, K., Mori, Y. H., and Nagashima, A., 1992, "Observational Study of Pool Boiling in Microgravity," *JSME Int. J*., **35**(2), p. 280.

Ostrach, S., 1982, "Natural Convection Heat Transfer in Cavities and Cells," *In the proceedings of the 7 th International Heat Transfer Conference*, **1**, pp. 365-379.

Paul, B., 1962, "Compilation of Evaporation Coefficients," *ARS Journal*, **32**, pp. 1321-1328.

Plesset, M. S., and Sadhal, S. S., 1982, "On the stability of bubbles in liquid-gas solutions," *Appl Sci. Res*, **38**, pp. 133-141.

Product Manual, FLORINERT® Electronic Liquid, 3M Center, St. Paul, MN.

Rainey, K. N., You, S. M., and Lee, S., 2003, "Effect of Pressure, Subcooling, and Dissolved Gas on Pool Boiling Heat Transfer from Microporous Surfaces in FC-72," *ASME Journal of Heat Transfer*, **125**, pp. 75-83.

Rohsenow, W. M., 1962, "A Method of Correlating Heat Transfer Data for Surface Boiling of Liquids," *Trans. ASME*, **84**, pp. 969-976.

Rohsenow, W. M., and Griffith, P., 1956, "Correlation of Maximum Heat Transfer for Boiling of Saturated Liquids," *Chem. Eng. Prog. Symp. Series*, **52** (18), p. 47.

Ruckenstien, E., 1963, "Physical Model for Nucleate Boiling Heat Transfer from Horizontal Surface," *Appl. Mech. Rev.,* **16**, Rev. 6055.

Rule, T. D., and Kim, J., 1999, "Heat Transfer Behavior on Small Heaters During Pool Boiling of FC-72," *ASME Journal of Heat Transfer,* **121**(2), pp. 386-393.

Stephan, K., and Abdelsalam, M., 1980, "Heat Transfer Correlations for Natural Convection Boiling," *Internal Journal of Heat and Mass Transfer,* **23**, pp. 73-87.

Siegel, R., 1968, "Effects of Reduced Gravity on Heat Transfer," *Advances in Heat Transfer,* **4**, pp. 143-227.

Siegel, R., and Howell, J. R., 1965, "Critical Heat Flux for saturated Pool Boiling from Horizontal and Vertical wires in reduced gravity," NASA Tech. Note TND-3123.

Straub, J., and Vogel, B., 1992, "Boiling Under Microgravity Conditions," *Proc. 1st European Symposium in Space,* ESA SP-353, p.269.

Straub, J., Zell, M., and Vogel, B., 1999 "Pool Boiling in Reduced Gravity Field," *Heat Transfer,* **1**, pp. 91-112.

Straub, J., 2001, "Boiling Heat Transfer and Bubble Dynamics in Microgravity," *Advances in Heat Transfer,* **35**, pp. 57-172.

Straub, J. 2002, "Origin and Effect of Thermocapillary Convection in Subcooled Boiling: Observations and Conclusions from Experiments Performed at Microgravity," *Annals of the New York Academy of Sciences,* **974**, pp. 348-363.

Sun, K. H., and Lienhard, J. H., 1970, “The Peak Pool Boiling Heat Flux on Horizontal Heaters,” *Int. J. Heat Mass Transfer*, **13**, pp. 1425-1439.

Tien, C. C., 1962, “A Hydrodynamic Model for Nucleate Pool Boiling,” *International Journal of Heat and Mass Transfer*, **5**, pp. 533-540.

Verkin, B. J., and Kirichenko, Y. A., 1976, “Heat Transfer Under Reduced Gravity Conditions,” *Acta Astronautica*, **3**, pp. 471-480.

Yaddanapuddi, N., and Kim, J., 2000, "Single Bubble Heat Transfer in Saturated Pool Boiling of FC-72", *Multiphase Science and Technology*, **12** (3-4), pp. 47-63.

Yang, S. M., Xu, Z. M., Wang, J. W., and Zhao, X. T., 2001, “On the Fractal Description of Active Nucleation Site Density for Pool Boiling,” *Internal Journal of Heat and Mass Transfer*, **44**, 2783-2786.

Yin, Z., Prosperetti, A., and Kim, J., 2004, “Bubble Growth on an Impulsively Powered Microheater,” *Int. J. Heat Mass Transfer*, **47**, pp. 1053–1067.

You, S. M., Simon, T. W., Bar-Cohen, A., and Hong, Y. S., 1995, “Effects of Dissolved Gas on Pool Boiling of a Highly Wetting Fluid,” *ASME Journal of Heat Transfer*, **117**, pp. 687-692.

Yu, B., and Cheng, P., 2002, “A Fractal Model for Nucleate Pool Boiling Heat Transfer,” *ASME Journal of Heat Transfer*, **124**, 1117-1124.

Xiao, B., and Yu, B., 2007, “A Fractal Model for Critical Heat Flux in Pool Boiling,” *Internal Journal of Thermal Sciences*, **46**, 426-433.

Zebib, A., Homsy, G. M. & Meiburg, E. 1985, “High Marangoni number convection in a square cavity,” *Phys. Fluids*, **28**(12), pp. 3467-3476.

Zuber, N., 1959, “Hydrodynamic Aspects of Boiling Heat Transfer,” *AEC Rep.,* AECU-4439, June.

Zuber, N, 1963, “Nucleate Boiling – The Region of Isolated Bubbles – Similarity with Natural Convection,” *Int. J. Heat and Mass Transfer*, **6**, pp. 53-65.